Dissertation

submitted to the

Combined Faculties of the Natural Sciences and Mathematics

of the Ruperto-Carola-University of Heidelberg, Germany

for the degree of

Doctor of Natural Sciences

Put forward by

M.Sc. Sonja Isabella Friman

born in Darmstadt

Oral examination: April 22, 2020

Laboratory investigations of concentration and wind profiles close to the wind-driven wavy water surface

Referees: Prof. Dr. Bernd Jähne

Prof. Dr. André Butz

Abstract

Studying the air- and water-sided boundary layers is vital to understand the exchange of momentum and gases between ocean and atmosphere. While the water-sided mass boundary layer can be studied with several imaging techniques, no such technique was available for the air side. In the scope of this thesis, a laser-induced fluorescence (LIF) technique was developed, where the tracer sulfur dioxide (SO_2) is illuminated with a UV laser and its fluorescence is imaged, yielding near-surface concentration profiles of SO_2 with a resolution of up to 20 μm. The profiles can be used to quantify reliable boundary layer thicknesses and gas transfer velocities, which was shown in a proof-of-principle experiment in a wind-wave tank.

In a second experiment at two fetches of a larger wind-wave tank, the SO_2 LIF technique was employed together with particle streak velocimetry, measuring local wind speeds, and surface elevation measurements. This experiment is the first simultaneous and collocated measurement of mass and momentum transfer in the air-sided mass boundary layer. The mean concentration and wind speed profiles as well as their fluctuations were analyzed and compared. Including the surface elevations, the modulation of the transport processes by waves was analyzed, resulting in wave-phase averaged transfer velocities.

Zusammenfassung

Die Untersuchung der luft- und wasserseitigen Grenzschichten ist wichtig für das Verständnis vom Transport von Impuls und Gasen zwischen Ozean und Atmosphäre. Während die wasserseitige Grenzschicht mit mehreren bildgebenden Techniken untersucht werden kann, gab es noch keine derartige Technik für die Luftseite. Im Rahmen dieser Arbeit wurde eine laserinduzierte Fluoreszenz (LIF)-Technik entwickelt, in der der Tracer Schwefeldioxid (SO_2) mit einem UV-Laser beleuchtet und seine Fluoreszenz abgebildet wird, was oberflächennahe Konzentrationsprofile von SO_2 mit einer Auflösung von bis zu 20 μm ergibt. Die Profile können für die zuverlässige Quantifizierung von Grenzschichtdicken und Gastransfergeschwindigkeiten genutzt werden, was in einer Machbarkeitsstudie in einem Wind-Wellen-Kanal gezeigt wurde.

In einem zweiten Experiment an zwei Fetches in einem größeren Wind-Wellen-Kanal wurde die SO_2 LIF-Technik zusammen mit particle streak velocimetry, welche lokale Windgeschwindigkeiten misst, und Messung der Höhe der Oberfläche eingesetzt. Dieses Experiment ist die erste zeitlich und örtlich simultane Messung von Massen- und Impulstransfer in der luftseitigen Massengrenzschicht. Die gemittelten Konzentrations- und Windprofile sowie ihre Fluktuationen wurden analysiert und verglichen. Mithilfe der Oberflächenhöhen wurde auch die Modulation der Transportprozesse durch die Wellen analysiert. Dies resultierte in nach der Wellenphase gemittelten Transfergeschwindigkeiten.

Contents

1 Introduction **1**

2 Theory **5**
2.1 Mass and Momentum Transport Mechanisms . . . 5
2.1.1 Diffusion . . . 5
2.1.2 Turbulence . . . 7
2.2 Air-Water Mass Transfer . . . 9
2.2.1 Mean Wind Profiles . . . 10
2.2.2 Transfer Velocity and Resistance . . . 13
2.2.3 Concentration Profiles . . . 14
2.2.4 Transfer Partitioning . . . 16
2.3 Transfer Models . . . 17
2.3.1 Stagnant Film Model . . . 17
2.3.2 Turbulent Diffusion . . . 17
2.3.3 Surface Renewal Model . . . 19
2.4 Interaction of Light and Matter . . . 20
2.4.1 Absorption . . . 20
2.4.2 Fluorescence . . . 22
2.5 Sulfur Dioxide in Water . . . 23

3 Methods **25**
3.1 Laser Induced Fluorescence of Sulfur Dioxide . . . 25
3.2 Particle Streak Velocimetry . . . 27
3.3 Surface Detection . . . 28
3.3.1 Curvilinear Coordinates . . . 29
3.4 Mass Balance . . . 30

4 Setup **35**
4.1 Wind-Wave Tanks . . . 35
4.1.1 Benjamin-tank . . . 36
4.1.2 Lizard-tank . . . 37
4.1.3 Water . . . 41
4.2 Overview of the Optical Setup at the Lizard-tank . . . 44
4.3 LIF Setup . . . 46
4.3.1 UV Laser . . . 46
4.3.2 UV Sensitive Cameras . . . 49

4.4 Surface Detection (LHC) Setup . . . 50
4.5 Flow Visualization (PSV) Setup . . . 52
4.6 Triggering . . . 53
4.7 Absorption Spectroscopy . . . 54

5 Calibration and Experiments **57**
5.1 Calibration . . . 57
5.1.1 Geometric Calibration . . . 57
5.1.2 Concentration Calibration . . . 59
5.2 Experimental Procedure . . . 63
5.2.1 Proof-of-Principle Experiment . . . 63
5.2.2 Fetch Experiment . . . 63

6 Data Analysis **67**
6.1 LIF Analysis . . . 67
6.1.1 Fluorescence Profiles . . . 67
6.1.2 Comparison of Profiles from both Experiments . . . 73
6.1.3 Profile Fitting . . . 74
6.2 LHC Analysis . . . 79
6.3 Pyranine bleaching . . . 80
6.4 PSV Analysis . . . 81
6.4.1 Algorithm . . . 82
6.4.2 Secondary Particles . . . 85
6.4.3 Eliminating Erroneous Detections . . . 87
6.4.4 Mean Wind Profile Fitting . . . 89
6.5 Combination Analysis . . . 90
6.5.1 PSV and LHC . . . 91
6.5.2 LIF and LHC . . . 92
6.5.3 LIF and PSV . . . 93
6.6 Wave Analysis . . . 94
6.7 Spectra Processing . . . 95

7 Results **99**
7.1 Wind Profiles . . . 100
7.1.1 Mean Wind Profiles . . . 103
7.1.2 Friction Velocities . . . 105
7.2 Global Transfer Velocities . . . 107
7.3 Concentration Profiles . . . 109
7.3.1 Mean Concentration Profiles . . . 112
7.3.2 Local Transfer Velocities . . . 113
7.3.3 Comparison of Local and Global Transfer Velocities . . . 116
7.4 Comparison of Mean Concentration and Wind Profiles . . . 118

7.5 Fluctuation Evaluation . . . 119
7.5.1 Mean Fluctuations . . . 119
7.5.2 Fluctuation Correlation . . . 121
7.6 Phase Evaluation . . . 123

8 Conclusion and Outlook **129**

A Appendix **131**
A.1 Solution of system of coupled differential equations . . . 131
A.1.1 Homogeneous Solution . . . 132
A.1.2 Inhomogeneous Solution . . . 132
A.2 Transmission of Camera Lens . . . 133
A.3 'Curtain Plots' . . . 134
A.4 Concentration Histograms . . . 138
A.5 Probe Data . . . 140
A.6 Data from Fits . . . 140
A.7 Friction Velocities from Wind Fluctuations . . . 142

Glossary **145**
List of Symbols . . . 145
Abbreviations . . . 147

Bibliography **149**

1 Introduction

The global carbon cycle has been the focus of many studies in the recent decades. This is motivated by a growing awareness that the rise of the atmospheric carbon dioxide (CO_2) concentration, as for example found in continuous CO_2 time series spanning over decades (R. F. Keeling and C. D. Keeling, 2017), is mainly caused by anthropogenic activities (IPCC, 2013). To understand the global carbon budget, ideally all sources and sinks have to be quantified. However, it is a tough objective to do this with high precision as the carbon cycle is subject to fluctuations and not all sources and sinks can be accessed and measured in a straightforward manner. Modeling plays a significant role in the budget calculations. The models contain parametrizations which are either obtained numerically, from models or from observations. Those parameters are typically easier to measure or estimate than the fluxes themselves. Therefore, it is of interest to quantify the fluxes as accurately as possible in experiments in dependence of the parameters. A schematic illustration of the main sources and sinks is shown in Fig. 1.1, as published in the 2017 report of the Global Carbon Project (Le Quéré et al., 2018). In the graphic, only the budget is given, i.e. the difference between uptake and release. It is evident that the uncertainties cannot be neglected.

The oceans play an essential role in the cycle not only of carbon dioxide, being a major sink for CO_2 (Gruber et al., 2019), but of other gases as well (Brooks et al., 2019). Field measurements of the gas transfer between atmosphere and ocean provide only local estimates, and as the exchange depends on many factors, the results from those local measurements can differ greatly due to varying conditions. The most important factors are the wind force, the characteristics of the wave field, the occurrence of surface films, possibly occurring bubbles and spray, the air and water temperatures and the salinity as well as the alkalinity of the water (Jähne, 2019; Wanninkhof et al., 2009). It is therefore of interest to acquire as much data as possible under a broad variety of conditions, in order to evaluate the influence of the parameters on the gas exchange.

Different parametrizations of gas exchange have been proposed, the majority taking into account only the influence of the wind speed and/or the mean sea surface slope, e.g. by Jähne (1982), Wanninkhof (1992) and Ho et al. (2011). As the system is very complex and dynamic, the resulting estimates of the gas transfer cover a wide range and may differ significantly from measurements. The uncertainty of the parametrizations is estimated to be in the order of a factor of two (Jähne, 2009).

Not only trace gases are transported from air to water and vice versa. Also heat and momentum are part of the atmosphere-ocean interaction. The transport of the scalar quantities mass, momentum and heat is mainly due to turbulence and diffusion. As the relevance of turbulence decreases towards the surface which turbulent eddies cannot penetrate, diffu-

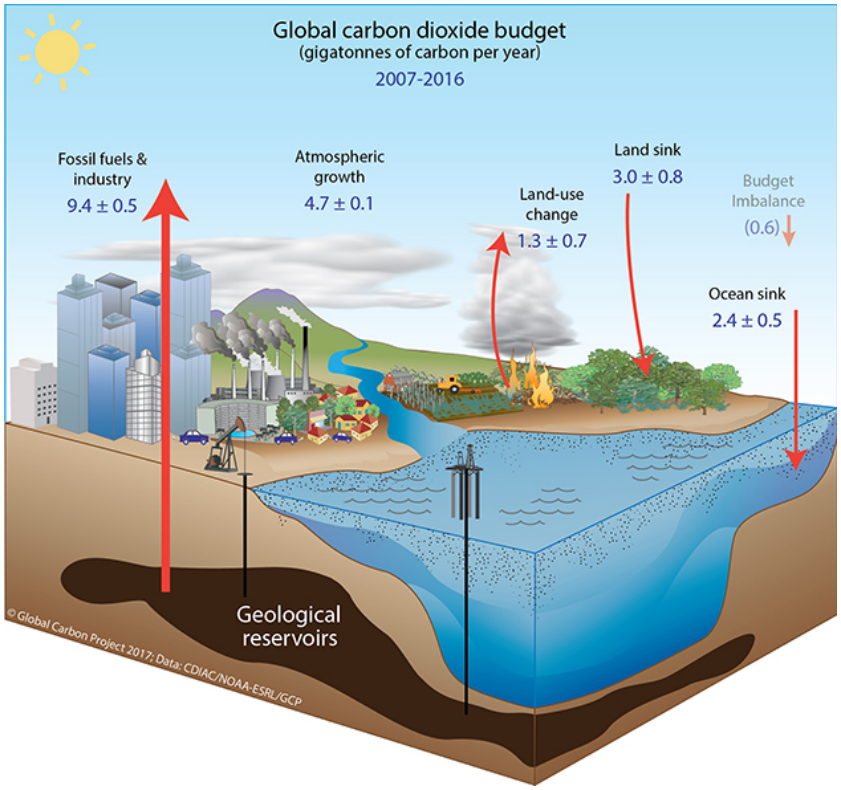

Figure 1.1: Budget of the global carbon cycle. The netto fluxes, i.e. the differences between uptake and release, are in $\mathrm{GtC\,yr^{-1}}$. The illustration was published in Le Quéré et al. (2018).

sion takes over as the main transport mechanism in the immediate vicinity of the surface. This layer is the bottleneck for gas transfer and is called the mass boundary layer. It exists both on the air- and on the water-side of the interface, while the dimensions are very different: its thickness in air is around 150 μm to 1.5 mm while in water, it extends only up to 10-350 μm (Jähne, 2019). Depending on the solubility of the gas, the bottleneck lies either on the air or on the water side. The commonly used variable to quantify gas transfer besides the mass flux is the transfer velocity, which depends on the mass boundary layer. However, to study the processes very close to the interface is not straightforward. Many studies in field experiments on the ocean focus on measuring the mass flux. The main field methods are the eddy covariance method (Aubinet, Vesala and Papale, 2012) and the dual tracer method (Watson, Upstill-Goddard and Liss, 1991).

Besides field experiments, laboratory studies are important for the evaluation of the empirical parametrizations and gain of understanding of the physics behind the air-water interactions. For this kind of research, wind-wave tanks, i.e. wind tunnels with a water section, are the study location. The conditions in the tanks differ from the ocean, mainly the limited fetch, i.e. the length of water exposed to the wind, and the limited height of the

tanks. However, when the focus lies on processes close to the interface, laboratory setups are very convenient. In particular, the fact that the influence of each parameter on the gas transfer can be studied separately by adjusting the conditions is a major benefit. Some wind-wave tanks even contain wave generators to simulate higher wave ages, i.e. the time that the wind has acted on a group of waves, to compensate for the limited fetch. Furthermore, annular wind-wave tanks exist, such as the Heidelberg *Aeolotron*, with a quasi infinite fetch.

A variety of lab based measurement techniques have been developed in the recent years, focusing on the transport mechanisms at the interface. In addition to the global averaging methods, such as absorption spectroscopy (Krall et al., 2019), with which mean transfer velocities can be deduced, several imaging techniques exist with the aim to visualize the transfer locally close to the surface.

To assess the influence of waves on the gas exchange, the wave field needs to be characterized locally. This can be done for example by illuminating the water from below with a coded light source. The illumination signal consists of gradients such that, using the refraction of the wavy surface, the wave slope can be obtained from the intensity of the transmitted light through the water (Kiefhaber et al., 2014; Klein, 2019).

Also, the momentum transfer from air to water can be visualized. This can be done for example by particle imaging (Buckley and Veron, 2018) where particles seeded into the air are illuminated with a laser sheet and imaged. By tracking the particles, the instantaneous wind field can be obtained and the momentum flux quantified. A further development of the technique, Particle Streak Velocimetry (PSV) makes use of a modulated illumination signal (Bopp, 2018). With this technique, the velocity of a particle can be obtained from a single image.

A technique called Boundary Layer Imaging (BLI) is based on the fluorescence of a pH indicator dye in the water which indicates the transfer of an alkaline gas (Kräuter, 2015; Klein, 2019). The fluorescence is excited with an LED array and the fluorescence is imaged from above. Thus, the mass boundary layer can be visualized and even its thickness quantified, because the fluorescence intensity is proportional to the thickness.

Another method aims at visualizing the heat transfer through active thermography (Kunz and Jähne, 2018). Nagel, Krall and Jähne (2015) showed that heat transfer velocities measured using active thermography measurements can be converted to gas transfer velocities, indicating that both quantities are transported by the same mechanisms.

In analogy to BLI on the water side, an approach to visualize the mass boundary layer in air was proposed by Winter (2011), using Laser Induced Fluorescence (LIF). Instead of a fluorescent dye, a tracer gas which fluoresces is used. The fluorescence intensity is in this case proportional to the gas concentration. The first test experiment using acetone as a tracer gas showed that the illuminance from dissolved acetone in the water deteriorated the images in such a way that the region close to the surface, the boundary layer, could not be resolved Krah (2014). Still, with this method, vertical concentration profiles in air were measured.

In this project, the measurement method of Krah (2014) was improved, using sulfur dioxide as a tracer. It fluoresces in the ultraviolet (UV) when excited with UV light. The benefit of using sulfur dioxide is its high solubility due to its acidity; the exact value of the solubility depends on the alkalinity of the water. Thus, by adjusting the pH value of the water, the influence of the solubility on the gas transfer can be studied. This approach will close a gap in the range of experimental techniques, because so far, no method is available for quantifying the air-side mass boundary layer thickness.

In the course of this project, a proof-of-principle experiment was conducted at a small wind-wave tank. The results gained from this experiment showed that the new technique can reliably resolve concentrations in the mass boundary layer. A second set of measurements were performed at two fetches of a larger wind-wave tank. In addition, momentum transport was studied simultaneously at the same fetches using the PSV technique developed by Bopp (2018) mentioned above. Furthermore, a method for measuring the surface elevation and a mass balance method were applied.

This thesis consists of the following chapters: In Ch. 2, the theoretical background of the topics connected to this project is presented, including the fundamental equations that describe gas transfer, the interaction between light and matter and the interaction between sulfur dioxide and water. Then, the four experimental methods applied in this thesis are introduced in Ch. 3. Chapter 4 gives a detailed description of the setups in both experiments, followed by a description of the calibration and experimental procedures in Ch. 5. A thorough account of the analysis of the data obtained with all four techniques is given in Ch. 6. In Ch. 7, the results deduced from the data, including gas transfer velocities, the concentration and wind profiles, the fluctuations and the modulation by the waves are presented. The thesis concludes with a summary of the results and an outlook in Ch. 8.

2 Theory

In this thesis, the transport of sulfur dioxide (SO_2) from air to water is investigated on the air side close to the wind-driven wavy air-water interface. Simultaneous measurements of the wind velocity field make comparisons of the gas and momentum transfer possible.

In the first part of this chapter, the theoretical background for the processes controlling air-water mass and momentum exchange is presented. A general description of the transport mechanisms in fluids is followed by a review of small-scale transfer models. Then, the interactions between light and matter used in this experiment are described: absorption and fluorescence; and finally the interaction of sulfur dioxide and water is investigated.

2.1 Mass and Momentum Transport Mechanisms

In this section, the basic fluid dynamic theory for the transport of mass and momentum is introduced: the mathematical description of the transport mechanisms for mass are followed by the corresponding formulation for momentum. Transport of mass and momentum as well as heat in a fluid is governed by a mix of random and directed motion.

The two random transport processes are molecular diffusion and turbulent flow. Even though they are characterized by seemingly random motion of molecules, the resulting transport tends to reduce gradients. Turbulence is generally more effective than diffusion as it is governed by larger-sized eddies than the small-scale diffusive motion of molecules. However, close to a "wall", e.g. the water surface, the eddy size and consequently the turbulence efficiency decreases and the diffusion takes over as the dominating process.

A relevant directed transport process is advection which is induced by the mean velocity field of a fluid.

This section covers only the considerations which are important for the treatment and interpretation of the experimental data and results. For a more detailed and complete representation of fluid dynamics, the reader is referred to textbooks, such as Kundu, Cohen and Dowling (2015).

2.1.1 Diffusion

Molecular diffusion is caused by the thermal motion of particles in combination with a concentration gradient. The random walk model describes the statistical process of the random motion (Pearson, 1905). Diffusion induces the motion of particles from regions with high to regions with low concentration c, thus reducing the concentration imbalance. This can be formulated mathematically by Fick's first law, which states for the diffusive

mass flux density $\vec{j}$:

$$\vec{j} = -D\vec{\nabla}c \tag{2.1}$$

with the diffusion coefficient D. Here, it is assumed that diffusion is isotropic and consequently, that D is a constant. The flux is directed against the concentration gradient.

Analogously, the viscous transport of momentum can be described with Newton's law of viscosity for an incompressible fluid. It states for the momentum flux density tensor $\boldsymbol{j}_m$, which is equal to the negative viscous stress tensor τ (Landau and Lifshitz, 1987):

$$j_{m,ik} = -\tau_{ik} = -\mu\left(\frac{\partial u_i}{\partial x_k} + \frac{\partial u_k}{\partial x_i}\right) \tag{2.2}$$

with the velocity field $\vec{u}$ and the dynamic viscosity μ, which is equal to the kinematic viscosity ν divided by the density of the fluid ρ. In the following, both the viscosity and the density are assumed to be constants.

To relate the diffusive momentum transport to the diffusive mass transport, the dimensionless **Schmidt number** Sc is defined as the ratio of the kinematic viscosity ν and the diffusion coefficient D:

$$Sc = \frac{\nu}{D}. \tag{2.3}$$

It is a characteristic number for a specific tracer and varies depending on the fluid: characteristic values for gases in air are $Sc \approx 1$, while gases in water have much higher Schmidt numbers.

Fick's second law states that the rate of change of the concentration is proportional to the second spatial derivative of the concentration. It can be derived by combining the continuity equation in the absence of sources and sinks

$$\frac{\partial c}{\partial t} + \vec{\nabla}\vec{j} = 0 \tag{2.4}$$

with Fick's first law, Eq. (2.1):

$$\frac{\partial c}{\partial t} = \vec{\nabla}(D\vec{\nabla}c) = D\Delta c. \tag{2.5}$$

The analog of the continuity equation for momentum is the Navier-Stokes equation (NSE)

$$\frac{\partial \vec{u}}{\partial t} + (\vec{u}\vec{\nabla})\vec{u} = -\frac{\vec{\nabla}p}{\rho} + \vec{g} + \nu\Delta\vec{u}, \tag{2.6}$$

which describes the conservation of momentum in the presence of external forces $\vec{g}$ and pressure gradients $\vec{\nabla}p$. Then, assuming no external forces or pressure gradients, the temporal change in the flow velocity $\vec{u}$ due to diffusion is expressed by

$$\frac{\partial \vec{u}}{\partial t} = \nu\Delta\vec{u}, \tag{2.7}$$

assuming a spatially and temporally constant viscosity.

2.1.2 Turbulence

Chaotic, nonlinear flows in fluids are denoted as turbulent flows. In general, such flows are temporally and spatially nonstationary. A characteristic feature of turbulence is the emergence of eddies. Because they can occur at a wide range of length scales, from microscale to macroscale, a general mathematical analysis of turbulent flows is difficult.

On relatively small scales, close to boundaries and under stationary conditions or if the flow is averaged over a long time, a description of turbulence in analogy to diffusion can be applied: **turbulent diffusion**, see e.g. in Kundu, Cohen and Dowling (2015). Here, Reynolds decomposition is introduced where the instantaneous and local velocity field $\vec{u}(\vec{x},t)$ at a position $\vec{x}$ and a time t is separated into its value averaged over time $\bar{\vec{u}}(\vec{x},t) = \langle\vec{u}(\vec{x},t)\rangle_t$, i.e. the expectation value of $\vec{u}(\vec{x},t)$, and the deviations from the mean value, the fluctuating velocity $\vec{u}'(\vec{x},t)$:

$$\vec{u}(\vec{x},t) = \bar{\vec{u}}(\vec{x},t) + \vec{u}'(\vec{x},t). \tag{2.8}$$

Similarly, the instantaneous and local concentration $c(\vec{x},t)$ is decomposed into its time average $\bar{c}(\vec{x},t) = \langle c(\vec{x})\rangle_t$ and fluctuation $c'(\vec{x},t)$:

$$c(\vec{x},t) = \bar{c}(\vec{x},t) + c'(\vec{x},t). \tag{2.9}$$

The transport equations for diffusion, Eqs. (2.5) and (2.7), are extended by including the terms for the turbulent diffusion, resulting in the continuity equation for the concentration

$$\frac{\partial c}{\partial t} + \vec{u}\vec{\nabla}c = D\Delta c \tag{2.10}$$

and the NSE for momentum transport, Eq. (2.6) under the assumption of no external forces or pressure gradients

$$\frac{\partial \vec{u}}{\partial t} + (\vec{u}\vec{\nabla})\vec{u} = \nu\Delta\vec{u}. \tag{2.11}$$

To obtain the expressions for the averaged quantities $\bar{c}$ and $\bar{\vec{u}}$, the Reynolds decomposition is inserted into the two equations before averaging them. This gives

$$\frac{\partial \bar{c}}{\partial t} = D\Delta\bar{c} - \overline{\vec{u}\vec{\nabla}c}. \tag{2.12}$$

The subtrahend can be replaced by the identity $\vec{u}\vec{\nabla}c = \vec{\nabla}\left(c\vec{u}\right) - c\vec{\nabla}\vec{u}$, where the second term vanishes for an incompressible fluid, because the continuity equation is in this case $\vec{\nabla}\vec{u} = 0$. Then, the averaging of the subtrahend in Eq. (2.12) yields

$$\overline{\vec{\nabla}(c\vec{u})} = \overline{\vec{\nabla}\left(\bar{c}+c'\right)\left(\bar{\vec{u}}+\vec{u}'\right)} \tag{2.13}$$

$$= \overline{\vec{\nabla}\Big(\underbrace{\bar{c}\bar{\vec{u}}}_{\text{I}} + \underbrace{\bar{c}\vec{u}'}_{\text{II}} + \underbrace{c'\bar{\vec{u}}}_{\text{III}} + \underbrace{c'\vec{u}'}_{\text{IV}}\Big)}. \tag{2.14}$$

The terms I to III vanish, only the last term remains after averaging: Terms II and III are equal to zero because the temporal average of a fluctuating quantity vanishes. Under the assumption that the concentration distribution and the wind velocity field depend only on the vertical coordinate and are otherwise homogeneous, the mean vertical flux is assumed to be negligible, such that there is no convergence or divergence. Since the derivative in the vertical direction vanishes, term I is equal to zero.

The remaining term IV is the correlation of the concentration and wind fluctuations and vanishes if both quantities are totally uncorrelated. It is also called "eddy covariance" and is the temporal average of the product of the fluctuations[1].

These considerations result in the following transport equation of a tracer with concentration c in a velocity field $\vec{u}$

$$\frac{\partial \bar{c}}{\partial t} = \vec{\nabla}\left(D\vec{\nabla}\bar{c} - \overline{c'\vec{u}'}\right). \tag{2.15}$$

The term in parentheses is equal to the total mass flux density $\vec{j}$, as expressed by extending the diffusive flux density by the turbulent term $\overline{c'\vec{u}'}$.

An analogous expression can be derived for the transport of momentum, with Einstein's summation convention:

$$\frac{\partial \bar{u}_i}{\partial t} = \frac{\partial}{\partial x_j}\left(D\frac{\partial}{\partial x_j}\bar{u}_i - \overline{u_j' u_i'}\right). \tag{2.16}$$

Both equations simplify when considering the vertical transport of the tracer in a flow with a mean orientation in the horizontal direction. In this study, the Cartesian coordinate system is chosen in the following way: x is the along-wind direction, y is the cross-wind horizontal wind direction, while z is the vertical direction pointing upwards. The origin of the coordinate system is set in such a way that $z = 0$ is the mean water level. Also, a notation convention in literature is introduced at this point, where the velocity field components in x, y and z direction are denoted as u, v and w, respectively. Then, the transport equations simplify to:

$$\frac{\partial \bar{c}}{\partial t} = \frac{\partial}{\partial z}\left(D\frac{\partial \bar{c}}{\partial z} - \overline{c'w'}\right), \tag{2.17}$$

$$\frac{\partial \bar{u}}{\partial t} = \frac{\partial}{\partial z}\left(\nu\frac{\partial \bar{u}}{\partial z} - \overline{u'w'}\right). \tag{2.18}$$

In analogy to the expression for the diffusive transport in the mass transport equation, the turbulent part, i.e. the eddy covariance, is replaced by the following expression, defining the turbulent diffusion coefficient $K(z)$ in the one dimensional case:

$$\overline{c'w'} =: -K(z)\frac{\partial \bar{c}}{\partial z}. \tag{2.19}$$

[1] The common notation for the eddy covariance is with covariance braces, $\langle c'\vec{u}'\rangle$, instead of the averaging bar which is the used notation here.

Analogously, the turbulent viscosity coefficient $K_m(z)$ for momentum transport is defined as:

$$\overline{u'w'} =: -K_m(z)\frac{\partial \bar{u}}{\partial z}. \tag{2.20}$$

This results in the following expression for the vertical component of the total mass flux density:

$$j = -\left(D + K(z)\right)\frac{\partial \bar{c}}{\partial z}. \tag{2.21}$$

The equation for the vertical transport of horizontal momentum in a horizontal flow j_m is then

$$j_m := j_{m,xz} = -\rho\left(\nu + K_m(z)\right)\frac{\partial \bar{u}}{\partial z} = -\tau_{xz}, \tag{2.22}$$

assuming no mean vertical flow ($\bar{w} = 0$). A characteristic variable for the momentum transfer is the **friction velocity** u_* which is defined as:

$$u_*^2 = \frac{|\tau_{xz}|}{\rho}. \tag{2.23}$$

The friction velocity in air and water can be converted into each other via the following equation which follows directly when assuming no-slip condition:

$$\rho_{\mathrm{w}} u_{*,\mathrm{w}}^2 = \rho_{\mathrm{a}} u_{*,\mathrm{a}}^2 \tag{2.24}$$

with the densities of air and water ρ_{a} and ρ_{w}. As in this thesis, all measurements are conducted in the air, only the air-sided consideration is of interest. Consequently, the notation is simplified to u_* in this thesis, meaning the air-sided friction velocity.

2.2 Air-Water Mass Transfer

Generally, turbulent transport is more efficient than diffusion, mainly due to the larger eddies. However, close to a boundary, which the turbulent eddies cannot penetrate, the turbulent transport decreases and diffusion becomes the main transport mechanism. In this experiment, the vertical transport of a tracer towards (and through) a water surface in a horizontally oriented wind field is considered. Here, the water surface is the boundary for the turbulent eddies. In the following considerations, a stationary mean horizontal flow and vanishing mean vertical flow ($\bar{w} = 0$) is assumed, as mentioned above in Sec. 2.1.2. Different approaches exist for the parametrization of the turbulent diffusion coefficient, all having in common that its value decreases towards the boundary. In Sec. 2.3, the most relevant models for this study are discussed. In the following, the basic concepts and equations for gas transfer are given.

2.2.1 Mean Wind Profiles

In order to obtain a vertical profile for the horizontal wind, Eq. (2.22) can be solved for the mean horizontal wind velocity $\bar{u}$. Since turbulent eddies cannot penetrate the interface, the turbulent transport decreases towards the surface and vanishes for $z = 0$. The momentum flux is constant for all heights above the water, namely equal to the shear stress. The horizontal wind velocity decreases towards the surface, while the gradient of the horizontal wind velocity has to increase towards the surface. Close to the surface, the viscous transport is dominant, such that only the viscous part of Eq. (2.22),

$$j_m = -\rho\nu\frac{\partial\bar{u}}{\partial z}, \tag{2.25}$$

needs to be considered. This leads to a linear profile in the vicinity of the surface, a layer named the **viscous boundary layer**, where the viscosity is the dominant transport mechanism.

Directly at the surface, the air-side velocity needs to be equal to the water surface velocity due to the no-slip condition which states that a fluid close to a solid boundary has the same velocity as the boundary itself. If no additional source of turbulence or motion are present in the water, the water velocity decreases with the depth. The gradient is, just as on the air side, largest directly at the surface, and here, too, a viscous boundary layer exists close to the boundary. However, as the Schmidt number and thus the ratio between viscosity and diffusion is much larger than one, the water-side viscous boundary layer is much thicker than the water-side mass boundary layer.

The water surface can be viewed as a solid wall for low wind velocities, as the vertical motion of the water surface due to waves is negligible compared to the air motion. Considering the momentum density $\vec{p}/V = \rho\vec{u}$ per volume V, a momentum solubility α_m can be defined as the ratio of the momentum in water and air in equilibrium:

$$\alpha_m = \frac{\rho_\mathrm{w} u_\mathrm{w}}{\rho_\mathrm{a} u_\mathrm{a}} = \frac{\rho_\mathrm{w}}{\rho_\mathrm{a}} \approx 800. \tag{2.26}$$

Explicitly, the velocity profile is continuous at the surface, while the momentum has a discontinuity, as illustrated in Fig. 2.2.

With the assumption of a smooth water surface, the mathematical description of the wind profile follows the **law of the wall** which is depicted in Fig. 2.1 in dimensionless coordinates. The latter are defined as follows: the height above the mean surface elevation z is multiplied by the ratio of the friction velocity u_* and the viscosity of the medium ν (air or water) while the surface velocity u_s is subtracted from the horizontal wind u, which is then divided by the friction velocity:

$$z^+ = \frac{z u_*}{\nu} \quad \text{and} \quad u^+ = \frac{u - u_s}{u_*}. \tag{2.27}$$

In the viscous boundary layer, the wind increases linearly with the height above the water, as expressed in Eq. (2.25): $u^+(z^+) = z^+$. Further away from the interface (the “wall”), a

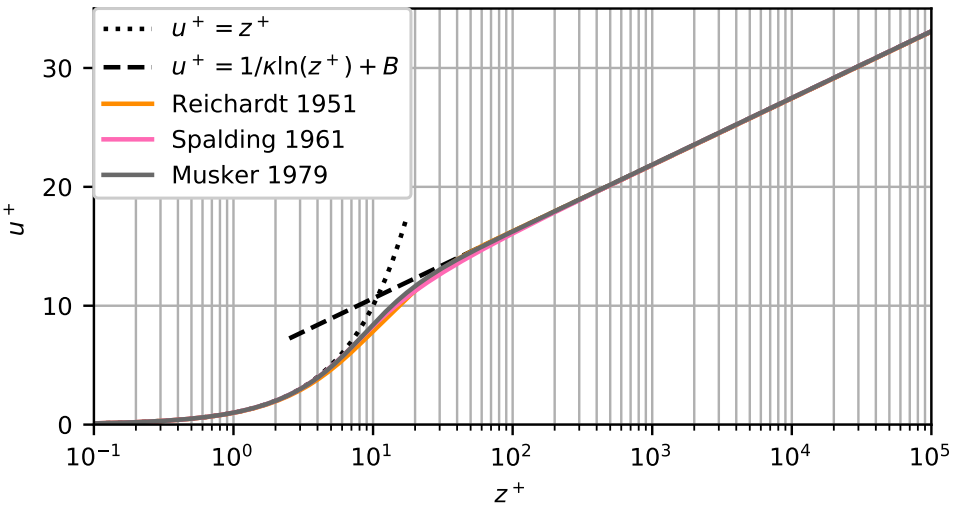

Figure 2.1: Mathematical description of the mean horizontal wind in dimensionless coordinates: the linear profile for small z^+ (dotted line) and the logarithmic function for larger z^+ (dashed line). The law of the wall as parametrized by Reichardt (1951), Spalding (1961) and Musker (1979) are plotted as well. For better comparison, a common value of $B = 5$ is applied.

logarithmic profile is established with the function

$$u^+(z^+) = \frac{1}{\kappa} \ln\left(\frac{z^+}{z_0^+}\right) = \frac{1}{\kappa} \ln\left(z^+\right) + B, \tag{2.28}$$

with the von Kármán constant κ, the roughness length $z_0 = z_0^+ \frac{\nu}{u_*}$ and the dimensionless parameter $B = -\frac{1}{\kappa} \ln\left(z_0^+\right)$. The value for κ has been determined experimentally to be around 0.41. Furthermore, a value for the parameter B has been found to be between 5 (Schlichting and Gersten, 2006) and 5.5 (Reichardt, 1951), yielding a value for the dimensionless roughness length of $z_0^+ \approx 0.11 - 0.13$. A derivation of Eq. (2.28) can be found for example in Kundu, Cohen and Dowling (2015).

The intersection of the logarithmic profile and the linear profile from the viscous layer is located at the dimensionless height 11 (Reichardt, 1951) or 11.7 (Townsend, 1976) which approximates the thickness of the viscous boundary layer z_l in dimensionless expression $z_l^+ = z_l \frac{u_*}{\nu}$. Several parametrizations are suggested for the transition from one function to the other.

Reichardt (1951) proposed the following function for the turbulent viscosity coefficient $K_m(z)$:

$$K_m(z) = \kappa u_* \left(z - z_l \tanh \frac{z}{z_l}\right) \quad \text{or} \quad K_m(z^+) = \kappa \nu \left(z^+ - z_l^+ \tanh \frac{z^+}{z_l^+}\right). \tag{2.29}$$

For z close to zero, the function itself and its first and second derivatives vanish, while for larger z, the function converges to κz. Solving Eq. (2.22) for u and inserting Eq. (2.29) yields

$$u(z) = -\frac{j_m}{\rho}\int_0^z \frac{1}{\nu + K_m(z')}dz' = -\frac{j_m}{\rho}\int_0^z \frac{1}{\nu + \kappa u_* \left(z' - z_l \tanh\frac{z'}{z_l}\right)}dz' \quad \text{or} \tag{2.30}$$

$$u^+(z^+) = -\frac{j_m}{\rho u_*^2}\int_0^{z^+} \frac{1}{1 + \kappa\left(z^{+\prime} - z_l^+ \tanh\frac{z^{+\prime}}{z_l^+}\right)}dz^{+\prime} \tag{2.31}$$

in dimensionless coordinates. The factor in the front of the integral in Eq. (2.31), $-j_m/(\rho u_*^2)$ is equal to unity according to Eq. (2.23).

Reichardt proposed a simplification of Eq. (2.31) with the aim to eliminate the integral. The resulting approximated profile in dimensionless coordinates is

$$u^+(z^+) = \frac{1}{\kappa}\ln\left(1 + \kappa z^+\right) - \frac{1}{\kappa}\ln\left(\kappa z_0^+\right)\left(1 - \exp\left(-\frac{z^+}{z_l^+}\right) - \frac{z^+}{z_l^+}\exp\left(-0.33 z^+\right)\right) \tag{2.32}$$

with z_0^+ as defined above over the parameter B.

Another parametrization was found by Spalding (1961) with a Taylor series and yields z^+ as a function of u^+:

$$z^+(u^+) = u^+ + z_0^+\left(\exp\left(\kappa u^+\right) - 1 - \kappa u^+ - \frac{\left(\kappa u^+\right)^2}{2!} - \frac{\left(\kappa u^+\right)^3}{3!}\right). \tag{2.33}$$

A third interpolation function was derived by Musker (1979), which is given in differential form:

$$\frac{du^+}{dz^+} = \frac{\kappa + C(z^+)^2}{\kappa + C(z^+)^2 + C\kappa(z^+)^3} \tag{2.34}$$

with the constant $C = 0.001093$.

All three expressions for u^+ are shown in Fig. 2.1, with $B = 5$ and $z_l^+ = 11.7$. They represent the law of the wall very well in the completely viscous and turbulent regions and are mutually consistent in the transition region.

At around $z^+ > 10^4$, the wake part of the profile begins where the flow resembles the wall-free turbulent flow regime. Several different approaches exist for a parametrization of this part of the profile, but this is outside the scope of this thesis.

In another approach to describe the mean wind profile one employs a polynomial function. This is presented in Sec. 2.3.2 where an analogous approach is used to parametrize the concentration profile.

2.2.2 Transfer Velocity and Resistance

As mentioned in the Sec. 2.1, the mean flux of a tracer is directed against a concentration gradient, neglecting bulk motion. Equation (2.21) solved for the concentration yields

$$\int_{c(z_1)}^{c(z_2)} dc = c(z_2) - c(z_1) = -j \int_{z_1}^{z_2} \frac{1}{D + K(z)} dz. \tag{2.35}$$

In analogy to electric resistance, the **transfer resistance** R is defined as the ratio of the concentration difference (the analogue to voltage) and the mass flux density (the analogue to current) between two regions:

$$R := \frac{\Delta c}{j} =: 1/k. \tag{2.36}$$

It has the dimension of an inverse velocity, while its inverse is defined as the **transfer velocity** k. In analogy with the electric resistance, the addition law for the transfer resistance is:

$$R_{1,2} + R_{2,3} = \frac{c(z_2) - c(z_1)}{j} + \frac{c(z_3) - c(z_2)}{j} = \frac{c(z_3) - c(z_1)}{j} = R_{1,3}, \tag{2.37}$$

which leads to an inverse addition law for the transfer velocities:

$$\frac{1}{k_{1,2}} + \frac{1}{k_{2,3}} = \frac{1}{k_{1,3}}. \tag{2.38}$$

Equation (2.36) can also be rewritten as

$$j = k\Delta c = \Delta c / R. \tag{2.39}$$

Thus, the mass flux between two regions of different concentrations is proportional to the concentration difference. This general expression is now adapted to the setting of this experiment: the transport from a region at height z above the surface to the surface is:

$$j = k(z)(c(z) - c_s), \tag{2.40}$$

where $c_s = c(0)$.

Since turbulence can be neglected in the vicinity of the surface, the transfer velocity from the surface to a certain height z can be directly deduced with

$$k(z) = D \left.\frac{\partial c}{\partial z}\right|_{z=0} (c(z) - c_s)^{-1}. \tag{2.41}$$

It is important to notice that in stationary conditions, the mass flux density j is a constant for all z due to mass conservation, while the transfer velocity k varies with z.

For the comparison of the conditions of different experiments, the measurement of the mass flux is not helpful if the concentration is not measured. Therefore, the comparison of the transfer velocities k is more meaningful as the information of the concentration gradient and the environmental conditions are included.

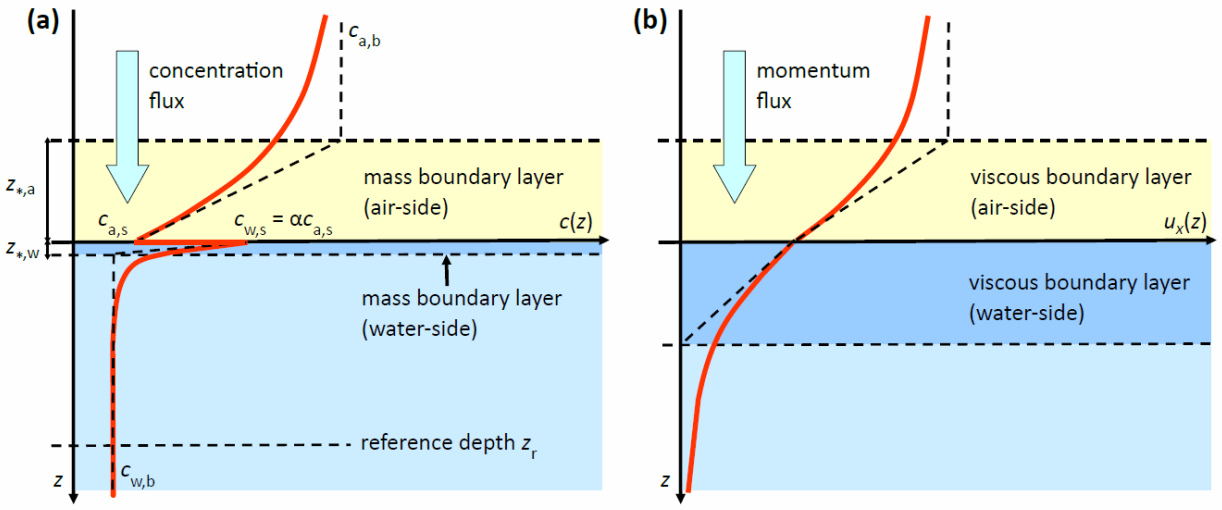

Figure 2.2: (a) Concentration and (b) velocity profiles close to the water surface with the boundary layers indicated, for the case of a dimensionless tracer solubility $\alpha > 1$, modified after Degreif (2006). The concentration profile reflects an invasion experiment. In this thesis, the vertical axis z is defined the other way around.

2.2.3 Concentration Profiles

Similar considerations as for the momentum transport in Sec. 2.2.1 can be applied for the mass transport with the aim to achieve a formulation for the vertical profile of the concentration. The mean profiles of both the concentration and the horizontal wind are shown in Fig. 2.2.

Because the mass flux density j as formulated in Eq. (2.21) is constant for all heights above the water surface z, the absolute change of the concentration increases with decreasing z. Thus, the concentration gradient is largest directly at the water surface. Because the mass flux is constant throughout the vertical axis, the mass flux can be calculated directly from the gradient at the surface, if the diffusion constant is known:

$$j = -D \left. \frac{\partial \bar{c}}{\partial z} \right|_{z=0} . \tag{2.42}$$

Depending on the concentration in the water and the solubility of the tracer, the concentration increases or decreases towards the water surface. In the following, the (initial) tracer concentration in the water is assumed to be negligible in relation to the air-side concentration. This setting is also called an **invasion** experiment. Furthermore, the dimensionless solubility α which is defined as the ratio of the water- and air-side concentrations c_w and c_a in equilibrium, $c_{w,e}$ and $c_{a,e}$, in analogy to the expression for the momentum solubility

α_m in Eq. (2.26),

$$\alpha = \frac{c_{\mathrm{w,e}}}{c_{\mathrm{a,e}}}, \tag{2.43}$$

is assumed to be larger than one. This is also the setting in the experiment. In this case, the transfer of the tracer is directed from the air to the water and the concentration in the air decreases towards the water surface, as depicted in Fig. 2.2a where an exemplary concentration profile in air and water close to the water surface is shown for a tracer with a solubility $\alpha > 1$.

As indicated in the figure, the air- and water-side concentration profiles meet the surface ($z = 0$) at different concentrations. This is due to the fact that the concentrations directly at the surface always are in equilibrium. If one would wait for a certain equilibration time, the final homogeneously distributed concentrations in the air and water would also fulfill Eq. (2.43).

This discontinuity of the concentration profile at the surface is eliminated with the following approach. Depending on the position of the "viewer", in the air or in the water, the expression for the concentrations are different: For the viewer on the air side, the concentration in the water is divided by the solubility. Similarly, for the viewer on the water side, the concentration in the air is multiplied by the solubility. In this experiment, all considerations of the concentrations are **air-sided**.

The layer where the turbulent transport is smaller than the diffusion, i.e. where $K(z) < D$, is named the **mass boundary layer**, and exists both on the air and water side, as indicated in Fig. 2.2a. It is defined to expand up to the height above the water where an extended straight line, which starts at the surface concentration and, having as slope the gradient at the water surface, reaches the bulk concentration. Therefore, its thickness z_* is defined as

$$z_* = \frac{c_b - c_0}{\frac{\partial \bar{c}}{\partial z}\Big|_{z=0}} = D\frac{\Delta c}{j} = \frac{D}{k} \tag{2.44}$$

where c_b denotes the bulk concentration in the air or water. With an increasing transfer velocity, the mass boundary layer gets thinner. Generally, an increase in the wind velocity causes an increase in the transfer velocity and thus a thinning of the mass boundary layers. Also, with decreasing values of the diffusion constant, the mass boundary layer becomes thinner. This results in generally thinner mass boundary layers in the water than in the air because typically, a tracer's diffusion coefficient in the air is around 10^4 times larger than in the water.

For the concentration profiles themselves, i.e. the mean concentration in dependence of the height above the surface, several different models exist. The most relevant ones for this experiment are discussed in Sec. 2.3.

2.2.4 Transfer Partitioning

As mentioned in Sec. 2.2.2, the transfer of a tracer from air to water (or vice versa) can be studied in the resistance model. The total resistance is equal to the inverse total transfer velocity. It can be separated into several parts at different depths or heights above the water which are connected in series. Thus, the sum of the partial resistances is the total resistance, see Eq. (2.37), and the sum of the inverse partial transfer velocities equals the inverse total transfer velocity, see Eq. (2.38). The total resistance for the transfer from air to water or vice versa can therefore be separated into the partial resistances in the air R_a and water R_w:

$$R_\mathrm{a} = -\frac{c_\mathrm{a} - c_s}{j} \quad \text{and} \quad R_\mathrm{w} = -\frac{c_s - c_\mathrm{w}/\alpha}{j}, \tag{2.45}$$

expressed for the air-side viewer. Then, the total resistance is the sum of both partial resistances:

$$R = -\frac{c_\mathrm{a} - c_\mathrm{w}/\alpha}{j} = R_\mathrm{a} + R_\mathrm{w}. \tag{2.46}$$

This results in the following expression for the air-side resistance

$$R_\mathrm{a} = \frac{c_\mathrm{a} - c_\mathrm{s}}{c_\mathrm{a} - c_\mathrm{w}/\alpha} R. \tag{2.47}$$

At higher wind velocities, additional resistances have to be considered in the model as also bubbles and spray take part in the gas exchange. They can be viewed as additional pathways which add parallel-connected resistances to the turbulence and diffusion mediated transfer. However, this is not relevant for the present discussion, as the wind speeds studied in these experiments do not suffice to create such conditions.

Münnich and Flothmann (1975) give an estimate of the magnitudes of the resistances in different layers and state especially a wide range of magnitudes for the transfer resistance in the water-side viscous boundary layer, depending on the solubility. In the case of highly soluble tracers, the resistance on the air side R_a is much larger than the one on the water side R_w/α. Therefore, the water-side resistance is negligible and the transfer of the tracer is denoted as “air-side controlled”. Similarly, the transfer of tracers with low solubility is “water-side controlled”. Furthermore, the effect of bubbles and spray is also highly dependent on the solubility.

In this study, sulfur dioxide was used as a tracer. Its solubility depends on the pH value of the water. Hence, by tuning the pH, the partitioning of the transfer between air and water can be varied.

In very basic conditions, as those considered in this study, the effective solubility of sulfur dioxide (see Sec. 2.5) is very high, see Fig. 2.4b. The mass transfer is thus highly air-side controlled. Applying Eq. (2.47) for this condition results in the approximate equality of the total resistance with the air-side resistance and thus in the equality of the total transfer velocity with the air-side transfer velocity. Therefore, by measuring the air-side transfer, the total transfer can be quantified.

2.3 Transfer Models

In the literature, several different models for the mass transfer have been proposed. Most of them propose a certain relation between the transfer velocity, the friction velocity and/or the Schmidt number of the tracer: $k \propto Sc^{-n}$ with the Schmidt number exponent n. However, as the Schmidt number of the tracer used in this study is nearly 1 in the air, those relations cannot be efficiently studied and distinguished with the present experiments. Nevertheless, the conceptual views of the transfer proposed by the main models are summarized. The only applicable model among the presented models, which is proposed by Deacon (1977) and based on the parametrization of the turbulent viscosity coefficient by Reichardt (1951), is explained in more detail.

2.3.1 Stagnant Film Model

The simplest gas exchange model is the film model. It was first proposed by Whitman (1923) for the absorption of gases by water. The model assumes a thin layer in the water directly below the interface where diffusion is the only transport mechanism. Outside of this film, only turbulence is present. The concentration profile is suggested to be linear in the film and constant below the film, defining the thickness of the film analogously as in Eq. (2.44).

In this model, by using Eq. (2.44), the following relation between transfer velocity, friction velocity and Schmidt number can be derived:

$$k = \frac{D}{z_*} = \frac{u_*}{z_*^+} Sc^{-1}. \tag{2.48}$$

This results in a Schmidt number exponent $n = 1$, however experiments show that this is an overestimation.

The assumption of instantaneous change between turbulence and diffusion at $z = z_*$ does not correspond well to experimental observations, but still, this simple model yields a good first estimate of the gas exchange and the Schmidt number exponent proportionality can be used as a lower limit.

2.3.2 Turbulent Diffusion

Deacon's Model

As mentioned above, there are several approaches to derive the turbulent diffusion coefficient. All have in common that the turbulence decreases continuously towards the air-water interface. Deacon (1977) applied Reichardt's parametrization of the turbulent viscosity, Eq. (2.29), for the turbulent diffusivity:

$$K(z) = \kappa u_* \left(z - z_* \tanh \frac{z}{z_*} \right) \quad \text{or} \quad K(z^+) = \kappa \nu \left(z^+ - z_*^+ \tanh \frac{z^+}{z_*^+} \right), \tag{2.49}$$

Here, z_* is the mass boundary layer thickness as defined in Eq. (2.44) and is assumed to have the same value as the viscous boundary layer thickness z_l. This is a reasonable assumption in the air for tracers with a Schmidt number of around 1 (Jähne, 1985). It follows that according to this approach, the turbulent transfer of momentum is equivalent to the turbulent transfer of mass.

In direct analogy to the wind profile, applying the equation for the turbulent diffusivity, Eq. (2.49), in Eq. (2.35), the concentration profile is derived to

$$c(z) = c_s - j \int_0^z \frac{1}{D + \kappa u_* \left(z' - z_* \tanh \frac{z'}{z_*}\right)} dz' \tag{2.50}$$

or as a function of the dimensionless z^+:

$$c(z^+) = c_s - j \frac{Sc}{u_*} \int_0^{z^+} \frac{1}{1 + \kappa Sc \left(z^{+\prime} - z_*^+ \tanh \frac{z^{+\prime}}{z_*^+}\right)} dz^{+\prime}. \tag{2.51}$$

Deacon states that this formula is valid for $z^+ \leq 50$. The dimensionless concentration is defined in this thesis as the concentration normalized by the concentration at $z^+ = 50$:

$$c^+(z^+) = \frac{c(z^+) - c_s}{c(z^+ = 50)}. \tag{2.52}$$

To derive an equation for the transfer velocity, the relation between concentration and transfer velocity as defined in Eq. (2.41) is applied. When this formula is integrated for $z^+ = 0$ to 50, the following approximate proportionality is derived for $0.6 < Sc < 10$ with an accuracy of about 1%:

$$k = \frac{u_*}{15.2} Sc^{-0.61}. \tag{2.53}$$

Hence, the Schmidt number coefficient is equal to $n = 0.61$ in this model. For higher Schmidt numbers, a different approximation is found, however, as the used tracer has a Schmidt number close to 1 in the air, this is not relevant here.

This model is only valid for low wind speeds when the water surface can be approximated by a wall. For the wind speeds and the fetches applied in this study, the Deacon model is applicable. At higher wind speeds, the transfer velocities are underestimated with this model.

Polynomial Approach

Close to the interface, the concentration profile can be represented by a Taylor expansion about $z = 0$ (Jähne, 1985; Coantic, 1986). The boundary conditions for the concentration and the wind velocity field need to be considered for the case of a **rigid wall** or a **free interface**, reducing the first terms of the Taylor expansion. For a rigid wall, the no-slip condition (see Sec. 2.2.1) leads to

$$u' = v' = w' = 0 \quad \text{for} \quad z = 0. \tag{2.54}$$

With the continuity equation for an incompressible fluid,

$$\frac{\partial u'}{\partial z} + \frac{\partial v'}{\partial z} + \frac{\partial w'}{\partial z} = 0, \tag{2.55}$$

the vertical derivative of the vertical wind fluctuations at $z = 0$ needs to vanish:

$$\left.\frac{\partial w'}{\partial z}\right|_{z=0} = 0. \tag{2.56}$$

Also, the concentration fluctuations vanish at the surface: $c' = 0$ for $z = 0$. Furthermore, the velocity field is assumed to be two dimensional. This is a justified assumption for studies in a linear wind-wave tunnel as in this study.

From these boundary conditions, Coantic (1986) derived the following equations for the mean concentration and horizontal wind profiles close to a rigid wall:

$$\bar{c}(z) = \bar{c}_s - \frac{j}{D}z + \frac{3z^4}{4!D}\left(\overline{\frac{\partial c'}{\partial z}\frac{\partial^2 w'}{\partial z^2}}\right)_0 + ... \tag{2.57}$$

$$\bar{u}(z) = \bar{u}_s + \frac{\bar{u}_*^2}{\nu}z + \frac{3z^4}{4!\nu}\left(\overline{\frac{\partial u'}{\partial z}\frac{\partial^2 w'}{\partial z^2}}\right)_0 + ... \tag{2.58}$$

The boundary conditions for a free interface reduce to

$$w' = 0 \quad \text{for} \quad z = 0, \tag{2.59}$$

as the other fluctuation components can be non-zero. Also, the vertical derivative of the vertical wind fluctuations can be different from zero at the surface. However, the concentration fluctuations are still assumed to vanish at the surface.

With this reduced set of boundary conditions, the first terms of the Taylor expansions for the concentration and horizontal wind profiles close to a free interface are:

$$\bar{c}(z) = \bar{c}_s - \frac{j}{D}z + \frac{2z^3}{3!D}\left(\overline{\frac{\partial c'}{\partial z}\frac{\partial w'}{\partial z}}\right)_0 + ... \tag{2.60}$$

$$\bar{u}(z) = \bar{u}_s + \frac{\bar{u}_*^2}{\nu}z + \frac{2z^3}{3!\nu}\left(\overline{\frac{\partial u'}{\partial z}\frac{\partial w'}{\partial z}}\right)_0 + ... \tag{2.61}$$

For the turbulent diffusivity $K(z)$ and viscosity $K_m(z)$, Coantic derived a z^3-proportionality for a rigid smooth wall and a z^2-proportionality for a free interface. The Schmidt number exponent n was found to be $n = 2/3$ for a smooth rigid surface and $n = 1/2$ for a free interface.

2.3.3 Surface Renewal Model

This model, developed by Higbie (1935) and Danckwerts (1951) for free surfaces and extended for a rigid interface by Jähne et al. (1989), proposes a different conceptual description

of mass transfer in the water close to the water surface: Certain water packages from the bulk are transported into the boundary layer by eddies where the diffusion is the only transport mechanism, remaining there for a certain time and are then replaced by new packages. Thus, the surface is continuously renewed through a statistical process and the surface water is transported into the bulk by eddy events.

In this model, the Schmidt number exponent is equal to 2/3 for a rigid water surface and 1/2 for a free water surface, just as in the previously described model.

As the surface renewal model is purely water-sided, it is not applicable to the air-side measurements in this thesis.

2.4 Interaction of Light and Matter

Light, or more generally electro-magnetic radiation, interacting with matter of any kind can be absorbed and scattered. If after the absorption, light is re-emitted, one speaks of photoluminescence. Fluorescence and phosphorescence are two special cases of photoluminescence. The latter happens if the emission is delayed in time due to forbidden transitions. This section introduces the basic concepts of absorption and fluorescence which are essential for the measurement technique developed here.

2.4.1 Absorption

For light incident on an absorber, the fraction of photons with wavelength λ transmitted after an optical path length l is given by the Beer-Lambert law[2]

$$tr(\lambda) = \frac{I(\lambda)}{I_0(\lambda)} = 10^{-\epsilon(\lambda)cl} = 10^{-abs(\lambda)} \tag{2.62}$$

with the incident and transmitted light intensities I_0 and I and the molar attenuation coefficient ϵ of the tracer. This fraction defines the **transmittance** tr, while the exponent is denoted as the **absorbance** abs. The transmittance can also be expressed in terms of the optical depth δ:

$$tr(\lambda) = e^{-\sigma(\lambda)\rho_N l} = e^{-\delta(\lambda)} \tag{2.63}$$

where σ is the **absorption cross section** and ρ_N the number density of molecules. Equations (2.62) and (2.63) are valid for a homogeneously distributed absorber. In the generalized case of N absorbing tracers with inhomogeneous concentrations $c_i(z)$ and number

[2] The law was originally discovered by P. Bouguer (1729), was further discussed by J. H. Lambert (1760) and then extended to liquids by A. Beer (1852). Thus, it should actually be called Bouguer-Lambert-Beer law.

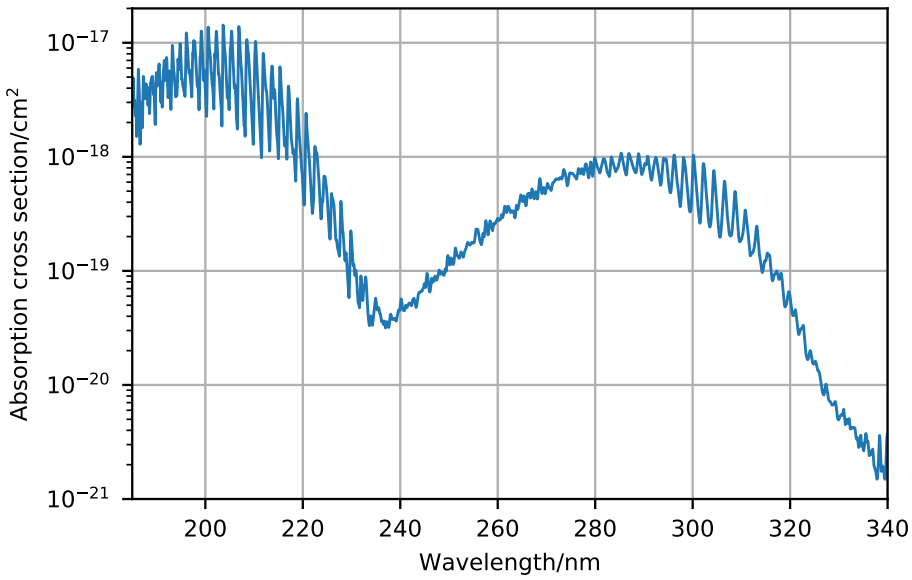

Figure 2.3: Absorption cross section of sulfur dioxide as a function of the excitation wavelength (Danielache et al., 2008).

densities $\rho_{N,i}(z)$ along the path, the absorbance and optical depth are given by:

$$abs(\lambda) = \sum_{i=1}^{N} \epsilon_i(\lambda) \int_0^l c_i(z)dz, \tag{2.64}$$

$$\delta(\lambda) = \sum_{i=1}^{N} \sigma_i(\lambda) \int_0^l \rho_{N,i}(z)dz. \tag{2.65}$$

The absorption of light by an absorber material is strongly dependent on the wavelength since light of different wavelengths triggers different mechanisms in atoms and molecules. Ultraviolet and visible light causes transitions of valence electrons in atoms and molecules, while infrared radiation excites molecular vibrations. In most cases, the absorption spectra show distinct absorption peaks which correspond to certain transitions or excitation energies.

Figure 2.3 shows the absorption cross section of sulfur dioxide, which is defined as

$$\sigma(\lambda) = \frac{\ln(10)}{N_A cl} \log(tr(\lambda)), \tag{2.66}$$

as measured by Danielache et al. (2008), with the Avogadro constant N_A. Larger values mean higher absorption efficiency. The absorption cross section ranges over four orders of magnitude in the depicted wavelength range.

2.4.2 Fluorescence

When electrons in excited states decay back to the ground state, the excess energy can be emitted as new photons with either the same energy as the incident photons (elastic scattering) or a lower energy (photoluminescence). If, in the latter case, the excited and the ground states are singlets, the electron does not flip its spin, which results in a short life-time of the excited state, on the order of nanoseconds. This leads to a nearly instantaneous emission of the **fluorescence** photon(s). The loss of energy relative to the incident photon is caused either by internal conversion, if an excited state decays to the lowest available vibrational state of the singlet state, or by the influence of the surrounding medium (solvent) which lowers the energy of the excited state. In the latter case, the difference in energy of the incident and emitted photon is called "Stokes shift".

If the spin of the electron is flipped in the decay to a singlet state, e.g. because the excited state is a triplet state that can be populated in an intersystem crossing process, the life-time of this state is much longer (on the order of milliseconds) owing to the forbidden spin transition, and one speaks of **phosphorescence**.

The fluorescence intensity, just as the absorbance, depends directly on the concentration of the tracer. Therefore, fluorescence is used in many applications where the aim is to quantify local tracer concentration distributions or profiles, and also in atmospheric trace gas measurements. When using a laser light source for the excitation, the method is called **laser induced fluorescence**. This method is applied in this experiment for measuring concentration profiles of sulfur dioxide.

Generally, the fluorescence efficiency is given by the ratio of the number of photons emitted by fluorescence to the number of absorbed photons, the quantum efficiency Φ. This is equivalent to the quotient of the fluorescence intensity to that of the absorbed radiation. It depends on the incident wavelength λ and the ambient temperature T. The reduction of the efficiency through interactions of the tracer with surrounding molecules is called **quenching**: either the interfering molecule ("quencher") bonds with a tracer molecule to form a non-fluorescent state or energy is lost in inelastic collisions between the tracer molecule and the quenchers. Quenching can be used to determine the concentration of a quencher if the fluorescence of a tracer molecule in the absence of the quencher is known because the quenching efficiency depends on the quencher concentration. Mohn and Emmenegger (2014) have studied, *inter alia*, the ability of oxygen to quench the fluorescence of sulfur dioxide. A further special quenching mechanism occurs when the incident photon causes a loss of fluorescence-ability of the molecule, e.g. by dissociating the molecule. This effect is called **photobleaching**.

The proposed measurement method is based on the assumption that the fluorescence intensity of a fluorescent gas I_f is linearly proportional to the gas concentration c. Furthermore, the detected fluorescence intensity depends on the wavelength λ and intensity of the excitation light I, the efficiency of the detector optics η_{opt} as well as the efficiencies of

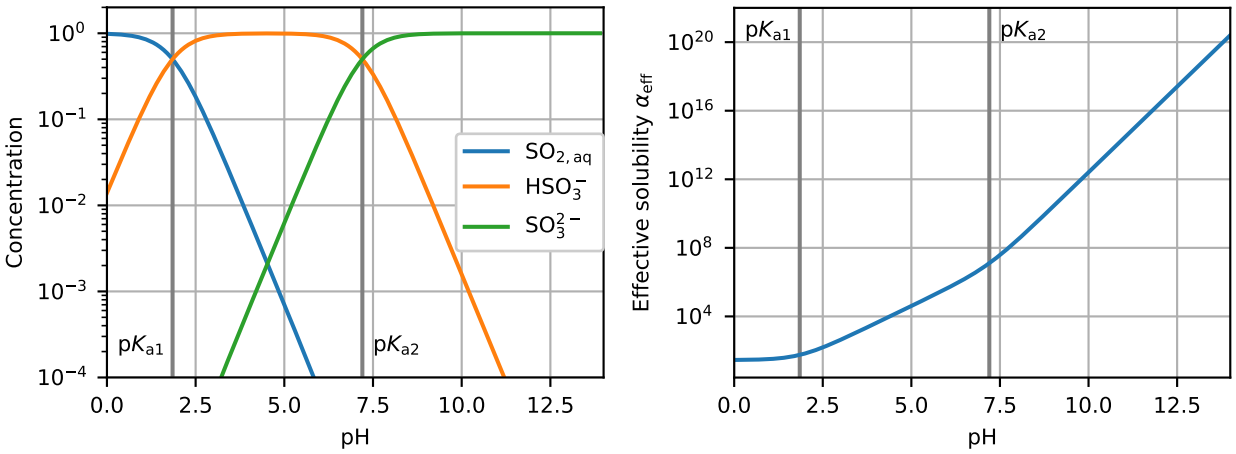

(a) (b)

Figure 2.4: (a) Bjerrum plot for SO_2 solved in water and (b) effective solubility of SO_2 in dependence of the water pH. The dissociation constants pK_{a1} and pK_{a2} are marked with grey lines in both plots.

both absorption and fluorescence, σ and Φ, as formulated by Thurber et al. (1998):

$$I_f(\lambda, T) = \frac{E(\lambda)}{hc/\lambda} \eta_{\text{opt}} dV c \, \sigma(\lambda, T) \Phi(\lambda, T). \tag{2.67}$$

Here, E is the laser fluence, which is connected to the intensity of a pulsed laser via $E(\lambda) = I(\lambda) f_l$ with the repetition rate of the pulsed laser f_l, hc/λ the energy of a photon at the excitation wavelength λ and dV the collection volume.

2.5 Sulfur Dioxide in Water

Sulfur dioxide is a gas, which is soluble in water. Its physical solubility α_{phys}, i.e. the fraction of the concentrations in the water and air phase in equilibrium, see Eq. (2.43), depends on the water temperature T. According to Henry's law (Henry, 1803), it is given by

$$\alpha_{\text{phys}}(T) = \frac{[SO_2]_w}{[SO_2]_a} = R_g \cdot T \cdot H^{cp}(T) \tag{2.68}$$

with the universal gas constant $R_g = 0.08205\,\text{l atm/(mol K)}$ and the Henry solubility H^{cp}. The latter is parametrized by (Burkholder et al., 2015) as $\ln H^{cp} = -39.72 + 4250/T + 4.525 \ln(T)$ [mol/(l, atm)]. Equation (2.68) results in a value for the physical solubility of 34 at $T = 25\,°\text{C}$. When sulfur dioxide is dissolved in water, it forms sulfurous acid which, depending on the water acidity, can dissolve further:

$$SO_2(aq) + H_2O \rightleftharpoons H_2SO_3 \overset{K_{a1}}{\rightleftharpoons} H^+ + HSO_3^- \overset{K_{a2}}{\rightleftharpoons} 2\,H^+ + {SO_3}^{2-}. \tag{2.69}$$

Thus, depending on the pH of the water, sulfur dioxide exists physically solved ($SO_{2(aq)}$), as bisulfite ion (HSO_3^-) or sulfite ion (SO_3^{2-}). The acid dissociation constants are

$$\begin{aligned} K_{a1} &= \frac{[H^+][HSO_3^-]}{[SO_2(aq)]} = 1.4 \cdot 10^{-2}\,\text{mol/l}, \\ K_{a2} &= \frac{[H^+][SO_3^{2-}]}{[HSO_3^-]} = 6.3 \cdot 10^{-8}\,\text{mol/l} \end{aligned} \tag{2.70}$$

(at a temperature of 25°C) and are often used in analogy to the pH value: $pK_{a1} = -\log_{10}(K_{a1}) = 1.85$ and $pK_{a2} = 7.2$ (Haynes, 2016). Figure 2.4a shows the occurrences of the three coexisting species in dependence of the pH value. In very acidic conditions, sulfur dioxide is mostly in an aquaeous solution. At medium pH, i.e. $pK_{a1} < \text{pH} < pK_{a2}$, bisulfite dominates, while in very alkaline water, sulfite is the dominating species.

Hence, to account for the chemical reactions, an effective solubility α_{eff} needs to be considered for the total amount of sulfur dioxide that is absorbed by water. α_{eff} is calculated from the concentration distributions for the three coexisting species with the acid dissociation constants as given in Eq. (2.70):

$$\alpha_{\text{eff}}(T, \text{pH}) = \frac{[SO_2]_w}{[SO_2]_a} = \alpha_{\text{phys}}(T) \cdot \left(1 + 10^{\text{pH}} K_{a1} + 10^{2\text{pH}} K_{a1} K_{a2}\right). \tag{2.71}$$

In Fig. 2.4b, the effective solubility is plotted against the pH value. The two pK_avalues are also marked in the plot. Clearly, α_{eff} increases exponentially with pH. In particular, for very alkaline conditions, the increase is very strong. This results in an effective solubility of $\alpha_{\text{eff}} = 2.5 \cdot 10^{14}$ for the target pH of 11 in the experiments described in this thesis.

In this thesis, the solubility α is used as a shorthand for the effective solubility α_{eff}.

3 Methods

In this section, the main methods used in this thesis are presented. The goal of this thesis was the simultaneous measurement of sulfur dioxide concentration profiles and wind velocities in the air as functions of the distance to the wavy water surface. For the concentration profiles, a new imaging technique was developed based on Laser Induced Fluorescence (LIF) of sulfur dioxide. The wind velocities were measured via Particle Streak Velocimetry (PSV), a further development of Particle Image Velocimetry (PIV). A direct detection of the wavy water surface was realized with the Laser Height Camera (LHC) method. Furthermore, the integrated transfer velocity measurements were conducted with a mass balance method, using the concentration measured via UV spectroscopy. The simultaneous application of these measurement techniques is the focus of the main set of experiments and constitutes the central challenge of this thesis.

3.1 Laser Induced Fluorescence of Sulfur Dioxide

In Sec. 2.4.2, fluorescence as a radiative relaxation process from an excited state is described. If the excitation is performed using laser light and the fluorescence occurs through spontaneous emission, the process is called Laser Induced Fluorescence (LIF).

The measurement technique developed here uses the fluorescence of sulfur dioxide. For the excitation, an ultraviolet light source is needed as SO_2 has a broad absorption band in the UV range with absorption cross sections up to $10^{-17}\,\mathrm{cm}^2$ (Manatt and Lane, 1993; for a detailed analysis of the absorption spectrum between 200 and 320 nm, see Belton, 1982). Figure 2.3 shows the absorption cross section spectrum as measured by Danielache et al. (2008). The distinct absorption lines originating from the vibrational fine structure of the excited states are clearly visible. Due to the efficient UV absorption, SO_2 has been used in various absorption and fluorescence measurements, e.g. in-situ atmospheric trace gas detection with LIF (Matsumi, Shigemori and Takahashi, 2005; Rollins et al., 2016) as well as imaging of flames (Honza et al., 2017) and exhaust-gases (Sick, 2002). Depending on the excitation frequency, it fluoresces in the UV to visible blue range (Sick, 2002; Simeonsson, Matta and Boddeti, 2012). Ahmed and Kumar (1992) analyzed both absorption and fluorescence efficiency in dependence of the excitation wavelength. Their measurements show that the absorption cross section has a maximum at a wavelength of around 200 nm, which is in accordance with the absorption cross section spectrum shown in Fig. 2.3. However, the fluorescence cross section is highly reduced in this range due to photo dissociation: if the excitation wavelength is less than 220 nm, the absorbed energy causes a dissociation of the molecule (Hui and Rice, 1972). The highest fluorescence efficiency was

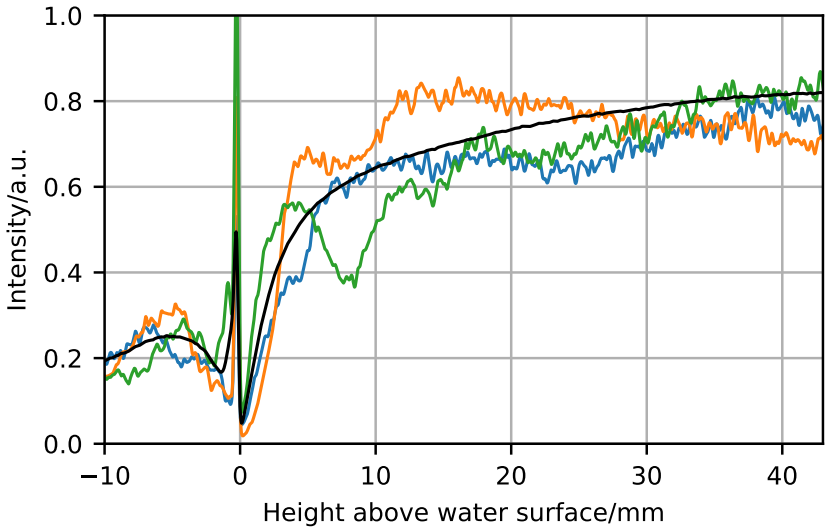

Figure 3.1: Three instantaneous LIF profiles (colors) and the mean profile, averaged over 240000 single images, corresponding to 20 minutes of measurement (black). On the abscissa, the surface elevation was subtracted from the vertical coordinate.

obtained with excitation at 228 nm.

The goal of this work is to use SO_2 LIF for measurements of concentration profiles with high spatial and temporal resolution. The method is based on the relation between concentration and fluorescence intensity which is defined in Eq. (2.67). The aim is to measure the concentration particularly in the air-sided mass boundary layer as close to the water surface as possible in order to gain a deeper understanding of the transport mechanisms in this layer. As LIF has already been successfully used to detect and quantify concentrations of SO_2 as mentioned above, the successful application of the technique in these experiments was anticipated.

In the experiments performed in a wind-wave tank, a certain concentration of sulfur dioxide is added to the closed air space. The laser beam used for the excitation of the gas traverses the air space vertically, normal to the water surface. The concentration-dependent fluorescence along the laser beam is continuously imaged at a high frame rate by a camera mounted outside the tank. Since the fluorescence is in the near-ultraviolet range, the camera has to be sensitive for ultraviolet radiation and the focusing optics and the window of the experiment section of the tank should be appropriate for the transmission of UV light. As the laser beam is directed vertically towards the surface, vertical concentration profiles can be obtained from the images. Several exemplary profiles are shown in Fig. 3.1, after a geometric calibration to translate the pixel coordinates to the height above the water level has been applied. The profiles can then be further processed to quantify the instantaneous and the average transfer velocity as well as the thickness of the boundary layer by fitting model functions to the profiles. Furthermore, by subtracting a mean profile from the instantaneous profiles, concentration fluctuations are obtained from the images. These

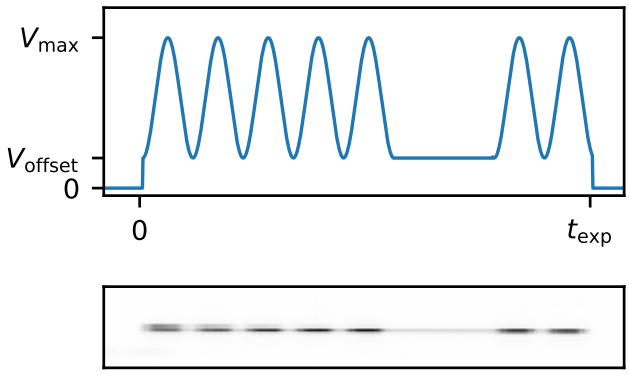

Figure 3.2: PSV laser trigger signal (top) and a picture of a PSV streak (bottom), showing the coded illumination in inversed grayscale. The particle propagates from left to right, in the direction of the wind. The exposure time of the camera t_{exp} is adjusted to the duration of the signal. The signal has an offset V_{offset} to increase the ability of the algorithm to connect the two streak parts separated by the gap. V_{max} denotes the maximum applied voltage for the signal.

are specifically interesting for studying the turbulent flux by combining the concentration fluctuations with vertical wind fluctuations.

3.2 Particle Streak Velocimetry

The wind velocities are visualized with an advanced version of Particle Streak Velocimetry (PSV), developed by M. Bopp (2018) and applied at the Lizard wind-wave tank by F. Kühlein (2019). This measurement technique is based on the flow measurement technique Particle Image Velocimetry (PIV). In PIV, light reflecting particles are added to the fluid, which follow the flow. They are illuminated, sequentially imaged and tracked from one image to the other, thus making the flow visible and a flow measurement possible. This general technique is well established with different methods to retrieve the flow information from the particle image, and has been applied in a large variety of applications (Raffel et al., 2007; Adrian and Westerweel, 2011).

One method is to obtain a flow vector from the motion of individual particles in two consecutive images taken by a camera in a technique called Particle Tracking Velocimetry (PTV). The distance the particles traveled between two exposures is then used to calculate the velocity vectors. For the analysis to work properly, a low particle density is necessary. Otherwise the algorithm has difficulties to correctly identify a given particle in two consecutive images. Higher particle densities can be analyzed statistically to determine the velocity field.

In PSV, the information of both the local flow direction and velocity is derived from a single image. This is achieved by varying the intensity of the light source, four overlayed

laser sheets in this setup, while the camera takes one image at a sufficiently long exposure time, such that the trajectory of the particle is imaged. The varied illumination signal consists of one harmonic (a shifted cosine) with a length of nine periods, where the sixth and seventh period are zeroed, see Fig. 3.2, which shows in addition to the illumination signal also an exemplary streak. Thereby, the direction of the motion can be determined. The velocity is obtained by fitting the illumination signal to an intensity profile of a streak. The faster the particle is, the longer is the streak. For slow particles, the individual harmonic periods might not be separable, but the gap between the fifth and eighth period is still distinguishable such that even at these low velocities, a flow vector can be determined. In order to have similar accuracy at different wind conditions, the frequency of the signal is adjusted to the wind speed, with higher frequencies for higher winds.

The method can be applied both in air and in water. For the choice of particles, the following conditions must be fulfilled:
1) The particles have to be small and have a density similar to that of the fluid in order to follow the flow completely, because the flow is directly determined from the motion of the particles. Thus, the buoyancy effect on the particles has to be negligible.
2) However, the particles should not be too small, since the resolution of the imaging system is limited and their brightness in the images must be sufficiently high.

In this experiment, ammonium chloride (NH_4Cl), the salt from the acid-base reaction of hydrochloric acid (HCl) and ammonia (NH_3) vapors,

$$NH_3(g) + HCl(g) \longrightarrow NH_4Cl(s) \tag{3.1}$$

was used as particles. The optical and geometrical properties of the salt comply with the prerequisites: very small, nearly spherical particles with diameters of around 1 μm.

The gas exchange measurements are sensitive to additional acids or bases added during the experiment: The mass balance should be closed during the experiment. Thus, no additional sinks for sulfur dioxide (as for example ammonia might react with sulfur dioxide to ammonium sulfite, $(NH_4)_2SO_3$) should be added. Moreover, the pH value should ideally be constant during the experiment. Thus it is important to avoid additional acids or bases except for those acids derived from the sulfur dioxide. Consequently, the amounts of the two reactants in Eq. (3.1) have to be equal and the reaction needs to be complete before the reactants enter the air volume of the tank. When the salt particles enter the water, they dissolve directly, not changing the pH value. Thus, the particles do not alter the chemistry in the tank and are chemically inert.

3.3 Surface Detection

In order to determine each particle's position relative to the water surface, the position of the latter has to be determined. For this, a third synchronous measurement technique is applied with a separate setup, the so called Laser Height Camera (LHC) technique. This method has been first applied by J. Horn (2013). The data processing algorithm used here is due to K. Schwarz (2016). Here again a LIF method is used where a laser sheet

illuminates a fluorescent dye mixed into the water. The fluorescence in the laser sheet is then imaged by a camera aimed at the water surface from the side at an oblique angle. Using image processing techniques, the upper edge of the fluorescence profile is detected via thresholding in every image and identified with the surface. From the time series of the detected surface, the phase of the dominant wave in every image can be calculated. This information can be used for wave phase-dependent averaging of measured quantities and profiles for wind conditions where non-negligible waves are present.

As the fluorescence intensity of the dye pyranine is pH dependent, it is important that the pH value remains almost constant during the whole measurement to ensure that the surface detection is correct since the latter depends on the intensity threshold. Otherwise, the threshold would need to be readjusted to the fluorescence intensity, and thus to the pH value, during the measurement. Because the sulfur dioxide is continuously being dissolved in water causing its pH to decrease, a buffer is used to counteract this effect.

3.3.1 Curvilinear Coordinates

When studying wave dependent properties, as in this work, it is helpful to make a coordinate transformation, especially in order to study the processes between wave crests. The method applied here follows the procedure as used by Bopp (2018). In this work, only the z coordinate is transformed by subtracting a term $f(\vec{x}, t)$ (see for example C. T. Hsu, E. Y. Hsu and Street, 1981; Troitskaya et al., 2011):

$$x^* = x \tag{3.2}$$
$$y^* = y \tag{3.3}$$
$$z^* = z - f(\vec{x}, t). \tag{3.4}$$

Other works also transform the x coordinate, e.g. such that planes of constant x^* are normal to the surface. One condition is posed on f: $f(\vec{x}, t)|_{z=0} = \eta(x, t)$, i.e. the function is at the surface equal to the elevation of the surface η. Two possible mapping functions are discussed in the following: the simple shift and the declining shift (Bopp, 2018). The simple shift transformation subtracts the surface profile η from the z coordinate:

$$f(x, t) = \eta(x, t). \tag{3.5}$$

Similarly, the declining shift also contains the surface profile, however represented through a sum of the modes in Fourier space, with the amplitudes a_n, phases Φ_n and wave vectors k_n. An exponential decline depending on the wave vector k_n is applied to each mode. Consequently, short wavelengths decline faster than long wavelengths:

$$f(x, z^*, t) = \sum_n a_n \cos(k_n x - \Phi_n) \exp(-\sigma_d k_n z^*), \tag{3.6}$$

where σ_d is the parameter controlling the strength of the decline. Figure 3.3 illustrates the effect of the simple shift compared to the declining shift for two values of the declining

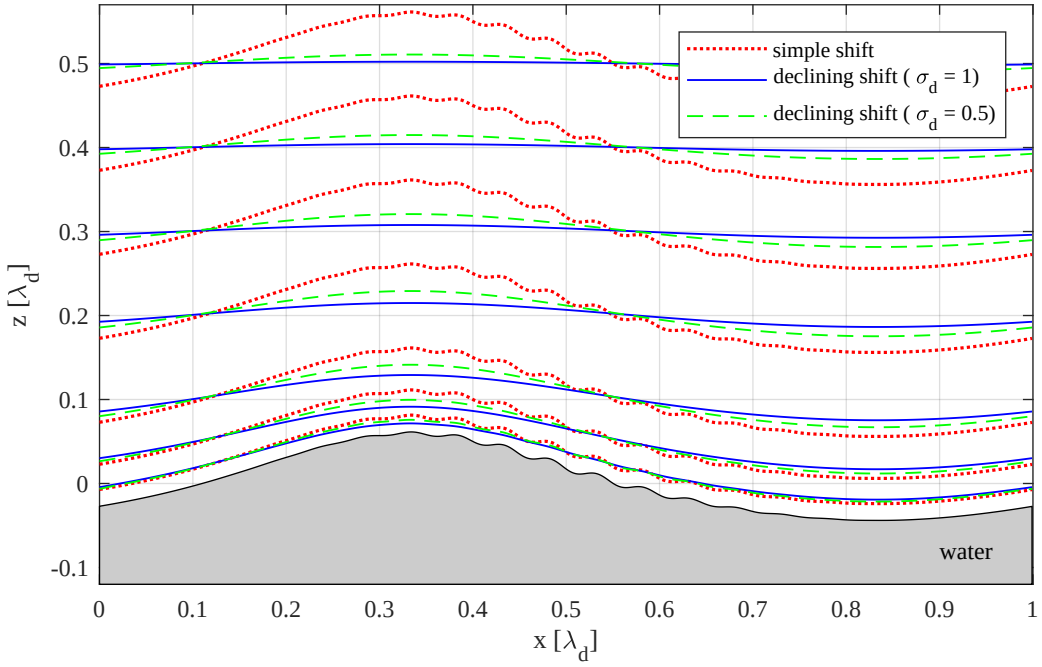

Figure 3.3: Illustration of the two curvilinear coordinate transformations, taken from Bopp (2018). The x and z coordinates are expressed in units of the wavelength λ_d. Besides the simple shift (red), the declining shift is shown with two values for the declining parameter (blue and green).

parameter. It is obvious that the effect of the smaller wavelengths is damped much faster with increasing distance to the surface than long wavelengths. Since the flow of air far above the surface is not affected by waves, the declining transformation yields a more natural description of the problem at hand.

3.4 Mass Balance

In the experiments described in this thesis, absorption spectroscopy, a well-established technique to measure gas concentrations, was used to quantify the average sulfur dioxide concentration in the "bulk", i.e. in the well-mixed region far away from the water surface. Here, light with a known spectrum is directed through the medium with the tracer in an unknown concentration. The concentration of the tracer can be deduced by calculating the absorbance $abs(\lambda)$ from the transmission $I(\lambda)$ and the light source spectra $I_0(\lambda)$, see Eq. (2.62), and comparing this to either the absorbance cross section or a spectrum taken at a known concentration.

The temporal evolution of the bulk concentration during a measurement obtained from both the LIF and the absorption spectroscopy methods can then be analyzed to calculate

the gas transfer velocity. This is based on the assumption that the box model, which is described in the following, is valid for the setup. The model simplifies the setting to two well-mixed volumes ("boxes"), one filled with air (V_a) and one with water (V_w), which are in contact over a surface A. The air- and water-side concentrations of a tracer, c_a and c_w, are considered from the air-side perspective in the following. They depend on each other and also on the gas flux into and out of the boxes: Gas flux coming into the air space $\dot{V}_\mathrm{in}$ with the concentration $c_\mathrm{a,f}$ as well as the leaking rate $\dot{V}_\mathrm{out}$. It is assumed that pressure in the air space remains constant. Consequently, the inward flux is equal to the outward flux: $\dot{V}_\mathrm{in} = \dot{V}_\mathrm{out} \equiv \dot{V}_\mathrm{a}$. Analogously, the water volume can have an influx and a leakage rate which again are assumed to be equal, namely $\dot{V}_\mathrm{w}$. The concentration in the influx water is $c_\mathrm{w,f}$.

With these assumptions, the tracer concentrations in the air and water volumes are described with the following system of coupled differential equations:

$$V_\mathrm{a}\dot{c}_\mathrm{a} = \quad kA\left(\frac{c_\mathrm{w}}{\alpha} - c_\mathrm{a}\right) + \dot{V}_\mathrm{a}c_\mathrm{a,f} - \dot{V}_\mathrm{a}c_\mathrm{a}, \tag{3.7}$$

$$V_\mathrm{w}\dot{c}_\mathrm{w} = \underbrace{-kA\left(\frac{c_\mathrm{w}}{\alpha} - c_\mathrm{a}\right)}_{\substack{\text{exchange between}\\ \text{air and water}}} + \underbrace{\dot{V}_\mathrm{w}c_\mathrm{w,f}}_{\substack{\text{leaks into}\\ \text{the box}}} - \underbrace{\dot{V}_\mathrm{w}c_\mathrm{w}}_{\substack{\text{leaks out}\\ \text{of the box}}} \tag{3.8}$$

with the dimensionless solubility of the tracer α, the ratio of the water- and air-side tracer concentrations in equilibrium, which is equal to the effective solubility as described in Sec. 2.5. A detailed derivation of the general solution of this system of coupled equations can be found in Nielsen (2004). This is of the form:

$$c_\mathrm{a}(t) = c_1 v_{\mathrm{a},1}\exp(\nu_1 t) + c_2 v_{\mathrm{a},2}\exp(\nu_2 t) + c_\mathrm{a,i} \tag{3.9}$$

$$c_\mathrm{w}(t) = c_1 v_{\mathrm{w},1}\exp(\nu_1 t) + c_2 v_{\mathrm{w},2}\exp(\nu_2 t) + c_\mathrm{w,i} \tag{3.10}$$

with the eigenvalues of the homogeneous system ν_1 and ν_2 and the corresponding eigenvectors $\vec{v}_1 = (v_{\mathrm{a},1}, v_{\mathrm{w},1})$ and $\vec{v}_2 = (v_{\mathrm{a},2}, v_{\mathrm{w},2})$. The constants c_1 and c_2 are determined by the initial and boundary conditions. The inhomogeneities in Eqs. (3.7) and (3.8) are due to the leaks into the boxes. They add the 'inhomogeneous' part $(c_\mathrm{a,i}, c_\mathrm{w,i})$ to the solution which is a special solution of the differential equations. Depending on the setup and the initial and boundary conditions, several assumptions and simplifications to the system of equations can be made which simplify the solutions accordingly.

In the first series of measurements at the smaller wind-wave tank, the proof-of-principle experiment, the tracer of volume V_input was introduced to the air volume with an almost instantaneous input. This simplifies the equations, as both volume change rates can be set to zero, since the leakage rates are negligible compared to the transfer rates. Thus, in this case, the system of differential equations is homogeneous. The initial condition is $c_\mathrm{a}(0) = c_\mathrm{a,0} = V_\mathrm{input}/V_\mathrm{a}$.

In the case of sulfur dioxide and the target pH value employed here being around 11, the solubility is of the order of 10^{14}. Therefore, the term c_w/α can be safely neglected in

the following. This decouples the equations and results in the following solution for the air-side concentration:

$$c_{\mathrm{a}}(t) = c_{\mathrm{a},0} \exp(-kAt/V_{\mathrm{a}}). \tag{3.11}$$

This means that in this simplified model, all sulfur dioxide is transferred into the water after a sufficiently long time: $c_{\mathrm{a}} \to 0$ for $t \to \infty$. See Sec. A.1 for the detailed derivation of the solution.

Using the second setup at the larger wind-wave tank, the tracer was added to the air volume continuously, expressed with $\dot{V}_{\mathrm{a}} c_{\mathrm{a,f}}$ in Eq. (3.7), and, as the water leakage rate is assumed to be negligible, the water volume is assumed to be constant. As in the considerations above the term c_{w}/α is neglected, due to the applied pH of 11 and the corresponding high solubility. This again simplifies the equations. However, due to the non-zero air leakage rate, the inhomogeneous solution contributes. For the solution, it is assumed that the initial gas concentration both in air and water is zero: $c_{\mathrm{a},0} = c_{\mathrm{w},0} = 0$. The homogeneous solution is similar to the one in the case above:

$$c_{\mathrm{a}}^{\mathrm{h}}(t) = c_1 v_1 \exp(-(kA + \dot{V}_{\mathrm{a}})t/V_{\mathrm{a}}). \tag{3.12}$$

Taking into account the inhomogeneity, the total solution for the air-side concentration is

$$c_{\mathrm{a}}(t) = \frac{\dot{V}_{\mathrm{a}} c_{\mathrm{a,f}}}{kA + \dot{V}_{\mathrm{a}}} \left(1 - \exp(-(kA + \dot{V}_{\mathrm{a}})t/V_{\mathrm{a}})\right). \tag{3.13}$$

After a certain equilibration time, the equilibrium concentration $c_{\mathrm{a}}(t \to \infty) = \frac{\dot{V}_{\mathrm{a}} c_{\mathrm{a,f}}}{kA + \dot{V}_{\mathrm{a}}}$ is reached. In reality, the equilibrium is only quasi-static because the total amount of the tracer in the box increases continuously and linearly over the duration of the experiment due to the continuous inflow of sulfur dioxide to the air volume, the inhomogeneous part $c_{\mathrm{a,i}}$ in Eq. (3.9). The complete derivation of the solution of this simplified system can also be found in Sec. A.1.

These considerations neglect the possible back transfer from the water to the air and that the solubility decreases with higher water-side concentrations. However, for the relatively short durations of the measurements, these effects remain small. Moreover, the decrease of the solubility is counteracted by adding buffer solutions to the water.

The two solutions, Eqs. (3.11) and (3.13), are plotted for the two wind-wave tanks and typical values for the transfer velocity k and the gas flux $\dot{V}_{\mathrm{a}}$ in Fig. 3.4. The rates of increase and decay depend directly on the exponent in the two equations, as shown in the figure. In the exponent, the effective height h_{eff} which is defined as V_{a}/A depends on the geometry of the wind-wave tank, having a value of around 0.5 m in the Benjamin-tank and 3 m in the Lizard-tank. As visible in Fig. 3.4b, a lower transfer velocity results in a higher equilibrium concentration, while a lower gas flux results in a lower equilibrium concentration. Therefore, the gas flux had to be adjusted in the experiments according to the expected transfer velocity to achieve similar equilibrium concentrations in the measurement phase (see Tab. 4.2).

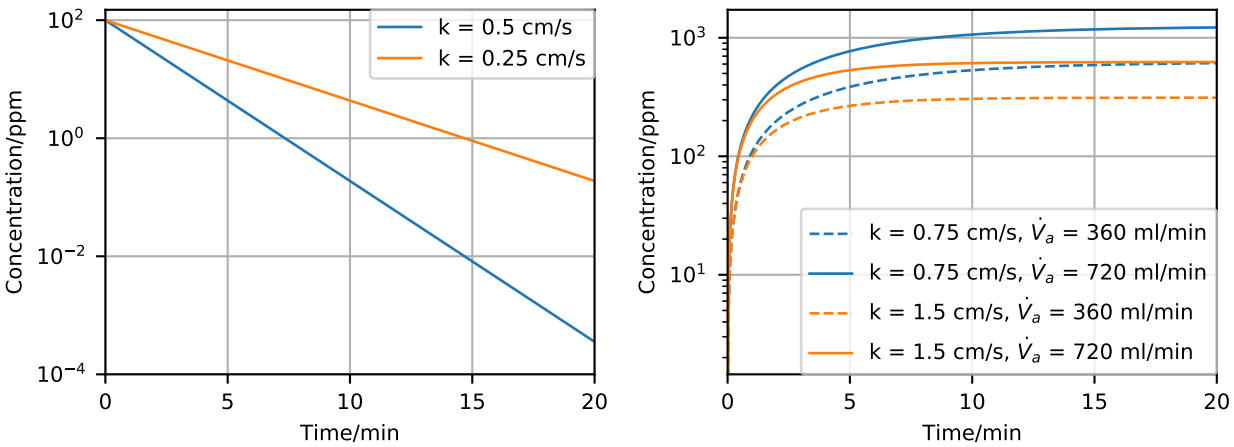

Figure 3.4: The air-side concentration as a function over time, as calculated via the mass balance with the (a) homogeneous and (b) inhomogeneous solution, Eqs. (3.11) and (3.13). For the setup-dependent constants, the dimensions of the two wind-wave tanks used in this thesis, the Benjamin-tank and the Lizard-tank, are applied in (a) and (b), respectively. Typical transfer velocities k as measured in the experiments are used. As the gas flux V_{a}, two values as used in the Lizard-setup are applied, while the concentration in the inflow is equal to 1. In both plots, the vertical axis is given in logarithmic scale.

4 Setup

The experiments described in this thesis were conducted at two wind-wave tanks, air- and water tight experimental setups where wind produced by a ventilator blows across a trough filled with water. Both wind-wave tanks were situated in the air-sea interaction laboratory at the Institute for Environmental Physics, Heidelberg University. The smaller one, named 'Benjamin'-tank, was used for a proof-of-principle measurement. As the experiment was successful, the setup was moved to another linear wind-wave tank called 'Lizard', which is larger and is thus more suitable for a study on the fetch-dependency of the mass and momentum transfer. Simultaneous measurements of LIF, PSV and LHC were conducted at two fetches.

In the first section of this chapter, the setups at the two wind-wave tanks used in the experiment are presented, including the buffers in the water. Then, the optical setup employed at both facilities is described: at the Benjamin-tank, only the LIF setup was applied, while at the Lizard-tank, LIF, PSV and LHC were used. Thereafter, the triggering scheme to ensure synchronous operation of the three methods at the Lizard-setup is characterized. Finally, the absorption spectroscopy as installed in both setups is described.

4.1 Wind-Wave Tanks

Two linear wind-wave tanks were used in the scope of this work: a smaller facility for the proof-of-principle measurements and a bigger one for the subsequent experiment with simultaneous PSV and LHC measurements. Table 4.1 shows an overview of the characteristics of the two facilities, which are described in more detail in the following.

Table 4.1: Dimensions of the two linear wind-wave facilities used in this work.

	Benjamin	**Lizard**
Wind forced water surface area [m^2][1]	0.46 ± 0.02	1.28 ± 0.02
Water depth(s) [cm]	3.0 ± 0.2, 12.0 ± 0.2[2]	9.0 ± 0.3
Air volume [l]	220 ± 10	3300 ± 300
Water volume [l]	20.6 ± 0.5	122 ± 4
Used fetch(es) [cm]	127 ± 5	75 ± 1, 234 ± 1
Friction velocities [cm/s]	$2.4 - 9.3$	$6 - 37$

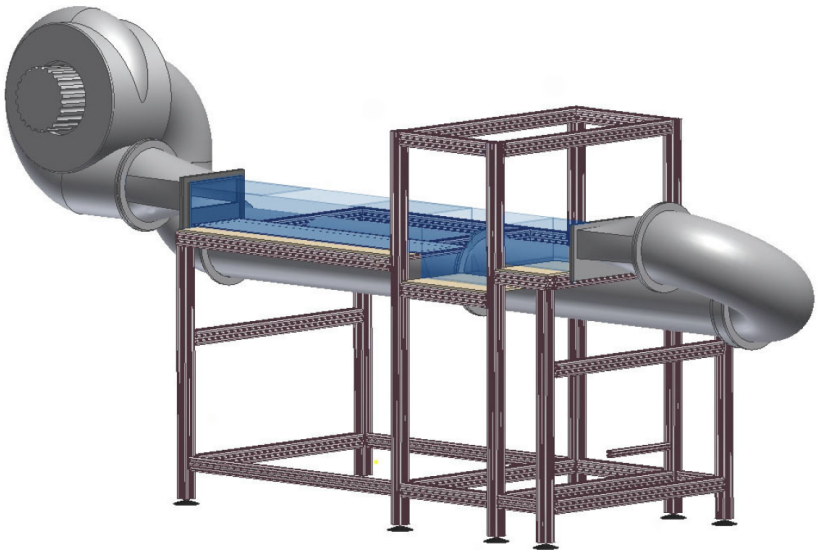

Figure 4.1: Technical drawing of the Benjamin-tank (Warken, 2010).

4.1.1 Benjamin-tank

The first facility, called 'Benjamin-tank' in the following, was used for the development and testing of the new measurement technique. It was built by Pius Warken and René Winter and detailed descriptions can be found in Warken (2010) and Winter (2011). The entire construction, which is sketched in Fig. 4.1, was about 3 m long, 1 m wide and 1.5 m high and consisted of a water section in the center, surrounded by an air recirculation duct with a fan for wind generation.

The water section was 25 cm wide and 191 cm long. A deeper section at the end of the water section was intended for experiments, therefore named the measurement section in the following. A sketch of this part of the facility is shown in Fig. 4.2 (Warken, 2010). The water depth was 3 cm in the shallow sections and 12 cm in the measurement section, while the air space above the water section was 10 cm high. Both air and water temperature were measured continuously in this section of the tank (two PT100 sensors with GMH 3710 by Greisinger). The access for the UV laser was situated at a fetch of 127 cm in the measurement section, too. The spectroscopic setup was situated downwind very close to the laser window in the roof above the water section and is further described in Sec. 4.7.

The walls and bottom of the experiment section consisted of 3.2 mm thick borosilicate glass BOROFLOAT® 33 by Schott AG (Mainz, Germany) with high UV transmittance. Figure 4.3 shows the transmittance curves of borosilicate glass with different thicknesses. It shows that possible scattered or reflected light with the laser wavelength (marked on the

[1] Water surface between the wind inlet and the wave absorber, thus the area where the wind hits the water.

[2] The water depth in the measurement section was deeper than in the rest of the water section (see Fig. 4.2).

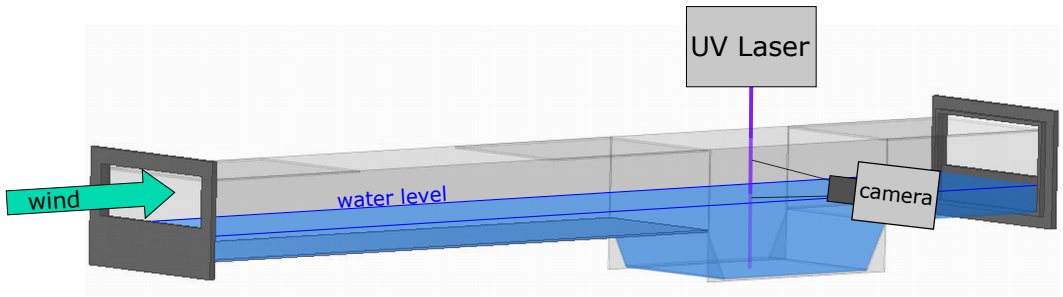

Figure 4.2: Sketch of the water section of the Benjamin-tank, showing the geometry of the LIF setup, adapted from Warken, 2010.

abscissa) does not penetrate the borosilicate glass. However, as the fluorescence of sulfur dioxide excited with light with a wavelength of 223 nm lies above 280 nm (Simeonsson, Matta and Boddeti, 2012), the choice of a thinner glass would be beneficial for the transmittance of the detectable fluorescence, but a reconstruction of the tank was technically not feasible. Both the transparent walls and small dimensions made the tank suited for first test measurements of visualization techniques in the development stage.

For a better mixing, the water was circulated through a bypass tubing system, where its pH value and conductivity were measured (GE 104 BNC electrode with GMH 3530 and LF 200 RW sensor with GMH 5430, both by Greisinger). The water temperature was measured close to the measurement section (PT100 sensor with GMH 3710 by Greisinger). The total water volume (including tubing and pumps) participating in the gas exchange was 20.6 l while the air volume was 220 l.

In the air recirculation duct behind the water section, a small tubing port was installed which was used for gas addition. There, the desired amount of SO_2 was added via a precise gas tight syringe. For an initial air-side SO_2 concentration of 100 ppm, a volume of 22 ml of the gas was needed per partial measurement.

For wind generation, a frequency converter was used to drive the motor of a radial ventilator. The wind speed was not measured during this experiment. However, from earlier experiments by Krah (2014), data exists of the air-side friction velocity u_* at varying driving frequencies set at the frequency converter. This adds some additional uncertainties to the estimate of the friction velocity as small changes in the geometry or of the water height already influences the wind field. Nevertheless, the data is good enough for this proof-of-concept measurements. For the wind conditions used in this experiment, the previously measured friction velocities range between 2.4 and 9.3 cm/s.

4.1.2 Lizard-tank

The second linear flume, named 'Lizard-tank', was used for the fetch experiment with simultaneous LIF, PSV and LHC measurements. With 7.7 m length and 1.5 m height, the whole construction has larger dimensions than the Benjamin-tank. It was built by

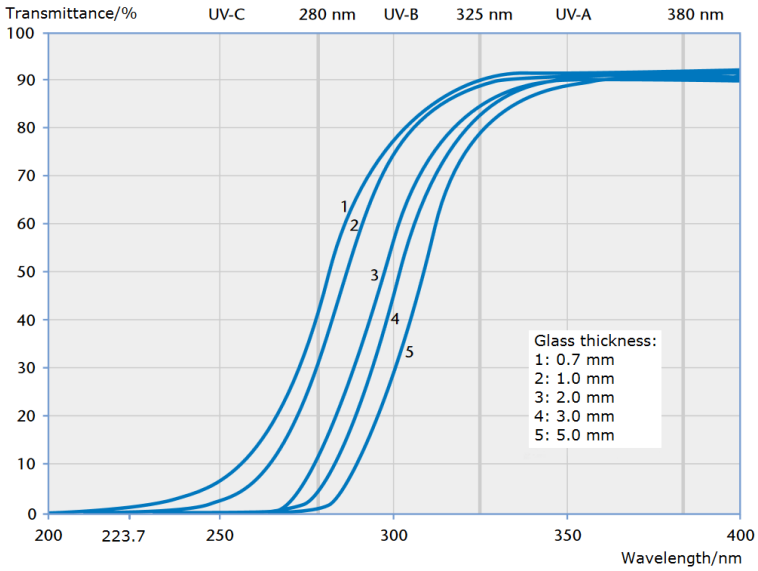

Figure 4.3: Transmittance curve of BOROFLOAT® glass with different thicknesses in the ultraviolet range, adapted from Schott (n.d.).

Alexandra Herzog and a thorough description including technical details is given in Herzog (2010). After a reconstruction, the tank in its current state is described in Friedl (2013). A sketch of the tank and the measurement equipment employed in the present study is shown in Fig. 4.4.

The axial ventilator (HF A 400 D by Hürner Funken) accelerating the air is located beneath the water section, connected to it through rectangular tubings. The air recirculation duct is made of foamed Polyvinyl Chloride (PVC) (Kömacel by Kömerling Plastics), the inside being covered completely with Polytetrafluoroethylene (PTFE) foil with a thickness of 0.25 mm, manufactured by Polytetra, improving the chemical resistance of the walls. As seen in Fig. 4.5, the water section has a uniquely formed cross section optimized for optical access to the water from the side. The base is narrow and widens upwards, the angle of the tilted segments being $16.8° \pm 0.3°$. Large observation windows made from borosilicate glass of 5 mm thickness are built in the bottom, one tilted side wall as well as the roof, making optical access from three sides possible. The non-transparent parts of the water section are made of the same materials as the air recirculation duct.

At a water level of 9 cm, the tank contains 3.3 m^3 of air, with the air space above the water being 23 cm high, and a total volume of 122 l of water, including 3.85 l of water in the bypass system. There are two bypasses: one is connected to the water inlet and containing a pump which creates a flow through the tubes from low fetch to high fetch for better mixing of the water. In the second smaller bypass where also a pump causes a flow in the same direction, a pH electrode is installed (GE 104 BNC electrode with GMH 3530 by Greisinger). The water segment itself is (388 ± 0.5) cm long and the water surface at the water level employed in the experiment is (38 ± 0.5) cm wide. A 0.8 m long wave absorber

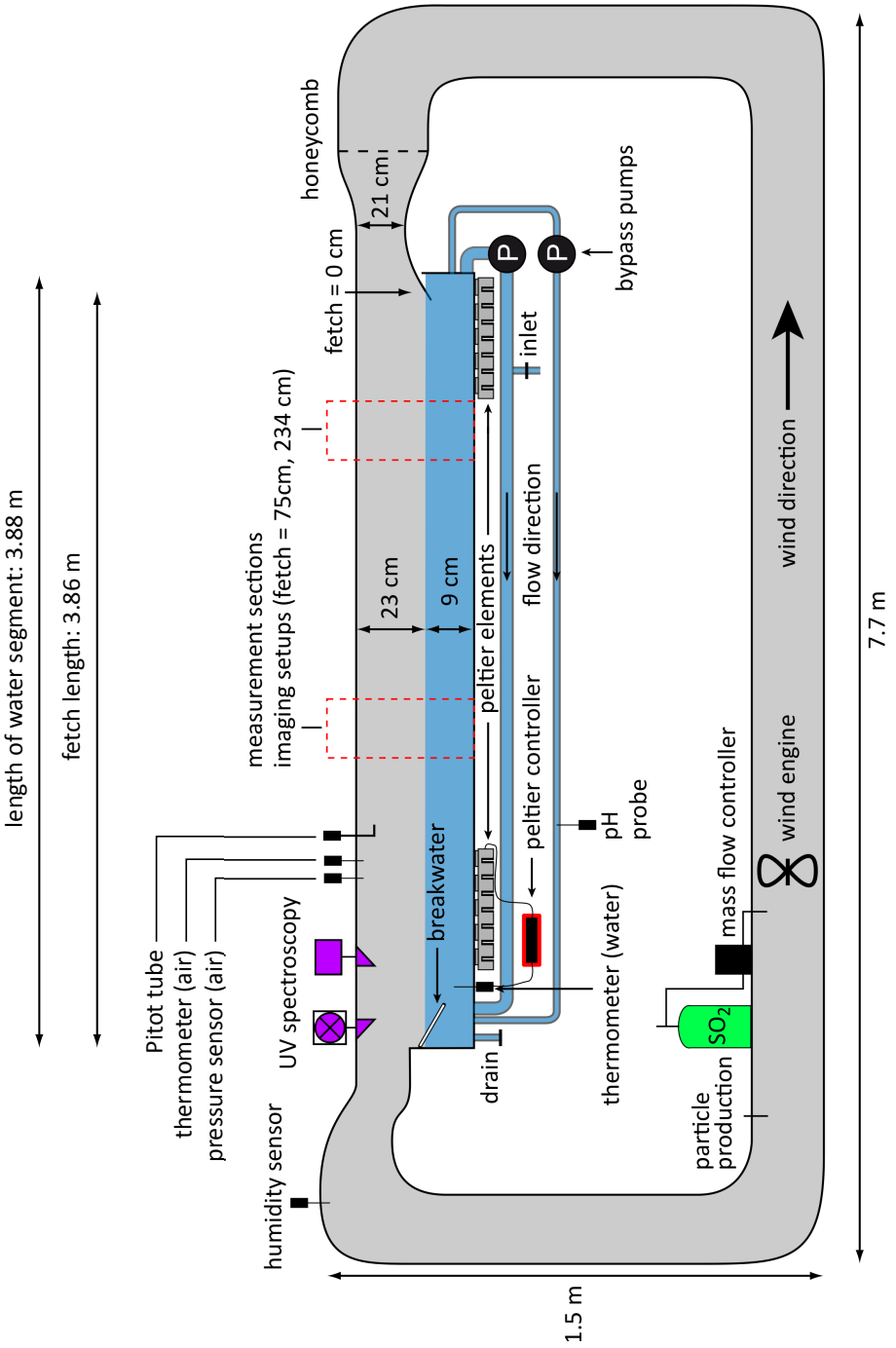

Figure 4.4: The Lizard tank and the measurement instrumentation, sketched from the side (modified after Papst, 2019; Friedl, 2013). The particle production setup is shown in Fig. 4.12.

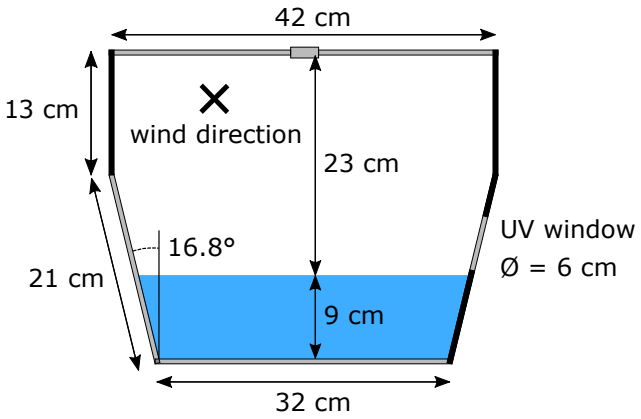

Figure 4.5: Cross sectional view of the water section, showing the windows in grey and non-transparent walls in black.

made of PTFE halftubes at the end of the water section reduces wave reflections. As the wind inlet protrudes over the first 22 cm of the water section and the breakwater disrupts 28 cm of the water surface, the wind forced surface area measures around 1.3 m^2. The experiment was conducted at two measurement sections, one located at a fetch of 75 cm and one at 234 cm.

During the experiments, the wind velocity was measured around 10 cm downwind from the high fetch measurement section with a Pitot tube and a differential pressure transducer (DIFF-CAP by Special Instruments), where the wind speed is deduced from the differential pressure with the air density (Kundu, Cohen and Dowling, 2015). For better comparison of the wind conditions with the other wind-wave tank, the friction velocities measured at different fetches and for different wind generator settings are taken from Friedl (2013), ranging between 6 and 37 cm/s. Also the air pressure and temperature as well as the water temperature are measured at this location of the tank (GMSD 1.3 BA sensor with GMH3110 and 2 PT1000 sensors with GMH 3710, both by Greisinger). The relative humidity of the air was recorded with a humidity sensor (HC2-S by Rotronic). At the highest fetch, above the breakwater, the spectroscopic setup was located, see Sec. 4.7. The laboratory temperature in the vicinity of the setup was also recorded (PT1000 sensor with GMH 3710 by Greisinger).

In this setup, a constant flux of sulfur dioxide was introduced into the tank during each experiment, using a digital mass flow controller, Model 35831S by Analyt-MTC.After a short equilibration time, an equilibrium between influx and transfer to the water is established, see Sec. 3.4. Thus, the air-side concentration is approximately constant during the whole experiment if the water's capacity to absorb sulfur dioxide, which depends on the pH and the buffer concentration, is not exceeded (see Sec. 4.1.3). This equilibrium phase is the interesting part of the measurement where the fluorescence images are best comparable between the measurements. However, the flux had to be adjusted according to the wind generator setting in order to obtain comparable equilibrium concentrations c_e (see

Fig. 3.4b). In Tab. 4.2, the fluxes and the resulting air-side equilibrium concentrations at the two fetches are listed for the different wind conditions. The flows were adjusted under the assumption that the wind speed is linearly proportional to the ventilator frequency and that the starting conditions, e.g. water level, water pH, water temperature, were exactly equal in all measurements. However, this is only an idealized assumption and explains why the equilibrium concentrations differ for different wind conditions.

In this setup, the same gas detector was used as at the Benjamin-tank for leakage monitoring.

Table 4.2: Wind generator frequencies W with the used SO_2 flows and the resulting equilibrium concentrations c_e for the measurements at Low Fetch (LF) and High Fetch (HF).

W Hz	Flow ml/min	c_e LF ppm	c_e HF ppm
5	180	523 ± 5	520 ± 15
10	360	505 ± 5	600 ± 5
15	540	506 ± 2	487 ± 1
20	720	470 ± 2	452 ± 2

4.1.3 Water

In both facilities, the humidity increases continuously when the tank is closed, filled with water and under operation. As also the air temperature rises due to the heat produced by the ventilators, condensation on surfaces such as walls, windows and optics is a possible consequence. To prevent this, the water was cooled in both facilities via Peltier temperature control units. In the Benjamin-tank, 40 Peltier elements (QC-127-2.0-15.0M by Cooltronic) were mounted on 5 fan cooled heat sinks below the water tank, connected directly to the aluminum base plate in the shallow region of the tank. The Peltier elements were regulated by a Peltier controller (TC3215 by Cooltronic) and the system could both cool and heat the water.

The temperature control setup in the Lizard-tank is very similar. It contains two separate arrays of 24 Peltier elements (QC-127-2.0-15.0M by Cooltronic) each, one at the lowest and one at the highest fetch of the water section. The setup is regulated by one Peltier controller (TC2812 by Cooltronic). A detailed description of the cooling setup in the Benjamin-tank and Lizard-tank can be found in Winter (2011) in the appendix and in Friedl (2013), respectively. During the measurements presented here, a target temperature of 16 °C was chosen, however this temperature was never reached due to the large amount of heat produced by the ventilators. Nevertheless, the systems achieved cooling of the water compared to the surroundings of a few degrees with a minimum temperature of $18 - 19$ °C, which already suffices to prevent condensation.

To keep the chemistry in the experiments simple, deionized water is used in both setups with a conductivity less than 0.1 μS/cm. The deionized water has an initial pH of around 5.6. In order to have the same measurement conditions at the start of each experiment, the water was made alkaline by mixing either NaOH or a buffer into the water (see below). Thereby, the pH is increased to above 11. Furthermore, a fluorescent dye, pyranine, needed for the surface detection is added to the water prior to each experiment of the fetch study in the Lizard-tank (see Sec. 4.4).

Sodium Hydroxide

The first set of experiments at the Benjamin-tank was planned in such a way, that all measurements were conducted successively with the same water charge. As adding sulfur dioxide to water makes it more acidic, starting the measurement series with already acid water, deionized water in this case, would lead to different starting conditions for successive measurements. Therefore, in order to have the same initial conditions, the water is made alkaline to a pH value larger than 11 by adding 1-molar sodium hydroxide solution (NaOH). The idea is that the sodium hydroxide reacts with the dissolved sulfur dioxide. The reaction equation is

$$H_2SO_3 + 2\,NaOH \longrightarrow 2\,H_2O + Na_2SO_3, \tag{4.1}$$

showing that the pH is kept constant due to the reaction of the sulfite ion with the sodium ions to sodium sulfite. This means that the amount of sodium hydroxide solution needed to neutralize a certain amount of sulfur dioxide is double the latter. Therefore, given the volume of pure SO_2 released into the air volume at each measurement, i.e. 22 ml which corresponds to 100 ppm and to 10^{-3} mol with the molar volume of an ideal gas, one finds that an amount of at least 2 ml 1-molar NaOH solution is theoretically needed per partial measurement to keep the pH value constant. Since 11 measurements with varying wind conditions were made, this sums up to 22 ml 1-molar NaOH solution.

Also the carbon dioxide in the lab air has to be considered. An initial CO_2 concentration in the air of 1000 ppm (this is the Pettenkofer-number, often referred to as the upper limit for good indoor air quality, Pettenkofer, 1858) is assumed. Furthermore, between the partial experiments, the tank was not opened such that no fresh air with additional carbon dioxide could enter. Then, because the reactions of CO_2 with water are analogous to those of SO_2, see next section, 20 ml 1-molar NaOH solution is needed to counteract a change in the pH value due to the solution of the CO_2 in the water. Hence, the total amount of 1-molar NaOH solution theoretically needed to keep the pH value constant during the experiment is 42 ml.

Test experiments showed that a minimum of 150 ml of 1-molar sodium hydroxide solution has to be added to the deionized acid water to raise the pH to 11, which was the target pH. Calculating the pH value resulting from adding this amount of sodium hydroxide to the water of the tank yields a theoretical value of 11.86. The reason for this discrepancy lies probably in the uncertainty of the pH probe. On the one hand, the electrode has an uncertainty of ± 0.05 and on the other hand, the probe is to be used in still water rather

than in a flow, as it is applied here in the bypass. Papst (2019) observes a systematic offset of -0.3 when the bypass pump is active compared to when it is turned off.

During the measurement series, the pH value stayed practically constant, since the SO_2 was directly neutralized in the alkaline water. Making the water that alkaline also increases the effective solubility of SO_2 to about 10^{15} and higher, as can be seen from Fig. 2.4b.

Carbonate Buffer

In test measurements in the larger Lizard-tank with the same method as in the Benjamin-tank, adding sodium hydroxide to the water, the pH value changed significantly during the duration of the experiment as the water became more and more acidic. The reason is that a much larger amount of SO_2 is introduced to the tank per measurement, since a constant flux was applied to reach equilibrium conditions. Therefore, the pH control had to be refined for the Lizard-tank: a carbonate buffer was used instead, consisting of sodium carbonate (Na_2CO_3) and sodium bicarbonate ($NaHCO_3$). The dissociation equilibrium between sodium carbonate and sodium bicarbonate is at a pH of 10.33 (Haynes, 2016), which is the pK_a value of carbonate at a temperature of 25 °C. Here, the following reaction equations illustrate the buffering effect of the solution:

$$H_2SO_3 + 2\,NaHCO_3 \longrightarrow Na_2SO_3 + 2\,H_2CO_3, \tag{4.2}$$

$$H_2SO_3 + Na_2CO_3 \longrightarrow Na_2SO_3 + H_2CO_3. \tag{4.3}$$

In both reactions, sodium sulfite and carbonic acid are the products while the pH remains constant. By adjusting the ratio of the two buffer components $[Na_2CO_3]/[NaHCO_3]$, the pH of the water can be tuned to a target pH, which is 11 in this setup. The ratio was calculated in the Henderson-Hasselbalch approximation:

$$\mathrm{pH} \approx \mathrm{p}K_\mathrm{a} + \log_{10}\left(\frac{[Na_2CO_3]}{[NaHCO_3]}\right) \tag{4.4}$$

with the following assumptions:

1. **The initial pH of the water is 7**, i.e. the water is initially neutral. However, the deionized water actually used in the experiment is slightly acidic. But an estimate of the amount of buffer needed to neutralize the acidic water is of the order of 10^{-3} mol. As this value is much smaller than the amounts used for the experiments, this circumstance adds only a small, negligible uncertainty to the resulting pH of the buffered water. Other factors add much larger uncertainties to the pH, as e.g. the uncertainty in the amount of the added buffer.

2. **The pH range is limited to $\mathrm{p}\boldsymbol{K}_\mathbf{a} \pm 1$**, i.e. the ratio of the concentrations of the two buffer components is smaller than 10, which is the case in this setup, see the following calculation.

Solving Eq. (4.4) for the concentration ratio with the target pH = 11 and the known $\mathrm{p}K_\mathrm{a}$ yields

$$\frac{[Na_2CO_3]}{[NaHCO_3]} = 10^{11-10.33} = 10^{0.67} = 4.68. \tag{4.5}$$

The necessary absolute concentration of the buffer in the tank water is calculated by an estimate of the total amount of sulfur dioxide added to the tank during one experiment. This is different at each wind condition since the SO_2 input flux is varied according to the wind speed, i.e. higher winds result in higher transfer velocities and call for higher gas input fluxes to the target in order to obtain the same equilibrium concentration. Thus, for the 20 Hz-measurements, approximately twice the amount of buffer was needed than for the 10 Hz-measurements, assuming that the wind speed is linearly proportional to the ventilator frequency and that the gas transfer is linearly proportional to the wind speed.

It was planned to limit the gas input flux to 30 min for each measurement. Combined with the flux, being between 180 ml/min for the lowest and 720 ml/min for the highest wind condition (see Tab. 4.2), a value for the amount of released SO_2 is approximately in the range of 5.4 to 21.6 l or 0.24 to 0.96 mol.

Since the air in the flume also contains carbon dioxide which tends to be dissolved in the water, this must also be taken into account. Assuming an initial CO_2 concentration of 1000 ppm in the air (see above) and 0 ppm in the water[3] and that all of the gas eventually is dissolved in the water[4], this results in 0.134 mol of CO_2. This molarity has to be added to the molarity of the sulfur dioxide, then the following equation needs to be solved for the concentrations of the buffer constituents:

$$n(Na_2CO_3) + 2n(NaHCO_3) \geq n(SO_2) + n(CO_2). \tag{4.6}$$

This implies that at least 33 to 96 g of Na_2CO_3 and 5.6 to 16.2 g of $NaHCO_3$ are needed to neutralize the sulfur dioxide and carbon dioxide, depending on the wind condition.

However, test experiments showed that these amounts did not suffice to keep the pH constant. For the two lowest wind conditions (5 and 10 Hz), a mixture of 280 g Na_2CO_3 and 47.4 g $NaHCO_3$ was used, while for the two highest wind conditions (15 and 20 Hz), the amount was doubled to 560 g Na_2CO_3 and 94.8 g $NaHCO_3$. The buffer was premixed in 2-4 l of deionized water, then the buffer solution was added to the tank water.

4.2 Overview of the Optical Setup at the Lizard-tank

In this section, an overview of the optical system consisting of three independent measurement setups which need to be paralleled and operated simultaneously is given. Then, in the subsequent three sections, the three independent measurement setups are described in detail.

Each of the three measurement techniques consist of a light source, i.e. one or more lasers, and a camera. The four lasers of the PSV setup and the LHC laser are each spread to a laser sheet and adjusted in such a way that their sheets cover the measurement Region Of Interest (ROI) centered around the LIF laser, as shown in the schematic illustration

[3] This is an idealizing assumption since the deionized water when filled into the tank already contains CO_2.

[4] This is probably not the case for the carbon dioxide as the solubility of carbon dioxide is typically around 1.

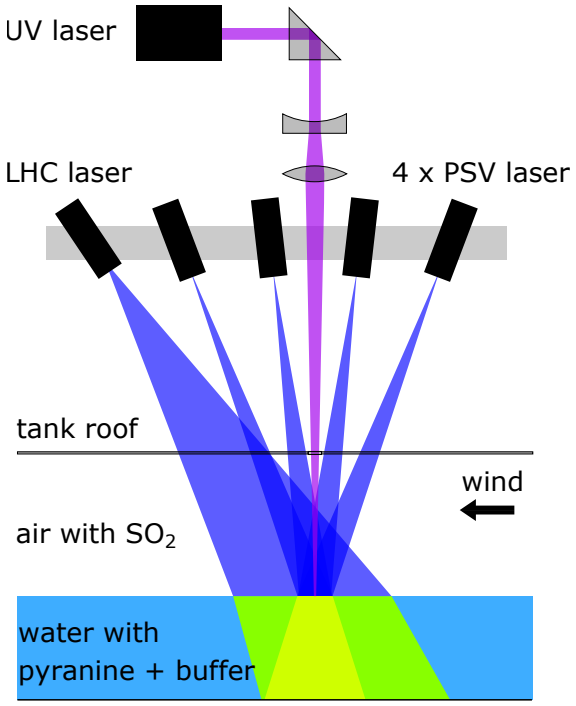

Figure 4.6: Schematic of the laser setup at the Lizard-tank.

in Fig. 4.6. All lasers are mounted above the wind-wave tank, their light entering the air-space of the tank through the top glass window, with the exception of the LIF laser: its light is in the UV and is absorbed by the window. Therefore, a small UV transmitting window is build into the top window at the location of the UV laser beam. The PSV and LHC cameras view the ROI which is illuminated by the laser sheets through the big side window of the tank. The fluorescent light from pyranine and the scattered light from the particles is in the visible range, and can therefore penetrate the borofloat glass. However, as the fluorescence from the sulfur dioxide is in the UV range and the borofloat glass' transmittance in the UV is limited, a thinner window with higher UV transmittance is located in the wall opposite to the large side window. In order to minimize reflections off the optics or windows from disturbing the images, the extra window is not located directly opposite to the LHC and PSV cameras, but is displaced in the wind direction by a few centimeters. Figure 4.7 shows the setup of the cameras in a cross sectional view of the tank.

The Field Of View (FOV) of the cameras in relation to each other is shown in Fig. 5.2: The LHC has a wider FOV of the surface, however with relatively low resolution, the PSV FOV is in the center of the LHC FOV and oriented vertically, while the LIF FOV is in the center of the other two FOVs.

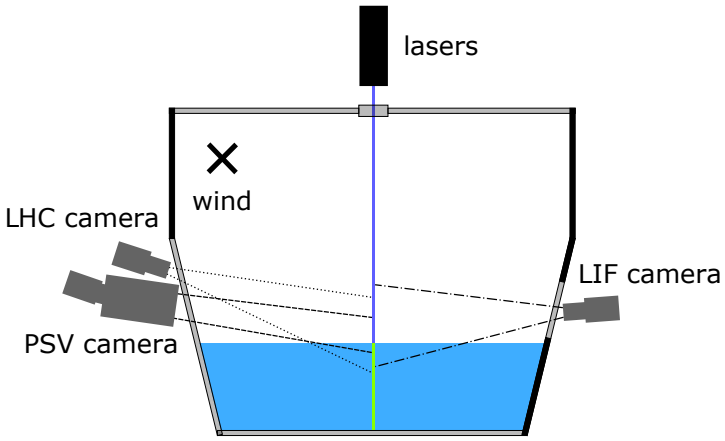

Figure 4.7: Schematic of the camera setup at the Lizard-tank. See also Fig. 4.5 for the dimensions. The three cameras are shown as if they are in one plane. As described above, this is not the case and serves only to simplify the illustration.

4.3 LIF Setup

The LIF setup consists of a UV laser as a light source and UV sensitive cameras for the detection of the fluorescence. Both tanks had to be adapted for the use of ultraviolet radiation.

This setup is the only one of the three setups which also was applied at the Benjamin-tank.

4.3.1 UV Laser

Sulfur dioxide, which is used as a tracer in this experiment, is excited by ultraviolet laser radiation. The laser is mounted above a special window with high UV transmittance such that the laser beam traverses the air volume above the surface before reaching the surface. The following prerequisites are posed on the laser:

The laser wavelength has to be in the high absorbance region of SO_2, but not below 220 nm where the fluorescence efficiency is reduced due to photodissociation (Hui and Rice, 1972). In Fig. 4.8, the absorption cross section of sulfur dioxide is shown as measured in the scope of this thesis and in the literature.

Furthermore, the lifetime of the excited states has to be longer than the fluorescence deexcitation time, otherwise the states will be deexcited by means of processes other than fluorescence, e.g. through collisions. This happened in first experiments with a laser at 266 nm where the fluorescence signal was smaller than the elastic scattering signal by several orders of magnitude. In the literature, the most commonly used wavelength for LIF with SO_2 is 223 nm (see for example Simeonsson, Matta and Boddeti, 2012).

The laser source used here is a Q-switched laser system, namely the IMPRESS 224 by Xiton Photonics, emitting UV laser pulses with a repetition frequency of 10 kHz and a

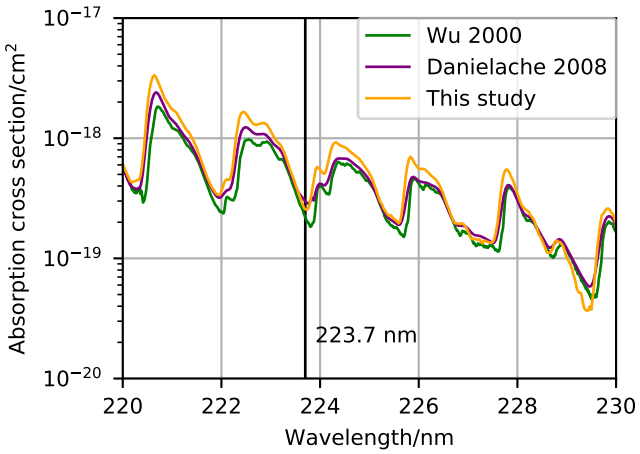

Figure 4.8: Absorption cross section of sulfur dioxide against the excitation wavelength, data from this study (orange) in comparison with values from literature (Wu et al., 2000; Danielache et al., 2008). The laser wavelength 223.7 nm used in this setup is marked by a vertical line. Only the part of the spectrum relevant for this thesis is shown.

pulse duration of up to 9 ns, a maximum average power of $200 - 300$ mW and an energy per pulse of $20 - 30\,\mu$J. The spectral profile of the laser is shown in Fig. 4.9 with a fit to the data, which gives a mean emission wavelength of 223.69 nm and a linewidth of 0.13 nm. As seen in Fig. 4.8, the wavelength of the laser lies in a dip of the absorption cross section curve. This is unfortunate for obvious reasons, but for lack of alternatives the application of this laser was the only possibility.

At both wind-wave tanks, the laser was positioned above the tank, see Figs. 4.2 and 4.6. In the test setup at the Benjamin-tank, it was mounted vertically very close to a laser window (quartz glass with high UV transmittance) in the tank roof. As the distance to the water surface was short, around 20 cm, no focusing optics ware needed. However, as the laser beam exits the laser head at an angle, this angle could not be corrected and the beam did not hit the water surface perpendicularly. This was corrected for in the analysis of the LIF data. Moreover, the skewed incident angle has the advantage that the risk for back reflections reaching the laser head is reduced.

At the Lizard-tank, the laser could not be mounted in the same way: the removable tank roof is the only access point where chemicals (e.g. buffer and dyes) can be added to the water or calibration targets put into the experiment section and the space above the tank is limited by the roof such that the laser cannot be mounted vertically. Therefore, the laser was mounted horizontally above the tank with a calcium fluoride prism which led the beam vertically towards the tank roof. Calcium fluoride (CaF_2) is commonly used in UV optics as it has very low absorbance in the ultraviolet range. As the distance between the laser head and the water surface in the Lizard-tank was much larger than in the Benjamin-tank, the divergence of the beam had to be corrected through a focusing telescope with two CaF_2

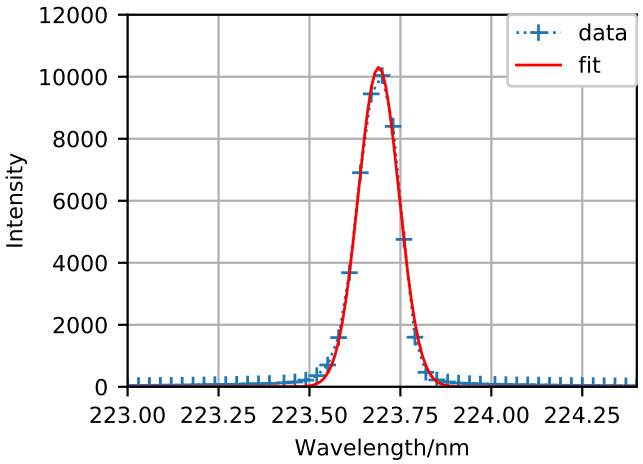

Figure 4.9: Spectral profile of the UV laser measured with the spectrometer used in the spectroscopic setup: data (blue) with a Gaussian profile fit (red).

lenses, a concave lens with a focal length of −25 mm and a convex lens with a focal length of 80 mm. In the measurement section, the diameter of the focused beam is very small, such that it was hard to determine at exactly which height the focus point was.

The laser beam entered the tank through a calcium fluoride window which is mounted over a hole in the roof window. During the first test measurements in the Lizard-tank, it was observed that the beam quality decreased with time[5]. The cause was found in an opaque spot that appeared on the CaF_2 window exactly where it is traversed by the laser beam. A possible origin was explained by Perkins (2019): the focused laser beam causes hydroxyl radicals (OH) to form from the water vapor, which then react with sulfur dioxide to form sulfuric acid (H_2SO_4), which then in turn reacts with the CaF_2 of the window to form hydrogen fluoride (HF):

$$H_2SO_4 + CaF_2 \longrightarrow 2\,HF + CaSO_4. \tag{4.7}$$

A similar reaction is described by Bauer et al. (2009) where carbon dioxide instead of sulfur dioxide acts as the acid source. Here, the end product $CaCO_3$ was detected and identified as the contamination on the calcium fluoride window. It is assumed that the analogous product of the reaction described above, $CaSO_4$, is the constituent of the opaque dots occurring at the beam position on the CaF_2 window.

In order to hinder water vapor from accumulating close to the laser window, a heat gun was directed on it from above, its temperature setting was adjusted to 50°C. However, this procedure only reduced the effect and was unable to completely prevent it.

[5]This effect had already been noted during the test measurements at the Benjamin-tank. However, the measuring time was much shorter and the beam quality was not affected to the extent that a counter measure had to be considered.

4.3.2 UV Sensitive Cameras

For fluorescence detection, a camera with high UV sensitivity and preferably low noise is needed. The proof-of-principle experiment at the Benjamin-tank was conducted using a DHYANA 95 camera by TUCSEN (Fuzhou, China) with a 2048×2048 pixels back-illuminated CMOS sensor. The sensor has high sensitivity in the ultraviolet range, with a quantum efficiency between 35 and 60% in the wavelength range of the sulfur dioxide fluorescence, and its pixels measure $11 \times 11\,\mu m^2$. In combination with the camera, a PENTAX UV lens (H2520-UVM) with a focal length of 25 mm and maximum aperture of f/2.0 was used. It has a maximum transmittance of 70% between 300 and 350 nm and in the fluorescence wavelength range, the transmittance is at least 69% (the transmittance spectrum is shown in Fig. A.2). The spatial resolution obtained from geometric calibration was 56.6 μm/px. By only reading out the central section of the sensor with 1024×256 pixels, a maximum recording speed of 40 fps was reached. The camera was positioned at the side of the tank, viewing the measurement section with the laser beam perpendicular to the wind direction (see Fig. 4.2). It was slightly tilted in the y-z-plane such that small waves would not shield the laser beam in the air close to the water surface which is the most interesting part for the measurements.

At the Lizard-tank, another camera was used: a BASLER acA3088-57um. Its CMOS sensor consists of 3088×2064 pixels, each measuring $2.4 \times 2.4\,\mu m^2$. Thus, it has a smaller chip and smaller pixels, but also a lower dark noise than the first camera, while the sensors' quantum efficiency in the ultraviolet range is comparable. Here, too, the Pentax 25 mm UV lens was used, resulting in a spatial resolution of 20.0 μm/px. As a thinner window was build into the second tank, shorter exposure times were possible. In this case, a recording speed of 200 fps was used. The exposure time is limited by the readout time of the camera, thus the maximum exposure time at the set recording speed was 4.848 ms.

In the Benjamin-tank, the windows' transparency in the ultraviolet range of the electromagnetic spectrum was sufficient for the first proof of principle of the measurement technique. However, as shown in Fig. 4.3, the thicker observation windows of the Lizard-tank in combination with a less sensitive camera sensor made the installation of a thinner borosilicate window necessary for sufficient fluorescence detection. The windows were places opposite to the large panorama window. To reduce interference by reflections off the window in the LHC and PSV cameras, the window was not positioned in line with the laser beams and the optical axes of the other two cameras, such that the LIF camera viewed the laser beam at an angle not only in the y-z-plane. As the LIF setup uses the laser light as a beam, not a sheet, the angle does not appreciably influence the sharpness of the images and the distortion can be compensated through geometric calibration with a calibration target and by division by reference images (see Sec. 5.1.1). This also reduces the vignetting effect caused by the lens. As the camera's exposure time coincided with both other laser signals (the triggering is described in Sec. 4.6), a filter was used to minimize the interference by fluorescence from the water or scattering from particles. The absorbance spectrum of the filter is presented in Fig. 4.10, along with the pyranine fluorescence spectrum and the wavelengths of the lasers used in this experiment. The figure shows that the absorbance

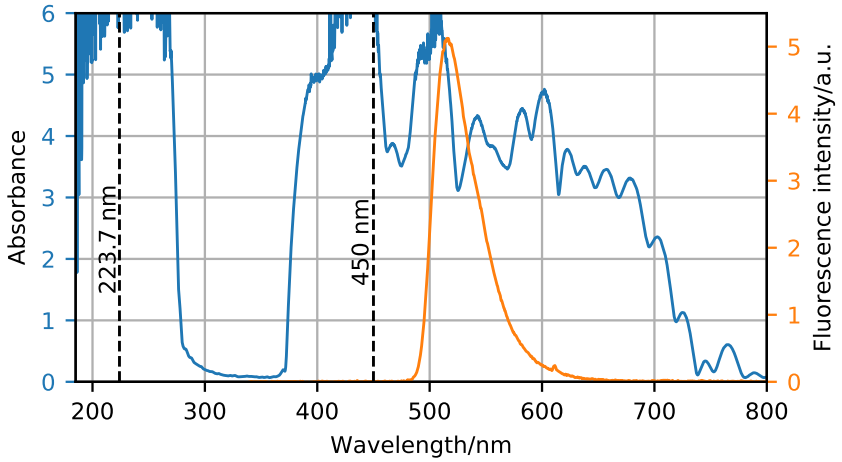

Figure 4.10: Absorbance spectrum of the filter used in the LIF setup (blue), measured with a Shimadzu spectrophotometer, and fluorescence spectrum (red) of pyranine in the basic state, measured with a spectrophotometer by Ocean Optics (Kräuter, 2015), with the wavelengths of the LIF laser (223.7 nm) and the PSV and LHC lasers (450 nm) marked with dashed lines.

is not perfect in the visible range, however, it is expected to reduce the interference of the pyranine fluorescence in the LIF pictures to an acceptable level.

4.4 Surface Detection (LHC) Setup

To facilitate the surface detection by means of the LHC measurement technique, the fluorescent dye pyranine is added to the alkaline water. It has different absorbance and fluorescence states, depending on the alkalinity of the water: the absorption maximum (and efficiency) as well as the fluorescence efficiency changes with the pH. Both absorbance and fluorescence increase with increasing pH. Figure 4.11 shows the pyranine absorbance spectrum in the tank water, after adding buffer and thus increasing the pH value to over 11, as well as the fluorescence spectrum, measured in water with a pH of 9 (Kräuter, 2015). Since only the fluorescence intensity increases with the pH, the spectrum is representative for water with different alkalinities, too. For fluorescence emission and absorption spectra at various pH values, see Kräuter (2015) and Papst (2019).

A blue laser diode, with the wavelength 450 nm and a maximum output power of 3 W, mounted above the glass roof of the tank was employed to excite the dye. The wavelength of the laser diode is chosen according to the absorbance spectrum of pyranine (see Fig. 4.11) showing a maximum absorbance in the visible range of the spectrum at 455 nm. The laser beam is widened to a sheet in wind direction with a cylindrical lens which is then focused on the water surface to minimize the width in cross wind direction, resulting in a sheet length of 6 cm and a width of 1 mm.

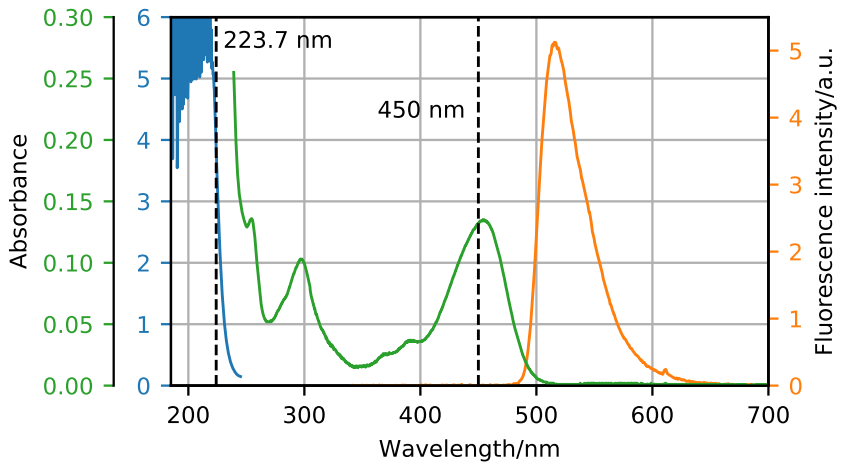

Figure 4.11: Absorbance (blue and green), measured with a SHIMADZU spectrophotometer, and fluorescence spectrum (red) of pyranine in the basic state, measured with a spectrophotometer by OCEAN OPTICS (Kräuter, 2015). The absorbance spectrum is shown twice with different scales for better visualization.

For the detection of the fluorescence, a camera of the type BASLER acA1920-155um is used, mounted on the side of the tank. Its CMOS sensor has 1920 × 1200 pixels with a pixel size of 5.86 × 5.86 μm^2, however only a segment of 512 × 400 pixels was used. The quantum efficiency is around 70%. With the reduced image size and in combination with a fast hard drive for storage of images (solid-state drive, SSD), a frame rate of 400 fps was achieved. The lens, a TAMRON 23FM16SP, has a focal length of 16 mm and a maximum aperture of f/1.4 and the resulting resolution from geometric calibration is 122 μm/px (see Sec. 5.1.1). The camera views the field of interest where the laser sheet meets the surface at an angle. A tilt-shift adapter was not required as the setup has a large depth of field. Sharp images were obtained when the camera was focused on the fluorescence line on the surface. A green band pass filter is attached to the lens to absorb reflections of the laser light.

The amount of pyranine needed for efficient surface detection depends on the pH of the water because the fluorescence efficiency depends on the alkalinity. Thus, before every measurement, the dye concentration is tested by turning on the laser sheet and viewing the fluorescence as imaged by the camera. A minimum of 100 mg was needed for a pH of 11. On the other hand, the amount of pyranine is limited by the fluorescence intensity in the PSV images: in particular, at low wind speeds and long exposure times, the fluorescence intensity from the pyranine saturates in the images for too high dye concentration and laser intensity.

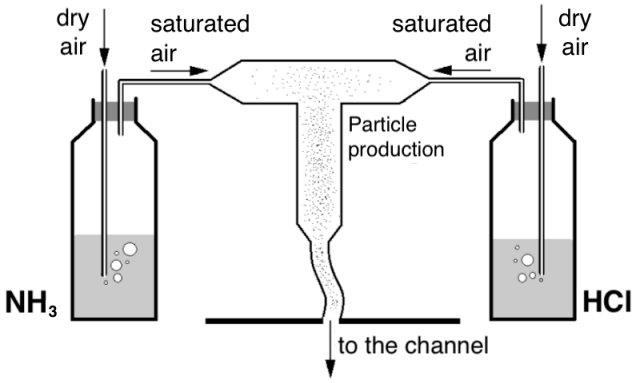

Figure 4.12: Sketch of the particle production with NH_3 and HCl (modified after Kühlein, 2019).

4.5 Flow Visualization (PSV) Setup

The particles used for the flow measurements via PSV are produced in the following way (see Fig. 4.12): a stream of dried air is led through two wash bottles, filled with high concentrated solutions of ammonia and hydrogen chloride (hydrochlorid acid), respectively. The flow is controlled by two digital mass flow controllers by Analyt-MTC. The two air flows containing ammonia and hydrogen chloride meet in a wider tube where the chemicals react to ammonium chloride. To get equal concentrations of the two reactants in the mixing tube, the air flux through the HCl solution is 14 times higher than the flux through the NH_3 solution because the saturation pressure of NH_3 is 14 times higher than for HCl. The salt crystals are flushed into the tank through a tube connected to the tank just in front of the axial ventilator such that it is evenly mixed into the air of the tank until it reaches the water section.

The setup is illuminated by a laser sheet produced by four laser diodes in order to have sufficiently high luminosity. The laser diodes are of the same type as the one used for the LHC setup. They are mounted horizontally in line above the tank, each in an aluminum heatsink with the electronics glued on top of the latter. Each laser beam is first focused by a spherical lens and then spread with a cylindrical lens with a focal length of $-25\,\mathrm{mm}$, producing a 1.5 cm long sheet at the water surface, the width being 1 mm. All four laser sheets are aligned in such a way that they overlap in the center of the camera FOV, approximately 1 cm above the water surface.

For particle detection, a camera of the same type as in the LHC setup is used. In this case, a section of 1920×800 pixels is read out, centered around the region of the LIF laser, at a frame rate of 200 fps. A tele macro lens with a focal length of 100 mm is used (type: Zeiss Makro-Planar T* 2/100 ZF), yielding a resolution of the optical setup of 12.5 μm/px. In order to avoid shielding by waves, the camera is mounted above the highest wave crests and views the illuminated region of interest at an angle. Thus, the sensor plane was tilted relative to the object plane of the laser sheet. The aperture is adjusted to f/8, causing

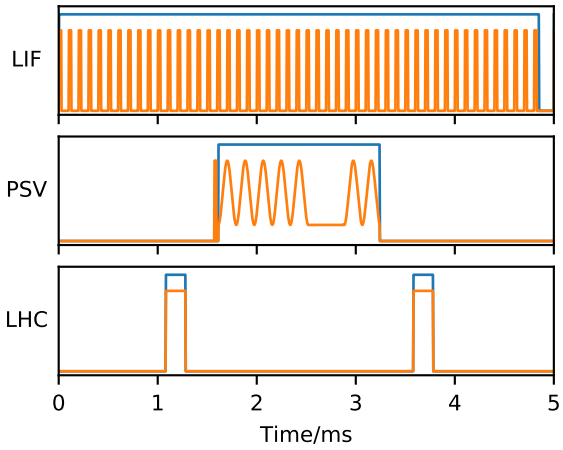

Figure 4.13: Scheme of the laser trigger signals (orange) and the camera exposure times (blue) of the LIF, PSV and LHC methods for one period of the LIF and PSV triggers and two periods of the LHC trigger.

a very narrow depth of field. Consequently, not the whole FOV can be in focus. This is corrected for using Scheimpflug optics: by tilting the lens plane, the focal plane can be aligned with the object plane. To achieve this, the lens is mounted on the camera body with a tilt-shift adapter. The angles between the three planes are determined using the Scheimpflug criterion (Jähne, 2012)

$$\tan(\theta') = -m \tan(\theta), \tag{4.8}$$

where θ' is the angle between the focal and lens plane, θ the angle between the sensor and lens plane and m the magnification factor. In this setup, the magnification factor is around 0.625 and the tilt-shift adapter has an angle of 4°. Therefore, the lens plane is tilted by 9.5° and the resulting total angle between focal and lens planes is 13.5°.

4.6 Triggering

In this section, the trigger scheme used in the fetch experiment is explained. The scheme is sketched in Fig. 4.13. In the proof-of-principle experiment, a trigger was not needed, since only the LIF camera was read.

In order to synchronize the measurements of all three imaging techniques, the lasers and cameras must be triggered. For the triggering, two function generators are available, providing two trigger outputs each. A problem in this context is that the maximum exposure time of the camera used in the LIF setup is reduced when an external trigger source is applied. On the other hand, in order to collect as much fluorescence light as possible, longer exposure times are favored. The problem is resolved by using the camera as the trigger source for all other devices. Thus, the LIF camera is operated with a repetition rate of 200 Hz and its trigger output is used as the external trigger for both function generators.

The first function generator triggers the LHC laser and camera with a TTL rectangle signal of 200 μs length with a repetition rate of 400 Hz and the PSV lasers and camera with the programmed signal with 200 Hz. The programmed signal consists of a 40 μs long trigger rectangle signal followed by a 20 μs break and the PSV signal for the laser, see Fig. 3.2. The duration of the latter as well as the exposure time are adapted to the wind velocity: the higher the wind, the shorter the signal. The lengths are chosen such that the particle streaks in the free stream section are approximately 150 pixels long. The rectangle signal triggers the onset of the PSV camera exposure and its timing accounts for the intrinsic, electronically caused trigger delay time. Both the PSV and LHC signals are delayed to the input trigger signal such that the PSV signal is positioned in the center of the exposure time of the LIF camera and centered between two succeeding LHC triggers. This ensures that the PSV and LHC methods do not interfere with each other. As the LIF camera has a filter which has the highest transmittance in the wavelength range of the LIF fluorescence, the light from the other lasers is not expected to disturb the LIF images.

The LIF laser is triggered by the second function generator with 49 pulses at a frequency of 10 kHz and a duty cycle of 25%.

The trigger settings are adjusted according to the wind condition: the PSV signal frequency as well as the signal delay relative to the LIF camera trigger is decreased for lower wind speeds, while the corresponding exposure time is increased. This is done in order to maintain the coincidence of the PSV and LIF exposures halfway between the two LHC signals. The LHC signal is not directly affected by the wind speed. However, for lower wind speeds, the pyranine fluorescence in the PSV images is strongly enhanced as the illumination and exposure times grow. Because an overexposure means loss of information and affects the image quality. This effect should be avoided with priority. Therefore, lower pyranine concentrations are used for the two low wind speed measurements at the high fetch. In order to reach similar fluorescence intensities as in the other measurements, the LHC illumination and exposure times were correspondingly increased.

4.7 Absorption Spectroscopy

In addition to measuring the gas concentration near the air-water interface using fluorescence, an in situ spectroscopic setup was installed in the roof of both tanks to quantify the SO_2 concentration averaged over the whole air volume. The spectroscopic setup consists of a deuterium lamp as ultraviolet light source, focusing optics made of quartz glass and a USB-spectrometer (Maya 2000 Pro by Ocean Optics). The light emitted by the lamp traverses a path of 16 cm in the Benjamin-tank and 39 cm in the Lizard-tank in the air between two UV transmitting prisms. A detailed description of the setup at the Lizard-tank can be found in Papst (2019).

The bulk sulfur dioxide concentration is obtained from the transmittance spectra (see Eq. (2.62)). Because the absorbance and bulk fluorescence intensities are proportional, these measurements provide a useful benchmark for the absolute and relative concentration series determined from the fluorescence profiles. Figure 4.14 shows a typical lamp spectrum

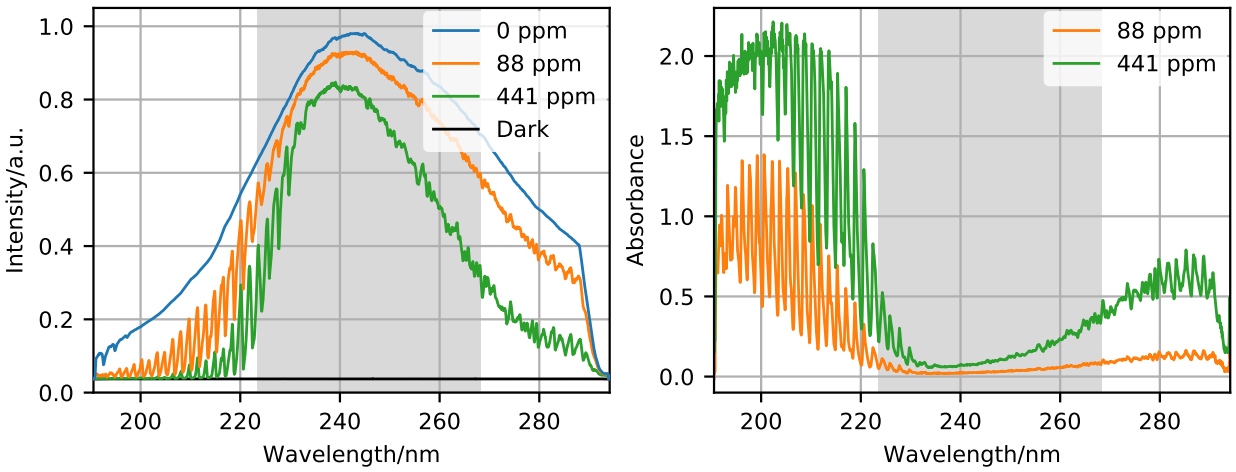

Figure 4.14: (a) Dark, lamp and transmittance spectra as well as (b) the resulting absorbance spectra at sulfur dioxide concentrations of 88 ppm and 441 ppm. The region used for the reference spectrum is highlighted in grey.

I_0 and dark spectrum I_{dark} as well as spectra at sulfur dioxide concentrations of 88 ppm and 441 ppm on the left. On the right, the resulting absorbance spectra, computed using the Beer-Lambert law, Eq. (2.62),

$$abs(\lambda) = -\log_{10}\left(\frac{I(\lambda) - I_{\text{dark}}}{I_0(\lambda)}\right), \tag{4.9}$$

are shown for two exemplary concentrations.

Due to the limited sensitivity of the spectrometer, the high absorbance regions at wavelengths below 220 nm reach saturation at high concentrations. This is clearly visible in Fig. 4.14b. Therefore, only the central spectral region between 224 and 260 nm is used for determining the concentration from a reference spectrum. The reference spectrum used for the analysis of all absorbance spectra is obtained from the concentration calibration measurement (see Sec. 5.1.2).

Furthermore, the absorption cross section was deduced from absorbance measurements at the Benjamin-tank with known concentrations and optical path length. Figure 4.8 shows the values for the absorption cross section obtained in this study in orange in comparison with literature values. Also marked is the laser wavelength employed in these measurements.

5 Calibration and Experiments

Both a geometric calibration as well as a concentration calibration were conducted. The procedures as well as the analysis routines are described in Sec. 5.1. In Sec. 5.2, the experimental procedures of the two conducted experiment series are delineated, including both the reference measurements and the measurement series.

5.1 Calibration

In this section, the calibration procedures are explained. First the geometric calibration, then the calibration of both absorbance and detected fluorescence in dependence of the sulfur dioxide concentration are outlined.

5.1.1 Geometric Calibration

Primarily, a geometric calibration is necessary to assign to every pixel a real-world coordinate. Furthermore, distortion and potential rotation owing to the orientation of a camera relative to the object is compensated through the calibration. A rectangular plate ('target') with a pattern made of crosses printed on it is used for the geometric calibration. The target is positioned in the measurement section at the position where the UV laser beam and the LHC and PSV laser sheets overlay, or in the case of the proof of principle measurement series in the UV laser beam. In the latter case, the laser beam was tilted by a few degrees in the wind plane because it exited the laser head already at an angle. Therefore, the target was positioned in such a way that the laser beam touched the target in the whole FOV of the UV camera.

During the calibration, the cameras are operated with longer exposure times than during the experiment, and a light source for homogeneous illumination of the target is needed as the blue laser sheet from above does not illuminate the vertically oriented target sufficiently. For the geometric calibration of the UV setup, a UV light source for the illumination of the target is needed due to strong chromatic aberration of the lens. For this, a deuterium lamp is used in combination with a UV band pass filter. The filter still has sufficiently high transmittance in the visible range that visible light reduces the quality of the calibration picture due to chromatic aberration. Figure 5.1 (a) shows the calibration picture when illuminated with UV light, while Fig. 5.1 (b) shows the chromatic aberration when illuminated with visible light instead of UV light. The geometric calibration was repeated frequently between the measurements.

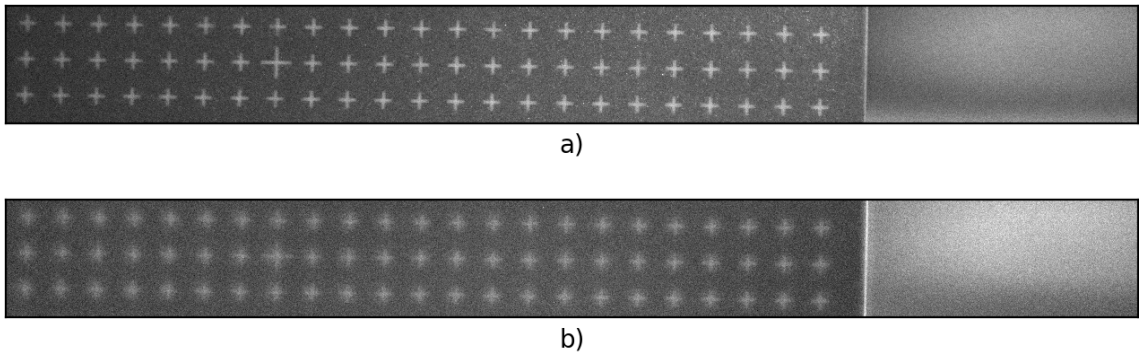

Figure 5.1: The LIF calibration picture with a) UV illumination and b) broadband visible illumination.

The calibration images for the PSV and LHC setup are analyzed via a program written in MATLAB, the LIF calibration images with a similar program written in PYTHON. Both programs perform the steps summarized in the following:

First, the background intensity is quantified. Then, the image is binarized into background and not-background, such that the crosses stand out in front of the surrounding background. The median point of each region is determined. Beginning at one point in one corner, the pixel positions of the median points are detected. From these pixel positions (X, Z) and the actual real-world positions (x, z), a calibration function is determined, using the following mapping function (Raffel et al., 2007):

$$x = \frac{a_{11}X + a_{12}Z + a_{13} + a_{14}X^2 + a_{15}Z^2 + a_{16}XZ}{a_{31}X + a_{32}Z + a_{33} + a_{34}X^2 + a_{35}Z^2 + a_{36}XZ} \tag{5.1}$$

$$z = \frac{a_{21}X + a_{22}Z + a_{23} + a_{24}X^2 + a_{25}Z^2 + a_{26}XZ}{a_{31}X + a_{32}Z + a_{33} + a_{34}X^2 + a_{35}Z^2 + a_{36}XZ} \tag{5.2}$$

$$a_{33} = 1. \tag{5.3}$$

with the 17 fit parameters a_{ij}. The parameter a_{33} is set equal to 1 as in Bopp (2018). The function assigns the corresponding real-world position to each pixel position. Its linear parts realize the perspective projection while its nonlinear parts take into account geometric distortions by the lenses.

This calibration procedure is very robust if the calibration image has good contrast and if no disturbing bright objects (e.g. dust) are visible in the image which could possibly be detected as target crosses. The cross target with the camera FOV's as well as the medium water level is shown in Fig. 5.2.

The LHC and PSV cameras are calibrated simultaneously with the same target position. With a larger central cross on the target, the coordinate systems of the two cameras are matched.

Because the LIF setup has a laser beam rather than a laser sheet and the laser beam is clearly visible in the LHC images in the water as an increase (or decrease of) the fluorescence

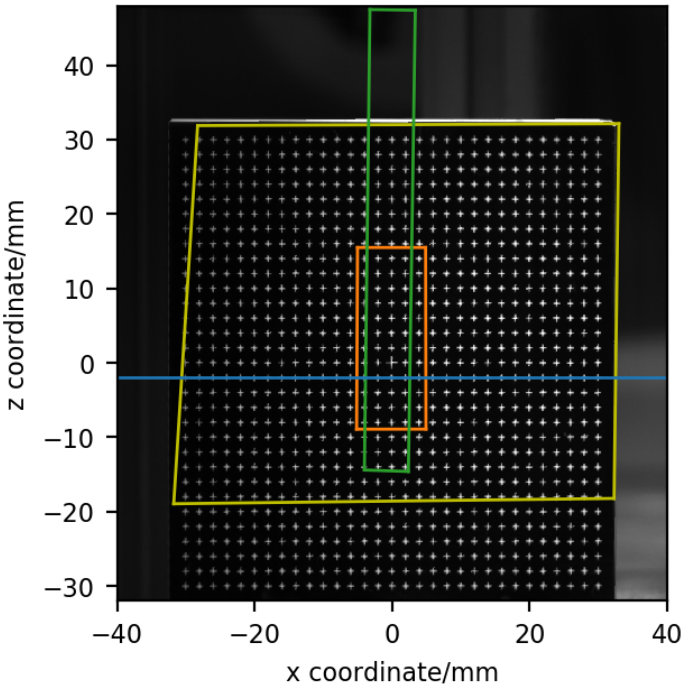

Figure 5.2: Matched field of views of the three cameras (LHC: yellow, PSV: orange, LIF: green) as the result of the calibration with the cross target. The FOV of the LIF camera is mirrored as it looks from the opposite direction than the LHC and PSV cameras. The mean water level as obtained from the surface detection algorithm is marked in blue.

(see Sec. 6.3). This allows for a straightforward matching of the along-wind positions of all three cameras. In addition, a transparent glass target with an engraved cross pattern at the laser sheet position is imaged by all three cameras as a backup. When illuminated from above with the blue laser sheet and from the side with the UV light source, the pattern is visible in all three cameras. Because the green pyranine fluorescence is not clearly visible in the LIF images due to the filter, which is transparent only in the UV, the vertical coordinate is later matched by employing the LHC surface detection (see Sec. 6.5.2).

5.1.2 Concentration Calibration

During the proof-of-principle measurements in the Benjamin-tank, a concentration calibration was not necessary as known amounts of sulfur dioxide were introduced into the tank for every measurement. Therefore, only the relative concentration was needed as also only quotient images were used for the analysis with relative intensities. This was not the case in the second measurement series as the sulfur dioxide was introduced continuously during the experiment in order to produce an equilibrium for constant measurement conditions. Thus, also the total concentration was of interest here. In the following, the calibration

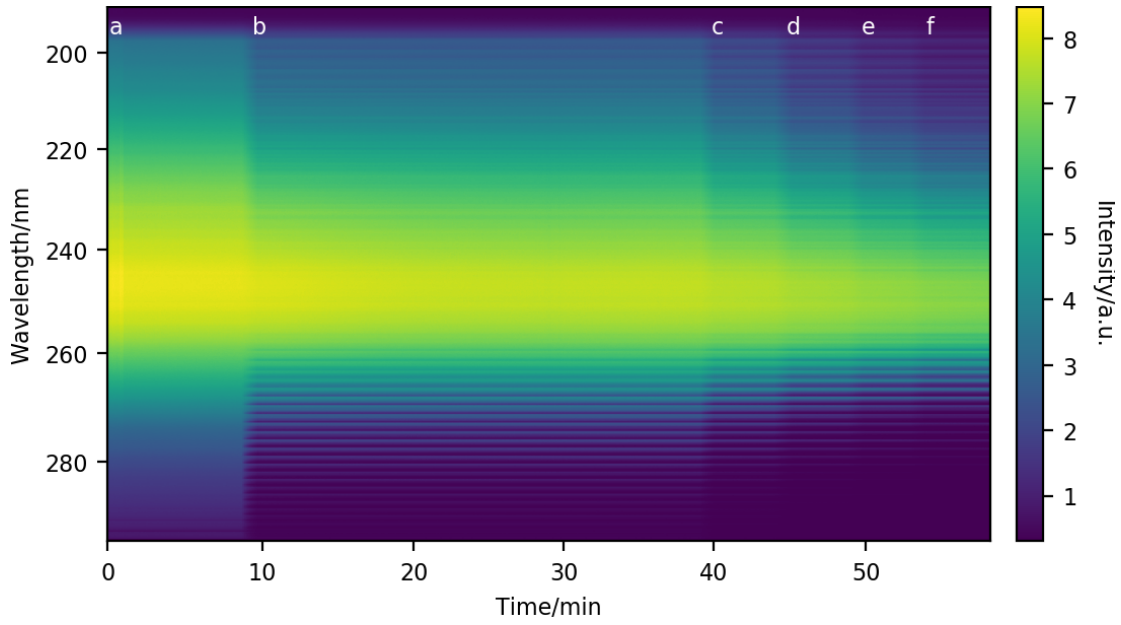

Figure 5.3: Concentration calibration of the Lizard-tank: Every 25th spectrum shown over the time, yellow corresponds to high intensities while violet to low intensities. A few minutes of lamp spectrum (region a) are followed by five successive steps of SO_2 addition (regions b to f), increasing the concentration stepwise.

measurement procedure is explained.

The calibration was conducted in the dry Lizard-tank. The spectroscopic setup was in operation during the whole measurement. With the mass flow controller, a constant flow of 360 ml/min sulfur dioxide was added to the tank for 50 sec. This corresponds to a concentration of 88 ppm, considering the volume of the tank. Then, an estimate of the leakage of the tank was obtained by observing the concentration during a 25 min timespan. Thereafter, four additional doses with the same amount of sulfur dioxide were added, increasing the concentration by 88 ppm with every step. By waiting a few minutes after each gas addition, it was ensured that the gas was well mixed into the air. The measured spectra are shown in an intensity plot in Fig. 5.3, with the time on the horizontal axis. In the plot, only every 25th spectrum is shown as the spectra were recorded at a high rate.

From the spectra, the absorbance was quantified, as described in Sec. 4.7. The result is shown in Fig. 5.4a. Because the saturation effect described in Sec. 4.7 is not relevant at low concentrations, a mean of three consecutive spectra at the lowest concentrations was used as a reference spectrum. For the calibration of the concentration probe, 1500 to 3000 spectra, obtained after the equilibration phase, were averaged. The result is shown by the red lines in Fig. 5.4a. Figure 5.4b shows the sulfur dioxide concentration as a function of the fitted absorbance factors with estimated uncertainties: The standard deviation and the uncertainty of the fit value were added up via error propagation to an uncertainty of the absorbance factors. For an uncertainty in the concentrations, both an error in the duration

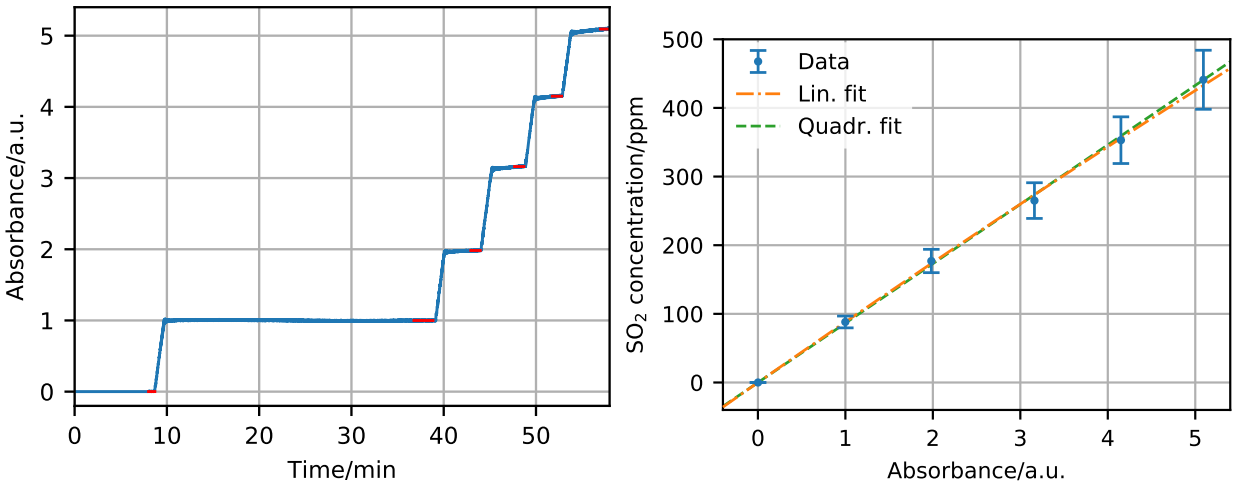

Figure 5.4: Results from the concentration calibration measurement: (a) Parameter from the absorbance spectrum fits against time. (b) Resulting calibration curve with the sulfur dioxide concentration plotted against the corresponding absorbance parameter obtained from the spectrum fits. Linear and quadratic fits are shown in green and orange, respectively. The uncertainties in the absorbance factors are not depicted in (b) for better illustration.

of the inflow and the uncertainty of the volume are included. The uncertainty of the flow as indicated in the data sheet of the mass flow controller is negligibly small compared to the other uncertainties.

Taking into account the uncertainties, both a linear and a quadratic function were fitted to the spectra. As the resulting parameters from the quadratic fit have larger uncertainties, the linear function is taken as the better fit. The fit result can then be used to translate the absorbance spectra taken during the measurements into absolute concentrations.

A similar approach was applied to the calibration of the fluorescence intensity versus the concentration. The sulfur dioxide concentration was increased in steps of 20 ppm up to a maximum total concentration of 200 ppm, and during the whole calibration, the gas fluorescence was imaged. Figure 5.5 shows the resulting series of fluorescence intensity profiles. The decrease of the intensity towards the edges of the FOV is due to vignetting (see Sec. 6.1.1). For each step, the fluorescence intensity was averaged over one minute. The resulting mean intensities are shown in Fig. 5.6 against the concentration. The uncertainty of the concentration was estimated as described above, while the uncertainty of the fluorescence intensity was calculated analogously to the uncertainty in the absorbance. The concentration uncertainties dominate and the fluorescence intensity uncertainties are negligible.

This measurement cannot be used as a true calibration just as the absorbance-concentration calibration, because the fluorescence intensity does not only depend on the

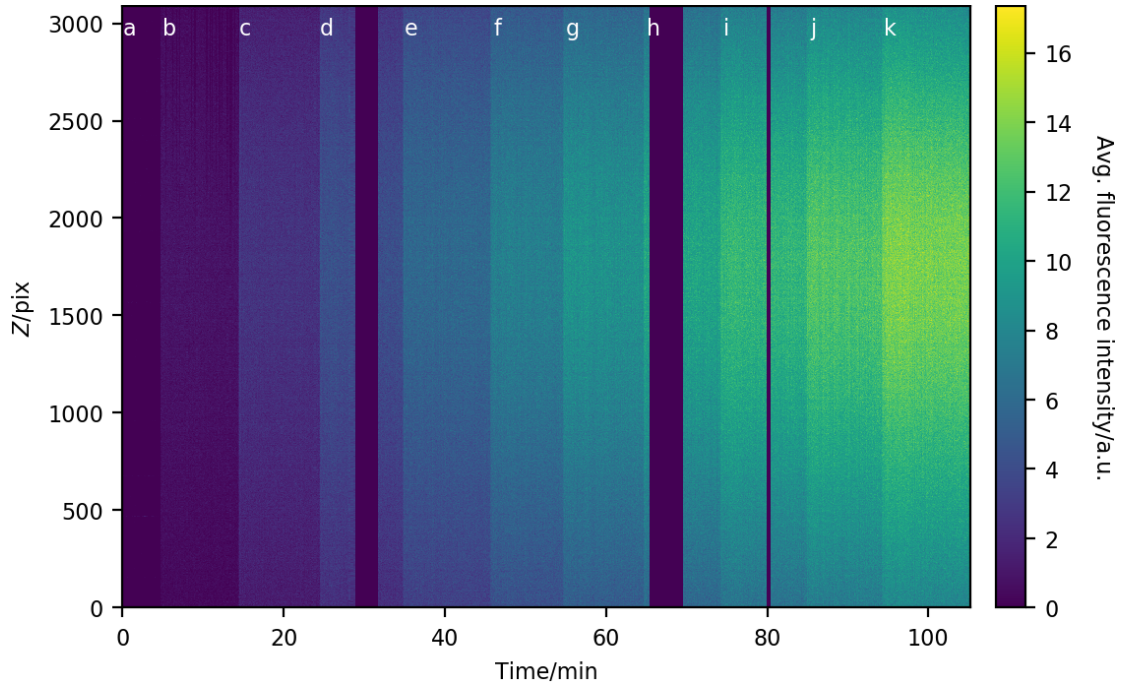

Figure 5.5: Fluorescence intensity of the central beam column over time in a *t*-*Z*-representation. Similar to Fig. 5.3, several dark images (region a) are followed by captures during a stepwise increase in the concentration (regions b to k), which leads to an increase of the fluorescence. The dark vertical stripes at around 30 min, 65 min and 80 min correspond to times where no images were taken.

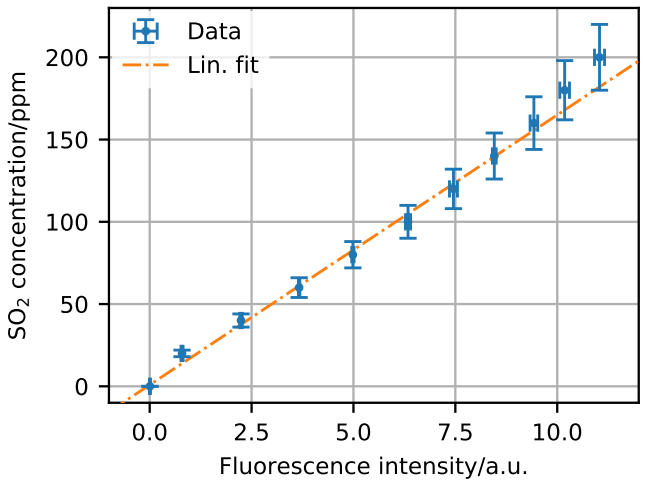

Figure 5.6: The resulting fluorescence calibration curve: Fluorescence intensity versus sulfur dioxide concentration (blue), and the linear fit to the data (red).

concentration, but also on the laser intensity, among others. The experiments showed that the laser intensity varied even during one measurement. Therefore, the fluorescence-concentration measurement can only be used as a proof that both quantities are proportional.

5.2 Experimental Procedure

5.2.1 Proof-of-Principle Experiment

Reference Measurement

Before filling the tank with water, a sequence of 1000 images without tracer and with the laser turned off were recorded (dark images). Next, a reference measurement with a sequence of 1000 images was carried out with the same initial sulfur dioxide concentration as in the real measurements (100 ppm) and the laser turned on (reference images). A constant wind ensured homogeneous mixing of the tracer in the air volume. Reference images at different wind conditions are not necessary as the wind speed has no influence on the reference profiles as long as the tracer is well mixed. Both dark and reference images are averaged to reduce noise.

Measurement Series

Then, the measurement with 100 ppm SO_2 in the air was repeated for 11 different wind speeds, this time with water in the tank. The wind generator settings used for the experiment correspond to reference friction velocities u_* between 2.4 and 9.3 cm/s (Krah, 2014). Higher winds produce too much disturbance due to waves, reducing the ability to measure close to the interface and even to detect it. All physical variables and absorbance spectra were logged continuously during the whole experiment. Images were recorded at 40 fps with an exposure time of 25 ms until the intensity of the fluorescence had decreased almost to zero, implying that essentially all SO_2 had been transferred to the water. This procedure resulted in around 20000 images per wind condition, corresponding to around 10 GB of data.

5.2.2 Fetch Experiment

Reference Measurements

Also here, dark images and reference images were recorded, but in a different manner: sulfur dioxide was added continuously to the dry closed tank (with the wind generator turned on) until a certain concentration, approximately the equilibrium concentration of the main measurements, was reached. The whole time, the LIF camera was recording such that images at various concentrations (also at zero ppm, thus the dark image) were obtained. At the maximum concentration, the wind generator frequency was varied for a later evaluation of the influence of vibrations caused by the wind generator on the image quality. In total, a few thousand images were exposed. During the whole measurement, the

concentration was monitored with the spectroscopy setup. Neither the flow measurements nor the height detection setup were operated as there was no water in the tank and the flow was not of interest for this calibration. Subsequently, the tank was flushed with water in order to cleanse it of SO_2.

Measurement Series

For every experiment, the setup had to be prepared separately in order to assure identical conditions at the beginning of each measurement. Buffer and dye were added to the fresh water, which was cooled by the Peltier setup, and the trigger signals and camera settings were adjusted to the wind generator setting. The spectroscopy setup was turned on as well as all probes. In Tab. A.1, the probe data is listed. For the measurement, the three optical setups, LHC, LIF and PSV, were operational, the sulfur dioxide flux and the particle production were turned on. The latter was active only for a short while, a few seconds, in order not to have too many particles in the tank. By contrast, SO_2 flowed in during the main part of measurement, for 30 min, and a quasi equilibrium was established between the influx of gas and the transfer to the water, as described by the solution of the mass balance equations, Eq. (3.13). Depending on the wind condition, the equilibration time varied. This is natural, since, as discussed in Sec. 3.4, the equilibration time depends on the transfer velocity. At the lowest wind speed at low fetch, equilibration took very long. Therefore, the flux was initially increased at the lowest wind speed at high fetch in order to reach the equilibrium concentration more quickly, and subsequently reduced again to the targeted value. The reason for this procedure is that the measurement time was limited by the disk space and the most interesting part for the measurements is in the quasi equilibrium phase. The measurement conditions and settings can be found in Tab. 5.1. Both the delay and exposure times of the PSV setup were adjusted to the wind condition in order for the exposure to be centered, while the LHC laser pulse duration and camera exposure time was only extended for the last two measurements, as described in Sec. 4.6. At zero delay at the function generator, the PSV signal is delayed to the trigger signal by 249 μs. This is an offset produced by the setup and has to be subtracted for the settings at the function generator. The duration of each measurement was set to 20 min, resulting in 240000 LIF images, 240000 PSV images and 480000 LHC images captured for every wind condition, resulting in at least 670 GB of data.

Table 5.1: Camera and laser settings for the fetch experiment: Wind generator frequency W, amount of added dye, PSV signal frequency ν_{PSV}, PSV delay τ_{PSV}, PSV exposure time Δt_{PSV}, LHC delay τ_{LHC} and LHC exposure time Δt_{LHC}. The LIF exposure time was the same for all measurements: 4.848 ms.

Fetch	W Hz	Dye mg	ν_{PSV} kHz	τ_{PSV} ms	Δt_{PSV} μs	τ_{LHC} μs	Δt_{LHC} μs
Low	5	57	5.5	1.58	1750	1079	200
	10	90	11	1.99	900	1079	200
	15	108	18	2.15	600	1079	200
	20	112	25	2.21	400	1079	200
High	5	38	5.5	1.58	1750	979	400
	10	81	11	1.99	900	1029	300
	15	91	18	2.15	600	1079	200
	20	97	25	2.21	400	1079	200

6 Data Analysis

In this chapter, the data processing methods and algorithms are presented. First, each of the data sets obtained with the imaging techniques, LIF, PSV and LHC, are separately processed. Second, the coordinate systems of the different methods are aligned before further processing. Third, the absorbance spectra are analyzed.

6.1 LIF Analysis

During each measurement in the proof-of-principle experiment, 20000 raw images were captured with the UV camera. In the fetch experiment, 240000 raw images were collected for every wind and fetch condition. Every image was analyzed to obtain a vertical fluorescence profile, the bulk fluorescence as well as the position of the surface. In the following, the processing method for the analysis of the LIF images is described. The processing is programmed in PYTHON.

For the evaluation of the raw images, (normalized) concentration profiles were obtained by using the reference images (see Fig. 6.1 on the left). In the proof-of-principle experiment, the surface position could be estimated from the concentration profiles as the signal from the water was very bright, see Fig. 6.1 on the right, such that a simple thresholding could be applied. This was not possible in the fetch experiment as the UV filter on the camera absorbed the light from the pyranine fluorescence efficiently. Therefore, the surface detection from the LHC was needed here for processing the LIF images, see Sec. 6.2.

The results from the proof-of-principle experiment have been published recently (Friman and Jähne, 2019), therefore some figures from the publication are used in this chapter, as mentioned in the captions.

6.1.1 Fluorescence Profiles

From Raw Images to Quotient Profiles

As formulated in Eq. (2.67) and demonstrated in the calibration measurement described in Sec. 5.1.2, the fluorescence intensity is linearly proportional to the tracer concentration. However, the efficiency of the optics is not equal for all pixels. For example, vignetting, which is the reduction of the brightness of an image towards the edges, and offset values of the pixels have to be taken into account in the analysis. Therefore, the dark images I_{dark} captured before the measurement are averaged and subtracted from all images to eliminate the offset values.

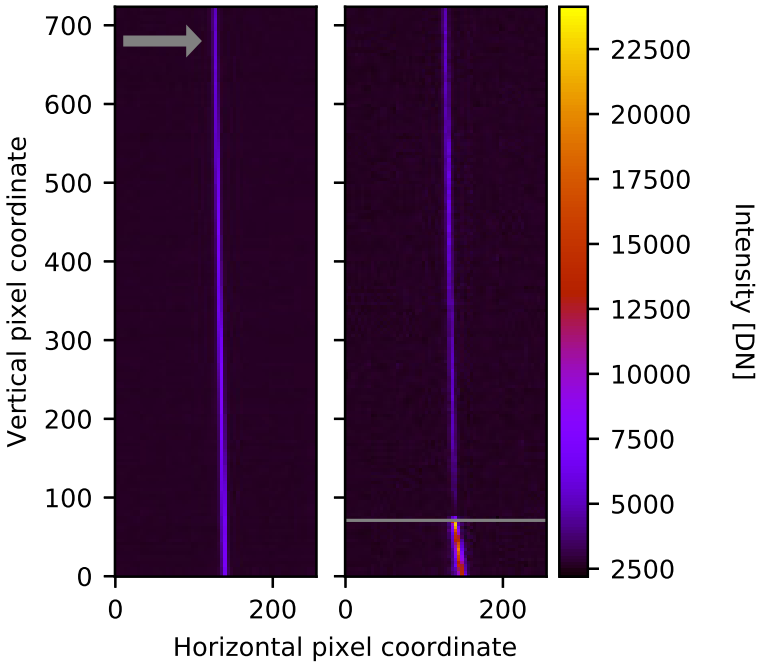

Figure 6.1: Left: Mean reference image I_{ref} with an arrow indicating the wind direction. Right: Raw image I from the measurement with the lowest wind speed. The water surface location is marked by a horizontal line. This figure was published in Friman and Jähne (2019).

To reduce the vignetting, a 'dry' measurement, where sulfur dioxide is added to the tank in the absence of water in the channel, with a uniform distribution of SO_2 is used as a reference image I_{ref}, which is equally corrected for the background. An exemplary reference image from the fetch experiment is shown in Fig. 6.2 where the vignetting effect is visible. It is rotated by 90° relative to the one in Fig. 6.1.

In the following, the procedures to obtain quotient profiles from the raw images used for both experiments is described.

In the proof-of-principle experiment, the background was subtracted from all images and the resulting images were rotated to compensate for the laser tilt in the images. This induced a slight smoothing of the image. The vertical axis was translated into distance above the surface z by geometric calibration and surface detection with thresholding. Then, an intensity profile was derived from every image by averaging over the central three pixels of the beam along the wind direction. These intensity profiles were then normalized via division by a reference profile which was derived through an analogous evaluation of a mean reference image, averaged over 1000 reference images. This resulted in quotient profiles Q:

$$Q(z) = \frac{I(z) - I_{\mathrm{dark}}(z)}{I_{\mathrm{ref}}(z) - I_{\mathrm{dark}}(z)} = \frac{c(z)}{c_{\mathrm{ref}}(z)} = \tilde{c}(z). \tag{6.1}$$

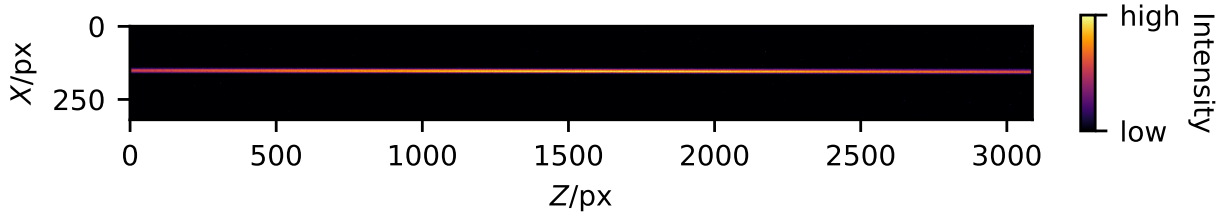

Figure 6.2: Mean reference image (averaged over 250 raw images) from the fetch experiment. Orange stands for high and black for low pixel values. The water surface position is at around $Z = 800$ pixels.

In the following, the tilde symbol marks a concentration which is normalized by the reference concentration.

In the fetch experiment, the position of the laser beam in the FOV of the LIF camera changed during the experiment due to vibrations. To compensate for this effect, the laser beam's x position had to be determined separately for each file of 250 images. This was done via fitting Gaussian distributions at two z-positions, one at the center and the second at the upper edge of the first image in each file. Since the determination of the laser beam position in each raw image would increase the total analysis time considerably, this was done only in the first image of each raw file. This procedure is justified since a test evaluation showed that the x positions of the beam in one raw file did not vary by more than 5 pixels. As the width of the laser beam in the images obtained during the fetch experiment spanned $10 - 20$ pixels, this procedure only resulted in fluctuations for the maximum intensity between adjacent profiles. This was later corrected, see Sec. 6.1.1.

By assuming that the beam has a linear shape, the beam position was estimated via fitting a linear function to the x-z coordinates obtained from the Gaussian fits. Then, for each z-coordinate, the mean fluorescence intensity was obtained with subpixel resolution: This was done by calculating a weighting factor according to the deviation of the calculated x-coordinate of the center of the beam to the nearest x-pixels and thus averaging over the three to four pixels closest to the central pixel values, applying the weighting factors. To reduce the noise level, the profile was smoothed by averaging over three adjacent values in z-direction.

The same procedure was applied to the mean reference image. By normalizing the intensity profiles by the reference profile, the quotient profiles were then derived. This is illustrated in Fig. 6.3, where the original profiles are shown in the top plot and the resulting quotient profile in the bottom plot. The intensity quotients decrease along the laser beam towards the surface. A continuous intensity decrease along the laser beam could be caused by the absorption of UV laser light by sulfur dioxide, such that the laser beam intensity itself decreases along its path through the air in the tank. However, the effect would be on the order of $10^{-3} - 10^{-4}$ (according to Eqs. (2.62) and (2.63)). An estimate of the effect on the transfer velocities derived from the concentration profiles is given in Sec. 6.1.3.

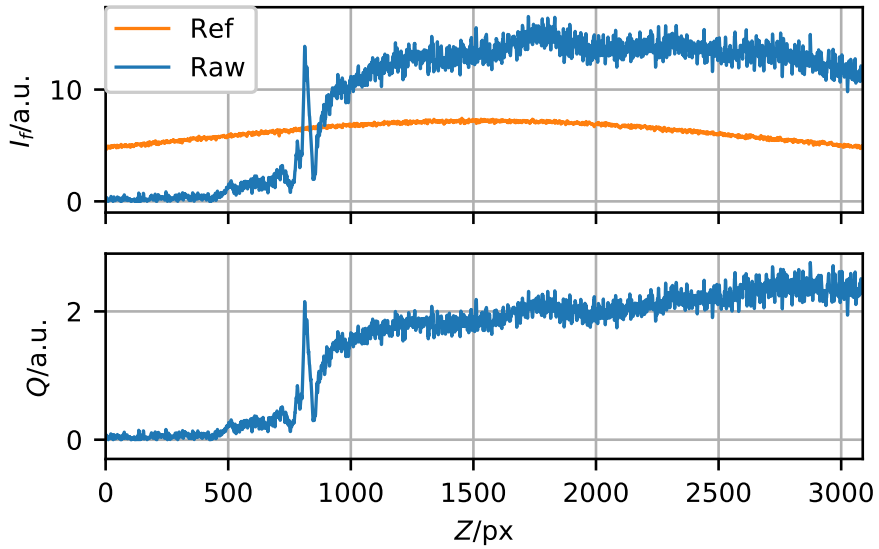

Figure 6.3: Top: Profiles from a reference image (orange) and a raw image (blue). Bottom: The resulting quotient profile. The height grows with increasing pixel number Z. The surface and thus $z = 0$ is located around $Z = 800$ pixels.

Cutting Profiles at the Surface

The profiles are further processed by using the geometric calibration to convert the vertical pixel scale into a physical distance above the water surface and discarding the part of the profile, which corresponds to positions below the surface; only the air-side profile are of interest.

In the images obtained in the proof-of-principle experiment, which were obtained without a UV filter, the quotient intensities from the water close to the surface show a distinct narrow peak due to reflections or scattering from the water, making the detection of the surface via thresholding feasible. A sequence of 1000 consecutive quotient profiles from the proof-of-principle experiment, corrected for the surface position, are shown in Fig. 6.4a.

This approach is not applicable for the fetch experiment. There, the surface elevation data obtained with the LHC is used both to shift the z-axis such that its origin corresponds to the mean water level and to separate the air-side profiles from the intensity from the water (see Sec. 6.5.2).

The z-coordinate minus the coordinate of the detected surface, i.e. the real height above the water, is denoted by $z_{\text{shift}} = z - \eta$.

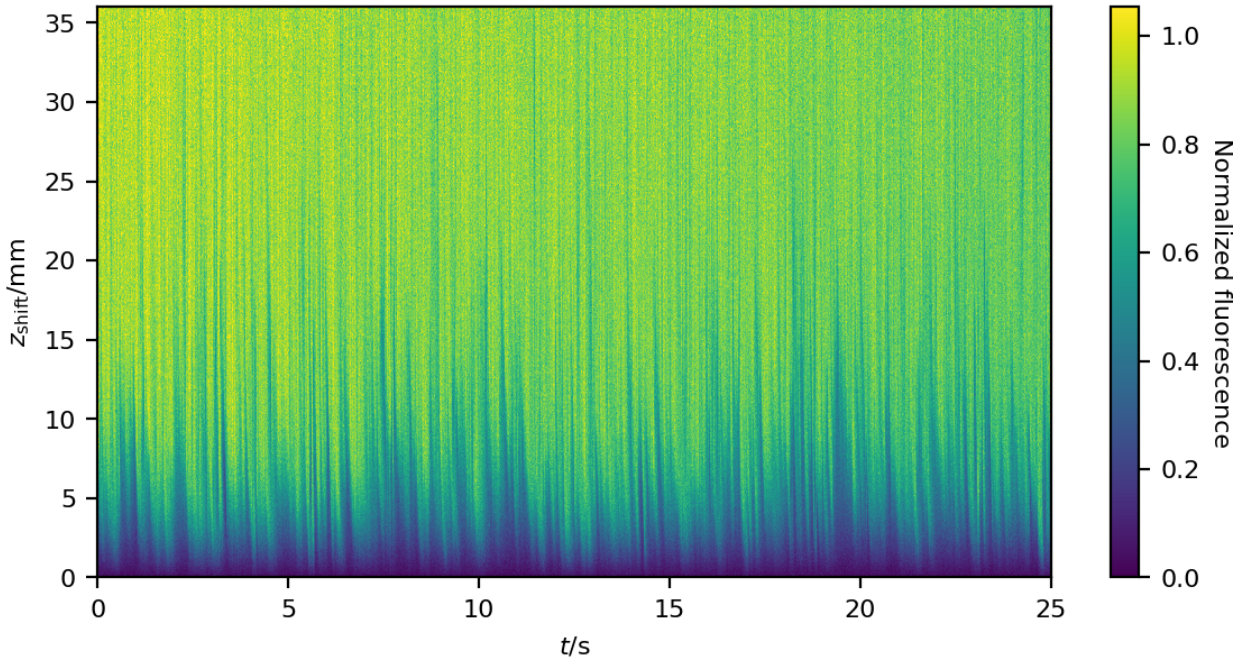

(a)

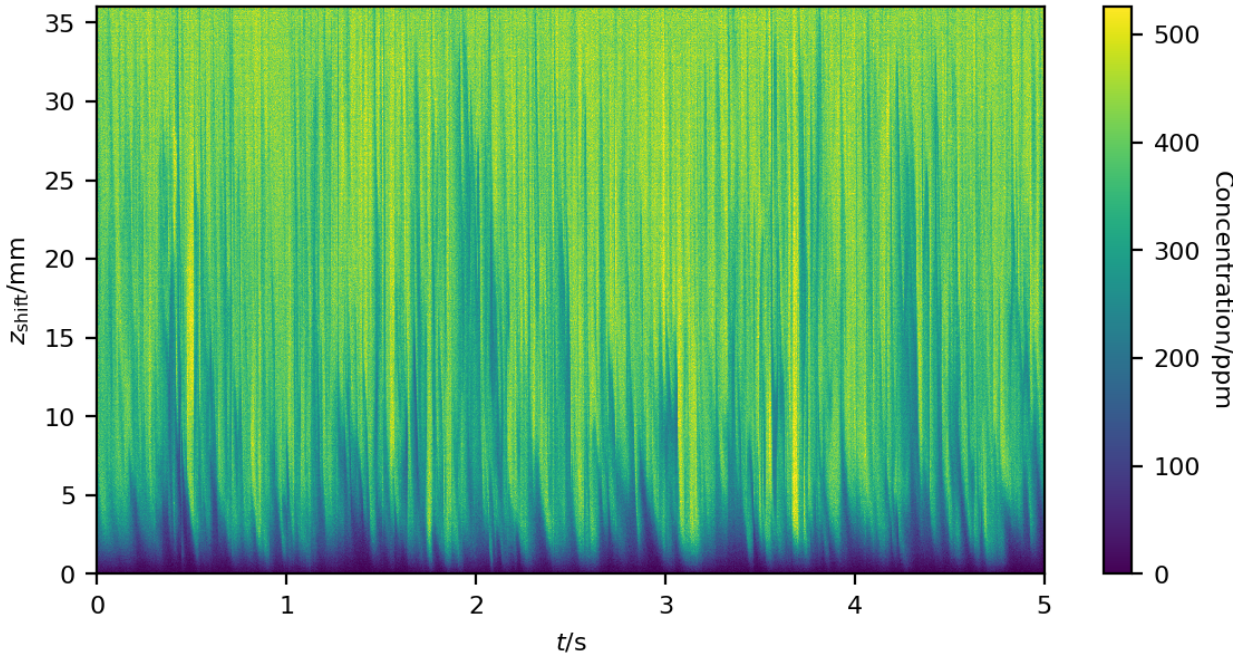

(b)

Figure 6.4: Time series of (a) 1000 quotient profiles at the lowest wind speed from the proof-of-principle experiment and (b) 1000 concentration profiles at the lowest wind speed at high fetch from the fetch experiment. Note the different time axes: In the proof-of-principle experiment, 1000 profiles encompass 25 s, while at the fetch experiment, the same number of profiles correspond to 5 s.

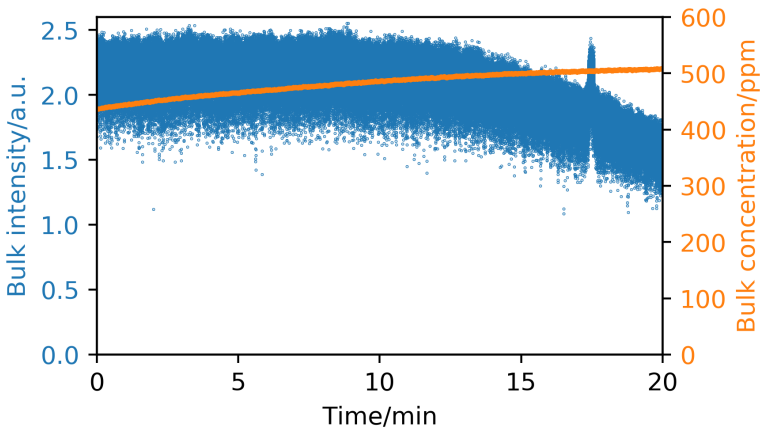

Figure 6.5: Bulk fluorescence intensity (blue) and bulk concentration (orange) plotted over time. Only every tenth measured fluorescence intensity is shown for better readability of the figure.

From Quotient Profiles to Concentration Profiles

During the fetch experiment measurements, it became evident that the fluorescence intensity changed appreciably even though the concentration remained almost constant. Several possible causes for this problem were identified. On the one hand, the laser intensity was subject to changes, the reason of which could not be determined. On the other hand, the laser transmission through the calcium fluoride window in the tank roof was changing due to chemicals agglomerating on the glass (see Sec. 4.3.1). Furthermore, the evaluation procedure for obtaining the profiles induced a fluctuation of the fluorescence between adjacent images.

Exemplarily, the bulk quotient intensity of the measurement at the lowest wind speed and high fetch is plotted in Fig. 6.5 along with the concentration determined from the absorption spectroscopy. While the concentration still increases slightly during the 20 minutes of measurement, the bulk fluorescence decreases to around 70% of the initial intensity and shows even an inexplicable peak near the end of the measurement. Furthermore, the bulk fluorescence, even though it is averaged over the top 5 cm of each profile, fluctuates at least an order of magnitude more than the concentration. The reason for this is probably the profiling procedure.

Therefore, each profile is normalized by the bulk fluorescence and then multiplied by the concentration obtained from the absorption spectroscopy, resulting in concentration profiles. This procedure was not applied to the data obtained in the proof-of-principle experiment because those measurements were not performed under stationary conditions. The translation of fluorescence profiles into concentration profiles is viable only because in the concentration calibration of the fluorescence (see Sec. 5.1.2), the assumption of a proportionality between concentration and fluorescence has been shown to be valid.

Figure 6.4b shows a series of 1000 consecutive concentration profiles from the fetch

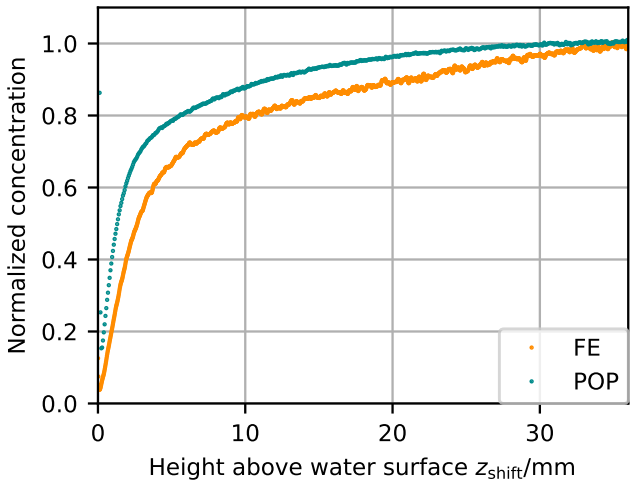

Figure 6.6: Normalized concentration from two measurements with similar friction velocities from the proof-of-principle experiment (POP) and the fetch experiment (FE).

experiment. The profiles are taken from the measurement at the lowest wind speed and high fetch. A cautious qualitative comparison with the quotient profiles in Fig. 6.4a obtained from the proof-of-principle measurement exhibits a rough similarity. The two figures cannot be compared in detail because many experimental parameters were different, wind velocity, fetch, channel height, camera exposure time to name a few.

6.1.2 Comparison of Profiles from both Experiments

The setup in the two experiments was different: the wind-wave tanks have different characteristics, the camera setup changed and also the experimental procedure, for example the addition of the sulfur dioxide to the tanks was not the same. Therefore, the measurements are truly independent and it is of interest to compare the two data sets.

Figure 6.6 shows two mean concentration profiles from measurements at both tanks under similar wind conditions. The data from the Benjamin-tank was obtained at a wind corresponding to $u_* = (7.9 \pm 0.5)\,\mathrm{cm/s}$ as measured by Krah (2014), while the data from the Lizard-tank was measured at a friction velocity of $(7.6 \pm 0.3)\,\mathrm{cm/s}$. The latter was deduced from the mean wind profile at the same wind condition. In the proof-of-principle experiment, the data was translated into quotient profiles, where the quotients are proportional to the concentration, while the profiles from the fetch experiment are directly transferred to concentration units via calibration. Therefore, the mean profiles in Fig. 6.6 are normalized by the value in the bulk to allow a direct comparison of the shapes.

It is evident that the shapes differ. The gradient of the profile from the Benjamin-tank decreases with the height above the surface and the concentration reaches a plateau at around $z_{\mathrm{shift}} = 30\,\mathrm{mm}$, while the gradient of the profile from the fetch experiment does not

reach zero in the FOV. The reason for this can be found in the different heights of the tanks, the Benjamin-tank having only a height of 10 cm while the Lizard-tank 's height is 23 cm. This induces that the influence of the roof on the wind field is stronger in the proof-of-principle measurements than in the fetch experiment. Furthermore, the wind field in the Benjamin-tank is not as homogeneous as in the Lizard-tank. This effect has to be considered when analyzing the profiles from the two experiments.

Still, the profiles in the boundary layer are similar on a qualitative level.

6.1.3 Profile Fitting

From the fluorescence (or concentration) profiles, several quantities can be determined, most importantly for this study the transfer velocity and the mass boundary layer thickness. The transfer velocity can be obtained from the proof-of-principle experiment by either observing the bulk fluorescence over time and fitting an exponential function to it, analogously to the evaluation of the absorbance, as described in Sec. 6.7. Furthermore, two model functions can be fitted to the mean profile to determine the transfer velocity averaged over the measuring time, as well as fitted to the single profiles to obtain instantaneous transfer velocities.

In the following, the fitting procedure is described. It is applied both to the quotient profiles in the proof-of-principle experiment and to the concentration profiles, obtained from the fetch experiment.

Single Profiles

Through fitting single concentration profiles, data on instantaneous transfer velocities and boundary layer thicknesses can be obtained.

As defined in Eqs. (2.41) and (2.44), the transfer velocity is proportional to the concentration gradient at the surface and inversely proportional to the concentration difference between surface and bulk. In Sec. 2.3.2, it was shown that the mean concentration close to the air-water interface can be represented by the first few terms in a Taylor expansion in z. In the air and at low wind velocities as applied in this experiment, the water surface can, as noted in Sec. 2.3.2, be approximated with a rigid wall. Then, the Taylor expansion approximation for a rigid wall, Eq. (2.57) contains polynomial terms of zeroth, first and fourth order. Under the assumption that the same function is valid for single profiles very close to the interface, the polynomial

$$c(z, c_s, c_1, c_2) = c_s + p_1 z + p_2 z^4 \tag{6.2}$$

is fitted to the single profiles within a fit region to bes defined below. The fit parameters c_s and p_1 correspond to the concentration and the concentration gradient at the surface, respectively. The fit parameter p_2 is not relevant for the calculation of the transfer velocities.

In Friman and Jähne (2019), a polynomial including zeroth, first and third order terms was fitted to the proof-of-principle data. However, the difference between the results ob-

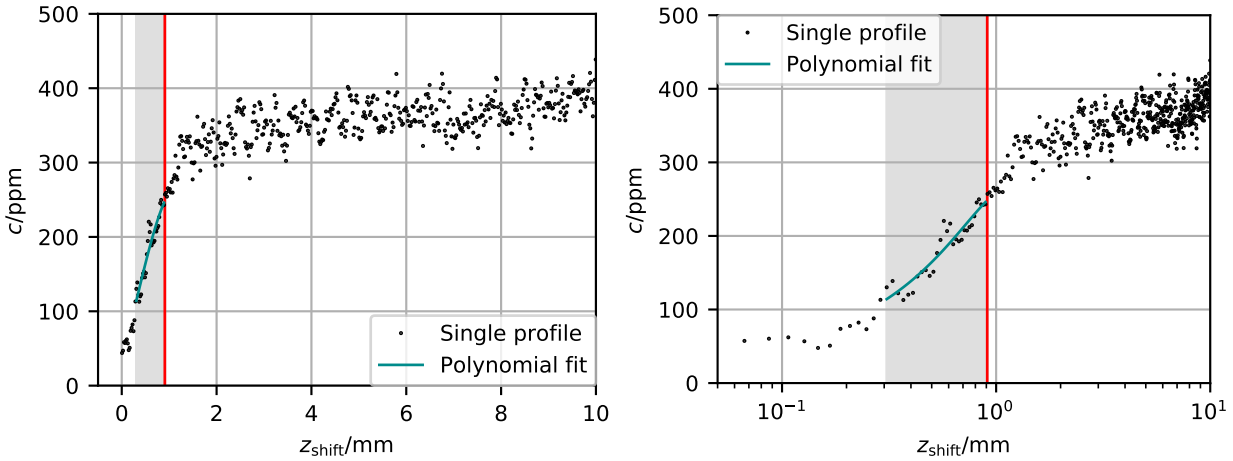

Figure 6.7: A single concentration profile obtained for the second highest wind condition at low fetch (black), fitted with the polynomial function, Eq. (6.2) (turquoise), (a) in linear representation and (b) in a semi-logarithmic plot with a logarithmic scale on the z axis. The fit range is marked in gray and the mass boundary layer thickness is marked by a red vertical line.

tained by fitting a polynomial with the third term being of third or fourth order is negligibly small.

For the proof-of-principle experiment, the lower limit of the fit region was set to the position of the minimum of the profile a few pixels above the water surface. Since the influence of the water was much stronger in the fetch experiment, 6 pixels above the minimum position was chosen as the lower fit limit.

For the upper limit, the height corresponding to the dimensionless thickness of the theoretical mass boundary layer $z_*^+ = z_* \, u_*/\nu = 11.7$ was chosen (Townsend, 1976), while for the friction velocities u_* the values derived from the mean wind profile determined in the corresponding measurement were employed, see Sec. 6.4.4. Consequently, the upper limit depends on the friction velocity and thus on the wind condition.

The concentration (or quotient) gradient at the surface was determined from the gradient at $z = 0$, i.e. the value of the fit parameter p_1. The concentration (or quotient) at the surface was identified as the value for c_s determined in the fit and for the bulk concentration (quotient), the concentration value at $z^+ = 50$ was used. Subsequently, the transfer velocity and the mass boundary layer thickness were calculated using Eq. (2.44).

In Fig. 6.7, a single concentration profile from the fetch experiment is shown, along with the polynomial fit plotted in turquoise and the fit range in gray. The results are presented both in a linear as well as in a semi-logarithmic plot, where the region of interest, namely the boundary layer, is more clearly represented.

By fitting a series of profiles from every condition at both experiments, a statistic of the transfer velocities can be obtained.

Mean Profiles

Also the mean concentration profiles were fitted to obtain a mean transfer velocity. In the case of the proof-of-principle experiment, only 1000 profiles obtained at the maximum concentration were averaged for the mean profile because the bulk concentration decreased very quickly during the measurements at the highest wind speeds. Since the measurements during the fetch experiment were conducted in a quasi-equilibrium, all 240000 profiles obtained from the LIF images were averaged to obtain the mean transfer velocity for each measurement. Due to the averaging, the fluctuations were suppressed in the mean profile. Moreover, by subtracting the mean profile from each single profile, fluctuation profiles were obtained.

The mean quotient profiles from the proof-of-principle experiment were fitted with a modification of the concentration profile of Deacon's turbulent diffusion model, see Eq. (2.50) in Sec. 2.3.2:

$$\tilde{c}(z) = \frac{c(z)}{c_{\mathrm{ref}}} = \tilde{c}_1 + \tilde{c}_2 \int_0^z \frac{1}{D + \kappa u_* \left(z' - z_* \tanh \frac{z'}{z_*} \right)} dz', \tag{6.3}$$

with the fit parameters $\tilde{c}_1 = c_s/c_{\mathrm{ref}}$ and $\tilde{c}_2 = -j/c_{\mathrm{ref}}$. The mass boundary layer thickness was set to $z_* = 11.7\nu/u_*$, which was also the upper fit limit even though Deacon (1977) states that this equation is valid up to $z^+ = 50$. The reason for using a lower upper limit on the fir region is due to the fact that the wind field in the Benjamin-tank was not ideal, as discussed in Sec. 6.1.2. For the friction velocities, the values obtained by Krah (2014) were used. The lower fit limit was the same as for the single profile fitting. Using Eq. (2.36), the transfer velocity was calculated from the fit results:

$$k = \frac{\tilde{c}_2}{\tilde{c}_b - \tilde{c}_1} = -\frac{j/c_{\mathrm{ref}}}{\tilde{c}_b - \tilde{c}_s} \tag{6.4}$$

with the bulk concentration $\tilde{c}_b = \tilde{c}(z^+ = 50)$.

For the fetch experiment, a different function was employed, which included the mass boundary layer thickness as a fit parameter:

$$c(z) = c_1 + c_2 \int_0^z \frac{1}{D + \kappa \frac{11.7\,\nu}{z_*} \left((z' - z_0) - z_* \tanh \frac{(z' - z_0)}{z_*} \right)} dz'. \tag{6.5}$$

A further fit parameter z_0 was added, to account for errors in the determination of the surface elevation. Thus, the fit function in Eq. (6.5) has four fit parameters: c_1, c_2, z_* and z_0.

As the model is valid for $0 < z^+ < 50$ (Deacon, 1977), the upper fit limit was $z^+ = 50$, while the lower fit limit was again the same as for the single profile fitting. The transfer velocity can directly be derived from the fit result for z_* via the definition of the mass boundary layer, Eq. (2.44).

Figure 6.8 shows the mean concentration profile obtained for the lowest wind condition at high fetch with the model fit. Again, the plot is shown both in linear and semi-logarithmic

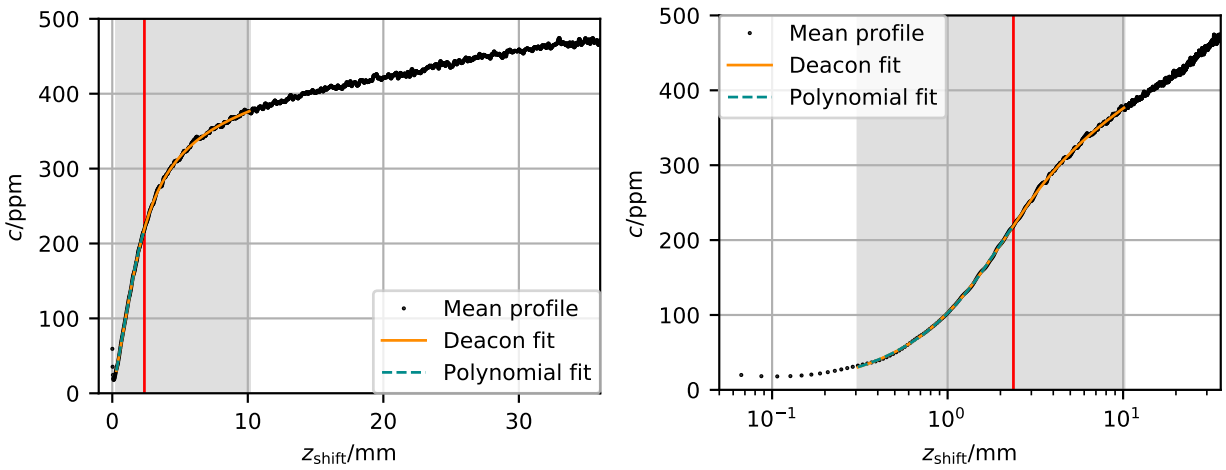

(a) (b)

Figure 6.8: The mean concentration profile from the lowest wind condition at high fetch (black), fitted with Deacon's model function Eq. (6.5) (orange) and the polynomial fit (turquoise), both in (a) linear and (b) semi-logarithmic plots. The fit range for Deacon's model is marked in gray, while the mass boundary layer thickness is marked with by the vertical line.

representation. Because the Deacon model is only valid in the case of a stationary state, the fit of the Deacon model could not be applied to the single profiles.

Furthermore, the mean profiles were also fitted with the polynomial fit as described for the single profiles in the previous section, yielding values for the mean transfer velocities, too.

Absorption by Sulfur Dioxide

As discussed in Sec. 2.4.1, light traversing a medium is in general subject to absorption. Therefore, the light intensity decreases exponentially along the path. Since fluorescence is proportional to the intensity of the impinging light, see Eq. (2.67), the intensity of the LIF signal drops with decreasing z not only due to the decreasing concentration, but also owing to absorption. One idea to quantify the impact of the absorption on the profiles would be to estimate the absorption from the concentration profiles, but those are obtained from the fluorescence profiles which already include the effect. Furthermore, the determination of the exact value of the absorbance is not straightforward because the absorption cross section spectrum and the laser spectrum were measured with different resolutions. Therefore, the absorption effect is not easy to quantify from the profiles themselves and a different approach is chosen to estimate the effect for every measurement condition in the fetch experiment.

Using a model concentration profile according to Deacon's model and Beer-Lambert's law, see Eqs. (2.62) and (2.63), a realistic model fluorescence profile for estimating the

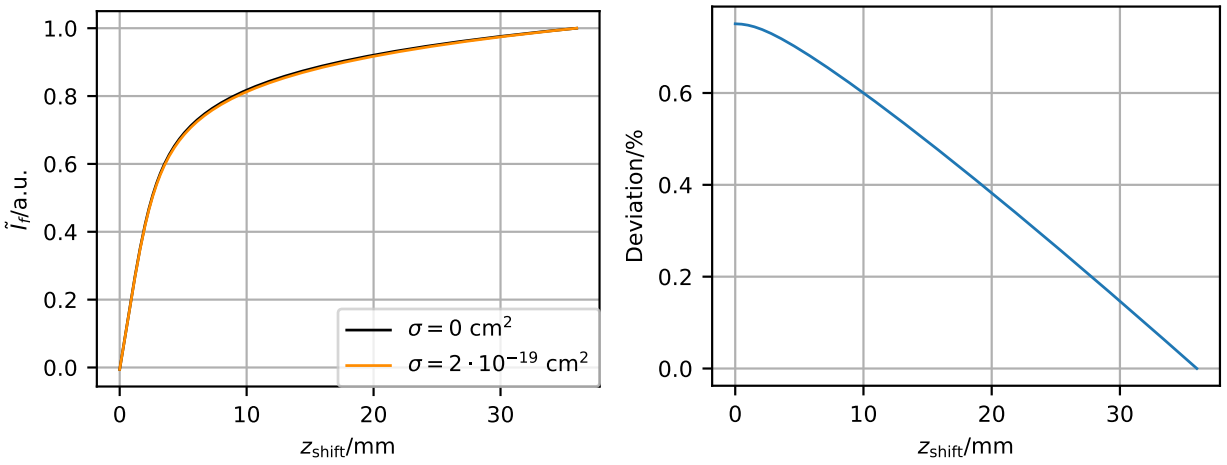

(a) (b)

Figure 6.9: (a) The normalized fluorescence intensity profile $\tilde{I}_f$, neglecting the absorption (black) and taking the absorption into account (orange), using Eq. (6.6). (b) The deviation of the two functions in (a), normalized by the realistic model profile with the not neglected absorption.

effect of absorption was constructed, using Eq. (2.67):

$$\tilde{I}_f(z) = \tilde{I}(z)\, c(z) = \tilde{I}_0 \prod_{i=1}^{n} \exp\left[-\sigma N_A c \left(\frac{z'}{i}\right) \frac{z'}{n}\right] \cdot c(z) \quad \text{with} \quad z' = z_{\max} - z. \tag{6.6}$$

Because the values of a few constants in Eq. (2.67) as well as the real initial laser intensity I_0 at the top of the air-space in the tank are unknown, a normalized intensity was considered. Furthermore, a mean absorption cross section $\sigma = 2{\cdot}10^{-19}\,\text{cm}^2$ was assumed for the estimate and the normalized initial intensity $\tilde{I}_0$ was set to unity. For the concentration profile $c(z)$, the Deacon model, Eq. (6.5), with the fit results from fitting the mean concentration profiles was applied. The integral in Eq. (2.65), which is the exponent in the Beer-Lambert law, was approximated by a step function with n steps of length 0.1 mm. For $z_{\max}$, the maximum z in the FOV of the LIF camera was chosen: 36 mm.

The realistic model profile was then compared to the idealized model profile with $\sigma = 0$ which is directly proportional to the concentration profile according to Deacon's model function. In Fig. 6.9a, both functions are shown, while the deviation is given in Fig. 6.9b, normalized by the realistic model profile. The maximum difference between both functions was 0.75%. Then, both the polynomial fit function, Eq. (6.2), and the Deacon model, Eq. (6.5), were fitted to the model profiles to estimate the effect of the absorption on the transfer velocities. The comparison of the transfer velocities from both model profiles showed that the absorption effect affected the transfer velocities from the fits by less than 1%. Because the uncertainties of the transfer velocities from the fits are larger, the absorption effect can be neglected.

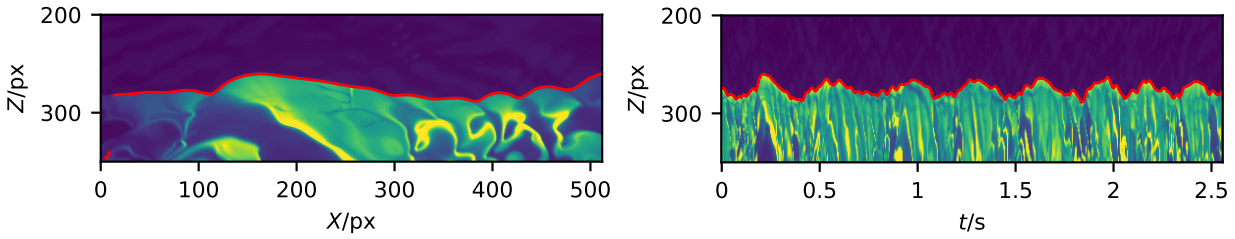

(a) (b)

Figure 6.10: (a) LHC raw image with detected surface (red). (b) Measured intensities in the central column (at $X = 256$) with the detected surface (red) in a t-Z-representation. This data is from the measurement at highest wind speed condition at the high fetch measurement section. Yellow stands for high intensities, dark purple represents low intensities. The bright parts represent the fluorescence from the water. In both figures, the Z-axis is limited to the interesting region.

As the concentrations were much smaller in the proof-of-principle experiment, the effect was assumed to be much smaller here, even negligible, and therefore, those measurements were also not corrected for absorption.

6.2 LHC Analysis

The data obtained with the LHC setup for measuring the surface height is analyzed with a MATLAB-algorithm written by K. Schwarz in her bachelor thesis. The output of the algorithm is a surface height profile for every image with sub-pixel precision. A brief summary of the algorithm is given in the following, for a detailed description see Schwarz (2016).

First, the LHC raw image is smoothed with a narrow binomial filter, then the average background level is determined by averaging the topmost part of the image. The background threshold is set to the background level plus 20 times the standard deviation of the whole image. Only the image pixels with values above this threshold are further analyzed, the background is eliminated. A binary image containing the selected pixels is eroded and dilated, i.e. the regions of interest are smoothed by eliminating small zones (e.g. from dust) and closing holes. Then, a vertical gradient filter is applied to the preprocessed image, the maxima of the gradient image regarding the binary image are found, and thereby the surface position for each pixel column is determined.

In Fig. 6.10a, an exemplary raw image from the highest wind condition at the high fetch measurement section with the detected surface is shown. The wind direction is from right to left. In the image, the higher pyranine fluorescence caused by the UV laser is visible in the center of the image. Figure 6.10b shows a t-Z-plot of the column at the position of the

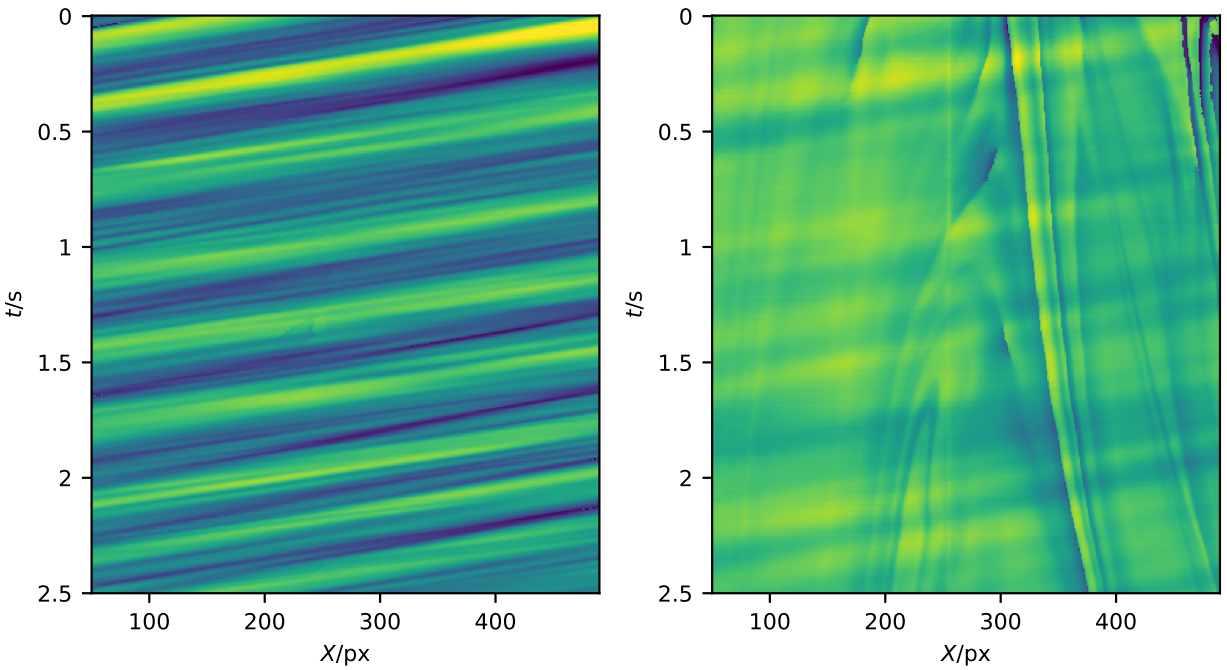

Figure 6.11: Intensity plot showing the detected water elevations (a) for the same measurement condition as Fig. 6.10, the highest wind speed, and (b) for the second lowest wind speed, both at high fetch. Yellow stands for positive, dark purple for negative surface elevations relative to the mean water level.

UV laser.

In Fig. 6.11, a series of consecutive water height profiles as detected by the LHC algorithm are shown in an intensity plot, at two different measurement conditions. The left figure shows an example for how this plot should ideally look like with a clean signal: a characteristic pattern composed of diagonals. Here, one diagonal of high intensity corresponds to a wave crest moving with the time from the right to the left side of the image. By contrast, the right figure exhibits less distinct diagonal features at a lower wind, as well as additionally discrete lines. The cause for this, pyranine bleaching, is discussed in the following section. However, it is worth to notice that the waves at high and low winds seem to have the same speed as estimated from the tilt of the diagonals.

6.3 Pyranine bleaching

The dye pyranine has high absorbance in the ultraviolet range of the spectrum, see Fig. 4.11, and the illumination with UV light causes fluorescence. However, at high intensities and long continuous exposures to ultraviolet radiation of the LIF laser, the pyranine molecules are subject to photolysis and a bleaching effect occurs (see Kiskin et al. (2002), and Nairn

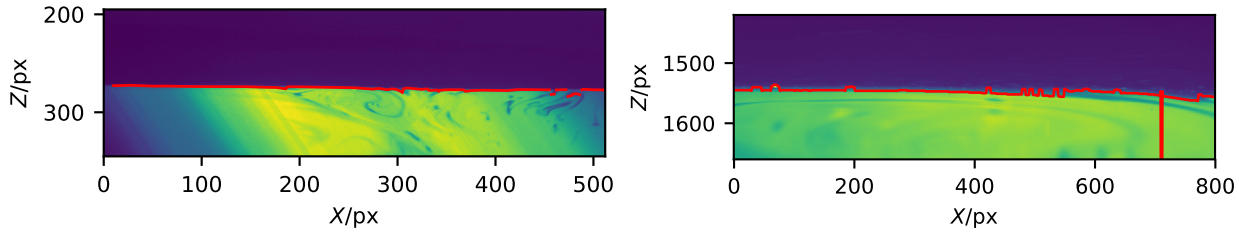

(a) (b)

Figure 6.12: Coincident (a) LHC and (b) PSV raw image with the detected surface (red) from both algorithms at the second lowest wind condition at high fetch. In both figures, the vertical axis is limited to the region of interest and multiple streaks of lower fluorescence intensity are visible.

and Forster (2015), where the dye's photostability was quantified during exposure to sunlight).

This effect is visible both in the images of the PSV and LHC camera, see Fig. 6.12, and causes surface detection problems, especially at low wind speeds, because the fluorescence intensity is reduced by bleaching. In the figure, the surface as detected by the corresponding algorithm is marked in red. It is clear that the detection is error-prone as the physical surface is expected to be smooth at these low wind speeds. In Sec. 6.5.1, the procedure applied to the erroneous surface detections is described.

As the surface water flows along with the wind, the darker regions generally follow, so that the water containing the bleached dye is mixed into the surrounding water. Sometimes, however, the non-fluorescent regions pursue other trajectories, as visible in Fig. 6.12a, even moving in both directions away from the location of the UV laser.

6.4 PSV Analysis

The PSV data is analyzed using a MATLAB algorithm written by M. Bopp in his PhD project with the aim to extract various flow characteristics from the particle images. The purpose of the measurements in his thesis was to extract shear stress profiles in the boundary layer and possibly even shear stress partitioning. As the purpose in this project is different, the determination of instantaneous wind vector fields in the area of interest for the LIF-measurement section is sufficient. Thus, only the first part, including the particle detection and position and vector quantification, of the existing algorithm is needed for the analysis. Figure 6.13 illustrates the results of the algorithm, the surface and streak detection. The description of the algorithm in the following sections largely follows the description in Bopp (2018).

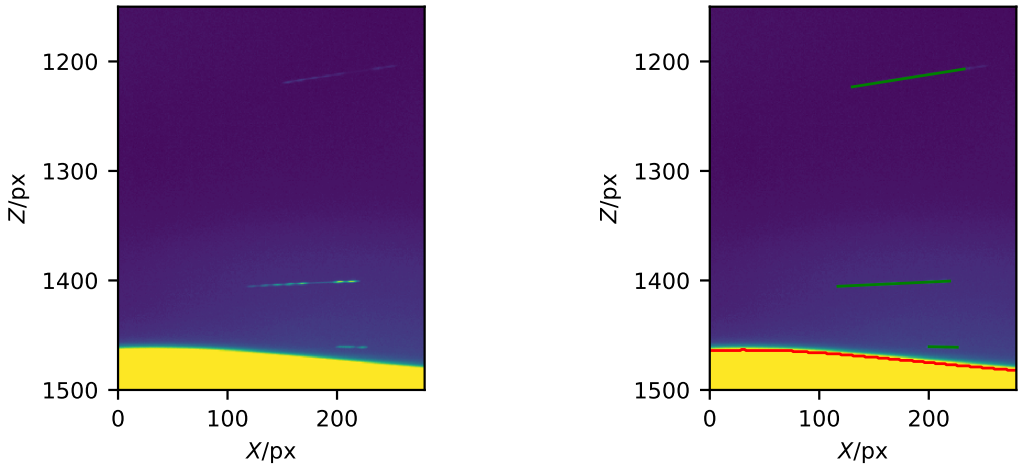

(a) (b)

Figure 6.13: PSV raw image (a) and the results from the PSV algorithm (b): the detected surface in red and streaks in green. The intensity range is adjusted for better visualization.

6.4.1 Algorithm

The data is saved in raw-files with 250 images, each. Each image is analyzed with the algorithm, resulting in the position of the detected surface as well as the position, length and orientation of the streaks.

Thresholds

For the processing, two thresholds are needed: one for the detection of the particles and one for detection of the surface. The thresholds are obtained by fitting a function to the histogram of the gray values, denoted g, of the first image of a raw file. Typically, the histogram shows two distinct peaks, a narrow one in the background and a wide one in the range of the brighter pixel values corresponding to the surface and the underlying water. The streaks are only a few pixels per image and are thus too few to be distinguished from either the surface or the background in the histogram. Consequently, the fit function to the histogram of the gray values consists of two Gaussian distributions

$$h(g, \sigma_b, \mu_b, a_b, \sigma_s, \mu_s, a_s) = a_b \exp\left(\frac{-(\mu_b - g)^2}{\sigma_b^2}\right) + a_s \exp\left(\frac{-(\mu_s - g)^2}{\sigma_s^2}\right) \tag{6.7}$$

with the fit parameters a_i, μ_i and σ_i for the background (b) and the surface (s) parts of the histogram. The thresholds for the particles g_p and the surface g_s are then calculated from the fit parameters as

$$g_\mathrm{p} = \max(b_1\sigma_b, b_2\mu_b), \tag{6.8}$$

$$g_\mathrm{s} = s(\mu_s + \mu_b) \tag{6.9}$$

with the parameters b_1, b_2 and s set manually before the evaluation is started. For most of the evaluations, the values were $b_1 = 4$, $b_2 = 1.5$ and $s = 0.15$, however sometimes they had to be adjusted to improve surface and particle detection for exceptional illumination conditions, e.g. for the low wind speed measurements where the surface was very bright. This procedure is repeated for every 12000 images (corresponding to one minute of measurements) to reduce the effect of fluctuations of the pyranine fluorescence due to bleaching or changes of the pH value.

Preprocessing

First, the background is detected in order to separate it from the streaks. The background image is obtained by applying a median filter of 9×9 pixels' size to the raw image, blurring fine structures like the particles, but leaving the surface nearly untouched, as it already extends vertically over several pixels. Then, those pixels in the raw image, which deviate from the median image by more than the threshold for particle detection, are replaced by the corresponding values in the median image, resulting in a background image, which is smoothed with a binomial filter.

The surface position is first estimated via the threshold g_s. As the surface extends over several pixels due to the non-zero width of the laser sheet and the high camera resolution, the maximum of the vertical gradient of the pixel values close to the first surface estimate is determined as the surface height. This information is stored for later evaluation.
Now, the background image is subtracted from the raw image and the pixel values below the surface are set to zero, yielding a preprocessed image, reduced to the region of interest, the air above the water, and ideally containing only particle streaks.

Orientation Field

The 'particle image' obtained in the last step is then further processed to extract a direction field along which the particle streaks are going to be collected. This was done by applying the structure tensor on the particle image, yielding an orientation vector in every pixel, i.e. the angle of the orientation.

Streak Detection

Now, the image is prepared for the main processing: the identification of the streaks. First, the particle threshold as defined before the evaluation, see above, is applied to the image, yielding a binary image. The binary image is then dilated, i.e. the connected areas with pixels above the threshold ('1') are expanded, being identified and marked as detections. Depending on the length of the streak, several detections can belong to one streak: the separate peaks of the signal, or, separated by the gap, the two parts of the signal. Therefore, those detections belonging to one streak are connected, using the orientation field: From one detection object, in steps of 0.5 pixels, all detections in both directions along the local orientation vector are collected, up to a maximum streak length limit.

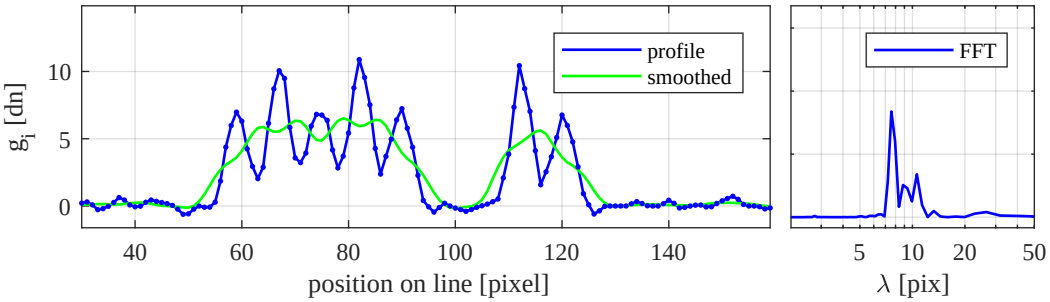

Figure 6.14: Streak profile (blue) with smoothed curve (green) on the left with the wavelength spectrum resulting from the FFT on the right. The wavelength with the highest peak is taken as the estimate for the PSV frequency. The figure is taken from Bopp (2018).

Profile Extraction

The next step is the determination of the direction and length of a streak, i.e. its velocity vector. A linear fit is applied to the streak pixels, weighted by their gray values, resulting in the direction of the streak. Along the line, the gray values are extracted in steps of 0.5 pixels, as weighted means of the adjacent pixels, yielding the streak gray-value profile.

Profile Fitting

A first estimate of the wavelength of the streak (in pixels) λ_{streak} is the maximum of the frequency spectrum of the gray-value profile from the application of a Fast-Fourier Transform (FFT) algorithm. The latter is applied to the profile minus a highly smoothed profile in order to eliminate long wavelengths. This procedure is illustrated in Fig. 6.14, where the profile, the smoothed profile and the FFT result are shown. The maximum of the FFT λ_{fft} is a good first estimate for the wavelength, i.e. the length of one period of the PSV signal in pixels, corresponding to 1/9 of the streak length, for longer streaks. For shorter streaks, the FFT does not yield a reliable result.

Finally, the PSV signal is fitted to the profile in the form of model profiles with different wavelengths. Those model profiles were generated with wavelengths λ_{fit} between 0 and 20 pixels in steps of 0.05 pixels and projected with a resolution of 0.5 pixels, simulating the limited camera resolution.

All streaks are fitted with model streaks with wavelengths ranging $0.9\lambda_{\text{fft}} < \lambda_{\text{fit}} < 1.1\lambda_{\text{fft}}$, while streaks shorter than the threshold streak length $l_{\text{thresh}} = 75$ px are additionally also fitted with all model streaks with streak lengths up to $\lambda_{\text{thresh}} = 1/9\, l_{\text{thresh}}$. This makes the fitting procedure slower, but also more accurate for shorter streaks.

The real profile is compared to the group of model profiles, oriented in both directions (both ‘upwind’ and ‘downwind’) and the best correlation with the lowest normalized

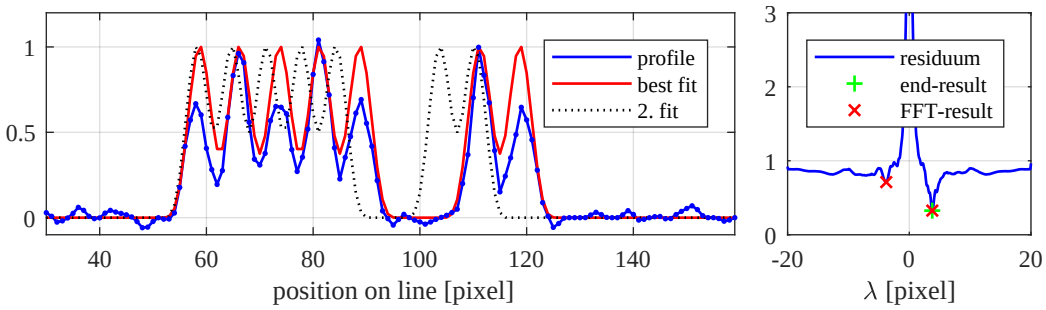

Figure 6.15: Streak profile (blue) with best (red) and second best (black dotted) fit on the left with the residuum for each wavelength on the right. The results from the FFT and the end result where the residuum is minimal are marked. The figure is taken from Bopp (2018).

residuum Θ,

$$\Theta = \frac{\sum |g_{\text{model},i} - g_{\text{profile},i}|}{\sum g_{\text{model},i}} \tag{6.10}$$

gives the wavelength and also the direction of the particle movement as the fit result for the streak. Fig. 6.15 shows the fit results for one streak including the residuum.

In summary, the PSV algorithm output is the detected surface (for comparison with the LHC surface detection) and the position, i.e. the position of the centroid of a streak, direction and wavelength of the detected particle streaks in each picture. From the latter data of the particles, the velocity vectors can be determined.

6.4.2 Secondary Particles

In the fetch experiment, a phenomenon was observed which posed a problem to the PSV algorithm: During the measurements, an increasing number of very light streaks, much smaller and thus fainter than the NH_4Cl particles, occurred. In the following, those scattering centers will be called 'secondary particles', even though they could be either droplets or particles. The secondary particles were particularly disturbing at low wind speeds close to the water surface, see Fig. 6.16b. The reason might be the high intensity of the fluorescence from the water in long exposures of the PSV camera, see Fig. 6.16a from the beginning of the measurement, where the background intensity is increased close to the surface. As they occurred in very high densities towards the end of the measurements, the algorithm had problems to separate these particles from the background and from the real particles. To illustrate this, the incorrectly identified streaks are colored white in Fig. 6.16b (the selection process is described in the next section). It is obvious that the number of false streaks increased compared to the beginning of the measurement. Also, the bright water surface enhanced the background brightness close to the surface such that the secondary

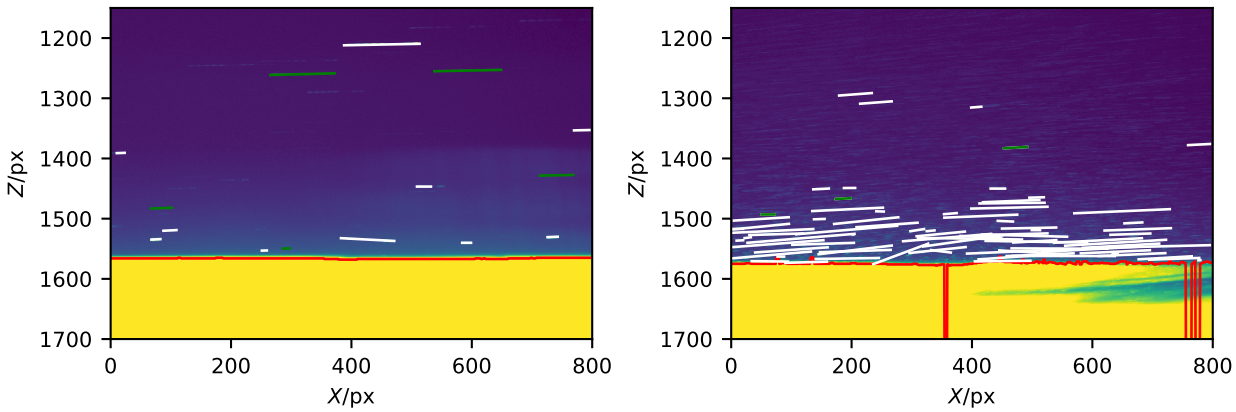

Figure 6.16: PSV raw images from the lowest wind speed measurement at low fetch, (a) from the beginning and (b) from the end of the measurement. The detected surface (red) is shown as well as the correctly (green) and incorrectly identified streaks (white). The intensity range is limited for better illustration. Also, the bleaching effect is visible in the fluorescence from the water in (b).

particles could not be eliminated by applying a simple threshold. Particles very close to the water surface interfere with the surface detection algorithm, thus causing incorrect identifications in the PSV images, which is again illustrated in Fig. 6.16b where the detected surface has 'jumps'.

The cause for these particles has so far not been clarified. A possible explanation in analogy to atmospheric chemistry is the following: The UV laser light and the UV spectroscopy setup produce ozone from oxygen via photo dissociation. The ozone can react further via two ways. In pathway one, the ozone molecule is again split into an oxygen molecule and a separate oxygen atom by the UV light of the spectroscopy setup, which then reacts with water to two hydroxyl radicals. The latter react with sulfur dioxide to sulfuric acid. In the second pathway, ozone directly reacts with sulfur dioxide to form oxygen and sulfur trioxide, which then forms sulfuric acid with water. In both cases, ozone plays a key role and the end product is sulfuric acid which is very hydrophilic and therefore acts as a condensation nucleus where water molecules are adsorbed, producing aerosol particles which appear as secondary particles in the images.

Another possibility is that the particle production in the mixing cell is not 100 % efficient and that therefore also gaseous ammonia enters the air in the tank and reacts with sulfur dioxide to ammonium sulfite which again can act as condensation nuclei for droplet production. These droplets could also be the cause for the secondary particles.

The reactions are in analogy to the formation of fine particulate matter (secondary inorganic aerosols) in the atmosphere which is controlled by the abundance of the reactive gases, among others SO_x, ammonia and water, as analyzed by Koziel, Aneja and Baek (2006).

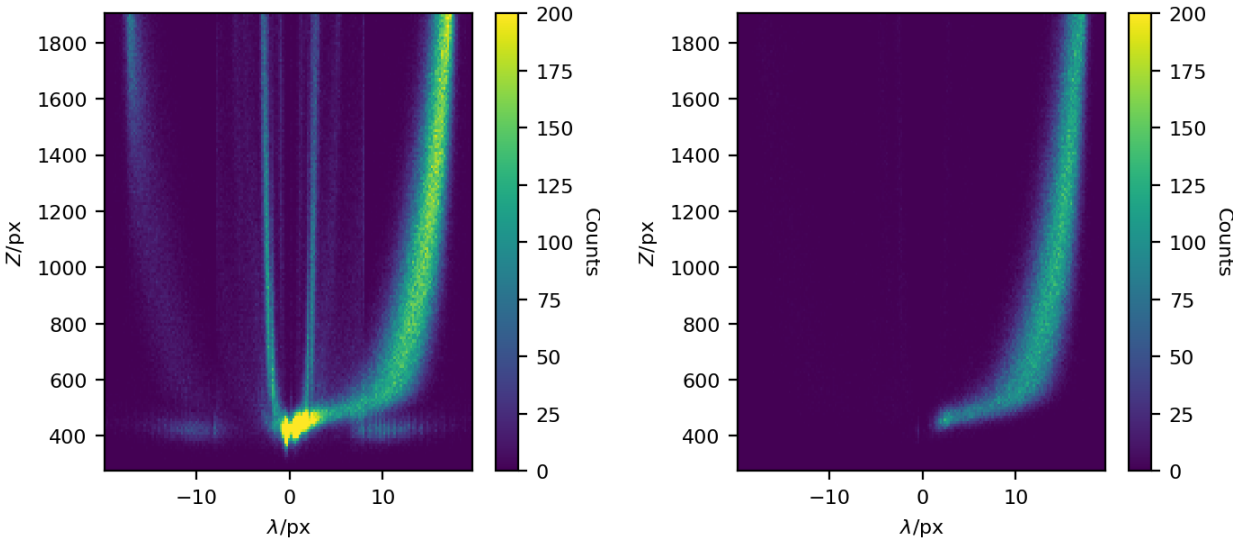

Figure 6.17: Histogram of all detections (a) and the detections passing the selection criteria (b) from the measurement at high wind and low fetch.

6.4.3 Eliminating Erroneous Detections

The PSV streak detection algorithm is not perfect: non-ideally imaged particles can be detected, but the fits might not work well for all streaks. In particular, incorrect identifications are caused by the secondary particles as discussed in the previous section. Therefore, it is important to sort the streaks identified by the detection algorithm according to their fit quality before the data is further analyzed. Figure 6.17a shows a histogram of all detections in one measurement over their vertical position in the image (z in pixels) and the wavelength obtained from the signal fit, which corresponds to 1/9 of the streak length. The mean logarithmic profile as expected from theory is visible, but also a high number of obviously incorrect identifications are visible. In general, also negative horizontal velocities are possible, especially close to the water surface behind waves with heights significantly larger than the mass boundary layer thickness where airflow separation occur in the lee of the wave, see for example Buckley and Veron (2018). However, the conditions at the present experiments had much lower wind speeds and thus, negative horizontal wind speeds should not occur. Consequently, negative wavelengths correspond to streaks detected flying in the direction opposite to that of the wind and are therefore incorrect identifications.

Close to the water surface at low z-values, high densities of secondary particles cause detections of clusters of several particles as one streak, as seen in Fig. 6.16b. These wrong detections are found in the histogram at $z \approx 400 - 450$ px and varying wavelengths. Generally, the secondary particles cause a high number of wrong detections, as discussed in the previous section, contributing significantly to the high number of detections at short wavelengths, as well.

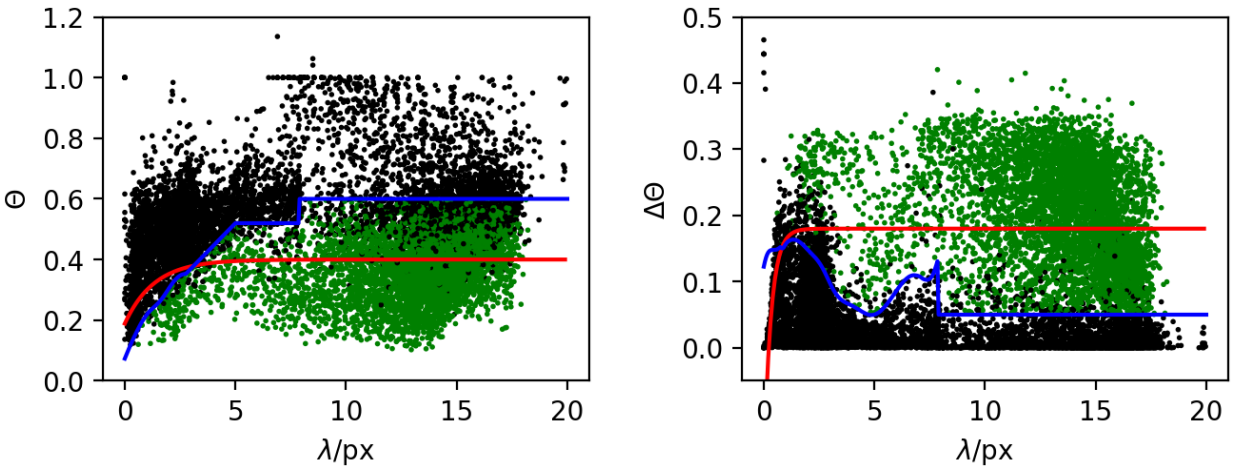

(a) (b)

Figure 6.18: The residuum Θ (a) and the difference of the two best fit residua ΔΘ (b) plotted over the streak wavelength for every 50th detection from the measurement at high wind and low fetch. The detections passing both selection criteria are plotted in green, the others in black. The red lines marks the threshold functions by Bopp (2018) while the blue lines represent the threshold functions employed in this experiment.

However, also the streaks farther away from the surface can be incorrectly fitted, e.g. when only one peak of the PSV signal is fitted as one streak. This causes the detection of short streaks with 1/9 of the mean wavelength at the corresponding z-position as visible in Fig. 6.17 as vertical lines looking like an echo of the logarithmic profile.

Those wrongly processed particles can be identified and eliminated by setting selection criteria on the fit residuum Θ and a second parameter which is characteristic for the quality of the detection: ΔΘ is the difference of the residua of the best fit and the second best fit, the latter being generally one with the same (or similar) wavelength as the best fit, but in the opposite direction. For example, for short streaks, the direction might be hard to determine, thus resulting in a small difference between the two residua. Low values for Θ and high values for ΔΘ indicate reliable detections and good streak fits.

Bopp (2018) determined wavelength-dependent functions for the two parameters by evaluating the overall quality of fit of the algorithm through the analysis of a simulated data set. As the real parameters of the simulated streaks were known, a fit to the limit between good and bad detections in the distributions of Θ and ΔΘ over the wavelength resulted in two functions. Using those functions on the PSV data produced here resulted in 'holes' in the streak histograms, similar to those observed by Kühlein (2019). The conclusion is that the residua have different distributions in the two experimental setups. Therefore, a new approach was used.

Again, the thresholds were chosen as functions of the wavelength. A first assumption

was that generally, due to the occurrence of secondary particles close to the water surface, see Fig. 6.16b, short streaks are less efficiently detected and fitted than long streaks, but also that more short streaks are detected than long ones. However, also long streaks were detected in those high streak density areas close to the surface, because of several streaks being detected as one. These detections typically showed high Θ values and close to zero $\Delta\Theta$ values.

The routine for the determination of the selection rules is the following: The detections were separated in bins according to their wavelengths, each bin having the width $\Delta\lambda = 0.1$ px. Then, a discrete approximation of the cumulative distribution function (CDF) was determined at the bin centers and interpolated. Finally, the threshold value was set to the Θ and $\Delta\Theta$ values which fulfilled

$$F_\Theta = f_1 + f_2\,\lambda, f_1 \epsilon [0.01, 0.1], f_2 \epsilon [0.015, 0.045], \tag{6.11}$$

$$F_{\Delta\Theta} = f_3 - f_4\,\lambda, f_3 \epsilon [0.6, 0.9], f_4 \epsilon [0.025, 0.04]. \tag{6.12}$$

The values for the parameters f_1 to f_4 had to be adjusted for every measurement in order to produce reasonable looking wind distributions. In other words: for increasing λ, the threshold for the residuum increased, such that higher values of Θ were accepted, while the threshold for the difference residuum decreased, leading to also lower difference residua to be accepted. For higher wavelengths, $\lambda > \lambda_{\text{thresh}}$, a constant threshold was used for both Θ and $\Delta\Theta$.

In Fig. 6.18, the two fit quality variables Θ and $\Delta\Theta$ as functions of the streak wavelength λ for one measurement are shown. The threshold functions are plotted in blue, in comparison to the functions that were used by Bopp (2018), shown in red. It is obvious that using the functions by Bopp (2018) would eliminate much more 'good' streaks.

Figure 6.17b shows the result of the sorting routine: only the expected form remains (even though also detections in this area were eliminated) with a very small number of wrong detections passing the selection rules.

In few measurements, where the wrong detections close to the water surface due to secondary particles were not completely eliminated by the Θ and $\Delta\Theta$ thresholding, a z_{shift}-dependent threshold was used to eliminate those wrong detections. The thresholds are shown with a red dashed line in the histograms in Figs. 7.1 and 7.2, showing the resulting horizontal wind histograms. The detections below the thresholds were rejected.

The outliers at larger heights above the water surface were eliminated by making a shortest coverage approach: the shortest λ-interval 'covering' the sum of 95% of the detections is selected, the outliers are rejected. The shortest coverage interval borders are marked in Figs. 7.1 and 7.2, with red lines. By averaging over the resulting horizontal velocities in the 95% intervals, mean wind profiles were obtained, which are marked in these plots by the black lines.

6.4.4 Mean Wind Profile Fitting

The mean horizontal wind profiles obtained in the previously described step were used to determine both the friction velocity u_* and the roughness length z_0 for every measurement.

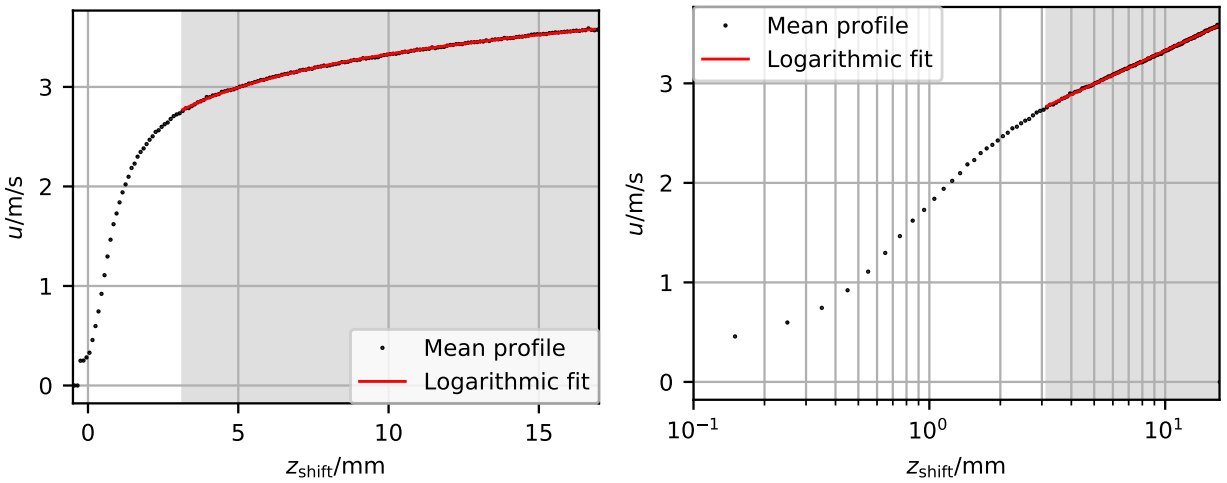

Figure 6.19: Mean wind velocity profile from the measurement at the second highest wind condition at low fetch with the logarithmic fit (red), with (a) linear and (b) logarithmic z_{shift} axis. The fit range is marked in gray.

This was done by fitting the dimensional version of the logarithmic profile, Eq. (2.28),

$$u(z) = \frac{u_*}{\kappa} \ln\left(\frac{z}{z_0}\right) \tag{6.13}$$

with the fit parameters u_* and z_0 to the mean wind profiles. According to literature, see for example Kundu, Cohen and Dowling (2015), the logarithmic function represents the real profile well for $z^+ > 30$. Thus, the lower limit of the fitting interval should be $z^+ = 30$. However, with this fit, u_* should be determined but the scaling of z^+ depends on u_*. Therefore, an iterative fitting routine was applied where not only the logarithmic function but also the lower fit limit $z^+ = 30$ was fitted in each iteration step. For the initial guess for the friction velocity, estimates from the measurements in Friedl (2013) were used. The fitting procedure was iterated ten times. This was sufficient, since the values for the fitting parameters u_* and z_0 converged quickly. For an estimate of the uncertainty of both fit parameters, the fit was repeated with the lower fit limit varied by $\pm 1\,\text{mm}$. The maximum deviation of the parameters was adopted as the uncertainty.

In Fig. 6.19, the mean wind velocity profile is shown together with the fitted logarithmic function for one examplary wind condition.

6.5 Combination Analysis

The data obtained from all three measurement techniques in the fetch experiment need to be combined. The procedure is described in this section. First, the PSV and LHC coordinates were aligned comparing the surface detections of the two algorithms. For each

PSV and LIF exposure, the two LHC surface data sets taken just before and just after were averaged and then aligned with the PSV data. Then, the curvilinear coordinates were calculated for the PSV particles. Thereby, the particle vectors are transformed into real-world velocity vectors.

Second, the LIF profiles were aligned to the LHC coordinate system. After this step, all three measurement techniques are spatially and timely synchronized and are in real-world coordinates.

Third, the PSV and LIF data are compared, to obtain simultaneous and collocated concentration and wind fluctuations.

6.5.1 PSV and LHC

This evaluation step was programmed in MATLAB by M. Bopp. The first step is the evaluation of the surface data obtained from the LHC algorithm. The result from the geometric calibration, the transformation functions, Eqs. (5.1) to (5.3), were used to transform the smoothed LHC surface data to real world coordinates. Also some outliers were eliminated with thresholding.

Then, the surface data as detected by the PSV algorithm was transformed to real world coordinates. Furthermore, the LHC surface data was averaged for the PSV times, i.e. two LHC surface profiles were averaged to obtain the LHC surface profile at the time of the PSV (and LIF) image capture. As the trigger signals were adjusted in such a way that the PSV capture lies exactly in the center between two LHC signals, both LHC signals were weighted equally.

Now, the mean of the surface data, which might be tilted, was subtracted from all data in order to correct for the mean water level. The PSV surface data was then compared to the corrected LHC surface data in order to eliminate an offset in both x and z direction, which might be caused by smaller calibration errors. Fig. 6.20 shows an exemplary LHC surface profile with the corresponding PSV surface profile after alignment.

The curvilinear coordinates (see Sec. 3.3.1) were then calculated, using only the simple shift transformation, Eq. (3.5). The declining shift transformation is needed only when the wave height is much larger than the viscous boundary layer thickness which was not the case under the wind conditions used of this experiment. Thus, the particle coordinates were transformed to z_{shift} by means of the geometric calibration, see Sec. 5.1.1. Furthermore, the velocity vector for every particle was calculated in real-world coordinates.

As mentioned above in Sec. 6.3, the pyranine undergoes bleaching by the UV laser light which possibly disrupts the detectable fluorescence at the water surface and thereby prevents correct surface detections by both PSV and LHC. At low wind speeds, this effect occurs in a higher percentage of the images than at higher wind speeds. Therefore, the data sets at the two lowest wind speeds were evaluated differently than the high-wind data. As there were no considerable waves at those wind conditions, the surface was approximated with a linear fit for $\eta(x)$ for every image, smoothing away wrong detections of the surface due to the pyranine bleaching. The resulting coordinates were then used in the subsequent analysis in the same manner as the surface detection data.

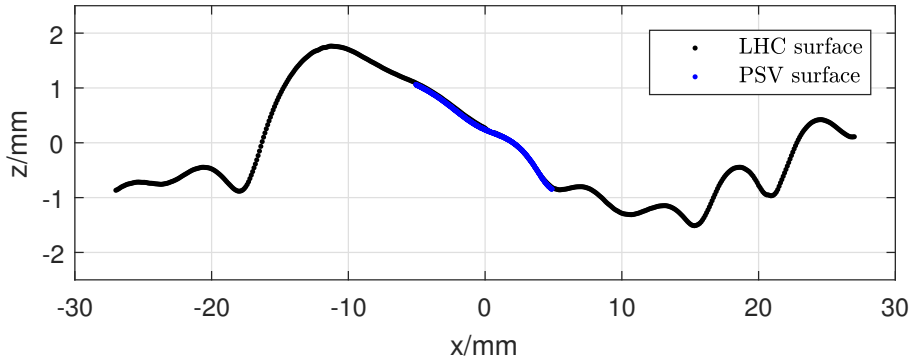

Figure 6.20: Surface detected by the LHC algorithm averaged for the PSV and LIF time (black) with the corresponding PSV surface (blue), after the alignment.

6.5.2 LIF and LHC

The transformed LHC surface data was then used in the analysis of the LIF data obtained in the fetch experiment, because in the latter, no surface detection was possible (see Sec. 6.1). First, the surface data at the position of the UV laser beam was compared to the raw, uncorrected LIF profiles in order to eliminate an offset due to the geometric calibration. Then, the LIF profiles were shifted, using the coordinate transformation deduced in the previous step for the UV laser's x position.

Figure 6.21 shows the result of the LIF height correction: a sequence of quotient profiles from two LIF measurements at the lowest and highest wind condition at low fetch. It is evident that the light originating from the fluorescence underwater, which is also much brighter than the bulk intensity of the SO_2 fluorescence, is not usable for surface detection purposes. Especially at high waves, the fluorescence shifts and is not constant while at the lowest wind condition, its distribution in relation to the surface is more or less similar in adjacent profiles.

Still, the fluorescence profiles can be used to manually adjust timing and spatial offsets because the waves are nevertheless still visible in the profiles. Furthermore, the good agreement of the profiles with the surface elevation obtained with this approach for low wind speeds, as described in the previous section, shows that this procedure is justified.

Another striking feature of the profile sequences shown in Fig. 6.21 is that the thickness of the boundary layers and the corresponding gradients are very different. This is discussed further in Sec. 7.3.

After this step, all three visualization techniques are synchronized, geometrically and timely. With the height corrected, the z axis is transformed into the z_{shift} axis by subtracting the water elevation. Then, the $c(z_{\mathrm{shift}})$ profiles can be averaged to yield the mean profiles $\bar{c}(z_{\mathrm{shift}})$.

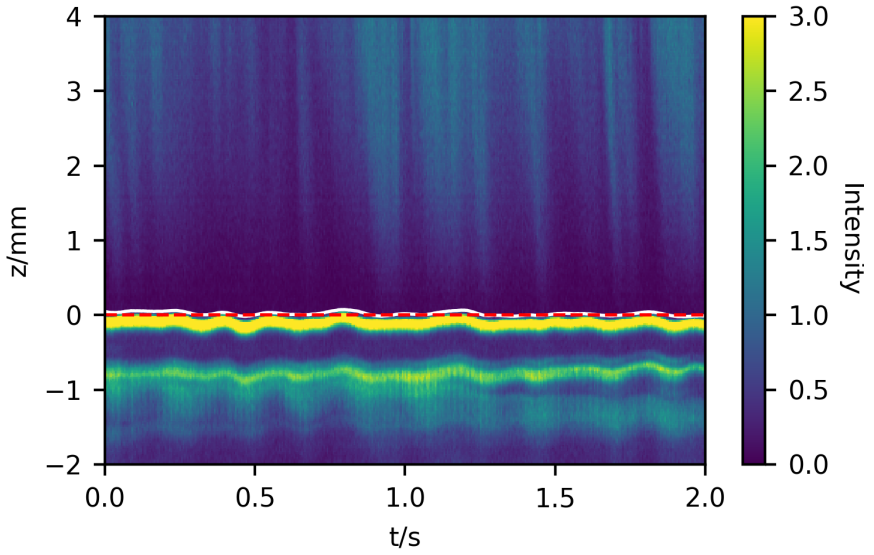

(a) 5 Hz, low fetch

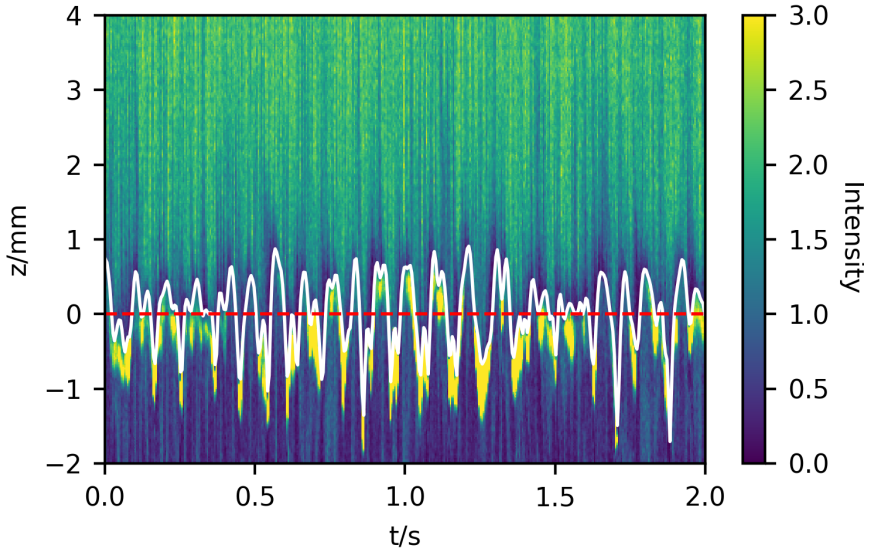

(b) 20 Hz, low fetch

Figure 6.21: A series of LIF profiles obtained from the measurements at the (a) lowest and (b) highest wind conditions at low fetch after the height correction, with the mean water level in red and the surface elevation from the LHC analysis in white.

6.5.3 LIF and PSV

The LIF profiles give continuous concentration values for the whole z axis in every image, but the PSV technique does not yield continuous wind profiles. Therefore the following procedure was applied: First, only those particles whose streak traverse or 'touch' the UV laser beam were selected for further analysis as only the local wind field around the laser

position is important for the analysis. This was done by sorting those particles out whose central x-coordinate minus the x-position of the laser at the z-position of the particle is larger than half their length in x-direction. Then, for every 'beam particle', the LIF concentration c at the corresponding height was determined. The fluctuating concentration c' was calculated by subtracting the mean concentration $\bar{c}$ at the corresponding height from c. The concentration fluctuations could then be correlated with the corresponding vertical wind fluctuations.

6.6 Wave Analysis

In order to study the phase dependence of several variables, e.g. the transfer velocity and the viscous boundary layer thickness, the surface elevation data obtained from the processed and averaged LHC data (see Sec. 6.5.1) from the two highest wind conditions were analyzed with respect to the wave properties. For the analysis of the phase dependence, the phase of the dominant wave is needed. The following procedure is based on the wave evaluation in Bopp (2018).

First, the dominant wave frequency f_d had to be derived from the time series of the local surface elevation at each x position. The power spectral density (PSD) for every x position was calculated and then averaged. The dominant wave frequency was then obtained from the maximum of the spectrum. The result is listed in Tab. 6.1. As expected, the dominant frequency decreases for higher wind conditions and higher fetch.

Table 6.1: Dominant wave frequencies for the four highest wind measurements at the fetch experiment, rounded to the nearest multiple of 0.5.

Fetch	W Hz	f_d Hz
Low	15	12.0
	20	11.0
High	15	8.0
	20	6.5

Second, a Fourier based band pass filter was applied to the elevation time series with the frequency range being $[0.5, 1.5]f_d$.

Finally, a Hilbert transformation of the filtered signals at each x position yielded the local dominant amplitude and phase at each time step. Thus, the phase and amplitude of the waves at the UV laser position could be derived. The results are shown exemplarily for the measurement at highest wind speed and high fetch in Fig. 6.22 with the surface elevation and the dominant wave height. When a wave traverses the measurement section, first its 'front' is visible, the leeward side of the wave. Here, a wave's phase is defined as $[-\pi, 0]$ for the windward side of the wave from trough to crest, and $[0, \pi]$ on the leeward side from crest to trough.

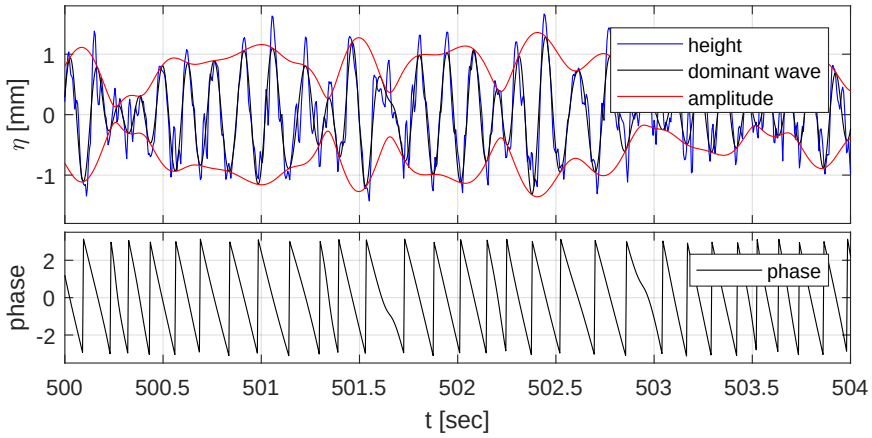

Figure 6.22: (Top) Surface elevation (blue) at the UV laser position with dominant wave height (black) obtained via the Fourier band pass filter and the amplitude of the dominant wave as an envelope (red) from the Hilbert transformation. (Bottom) The phase of the dominant wave from the Hilbert transformation.

6.7 Spectra Processing

The transmittance spectra recorded with the absorption spectroscopy setup were evaluated with the following procedure to yield a time series of the absorbance or concentration. As described in Sec. 4.7, a dark and lamp spectrum as well as the transmittance spectrum were used to obtain the absorbance spectrum. The latter was then fitted with a model containing three components: a reference absorbance spectrum $abs_{\mathrm{ref}}(\lambda)$, an array with linear dependence of the wavelength $lin(\lambda)$, and an offset a_0:

$$abs_{\mathrm{meas}}(\lambda) = a_2\, abs_{\mathrm{ref}}(\lambda) + a_1\, lin(\lambda) + a_0, \tag{6.14}$$

with the fit parameters a_2, a_1 and a_0. The latter two components are necessary to compensate for changes in the lamp spectrum or intensity (Krall, 2013). The fit parameter a_2 corresponds to the fitted mean absorbance at the time of the measurement which was then further used for the mass balance fits. Thus, with this fitting routine, a mean absorbance time series was calculated for every measurement.

In the fetch experiment, a concentration calibration as described in Sec. 5.1.2 was performed, thus enabling the translation of the absorbance values to bulk concentration values.

The absorbance or concentration time series were then fitted with the modeled concentration functions as determined from the mass balance method, see Sec. 3.4.

Equation (3.11) was fitted to the absorbance series obtained from the proof-of-principle experiment. Two exemplary absorbance time series are shown in Fig. 6.23, one from the lowest and one from the highest wind condition. The fit function is plotted in red, showing very good agreement. It is evident that the exponential decay of the absorbance is quicker

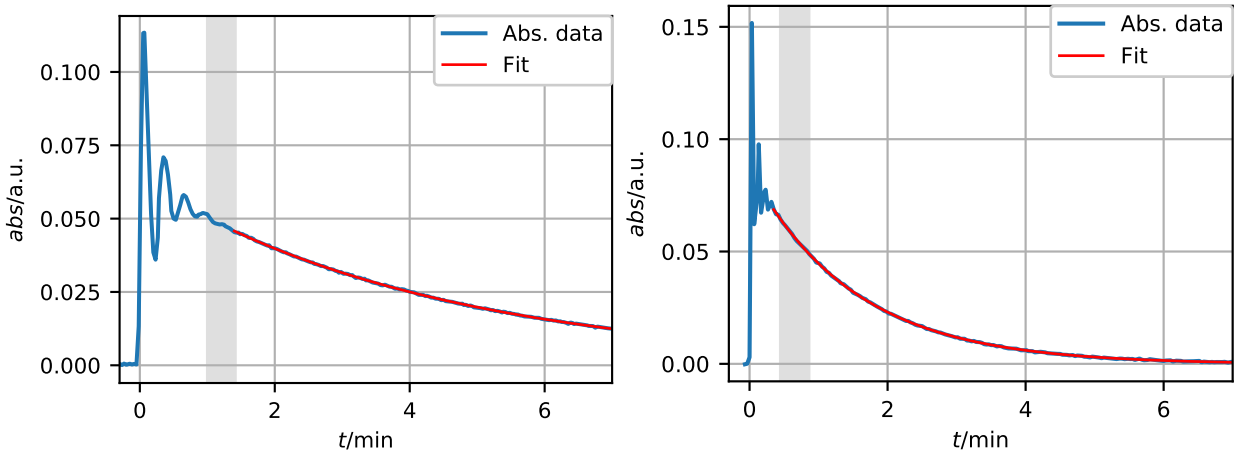

(a) 5 Hz (b) 15 Hz

Figure 6.23: The absorbance as a function of time as obtained by the evaluation of the absorption spectra (blue), for the (a) lowest and (b) highest wind speeds in the proof-of-principle experiment, along with the fitted function from the mass balance calculations, Eq. (3.11). The gray areas mark the 25 seconds time window where the LIF data was averaged for the mean profiles.

at high wind than at low wind. Furthermore, directly after the addition of the sulfur dioxide at $t = 0$, the absorbance (and thus the concentration) oscillates strongly until the tracer is well mixed into the air volume.

The concentration data from the fetch experiment were fitted with Eq. (3.13). In Fig. 6.24, two exemplary concentration time series, one from the lowest wind condition at high fetch and one from the highest wind condition at low fetch, are shown along with the corresponding fit function. Also here, the fit function matches the data quite well. In comparing the two graphs, the different equilibration times, i.e. the times until the system has reached the quasi-equilibrium, are directly visible: at the lowest wind condition, the equilibrium concentration was still not reached after 40 min even though the SO_2 flux was adjusted to reduce the equilibration time (see Sec. 5.2.2), while at the highest wind speed, the equilibrium concentration was reached already after around 15 min. This is also discernible in the decay after turning the sulfur dioxide flow off when the concentration decreases exponentially.

It was decided not to fit the decay function, Eq. (3.11), to this part of the time series because with time, the humidity in the tank increased and thus also the possibility of water condensation on the prisms of the spectroscopic setup, despite the fact that the tank water was being cooled. At some measurements, especially at high winds, this reduced the height of the transmittance spectra drastically in the course of the measurements. Therefore, only the beginning of the measurements was used for the fits.

The naive uncertainties of the fit parameters given by the fit algorithm were very small, because of the high number of data points and the good agreement between the data and

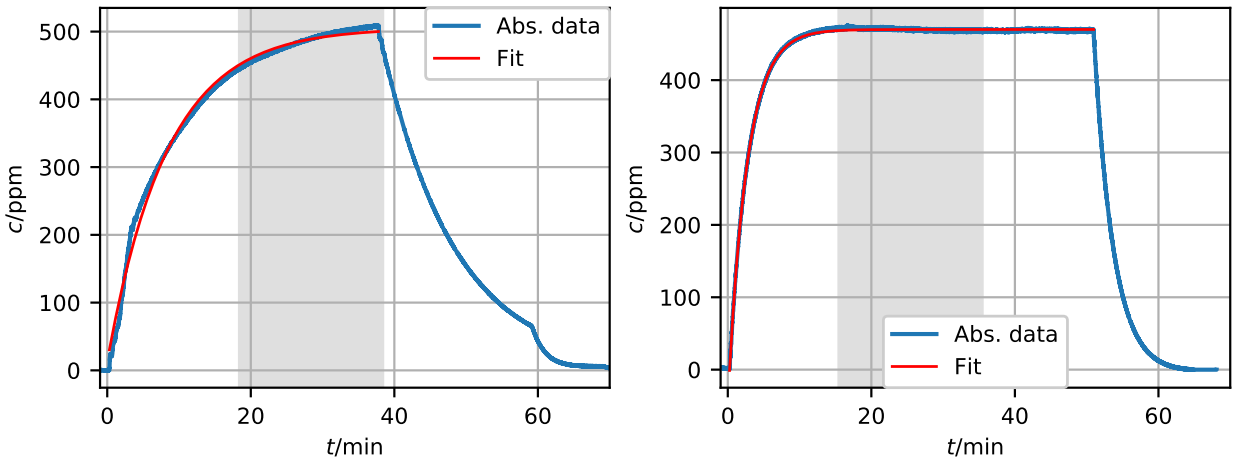

(a) 5 Hz, high fetch

(b) 20 Hz, low fetch

Figure 6.24: The concentration as a function of time as obtained by the evaluation of the absorption spectra (blue), for the (a) lowest and (b) highest wind speeds at the two fetches in the fetch experiment, along with the fitted function from the mass balance calculations, Eq. (3.13). The gray areas mark the 20-minutes time windows where the LIF, PSV and LHC data were analyzed, assuming a quasi equilibrium state.

the model. Even the fit applied to the measurement where the SO_2 flux was changed yielded reasonable fit results and a reliable value for the transfer velocity. However, the fit results depend on the fit limits as well as the input parameters: the surface area A and the air volume V_a have the largest uncertainties which should not be neglected. Thus, to get a better estimate of the true parameter uncertainties in dependence of the fit limits, the fits were repeated with the lower fit limit being increased by 1 min. This reduced the data points in the critical part of the distribution at the beginning of each measurement where the change of concentration is the fastest. This procedure yielded more realistic uncertainties of 1 to 5%. To estimate the influence of the input parameters A and V_a on the uncertainties, the fit was repeated with varying combinations of $A \pm dA$ and $V \pm dV$. The largest deviations from the transfer velocities obtained without uncertainties were around 10% and thus taken as the estimated uncertainties.

7 Results

In this chapter, the results from the analysis of the data obtained in this project are presented.

To better understand the mass and momentum transport mechanisms, the wind conditions needed to be characterized. This was done by evaluating the wind profiles and obtaining the friction velocity and roughness length from the mean wind profiles, see Sec. 7.1.

One of the main focuses of this thesis was to obtain transfer velocities from various sources. Four methods to determine either instantaneous transfer velocities or the transfer velocity averaged over a whole or part of an experiment were applied in this study:
1) The bulk fluorescence was evaluated with a mass balance method in the proof-of-principle experiment to obtain a global mean transfer velocity, averaged over the respective experiment.
2) The absorbance as obtained from absorption spectroscopy was analyzed with a mass balance method, too, yielding the mean global transfer velocity of a measurement.
3) The mean concentration or quotient profile of a measurement was used to obtain a local mean transfer velocity via fitting a model function.
4) The single concentration or quotient profiles were fitted with a polynomial and a model function to calculate the instantaneous local transfer velocities.

The methods 2), 3) and 4) were applied in both experiments. The methods are separated into global and local techniques: The first two methods yield globally averaged transfer velocities, averaged over the total water area, all fetches and wind conditions present at different locations in the wind tank. The results from the global methods and both experiments are given in Sec. 7.2. In contrast, the profile fitting methods give rise to mean local and instantaneous local transfer velocities. The local transfer velocities are presented in Sec. 7.3.2. In Sec. 7.3.3, the global and local transfer velocities are compared qualitatively.

The comparison of the concentration data from both experiments is given in Sec. 7.4. Furthermore, the concentration and wind data were analyzed with respect to their fluctuations, see Sec. 7.5.

The measurements at the highest wind conditions, where waves occurred, were also evaluated with respect to the modulation with the phase of the dominant wave. This was done by including the wave analysis of the respective surface elevation data. In Sec. 7.6, the results of this evaluation are presented.

7.1 Wind Profiles

In Sec. 6.4, the evaluation of the PSV data is described. The resulting horizontal velocities are shown as histograms in Figs. 7.1 and 7.2. In the z-direction the bins have a width of 0.1 mm. Also shown are the 95% coverage intervals as well as the mean of the data points in the intervals.

The general shape of the histograms satisfies the expectation of logarithmic dependence on z with a linear component close to the water surface. It seems that the procedure adopted to eliminate the erroneous detections yields smooth and homogeneous distributions. The histograms can be compared with the histograms in Kühlein (2019), where measurements at the same wind conditions and similar fetches at the Lizard-tank were conducted. The same PSV and LHC setup was used there as well. Those measurements were evaluated with the old filtering procedure by Bopp (2018), resulting in holes and irregularities in the distributions caused by the filtering procedure and a non-optimal choice of the threshold streak length l_{thresh} (see also Sec. 6.4.1). As a consequence, the mean profiles exhibit bends in the region where the profiles should be linear according to the theoretical description, discussed in Sec. 2.2.1. Furthermore, lower PSV signal frequencies were applied at all wind conditions which also reduces the efficiency of the PSV algorithm. Finally, the pyranine concentration and the alkalinity of the water were different, inducing different surface detection efficiencies. And also, the issues with pyranine bleaching due to the UV laser and secondary particles were not present at the previous measurements. Therefore, a detailed comparison of the profiles from the previous study to the ones obtained here cannot be performed, only the overall shape and the shape at higher z_{shift} can be compared. The histograms in the z_{shift}-bins are seemingly tilted, the maximum value not being in the center of the 95% interval, resembling a skewed Gaussian distribution. The width of the histograms per z_{shift}-bin increased with increasing z_{shift} for low wind conditions. However, with increasing wind velocity, the width of the histograms close to the surface increases, probably because of the onset of waves. With increasing fetch, the overall width of the distributions per z_{shift}-bin increased, and with increasing wind generator setting, also the maximum wind speed in the bulk increased. All those general observations are in accordance with the measurements in Kühlein (2019).

As Kühlein (2019) applied only the PSV and the LHC methods, the occurrence of secondary particles did not pose a problem for his measurements. Still, in the immediate vicinity of the surface, the mean wind profiles deviate from the theoretical expectation.

Similar irregularities of the mean profiles in the vicinity of the surface occur in the profiles of this study, independent of the fetch. However, the cause of these irregularities is presumably different. At the low wind conditions (5 to 10 Hz), the high density of detections in the lowest 0 to 2 mm causes a bend in the linear region of the profile. At 15 Hz, this effect is smaller, but still visible. The two measurements at the highest wind condition, 20 Hz, show no increased density of detections at the surface. Probably due to the filtering procedure, the high fetch measurement shows even a distinct decrease in the number of detections at low u-values near the surface. Still, at both fetches, the mean wind profiles show better linearity in the boundary layer than the profiles at lower

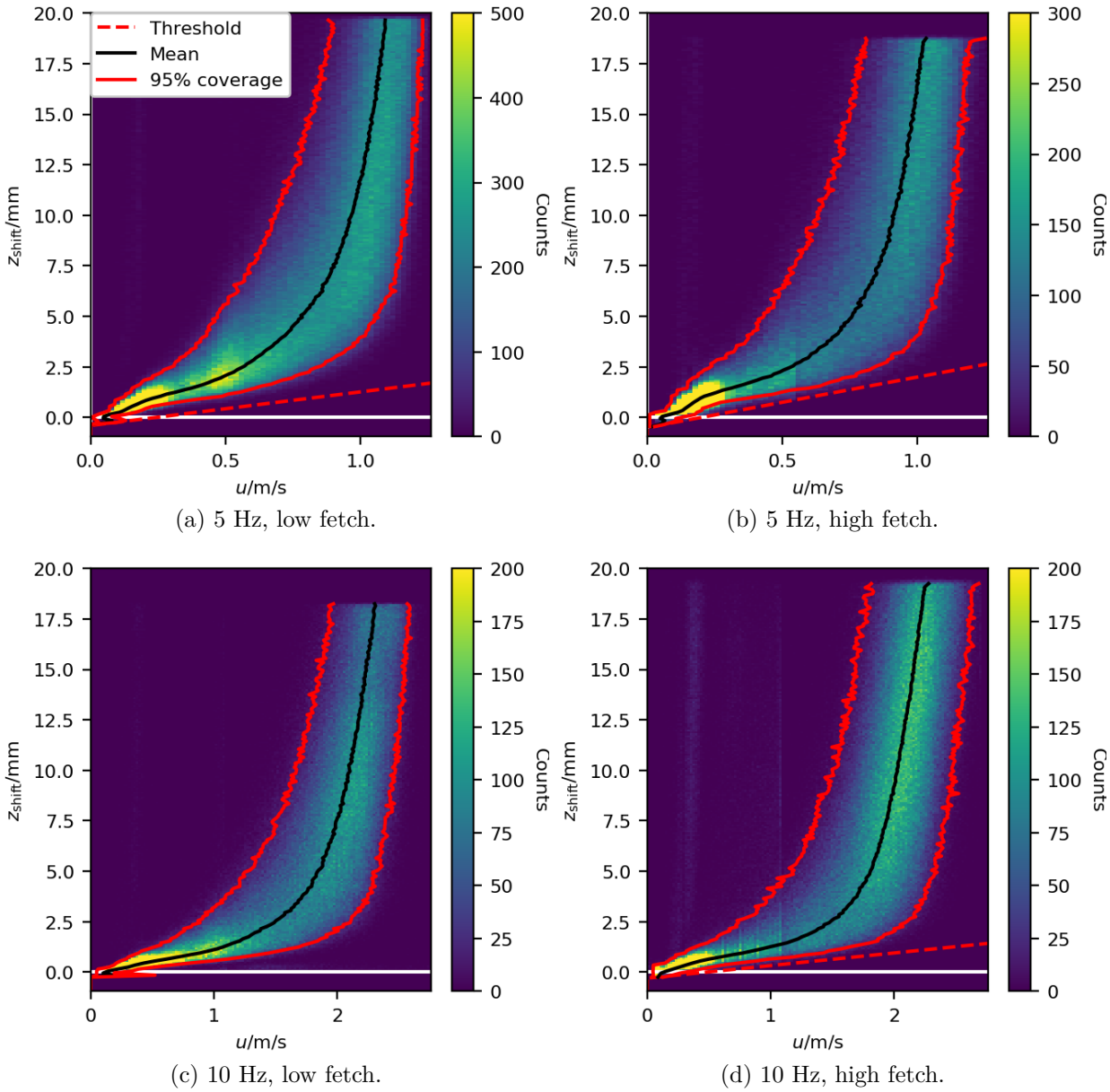

(a) 5 Hz, low fetch.

(b) 5 Hz, high fetch.

(c) 10 Hz, low fetch.

(d) 10 Hz, high fetch.

Figure 7.1: Histograms of the horizontal wind-speeds u for the height above the water surface z_{shift}, measured at the two lowest wind speeds at low fetch (a, c) and high fetch (b, d) in the fetch experiment. The water level ($z_{\text{shift}} = 0$) is marked with a white line, while the 95% coverage interval at each height bin as well as the mean of the interval are marked with red and black lines, respectively. In a few measurement conditions, where erroneous detections in the vicinity of or directly at the surface were not properly sorted out by the selection criteria described in Sec. 6.4.3, a threshold was applied to eliminate them. This threshold is marked by a red dashed line.

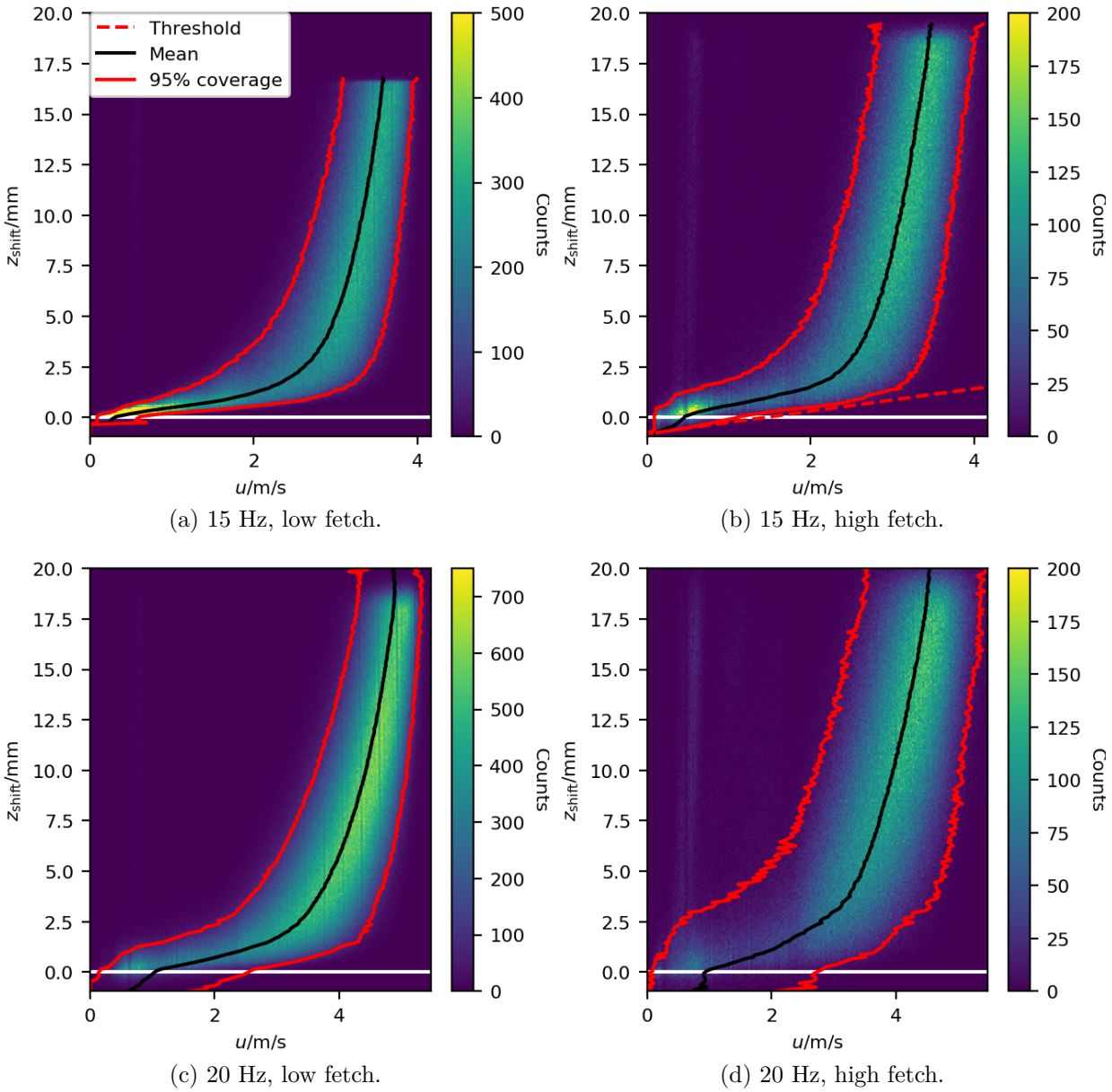

(a) 15 Hz, low fetch.

(b) 15 Hz, high fetch.

(c) 20 Hz, low fetch.

(d) 20 Hz, high fetch.

Figure 7.2: Histograms of the horizontal wind-speeds u for the height above the water surface z_{shift}, measured at the two highest wind speeds at low fetch (a, c) and high fetch (b, d) in the fetch experiment. The water level ($z_{\text{shift}} = 0$) is marked with a white line, while the 95% coverage interval at each height bin as well as the mean of the interval are marked with red and black lines, respectively. In a few measurement conditions, where erroneous detections in the vicinity of or directly at the surface were not properly sorted out by the selection criteria described in Sec. 6.4.3, a threshold was applied to eliminate them. This threshold is marked by a red dashed line.

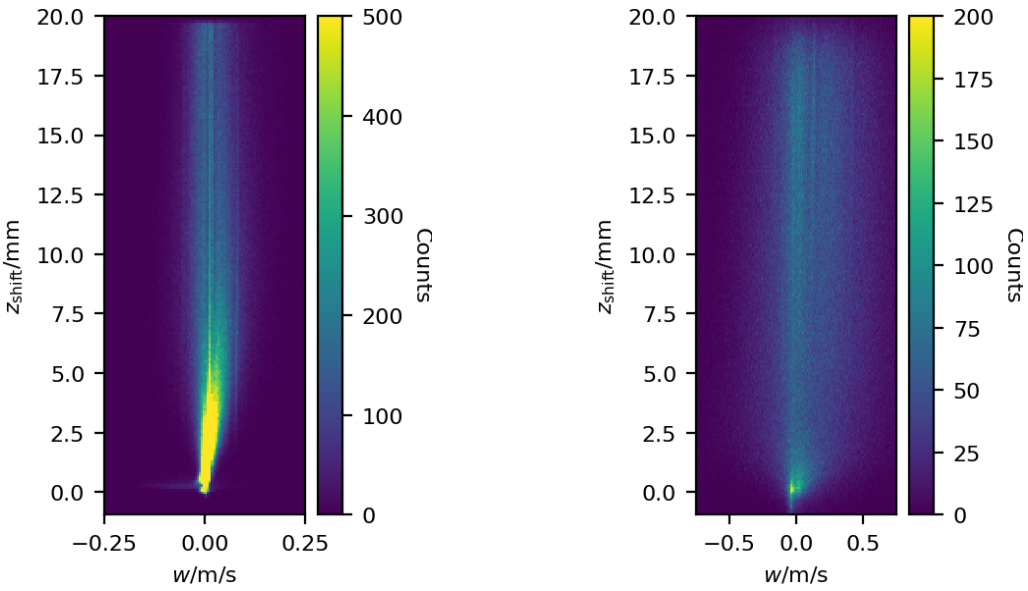

(a) 5 Hz, low fetch.

(b) 20 Hz, high fetch.

Figure 7.3: Histograms of the vertical wind-speeds w for the height above the water surface z_{shift}, measured (a) at the lowest wind speeds at low fetch and (b) at the highest wind speed at the highest fetch.

wind speeds. The influence of erroneous surface detections due to pyranine bleaching is difficult to estimate. Generally, the influence should be larger at lower wind speeds, as discussed in Sec. 6.3 and shown exemplary in Fig. 6.11.

To summarize these qualitative considerations: The general shape of the histograms and the mean wind velocity profile are in accordance with the expectations from theory and previous measurements. In the logarithmic layer, the measurements seem reliable and can be utilized in further analysis. However, in the vicinity of the surface, irregularities occur both in the histograms and the mean velocity profiles, caused by secondary particles, erroneous surface detection and the evaluation algorithm. Consequently, further work is needed to obtain reliable profiles in the viscous boundary layer.

Besides the horizontal wind velocities, the PSV algorithm also derives vertical wind velocities from the particle streak images. Examplarily, the resulting histograms from two measurements are plotted in Fig. 7.3. The mean vertical velocity vanishes at each height while the fluctuations grow with the height above the water surface.

7.1.1 Mean Wind Profiles

For better comparison of the mean profiles in all experimental conditions, they are shown together in Fig. 7.4, both with the z_{shift} axis in linear and logarithmic representation. As mentioned in the previous section, the general shape of the profiles is in accordance with the

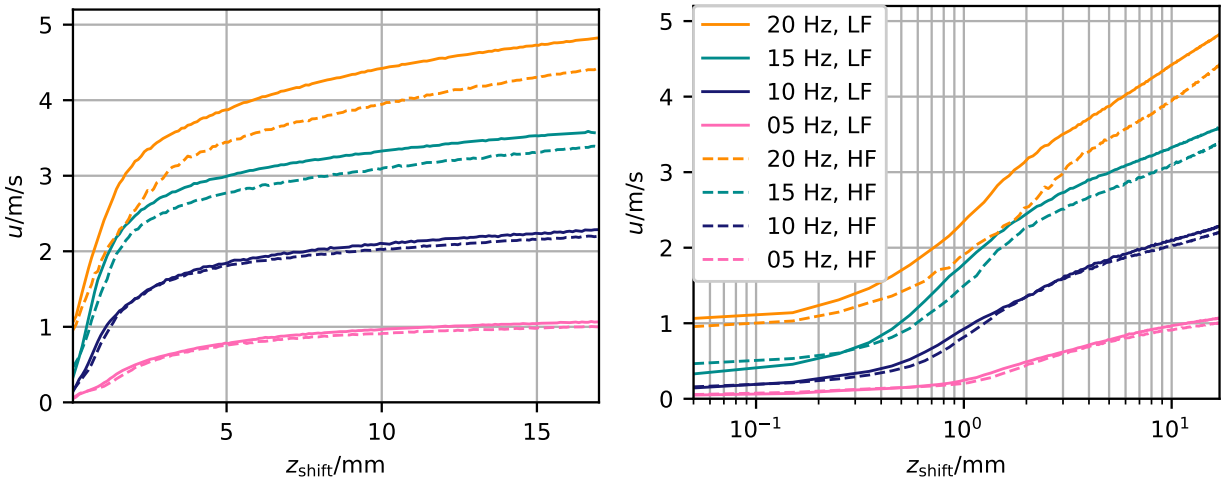

Figure 7.4: Mean wind velocity profiles from all eight measurements obtained from the fetch experiment, with the abscissa (a) in linear and (b) logarithmic representation. The results obtained at low fetch (LF) are shown by full lines, the ones at high fetch (HF) by dashed lines.

theoretical expectation, i.e. a linear shape close to the interface and a logarithmic profile farther away. All of the low wind profiles (5 to 10 Hz) show a deviation from the linear behavior in the viscous boundary layer due to the experimental difficulties.

In the plot, the fetch dependence of the mean wind profiles can be directly analyzed. For the lowest wind conditions, the profiles at the two fetches match very well, though the high fetch data lie a bit below the low fetch data. Still, this difference is in the range of the uncertainty of the mean wind values and could also be due to low statistics in some measurements.

For the higher wind conditions, it is apparent that the profiles from the high fetch measurements show lower velocities than the profiles at low fetch. This contradicts the wind profile measurements in Friedl (2013), where the maximum wind speed increases with the fetch. However, those measurements were conducted with a Pitot tube, which cannot be positioned to close to the water surface due to the risk of being hit by waves. Especially at high winds, this could lead to incorrect wind velocity estimates because the profiles do not extend down to the interesting part, the viscous boundary layer.

As the results of Kühlein (2019) also show slightly decreasing maximum wind speeds with the fetch for measurements at three fetches, the explanation might be found in the algorithm or in physical processes. Further studies with better statistics than in the measurements in this thesis and in the previous experiment are needed to resolve this issue.

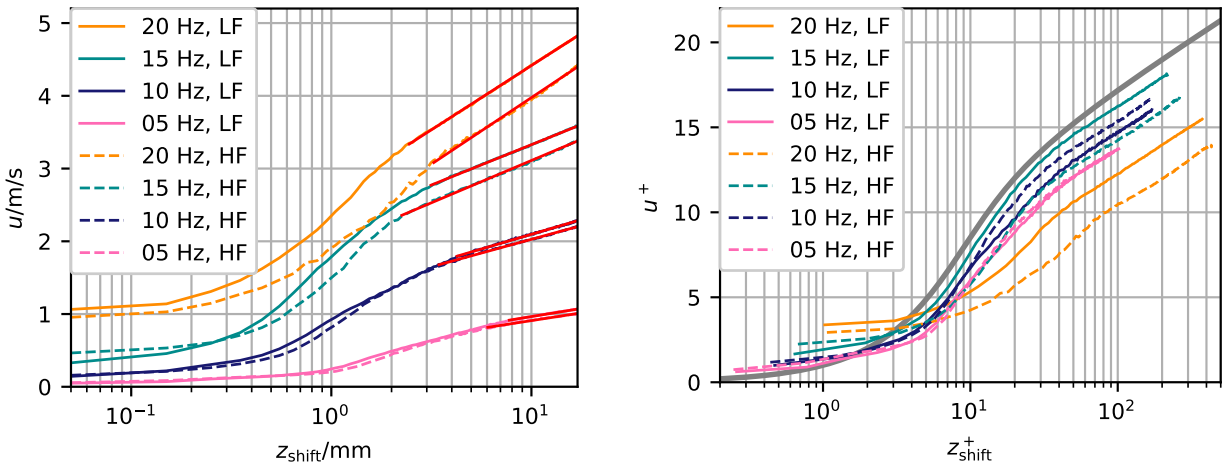

(a) (b)

Figure 7.5: Mean wind velocity profiles from all eight measurements at the Lizard-tank (a) with the corresponding logarithmic fits (red) and (b) in dimensionless coordinates, both with the abscissa in logarithmic representation. In (b), the function $u^+(z^+)$, Eq. (2.31), for the turbulent diffusion model is plotted as a thick gray line.

7.1.2 Friction Velocities

From the shape of the mean horizontal wind profiles and the implications discussed above, it is evident that the friction velocities from Friedl (2013) cannot be used in this study. Therefore, the friction velocities were determined from the mean wind profiles of this study. As described in Sec. 6.4.4, the mean wind profiles were fitted with a logarithmic function to obtain the friction velocities and the roughness lengths. Another possibility to obtain the viscous shear stress would be to use the gradient at the surface, see Eq. (2.25). However, this method is not applicable in the present context, since, as discussed in the previous section, the shape of the profiles in the viscous boundary layer are not reliable. The wind profiles and their logarithmic fits are shown in Fig. 7.5a with the abscissa in logarithmic representation.

In Figs. 7.6a and 7.6b, the two fit variables resulting from the fits are presented. The values are listed in Tab. A.2. The friction velocities do not show a clear fetch dependence, as the data for both fetches have similar values and their uncertainties overlap. This is in disagreement with the results of in Friedl (2013) (also shown in Fig. 7.6a) where the friction velocity increases with the fetch. Nevertheless, the overall shape is similar as the friction velocity increases with the wind generator frequency. The values obtained in this study lie between the ones of previous measurements. The dependence of the roughness length on the wind generator setting shown in Fig. 7.6b exhibits a characteristic shape, similar to a shifted parabola with a minimum around 13 to 14 Hz.

The roughness length as a function of the friction velocity is plotted in Fig. 7.6c. Fur-

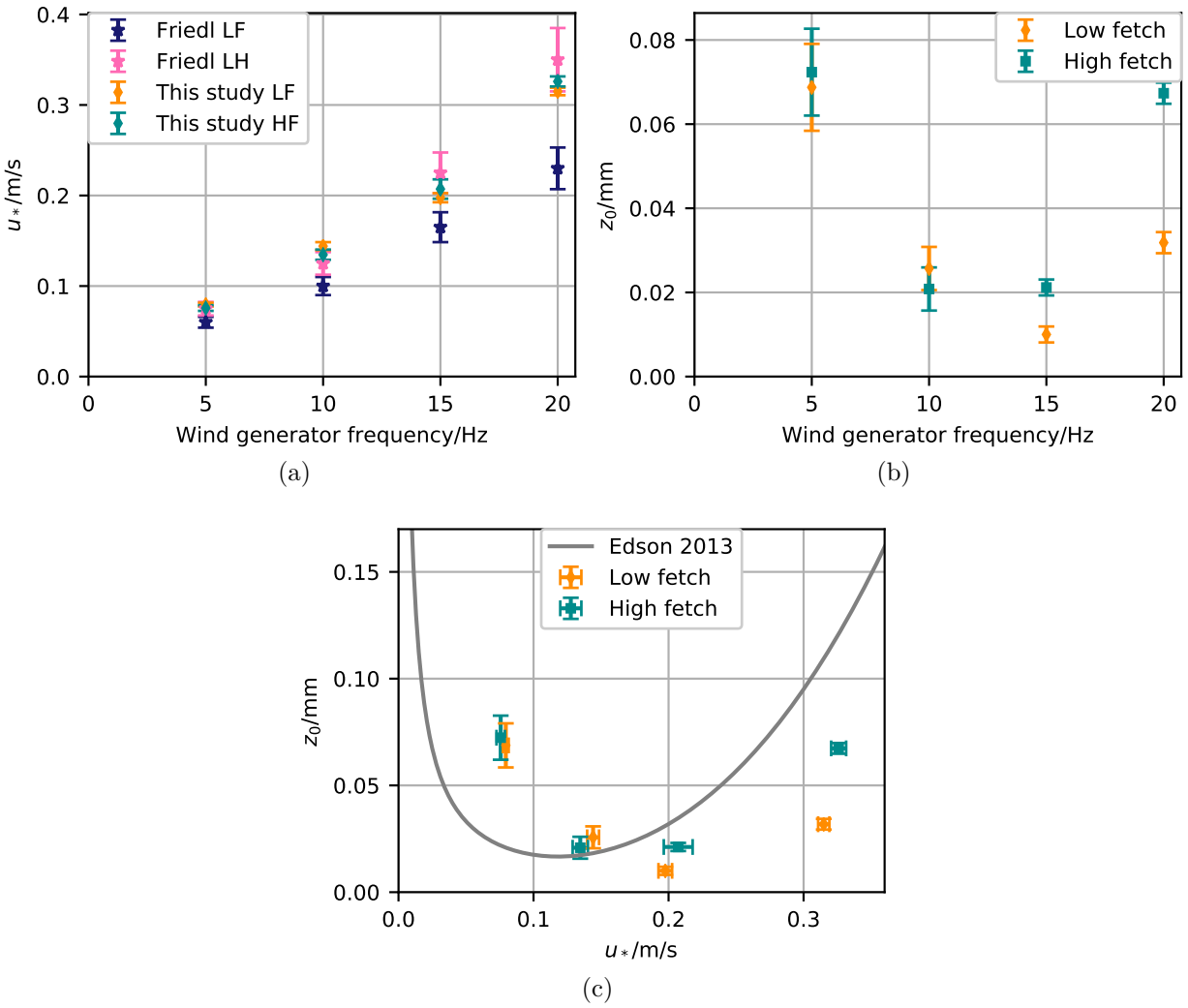

Figure 7.6: Results of the logarithmic fits of the mean wind profiles: (a) the friction velocities with data from Friedl (2013), and (b) roughness lengths. (c) The roughness length as a function of the friction velocity with a parametrization for $z_0(u_*)$ (gray) (Edson et al., 2013).

thermore, the following parametrization of $z_0(u_*)$ of Edson et al. (2013) is shown:

$$z_0 = 0.11\frac{\nu}{u_*} + \alpha_{\mathrm{Ch}}\frac{u_*^2}{g} \tag{7.1}$$

with the gravitational acceleration g and the Charnock coefficient α_{Ch}. The latter is given in a wind-dependent formulation as:

$$\alpha_{\mathrm{Ch}} = m_{\mathrm{Ch}}\, U_{10N} + b_{\mathrm{Ch}} \tag{7.2}$$

with the empirically determined parameters $m_{\mathrm{Ch}} = 0.0017\,\mathrm{m}^{-1}$ and $b_{\mathrm{Ch}} = -0.005$. Equation (7.1) consists of a smooth part (the first summand) and a wave part (the second

summand). The wind speed at 10 m height is adjusted to neutral conditions, U_{10N}, is calculated via the logarithmic wind profile, see Eq. (6.13) for $z = 10$:

$$U_{10N} = \frac{u_*}{\kappa} \ln\left(\frac{10}{z_0}\right) \tag{7.3}$$

As z_0, α_{Ch} and U_{10N} are interdependent, z_0 was calculated selfconsistently by an iteration in 50 steps.

The parametrization underestimates the data for $u_* < 0.1\,\mathrm{m/s}$ and overestimates the data for $u_* > 0.1\,\mathrm{m/s}$. This is explained by the fact that the parametrization was derived empirically from ship measurements on the ocean with much larger fetches than would be possible in the linear wind-wave tanks employed in this study. Therefore, the waves in the tanks are not comparable to those at similar wind conditions on the ocean and the overestimate of the roughness lengths at larger friction velocities is expected.

Still, the general shape is similar and also comparable to simulated data in Varlas et al. (2018). First a decrease to a minimum, then an increase again with increasing friction velocity. This characteristic shape is understood in terms of a thinning of the viscous boundary layer, causing a reduction of $z_0(u_*)$, followed by the onset of waves, which induces an increase of the roughness. This is in accordance with the observations that the first waves occur at the medium wind generator setting 15 Hz, implying that the wave regime starts here.

In Fig. 7.5b, the mean wind profiles are plotted in dimensionless coordinates, where the friction velocities obtained from the data are used. According to theory, see Sec. 2.2.1, the profiles should collapse onto the model curve, which is shown in the figure by the thick gray line, when using the dimensionless coordinates. The profiles generally lie below the curve but are relatively close, and the bend in the bridge layer between the linear and logarithmic profiles is approximately at the same position as in the model curve. The reason for the underestimation might be found in the PSV analysis procedure. Moreover, it is evident that the profiles measured at the highest wind deviate the most from the others, while the rest are relatively similar. This is probably also due to waves occurring at those wind speeds.

7.2 Global Transfer Velocities

Two of the four methods applied in this study to determine transfer velocities make use of the bulk concentration, i.e. the concentration in the well mixed layer above $z^+ = 50$. The absorbance, measured with a spectrometer, and the fluorescence in the bulk, deduced from the LIF images, were analyzed with the mass balance method. The resulting transfer velocities are plotted in Fig. 7.7, while the data obtained for the fetch experiment is listed in Tab. A.2. In the case of the Benjamin-tank, the data is plotted against the local friction velocities measured by Krah (2014), while for the fetch experiment, the friction velocities obtained from the logarithmic fits of the mean wind velocity profiles were averaged for the

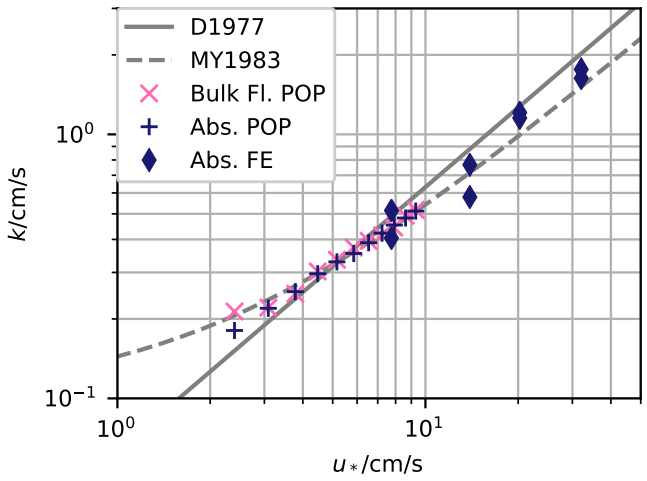

Figure 7.7: The transfer velocities as a function of the friction velocity, as measured with the bulk methods, in a double logarithmic plot: Absorbance (Abs.) and Bulk Fluorescence (Bulk Fl.). Crosses represent values measured during the proof-of-principle experiment (POP), while diamonds show results from the fetch experiment (FE). Also the parametrizations by Deacon (1977) (D1977) and Mackay and Yeun (1983) (MY1983) are plotted in gray. The bars representing the uncertainties in u_* and k were left out for better visualization. The uncertainties are around 10% for the fetch experiment (see Tab. A.2) and much smaller for the proof-of-principle experiment.

wind conditions. As globally averaged friction velocities were not available, the averaging over the data from two fetches was the best possibility to obtain an estimate of the globally averaged transfer velocity. Also, two parametrizations for the transfer velocity as a function of the friction velocity are shown: the model by Deacon (1977), see Eq. (2.53), and a model by Mackay and Yeun (1983):

$$k(u_*) = 0.1 + 46.2 \cdot 10^{-3}\, u_*\, Sc^{-2/3}. \tag{7.4}$$

To calculate the Schmidt number for SO_2, for the kinematic viscosity of air the value $\nu = 15.3\,\mathrm{mm^2/s}$ (Kadoya, Matsunaga and Nagashima, 1985) and for the Diffusion coefficient of SO_2 in air the value $D = 14.442\,\mathrm{mm^2/s}$ was calculated (Yaws, 2014). Thus, a Schmidt number of $Sc = 1.06$ was found.

Before interpreting the data, it should be noted that the transfer velocities from the two bulk methods are averaged over the water surface, while the friction velocities were measured locally. Thus, global values are compared to local values. However, the global transfer velocities as a function of the local (or averaged over the two fetches for the fetch experiment) friction velocities are in accordance with the parametrization by Mackay and Yeun (1983). The data from both experiments match and are consistent with a linear relation between u_* and k.

The global transfer velocities can be compared with field measurements conducted by Porter et al. (2020) at similar friction velocities. The values from the field study are lower than the ones obtained in this study. This is consistent with the expectation from Mackay and Yeun (1983) that measurements in the field might yield lower values for k than in the lab.

7.3 Concentration Profiles

The fluorescence images obtained from the LIF data were analyzed as described in Sec. 6.1. The procedure resulted in one instantaneous concentration profile per time step, i.e. 240000 profiles per measurement condition. This is different from the statistics of the PSV method where around 10-20 particle streaks per image were detected. Clearly this is not sufficient for extracting instantaneous wind profiles. This has to be kept in mind when comparing the data and analyzing the fluctuations, see Sec. 7.5. In Figs. 7.8 and 7.9, the concentration data from the eight different measurement conditions of the fetch experiment are shown: Single profiles from every minute are plotted exemplarily to visualize the fluctuating character of the single profiles, while the mean profile averaged over all 240000 measurements is shown in black. For a similar histogram depiction of the concentration as in Figs. 7.1 and 7.2 for the horizontal wind velocities, see Figs. A.6 and A.7.

The following qualitative observations are made: The maximum concentration in the bulk is similar in all measurements and characterizes the equilibrium between the adjusted influx of sulfur dioxide and the flux into the water. However, the bulk concentration is obtained from the absorbance as described in Sec. 6.1.1, and is thus not further evaluated here. With increasing wind, the fluctuations seem to decrease. This could be due to increasing frequencies of the eddies compared to the exposure time of the LIF camera, which is kept constant for all measurements, causing a reduction of the amplitude of the fluctuations due to smoothing. The fluctuations decrease towards the surface, which is expected as the wind profile is laminar in the viscous boundary layer. Also, the mean concentration profiles are smoother at higher wind speeds.

All the above observations can also be made on the so-called 'curtain' plots in Sec. A.3. There, a series of 1000 profiles is shown for every measurement condition. In that depiction, the decrease of the turbulent structure with increasing wind field is clearly discernible.

Since sulfur dioxide has a very high solubility at the pH value prepared for the measurements, the concentration should collapse to nearly zero with decreasing height above the surface. However, this layer could not be resolved in the experiment because the light from the water was disturbing the fluorescence signal from the sulfur dioxide in the air.

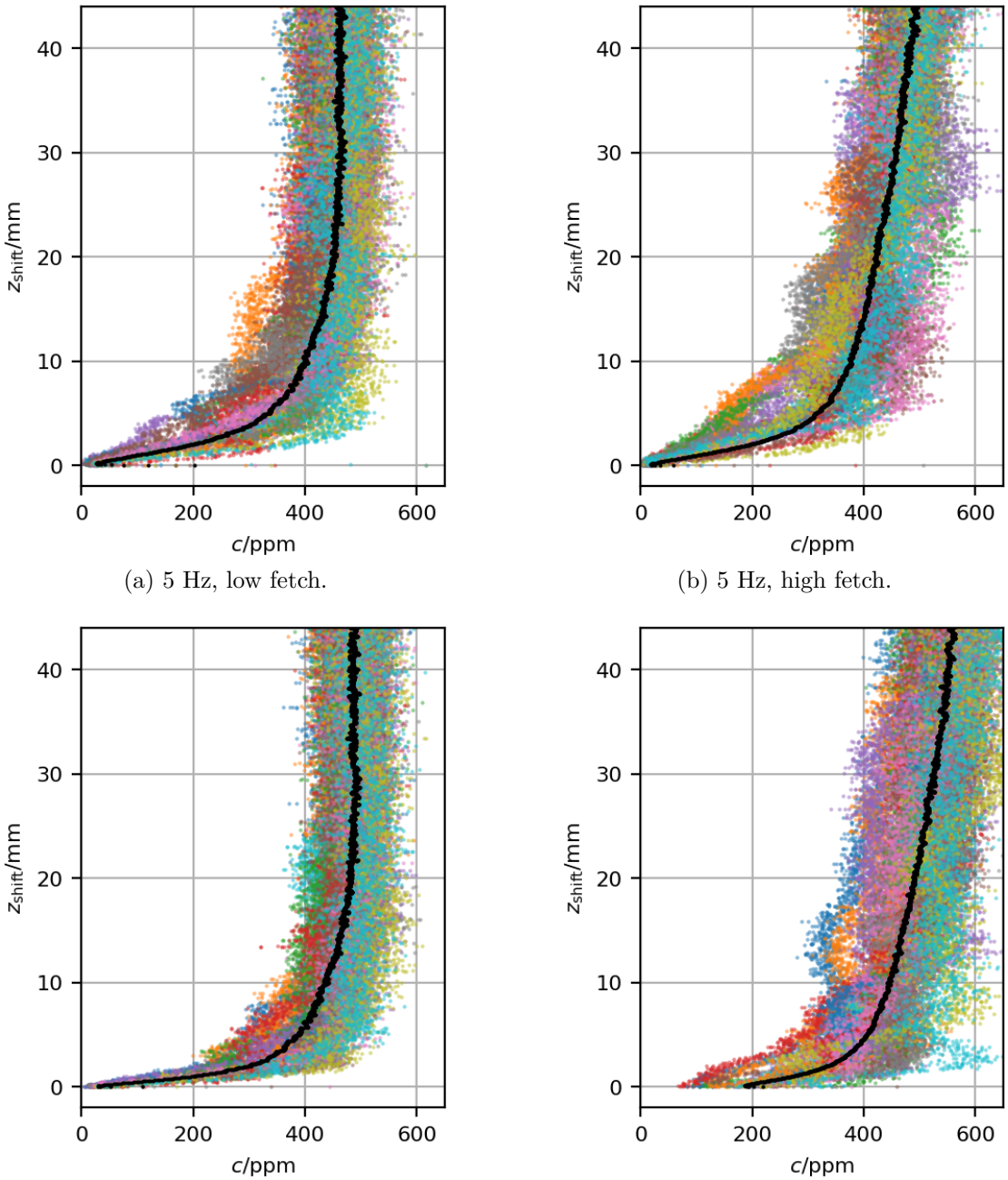

(a) 5 Hz, low fetch.

(b) 5 Hz, high fetch.

(c) 10 Hz, low fetch.

(d) 10 Hz, high fetch.

Figure 7.8: Concentration profiles from every minute, measured at the two lowest wind speeds at low fetch (a, c) and high fetch (b, d) from the fetch experiment. The profile in black represents the average over all 240000 profiles (equal to 20 minutes of measurement). The different colors represent single profiles.

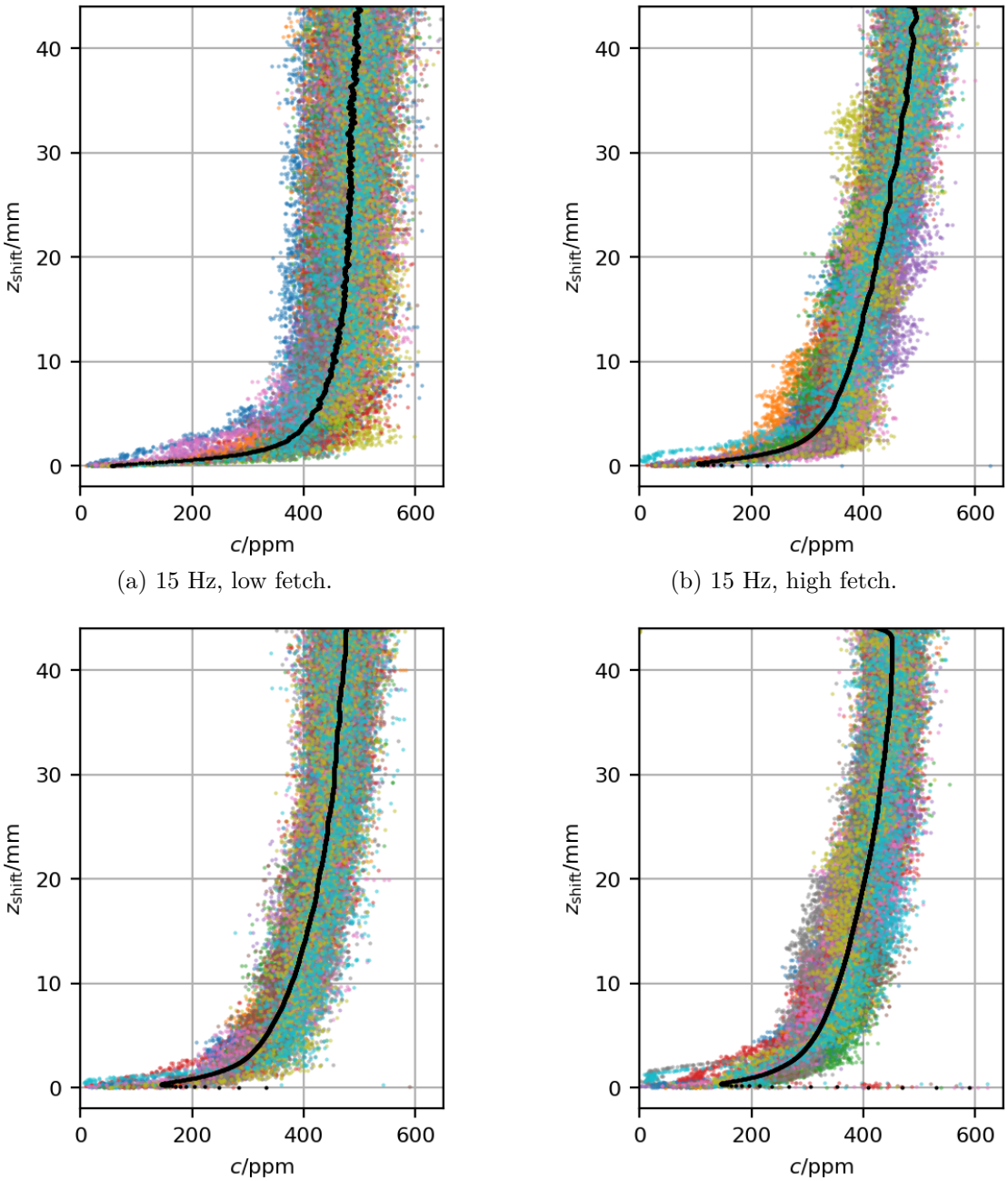

(a) 15 Hz, low fetch.

(b) 15 Hz, high fetch.

(c) 20 Hz, low fetch.

(d) 20 Hz, high fetch.

Figure 7.9: Concentration profiles from every minute, measured at the two highest wind speeds at low fetch (a, c) and high fetch (b, d) from the fetch experiment. The profile in black represents the average over all 240000 profiles (equal to 20 minutes of measurement). The different colors represent single profiles.

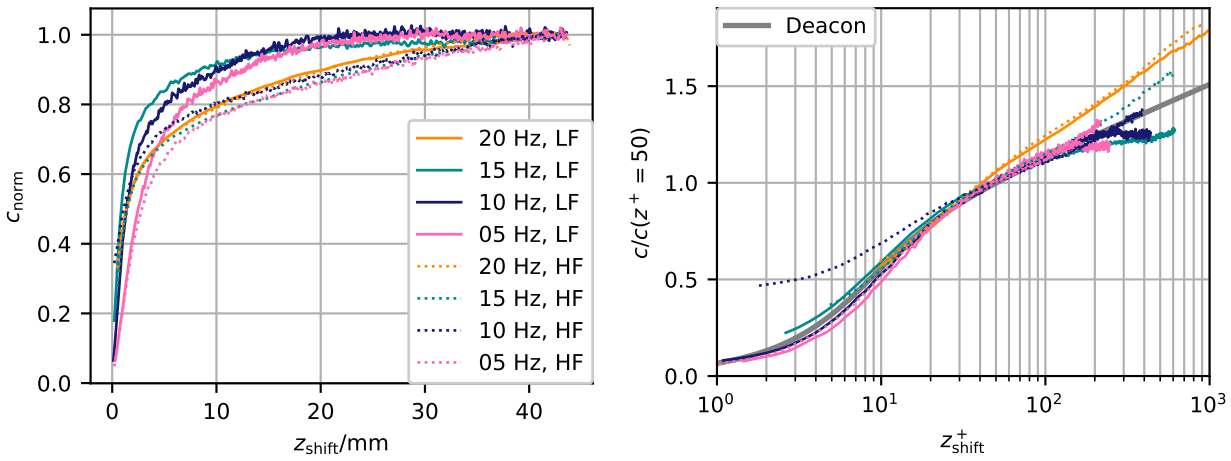

(a) (b)

Figure 7.10: Mean concentration profiles from all eight measurements of the fetch experiment, with the abscissa (a) in linear and (b) in logarithmic representation. The results obtained at low fetch (LF) are plotted as a full line, the ones at high fetch (HF) as a dotted line. In (b), the abscissa is in dimensionless coordinate z^+, defined using the friction velocities deduced from the wind profiles. Also shown by the gray thick line is the result of the turbulent diffusion model. The concentration is in (a) normalized by the concentration at the 20 topmost pixels and in (b) by the bulk concentration at $z^+_{\mathrm{shift}} = 50$.

7.3.1 Mean Concentration Profiles

The mean concentration profiles from every condition in the fetch experiment, which are shown in black in Figs. 7.8 and 7.9, are plotted together in Fig. 7.10. In Fig. 7.10a, the concentrations are normalized by the concentration averaged over the top 20 pixels. This representation enables the evaluation of the bulk transport: already in Figs. 7.8 and 7.9, it was evident that the profiles from the low wind conditions at low fetch show a different shape than the ones at higher fetch and higher wind. For the first set of profiles, a nearly constant bulk concentration is reached at around $z_{\mathrm{shift}} = 20\,\mathrm{mm}$ for the low wind conditions, while all high fetch profiles and the profile from the measurement at 20 Hz at low fetch increase continuously in the FOV. The reason for this is so far not understood.

In Fig. 7.10b, the abscissa is the dimensionless $z^+_{\mathrm{shift}} = z_{\mathrm{shift}} u_* / \nu$ and is plotted in logarithmic scale. The concentration is here normalized by the bulk concentration at $z^+_{\mathrm{shift}} = 50$. From the turbulent diffusion model, which was used to fit the mean concentration profiles in Sec. 6.1.3, it was expected that the profiles in dimensionless coordinates would match, all having the same shape, namely Eq. (2.51). This function is shown in the figure in gray. All profiles except three follow the model curve for $z^+_{\mathrm{shift}} < 100$. The three outliers consist of the two highest wind measurements at both fetches and the high fetch measurement at the second lowest wind condition. The latter varies from the theoretical curve only in the

boundary layer region which can be understood in terms of light emitted from the dye in the water degrading the fluorescence signal close to the surface. As was the case for to the wind velocity profiles, the two measurements at the highest wind conditions deviate from the others. An explanation could be found in the onset of waves at those wind conditions. This issue was discussed in more detail in Sec. 7.1.

The shape of the mean concentration profiles in the bulk region, above approximately $z^+_{\text{shift}} = 100$, begin to deviate. This could be due to the onset of the wake part of the profile. According to the models, the turbulent layer extends to around $z^+ = 10^4$, but the limited height of the tank restricts the wind field. Consequently, the deviations might be caused by the limited height of the tank.

7.3.2 Local Transfer Velocities

From both the mean and the single concentration profiles, local transfer velocities were obtained. The mean profiles were fitted with both a polynomial function and the Deacon model function (see Sec. 6.1.3), while the single profiles were only fitted with the polynomial function because the Deacon model is valid only under stationary conditions (see Sec. 6.1.3). This was done for both experiments.

The following notation is introduced for the local fit methods: PM stands for transfer velocities obtained from fits of the mean profiles with the polynomial function and DM for transfer velocities obtained from Deacon model fits to the mean profiles, while PS denotes k's obtained by averaging over the transfer velocities obtained by fitting single profiles from one measurement with the polynomial function.

The results from the mean profile fits are shown in Fig. 7.11a together with the parametrizations by Deacon (1977) and Mackay and Yeun (1983). The data from the proof-of-principle experiment is underestimated by the models, while the data from the fetch experiment spread evenly around the parametrizations. Interestingly, the Deacon fit yielded smaller values relative to the values from the polynomial function for the proof-of-principle data, with the opposite trend for most of the fetch experiment data.

In Fig. 7.11b, the transfer velocities resulting from averaging over 1000 measurements in the case of the proof-of-principle experiment and 12000 in the case of the fetch experiment, which were obtained from single profile fits, are plotted. Again, the parametrizations underestimate the proof-of-principle data, while the data from the fetch experiment is distributed around the model functions. The transfer velocities obtained for the fetch experiment with all three fit methods is given in Tab. A.2.

The uncertainties were omitted in Fig. 7.11a because they were negligibly small, but can be found in Tab. A.2 for the fetch experiment data. In the second figure, the standard deviations of the single, instantaneous transfer velocities are shown as error bars. As expected, they are much larger for the fetch experiment because the exposure times were shorter. Longer exposure times induce averaging over a larger number of turbulent eddies and smoothing of the profiles.

Furthermore, the error bars grow with the increasing friction velocity. For the highest wind speeds they are even larger than the mean values. This is probably not due to a

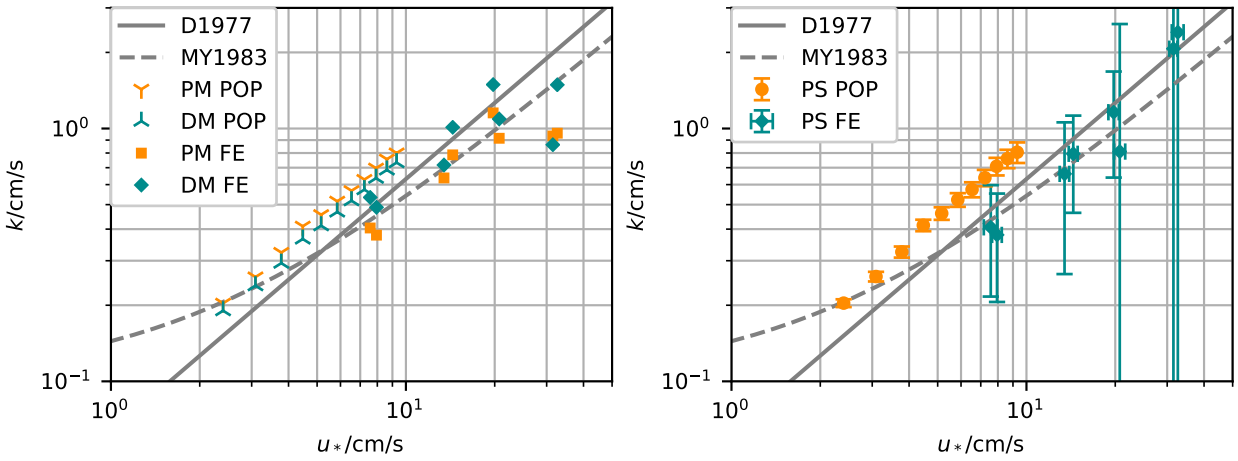

Figure 7.11: The local transfer velocities as a function of the local friction velocity, in double logarithmic plot: from (a) mean profile fits and (b) single profile fits. The mean profiles were fitted with the Deacon model (DM) and the polynomial function (PM), while the single profiles were only fitted with the polynomial function, where the mean of the single transfer velocities is plotted here (PS). POP stands for proof-of-principle experiment and FE denotes the fetch experiment. Also the parametrizations by Deacon (1977) (D1977) and Mackay and Yeun (1983) (MY1983) are plotted in gray. In (a), the uncertainties of u_* and k were suppressed for better visualization. The uncertainties are less than 5%. In (b), the vertical uncertainty bars represent the standard deviations of the single transfer velocities.

physical reason but to the fact that light from the fluorescence in the water distorted the lower parts of the fluorescence profiles and induced a reduction of the fit ranges, which were already narrow due to higher winds and thinner boundary layers. Using fewer pixels for the fit increases the uncertainties of the estimated parameters.

Still, the mean values of the instantaneous transfer velocities match reasonably well with the model functions and the values obtained by the mean profile fitting. Actually, for the measurements obtained at the highest wind speeds, the transfer velocities obtained from the fits to the single profiles agree better with the model functions than the values deduced from the mean fits. This is not expected, since the mean concentration profiles of these two measurements in dimensionless coordinates deviate from the other data (see Fig. 7.10b).

As the friction velocities from the eight measurements at the Lizard-tank do not show a fetch dependence, the same is expected for the transfer velocities, since according to the transfer models (see Sec. 2.3) the transfer velocities should be proportional to the friction velocities. Figure 7.12 shows the local transfer velocities obtained in the fetch experiment. It is evident that the data is consistent with the models and no clear fetch dependency

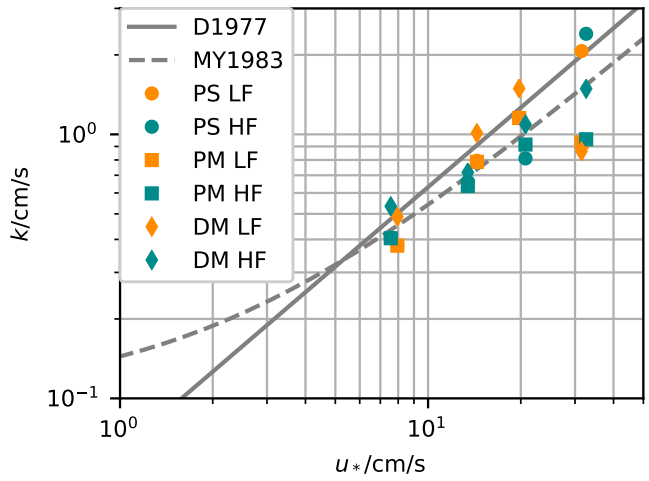

Figure 7.12: The local transfer velocities from the fetch experiment as a function of the local friction velocity, in double logarithmic scale: The mean profiles were fitted with the Deacon model (DM) and the polynomial function (PM), while the single profiles were only fitted with the polynomial function (PS). LF stands for low fetch and HF for high fetch. The parametrizations by Deacon (1977) (D1977) and Mackay and Yeun (1983) (MY1983) are plotted in gray. The bars representing the uncertainties in u_* and k were left out for better visualization. The same data is shown as in Fig. 7.11, with the marker color denoting the fetch.

is visible in the graphs. Contrary to the measurements by Kunz and Jähne (2018), who observed an overshoot of the water-sided part of the heat transfer velocity at low fetches, no fetch effects are found here for the air-side controlled transfer.

The ability of the fit algorithm to determine instantaneous transfer velocities from single concentration profiles is assessed by comparing the spread of the single transfer velocities around the mean value with the uncertainty of the mean value. This is shown in Fig. 7.13, where two histograms of single transfer velocity measurements in each experiment are shown. The uncertainty is illustrated with a Gaussian distribution with a width of the average uncertainty of the single fits. In both cases, the mean fit uncertainty is smaller than the width of the histogram. Consequently, the single fit algorithm yields reliable instantaneous transfer velocities for both experiments. The data shown in Fig. 7.13 is representative for the other measurements. The conclusions made above are valid for all measurements.

Even though the measurements in Fig. 7.13 were conducted under similar wind conditions with comparable friction velocities, the width and the shape of the histograms differ. This is probably due to better statistics and shorter exposure times in the fetch experiment.

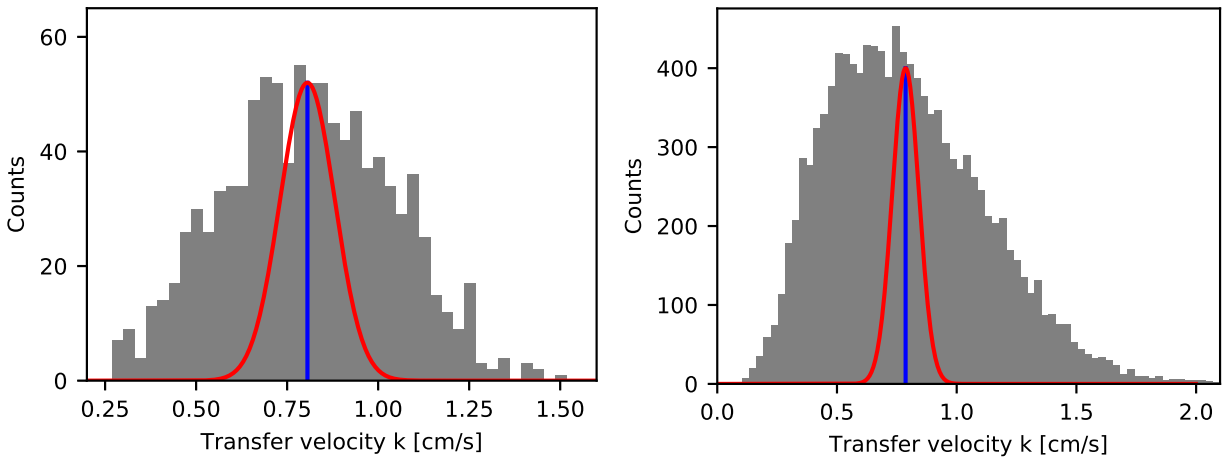

(a) (b)

Figure 7.13: Transfer velocities resulting from the single profile fitting from both experiments, shown in histograms: (a) 1000 transfer velocities from the highest wind condition of the proof-of-principle measurement ($u_* = 9.3\,\mathrm{cm/s}$) and (b) 12000 transfer velocities from the second lowest wind condition at low fetch of the fetch experiment ($u_* = 13\,\mathrm{cm/s}$). The mean values are marked with a vertical line. Gaussian distributions with a width equal to the mean fit uncertainty of the single fits are plotted in red. Note the different scales on the horizontal axis. Figure (a) was published in Friman and Jähne (2019).

7.3.3 Comparison of Local and Global Transfer Velocities

In Fig. 7.14a, the transfer velocities obtained with all four methods are shown. It is evident that all values match both model functions. A different depiction where the global and local methods are separated by color, is shown in Fig. 7.14b. In this depiction, it is evident, that the global methods coincide with the parametrization by Mackay and Yeun (1983), while the local methods do not show a clear preference for either of the two proposed parametrizations.

Moreover, the data from the proof-of-principle measurement show a different tendency. The interpretation that the locally measured transfer velocities overestimate the results averaged over the whole water surface is invalidated by the data from the fetch experiment which is plotted against mean friction velocities obtained by averaging over values from two fetches. For a detailed analysis of this issue, globally averaged friction velocities would be needed.

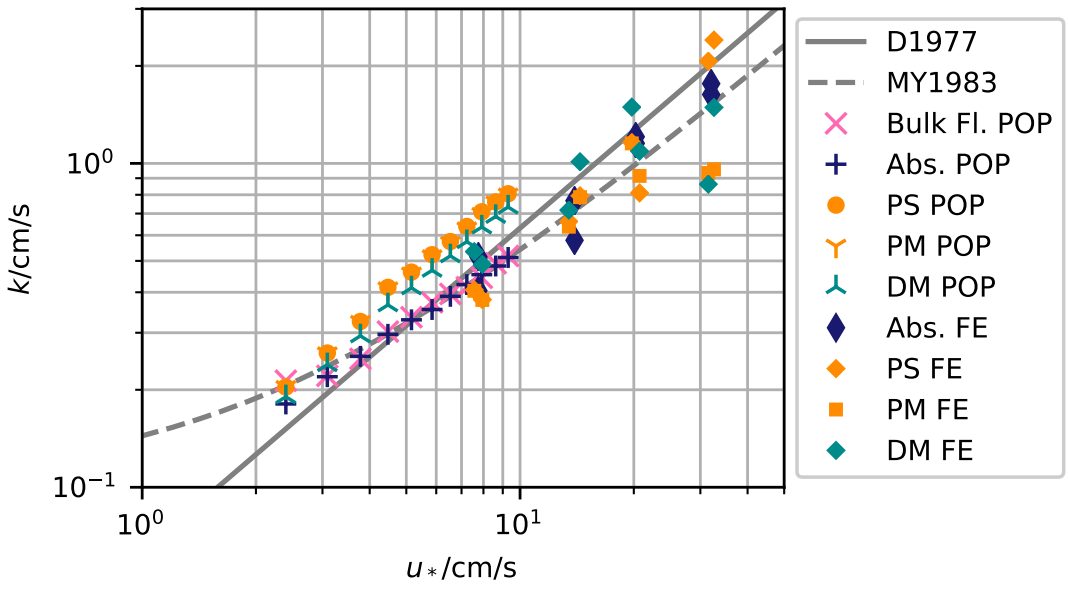

(a)

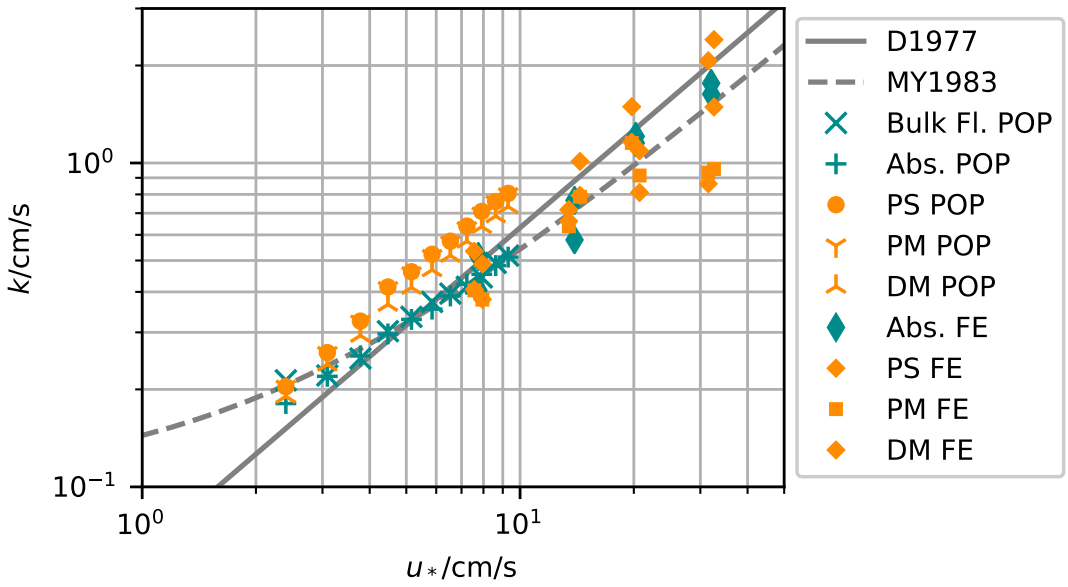

(b)

Figure 7.14: The transfer velocities obtained with all four techniques in the proof-of-principle (POP) and fetch experiments (FE): Bulk fluorescence (Bulk Fl.), absorbance (Abs.), polynomial fit (mean: PM, and single: PS) and Deacon model fit (DM). Also the parametrizations by Deacon (1977) (D1977) and Mackay and Yeun (1983) (MY1983) are plotted in gray. In (a), the color code matches the method (see legend), while in (b), the global methods are marked in orange and the local methods in petrol.

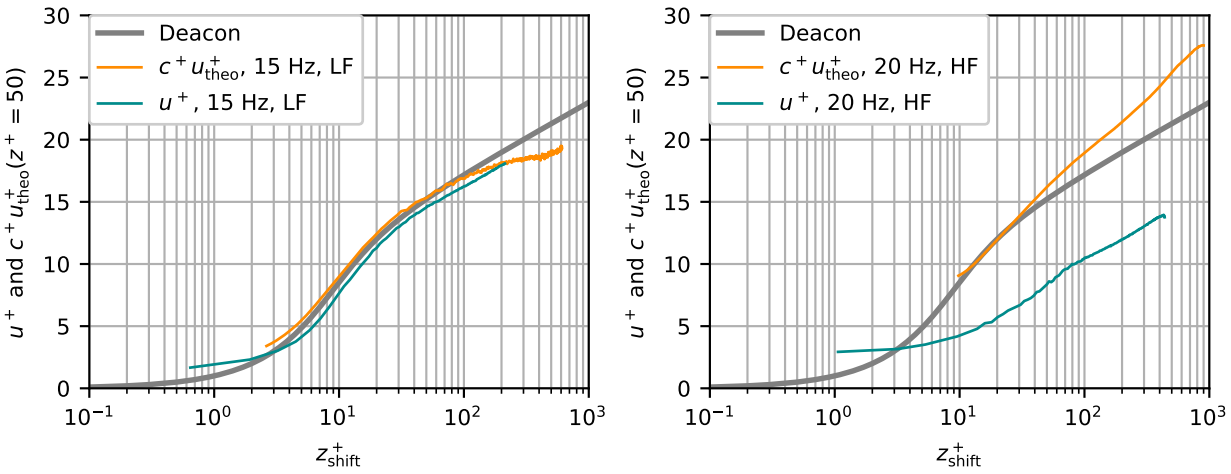

(a) (b)

Figure 7.15: Mean concentration and horizontal wind profiles from two measurements, (a) the second highest wind condition at low fetch and (b) the highest wind condition at high fetch, in dimensionless coordinates. The dimensionless concentration c^+ is multiplied with the model bulk value at $z^+ = 50$, as given in Eq. (7.5).

7.4 Comparison of Mean Concentration and Wind Profiles

The mean wind and concentration profiles have been evaluated separately and were discussed in Secs. 7.1.1 and 7.3. They match the prediction of the turbulent diffusion model reasonably well, with the exceptions of the data from the two highest wind speeds. In dimensionless coordinates, the model functions describing $c^+(z^+)$ and $u^+(z^+)$ are given by Eqs. (2.31), (2.51) and (2.52). If the Schmidt number is nearly one, as is the case for sulfur dioxide, it can be set to one. The aim is to examine whether $c^+(z^+) = (c(z^+) - c_s)/c_b = (u(z^+) - u_s)/u_b$ is valid for the data. Since $u^+(z^+) = (u(z^+) - u_s)/u_*$, c^+ needs to be normalized with the bulk wind speed in dimensionless coordinates, $u_b^+ = u_b/u_*$,

$$c^+(z^+)\, u_b^+ = u^+(z^+). \tag{7.5}$$

In Fig. 7.15, two exemplary data sets are shown with the proper normalization. Fig. 7.15a shows the dimensionless mean concentration and wind profiles from the measurement at the second highest wind condition at low fetch as an example for data which matches the model curve well. By contrast, in Fig. 7.15b the corresponding data from the measurement at high wind and high fetch is plotted, where both mean profiles deviate from the theoretical profile. The concentration data lies above the theoretical curve, while the wind data lies mostly below. More measurements at high wind conditions are necessary to find an explanation for this finding.

From both the wind and the concentration profiles, the parts close to the surface which are under influence of light from the water were removed. It is evident that close to the

surface the PSV method has a better resolution than the LIF method. This is because the LHC surface measurement disturb only the LIF images due to the long exposures and the filter which did not absorb all of the fluorescence light from the pyranine in the water.

The observation that some mean concentration profiles reach a plateau above around $z^+_{\text{shift}} = 100 - 200$ cannot be correlated with the wind profiles because the FOV of the PSV camera was smaller than the one of the LIF camera, cutting off the interesting part where the flattening occurs (see Fig. 7.15a).

7.5 Fluctuation Evaluation

In this section, the fluctuations of the concentration profiles as well as of the wind vectors deduced from the PSV method are discussed. The fluctuations c', u' and w' were calculated by subtracting the mean value at the corresponding height from each measured value. The u fluctuations correspond to the width of the histograms in Figs. 7.1 and 7.2.

7.5.1 Mean Fluctuations

In Figure 7.16, the root mean square (corresponding to the absolute mean value) of the fluctuations c', u' and w' per height bin are plotted for every measurement of the fetch experiment against the dimensionless height above the surface z^+_{shift}.

The plot of the concentration fluctuations shows an interesting feature: all profiles have a maximum at approximately the same position. The position interestingly is very close to $z^+ = 11.7$ which is the theoretical boundary layer thickness. However, especially for the measurements at high winds, the influence of the light from the dye in the water disturbs the profiles. This is the case, even though the plot is already limited to the part where the concentration values were deemed reliable. Nevertheless, the maximum has a similar value in all profiles.

A similar observation is made in Fig. 7.16b where the mean absolute velocity fluctuations in wind direction are shown. The plots exhibit a maximum at around the same position. Here, the normalized fluctuation amplitude increases with the wind and the fetch. However, the profiles from the highest wind speeds are again anomalous as expected, exhibiting a decrease of the fluctuations relative to the second highest wind speed around the boundary layer thickness.

Figure 7.16c shows the mean absolute fluctuations in the vertical wind velocity. Again, the profiles show maxima at the same z^+_{shift} position, however at a larger height, around $z^+_{\text{shift}} \approx 60 - 80$. The amplitude again increases with the wind and the fetch, just as for u', with the known exception of the two measurements at the highest wind speed. Towards the surface, all profiles decrease to zero, except for the highest wind conditions which have an offset. This is probably again due to waves and secondary particles, disturbing the detections and the evaluation algorithms.

The measured wind fluctuation profiles are consistent with wind tunnel measurements

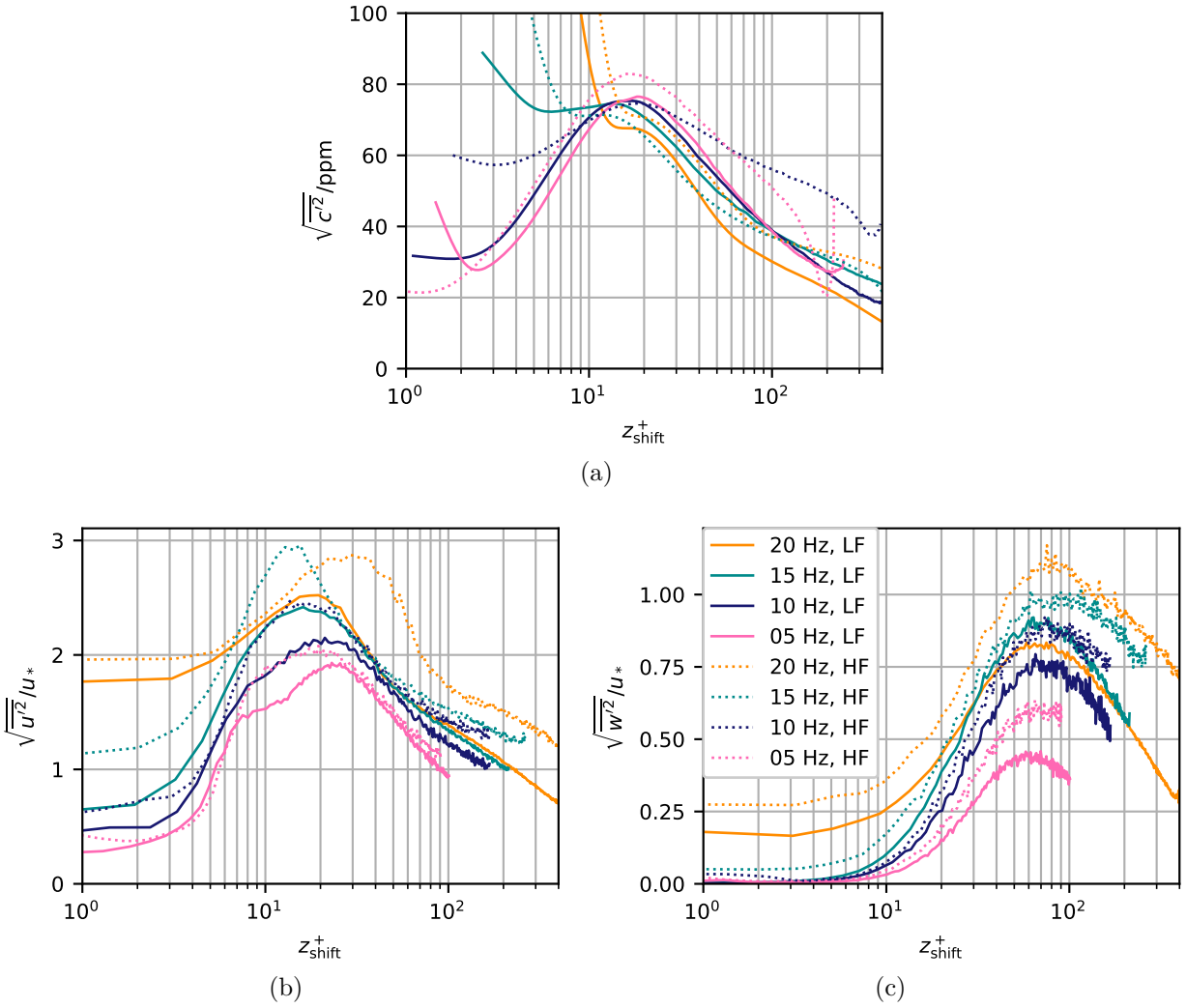

Figure 7.16: Root mean-square deviations of the (a) concentration, (b) horizontal and (c) vertical wind profiles, for all eight measurement conditions. The abscissa is dimensionless, while the ordinates in the for the two wind components are normalized by the friction velocities.

conducted by Laufer (1954) and Klebanoff (1955). Furthermore, c' measurements in water show similar characteristic profiles, where the maximum of the fluctuations is also positioned approximately at the boundary layer thickness, too: see for example Münsterer (1996), Herlina and Jirka (2008) and Friedl (2013).

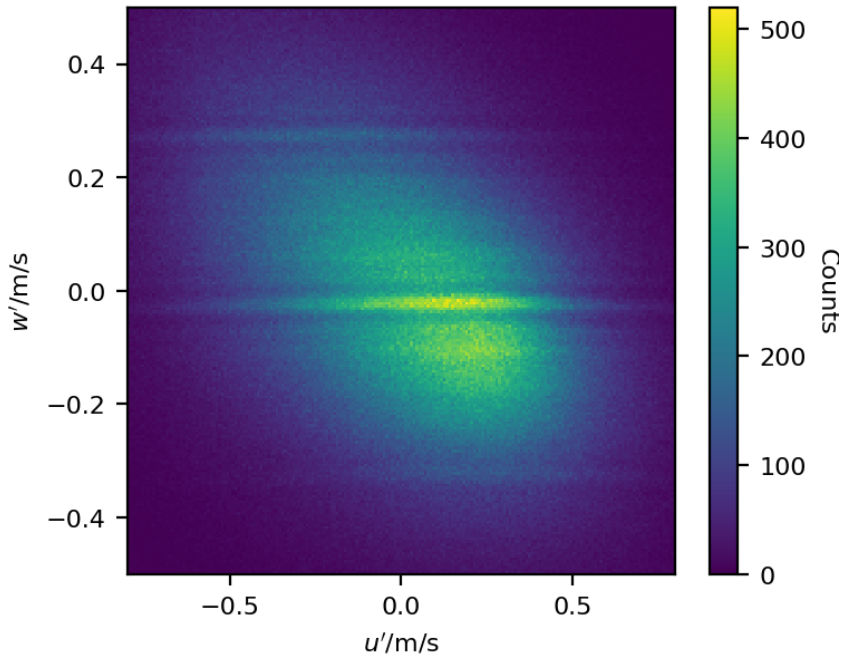

Figure 7.17: Histogram of the horizontal wind fluctuations versus the vertical wind fluctuations, for $z^+_{\text{shift}} > 50$, from the measurement at the highest wind speed at low fetch. The reason for the horizontal stripes is unknown. They may be an artifact of the particle detection, the streak fitting or the selection algorithm.

7.5.2 Fluctuation Correlation

The turbulent shear stress is defined as $\tau_{\text{turb}} = -\rho\overline{u'w'}$. The total shear stress is the sum of the viscous shear stress (in the viscous layer) and the turbulent shear stress (above of the viscous layer). Thus, from the horizontal and vertical wind velocity fluctuation above the viscous layer, the friction velocity can be calculated via Eq. (2.23).

In Fig. 7.17, u' and w' are plotted from the measurement at the highest wind speed at low fetch, for $z^+_{\text{shift}} > 50$. It is evident that a correlation exists as the histogram shows a tilted profile, i.e. negative fluctuations in u are correlated with positive values of v' and vice versa. Also the Pearson correlation coefficient of the data is -0.32. This agrees with the theoretical expectation that the correlation is negative when the momentum flux is directed downwards towards the water. The mean value of the product is $\overline{u'w'} = -0.034\,\text{m}^2/\text{s}^2$. Thus, the resulting value for the friction velocity is $u_* = 0.18\,\text{m/s}$, which is less than the value obtained from the logarithmic fit to the mean horizontal wind profile, $u_* = 0.31\,\text{m/s}$. In Sec. A.7, friction velocities as derived from the wind fluctuations of all measurements are presented.

By selecting only the streaks that cross the UV laser beam and calculating the concentration fluctuation at the corresponding heights, c' and w' can also be compared. They are

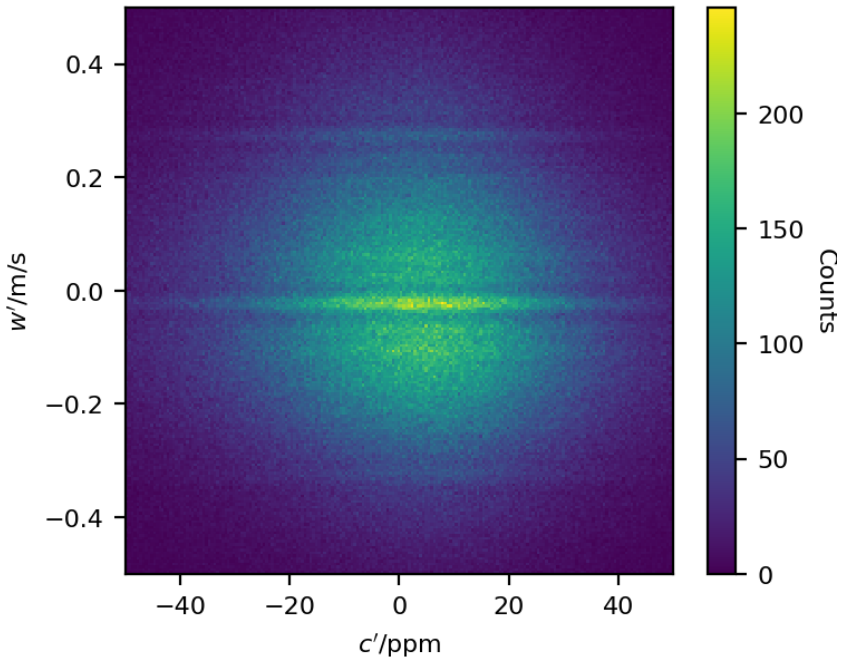

Figure 7.18: Histogram of the horizontal wind fluctuations versus the vertical wind fluctuations, for $z^{+}_{\mathrm{shift}} > 50\,\mathrm{mm}$, from the measurement at the highest wind speed at low fetch. The reason for the horizontal stripes is unknown. They may be an artifact of the particle detection, the streak fitting or the selection algorithm.

plotted in Fig. 7.18 for the same measurement as in Fig. 7.17. Shown there is the measurement where the largest number of particles were released into the channel and thus also detected. Still, the statistics are not sufficient to derive flux profiles. However, the mean of the correlation can be calculated and yields for this measurement $\overline{c'w'} = -0.23\,\mathrm{ppm\,m/s}$. No correlation is evident from the histogram, which is confirmed by a very low Pearson correlation coefficient of only -0.017. The value obtained by averaging over all particles crossing the UV laser beam is negative, which is expected since also the mass flux should be directed downwards.

7.6 Phase Evaluation

For the measurements at the two highest wind conditions, the phase of the dominant wave at the position of the UV laser beam was derived (see Sec. 6.6). With this data, both the concentration profiles and the wind velocity data from the particle streaks crossing the UV laser beam were averaged according to the phase of the dominant wave at the corresponding x position. In Fig. 7.19, the resulting graphs are shown for the highest wind condition at high fetch where the waves as well as the effects were largest. The mean wave height is marked in red. The very bright region directly at the surface in the wave trough in Fig. 7.19a is not a real concentration but the remnant from the surface illuminance which disturbed the images. The disturbance is largest on the lee side of the wave.

As the mean horizontal wind and concentration match and the mass and momentum transfer is analog in air, it is expected that the corresponding phase diagrams look similar. That this is the case as can be seen in Figs. 7.19a and 7.19b. Both show the same characteristic shape of the boundary layer, which is thinner on the windward side of a wave and thicker on the lee side. It is evident that the statistics are poorer for the wind measurements as more noise is visible in the profiles. The phase averaged vertical wind velocity is also modulated with the waves. It follows the waves, as would be expected because air is essentially incompressible under the present conditions (Bopp, 2018). On the lee side, the wind is directed downwards, while on the windward side of the wave, it is directed upwards. The mean vertical wind averaged over all phases is zero, as was found above in Sec. 7.1. The maximum vertical wind speed is an order of magnitude smaller than the maximum horizontal wind speed.

The phase averaged fluctuations, i.e. the phase averaged deviations from the mean profile, for example $\widetilde{c'} = \overline{c'_\varphi}$ (φ being a certain phase interval), were calculated and are shown in Fig. 7.20. All values are positive on the wind ward side and negative on the lee side.

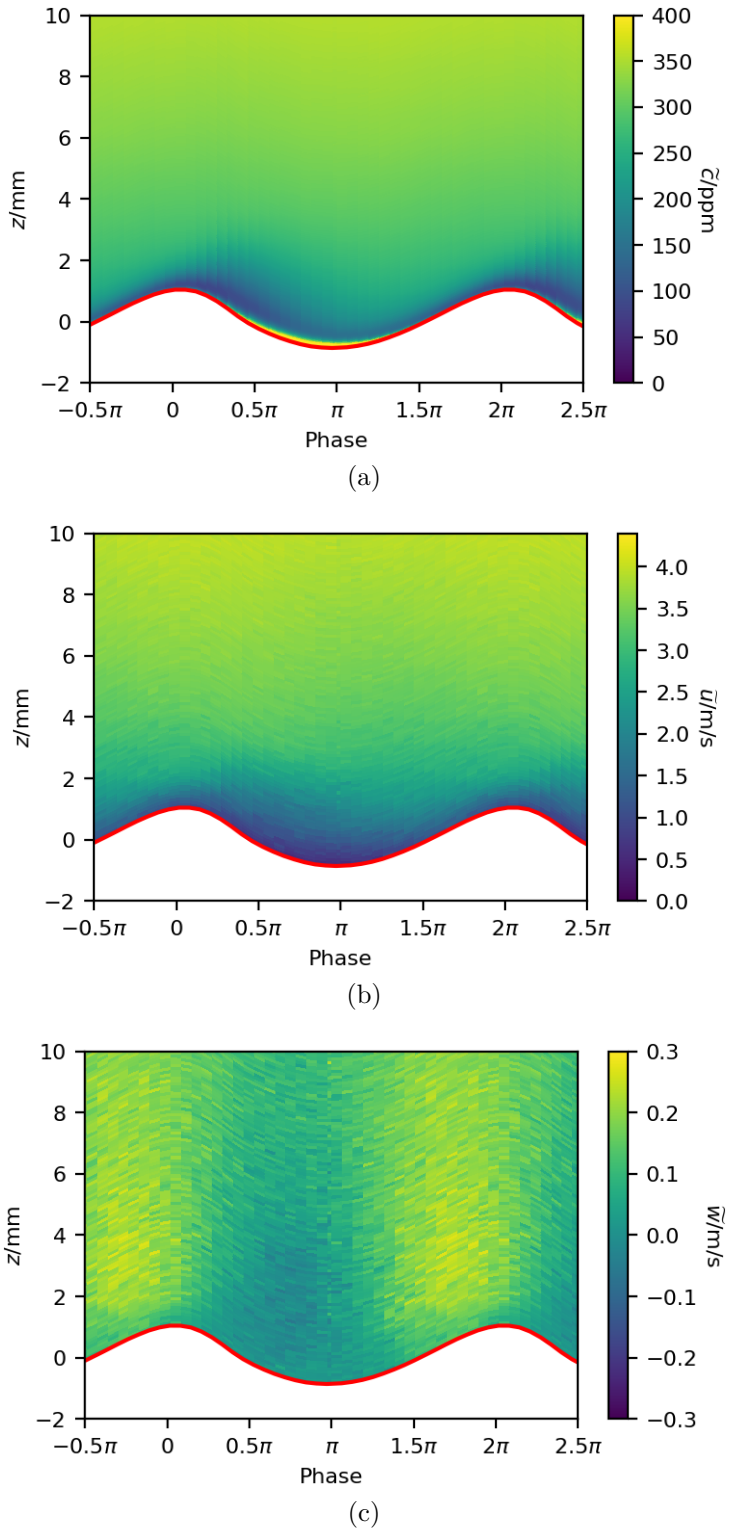

(a)

(b)

(c)

Figure 7.19: (a) Concentration, (b) horizontal and (c) vertical wind profiles, averaged over the phase, from the measurement at the highest wind condition at high fetch. The mean wave height is marked with a red line. The wind direction is from left to right.

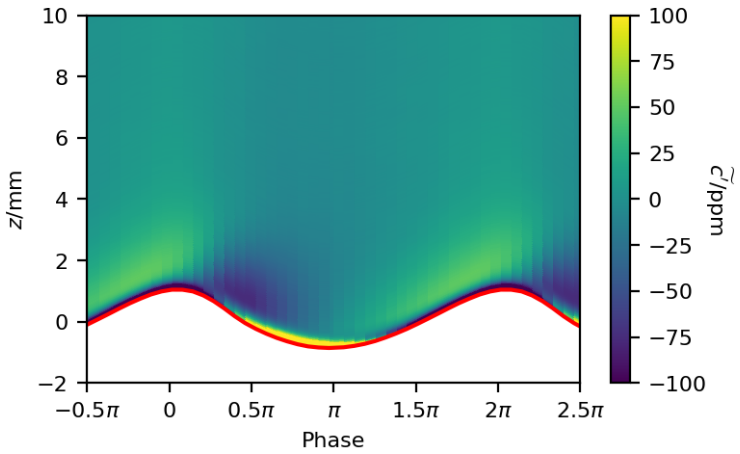

(a)

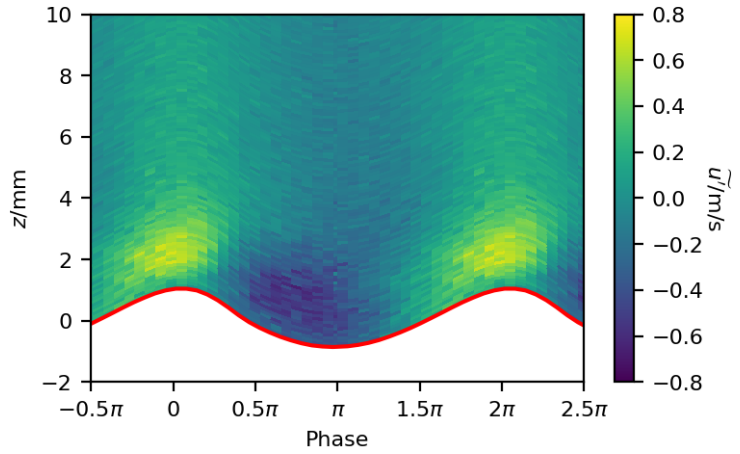

(b)

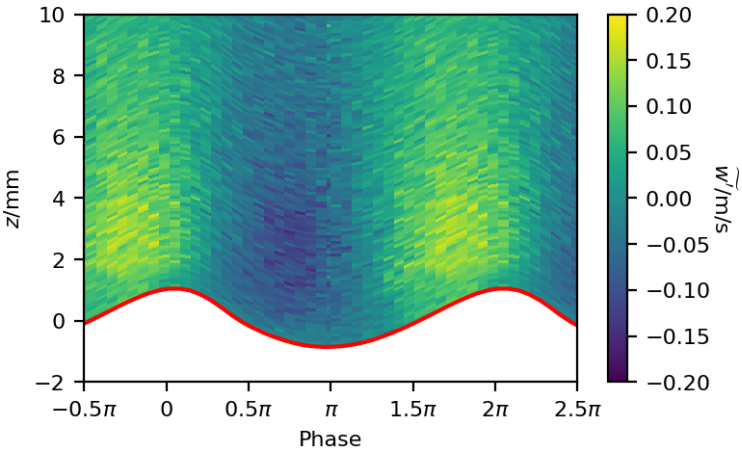

(c)

Figure 7.20: (a) Concentration, (b) horizontal and (c) vertical wind fluctuation profiles, averaged over the phase, from the measurement at the highest wind condition at high fetch. The mean wave height is marked with a red line. The wind direction is from left to right.

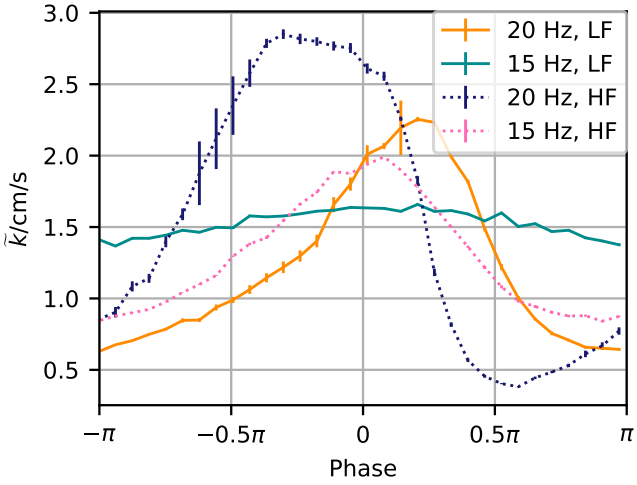

Figure 7.21: Wave phase averaged transfer velocities from the Deacon model fits to the wave phase averaged concentration profiles from the measurements at the medium and highest wind conditions at both fetches. The corresponding values for transfer velocities obtained by the Deacon model fit on the mean concentration profiles are 0.86 cm/s and 1.5 cm/s for the highest and second highest wind speed condition at low fetch and 1.5 cm/s and 1.1 cm/s for the highest and second highest wind speed condition at high fetch.

To obtain values for the dependence of the thickness of the mass boundary layer and the transfer velocity of the wave phase, the phase averaged concentration profiles are fitted with the Deacon model. However, to do this, an upper fit limit is needed. A straightforward ansatz would be to fit the phase averaged wind profiles first with the logarithmic profile and then use the phase-dependent friction velocities to calculate the fit limits. However, the results from those fits were not reliable as the noise was too large. Therefore, a simpler approach was adopted, where the mean friction velocity from the mean wind profile was used.

In Fig. 7.21, the wave phase averaged transfer velocities are shown for the four phase evaluated measurements. All graphs have in common, that the minimum lies in the wave trough, however the position of the maximum transfer velocity is not the same for all measurements. The modulation of the transfer velocity at the highest wind condition at high fetch is similar to the modulation of shear stress in Bopp (2018) as would be expected as the mass and momentum transfer should be analog. The reason why the shape of the modulation differs between the measurements is not known. More measurements at higher winds are necessary for a more detailed evaluation as the wave height is still very low in the present measurements.

The results for the wave phase averaged mass boundary layer thickness $\tilde{z}_*$ are shown in Fig. 7.22 with the concentration profiles and the mean wave height. In the figure, $\tilde{z}_*$ is added to the mean wave height $\tilde{\eta}$ for a better comparisons with the profiles in the background

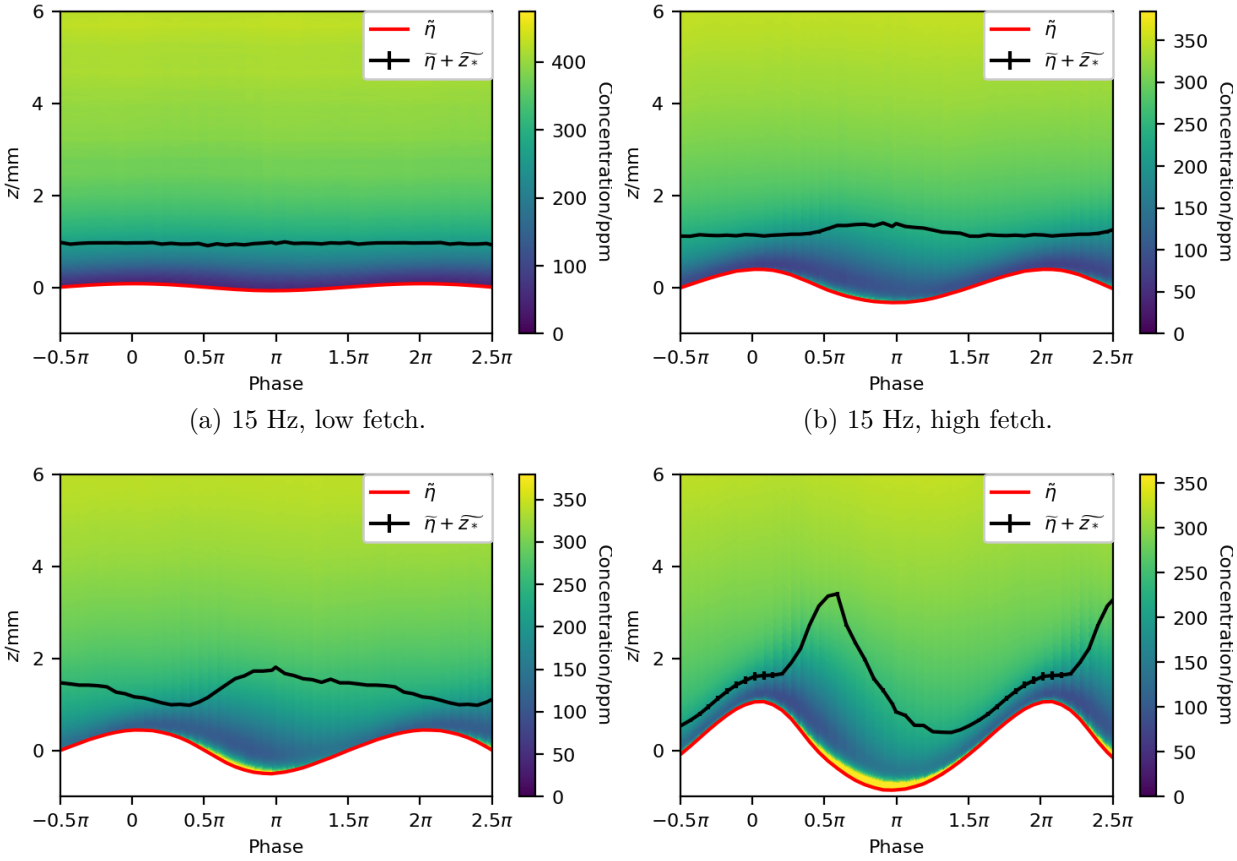

(a) 15 Hz, low fetch.

(b) 15 Hz, high fetch.

(c) 20 Hz, low fetch.

(d) 20 Hz, high fetch.

Figure 7.22: Wave phase averaged concentration profiles with the mean wave height (red) and the mass boundary layer thickness z_* added to the mean wave height (black), shown for the measurements at the medium and highest wind conditions at both fetches.

and to compare the wave height with $\tilde{z_*}$. As expected, $\tilde{z_*}$ is thinner on the windward side and thicker on the lee side. The measurement at the highest wind speed at high fetch is again the one which is best consistent with theory.

8 Conclusion and Outlook

The boundary layers in air and water are of special interest in the study of air-sea interaction as they form the bottleneck for the transfer of mass, momentum and heat. In this project a method to determine air-sided vertical concentration profiles of a tracer gas in the vicinity of a wind-driven wavy water surface in a wind-wave tank was developed. With high temporal and spatial resolution, the transport mechanisms in the mass boundary layer were assessed.

The measurement technique employed in the experiments is based on a laser induced fluorescence (LIF) method, proposed by Winter (2011) and tested with acetone as the tracer by Krah (2014). In this study, the tracer gas was sulfur dioxide, which fluoresces in the UV. The gas was excited with a pulsed UV laser at a wavelength of 224 nm. A first test experiment at a small wind-wave facility showed promising results which are published in Friman and Jähne (2019): It was possible to deduce vertical concentration profiles close to the air-water interface and thus to quantify the mass boundary layer thickness from the resulting profiles using this method.

A further experiment with simultaneous application of the LIF setup, a particle streak velocimetry (PSV) setup for wind velocity measurements and a laser height camera (LHC) setup for surface elevation measurements was performed. The measurements were conducted with four different wind conditions at two fetches each in a larger wind-wave facility. This enabled the comparison of mass and momentum transfer both averaged over a whole measurement and locally in time and space, accounting for fluctuations of concentration and wind velocity. Furthermore, by conducting a wave analysis of the surface elevation data, concentration and wind profiles averaged over the dominant wave phase were obtained for the measurements at the two highest wind speed conditions at both fetches.

The results show that for sulfur dioxide, the concentration and horizontal wind profiles are similar, with exceptions when waves occur, as expected of a gas with a Schmidt number of approximately 1. For the detailed analysis of fluctuation correlations, better statistics would be needed as the number of particle streaks crossing the laser beam detected per measurement is not sufficient for a statistical analysis. However, the mean fluctuation profiles of concentration, horizontal and vertical wind are consistent with the theory. The phase averaged wind velocity profiles compare well with those in Bopp (2018). The phase averaged concentration profiles were used to derive phase averaged transfer velocities and mass boundary layer thicknesses. The data at the highest wind speed condition at high fetch shows the best agreement with the phase averaged viscous shear stress as measured in Bopp (2018).

The measurements show that the setup could be improved in various ways. First, a different UV laser for the excitation of sulfur dioxide with a wavelength corresponding ideally to a peak of the absorption cross section in the range between 220 nm and 224 nm is desirable. This would yield a higher absorption efficiency and better fluorescence intensity and thus increase the image quality of the LIF signals. Simply using higher air-side mean SO_2 concentrations in the invasion experiment would not have the same effect because the increased absorption of the laser light by SO_2 would decrease the laser intensity along the beam path. With higher laser powers and/or increased fluorescence efficiency, LIF measurements with a laser sheet become feasible, as in Krah (2014) with acetone, allowing the extraction of two dimensional concentration profiles.

Second, the statistics of the PSV method and the LIF method differ greatly as the LIF method delivers a continuous vertical concentration profile per captured image while in each PSV, only around 10-20 streaks are detected. A straightforward possibility to improve statistics would be to apply higher particle densities. However, this would lead to lower efficiency of the PSV algorithm. By contrast, longer measurements or a different particle imaging technique, ideally producing an instantaneous wind velocity field per image, would improve the statistics.

Third, the biggest problems caused by the simultaneous application of the three measurement methods was the occurrence of secondary particles due to unwanted chemical reactions, the bleaching of the fluorescent dye in the water by the light of the UV laser and the fluorescence intensity from the water being visible in the LIF images. All three effects deteriorated the results from the second experiment. Therefore, all observed interactions between the measurement setups need to be assessed and if possible counteracted, by for example using a different dye fluorescing at a different wavelength or simply a better suited filter for the LIF camera, or improving mixing in the particle production tube.

Fourth, the application of higher frame rates at the second experiment compared to the proof-of-principle experiment already improved the ability to measure the turbulent fluctuations. Even higher frame rates would be beneficial for the evaluation of the fast transfer mechanisms.

More measurements with other parameters and under different conditions and possibly also the application of different setups could be of interest. In the following, a few examples are given.

The solubility of sulfur dioxide increases with the alkalinity of water, and ranges over many orders of magnitude. This is an interesting feature because the partitioning of the transfer resistance between air and water depends on the solubility. Therefore, measurements with the same wind conditions and varying pH value of the water would be interesting. By changing the temperature and/or salinity of the water, the effects of these parameters on the gas transfer velocities could be studied individually. Higher waves would be of interest for the studies of the mass boundary layer thickness in dependence of the wave phase. Thus, experiments at higher wind speed conditions and at the Heidelberg *Aeolotron* with infinite fetch would allow studies at higher wave ages.

A Appendix

A.1 Solution of system of coupled differential equations

In the following, the solution of the system of coupled differential equations describing the air- and water-side concentrations (Eqs. (3.7)) of a tracer is derived. More details can be found in Nielsen (2004). Eqs. (3.7) can be written as a matrix equation:

$$\begin{pmatrix} \dot{c}_\mathrm{a} \\ \dot{c}_\mathrm{w} \end{pmatrix} = A \begin{pmatrix} c_\mathrm{a} \\ c_\mathrm{w} \end{pmatrix} + G = \begin{pmatrix} a_{11} & a_{12} \\ a_{21} & a_{22} \end{pmatrix} \begin{pmatrix} c_\mathrm{a} \\ c_\mathrm{w} \end{pmatrix} + \begin{pmatrix} g_1 \\ g_2 \end{pmatrix}, \tag{A.1}$$

where the matrix elements are given by:

$$a_{11} = -\left(\frac{kA}{V_\mathrm{a}} + \frac{\dot{V}_\mathrm{a}}{V_\mathrm{a}} \right), \tag{A.2}$$

$$a_{12} = \frac{kA}{\alpha V_\mathrm{a}}, \tag{A.3}$$

$$a_{21} = \frac{kA}{V_\mathrm{w}}, \tag{A.4}$$

$$a_{22} = -\left(\frac{kA}{\alpha V_\mathrm{w}} + \frac{\dot{V}_\mathrm{w}}{V_\mathrm{w}} \right), \tag{A.5}$$

$$g_1 = \frac{\dot{V}_\mathrm{a} c_\mathrm{a,f}}{V_\mathrm{a}} \tag{A.6}$$

$$g_2 = \frac{\dot{V}_\mathrm{w} c_\mathrm{w,f}}{V_\mathrm{w}}. \tag{A.7}$$

The ansatz to find the solution for the inhomogeneous system

$$\begin{pmatrix} c_\mathrm{a} \\ c_\mathrm{w} \end{pmatrix} (t) = c_1 \vec{v}_1 \exp(\lambda_1 t) + c_2 \vec{v}_2 \exp(\lambda_2 t) + \begin{pmatrix} c_\mathrm{a,i} \\ c_\mathrm{w,i} \end{pmatrix}. \tag{A.8}$$

is to first solve the homogeneous system and then to determine the inhomogeneity $(c_\mathrm{a,i}, c_\mathrm{w,i})$ (the special solution) which is added to the homogeneous solution. The initial conditions are then used to find the factors c_1 and c_2.

A.1.1 Homogeneous Solution

To find the eigen values λ_1 and λ_2 of the homogeneous system, ignoring the inhomogeneity (g_1, g_2), the equation $\mathrm{Det}(A - \lambda \mathrm{Id}) = 0$ is solved for the eigenvalues. The solutions are

$$\lambda_{1,2} = \frac{a_{11} + a_{22}}{2} \pm \sqrt{\left(\frac{a_{11} + a_{22}}{2}\right)^2 - a_{11}a_{22} + a_{12}a_{21}}. \tag{A.9}$$

The eigen vectors $\vec{v}_1 = (v_{\mathrm{a},1}, v_{\mathrm{w},1})$ and $\vec{v}_2 = (v_{\mathrm{a},2}, v_{\mathrm{w},2})$ are determined by

$$(a_{11} - \lambda_1)v_{\mathrm{a},1} + a_{12}v_{\mathrm{w},1} = 0 \tag{A.10}$$
$$a_{21}v_{\mathrm{a},2} + (a_{22} - \lambda_2)v_{\mathrm{w},2} = 0, \tag{A.11}$$

choosing $v_{\mathrm{a},1} = a_{12}$ and $v_{\mathrm{w},2} = a_{21}$, such that the eigen vectors are:

$$\vec{v}_1 = \begin{pmatrix} a_{12} \\ \lambda_1 - a_{11} \end{pmatrix} \text{ and } \vec{v}_2 = \begin{pmatrix} \lambda_2 - a_{22} \\ a_{21} \end{pmatrix}. \tag{A.12}$$

With c_1 and c_2 chosen according to satisfy the initial and boundary conditions, the homogeneous solution is found.

When applying the assumptions and conditions as defined in Sec. 3.4 for the proof-of-principle experiment, the following simplifications apply: $a_{12} = 0$ and $a_{22} = 0$ because of the high value of the solubility in the experiment as well as the water leakage assumed to be zero. Then, the eigenvalues reduce to

$$\lambda_1 = a_{11} = \frac{-kA}{V_{\mathrm{a}}} \text{ and } \lambda_2 = 0. \tag{A.13}$$

With the initial condition $c_{\mathrm{a}}(0) = c_{\mathrm{a},0}$, the homogeneous solution then simplifies to

$$c_{\mathrm{a}}(t) = c_{\mathrm{a}}(t) = c_{\mathrm{a},0} \exp(-kA/V_{\mathrm{a}}t). \tag{A.14}$$

A.1.2 Inhomogeneous Solution

In the following, the inhomogeneous solution using the assumptions and initial conditions as described in Sec. 3.4 for the fetch experiment is calculated. The eigenvalues for the homogeneous solution with the second set of conditions is

$$\lambda_1 = -\frac{kA + \dot{V}_{\mathrm{a}}}{V_{\mathrm{a}}} \text{ and } \lambda_2 = 0. \tag{A.15}$$

To determine the solution for the inhomogeneous system, the additional term is assumed to be constant in time, thus $\dot{c}_{\mathrm{a,i}} = \dot{c}_{\mathrm{w,i}} = 0$. This leads to:

$$a_{11}c_{\mathrm{a,i}} + g_1 = 0 \Rightarrow c_{\mathrm{a,i}} = -\frac{g_1}{a_{11}} = \frac{\dot{V}_{\mathrm{a}}c_{\mathrm{a,f}}}{kA + \dot{V}_{\mathrm{a}}}. \tag{A.16}$$

From the initial condition $c_{\mathrm{a}}(0) = 0$ it follows:

$$c_1 v_{\mathrm{a},1} \exp(\lambda_1 \cdot 0) + c_{\mathrm{a,i}} \Rightarrow c_1 v_{11} = -c_{\mathrm{a,i}} \tag{A.17}$$

and the resulting solution of the inhomogeneous differential equation is

$$c_{\mathrm{a}}(t) = \frac{\dot{V}_{\mathrm{a}} c_{\mathrm{a,f}}}{kA + \dot{V}_{\mathrm{a}}} \left(1 - \exp(-(kA + \dot{V}_{\mathrm{a}})t/V_{\mathrm{a}})\right). \tag{A.18}$$

In this case, $c_{\mathrm{a,i}}$ is equal to the equilibrium concentration.

A.2 Transmission of Camera Lens

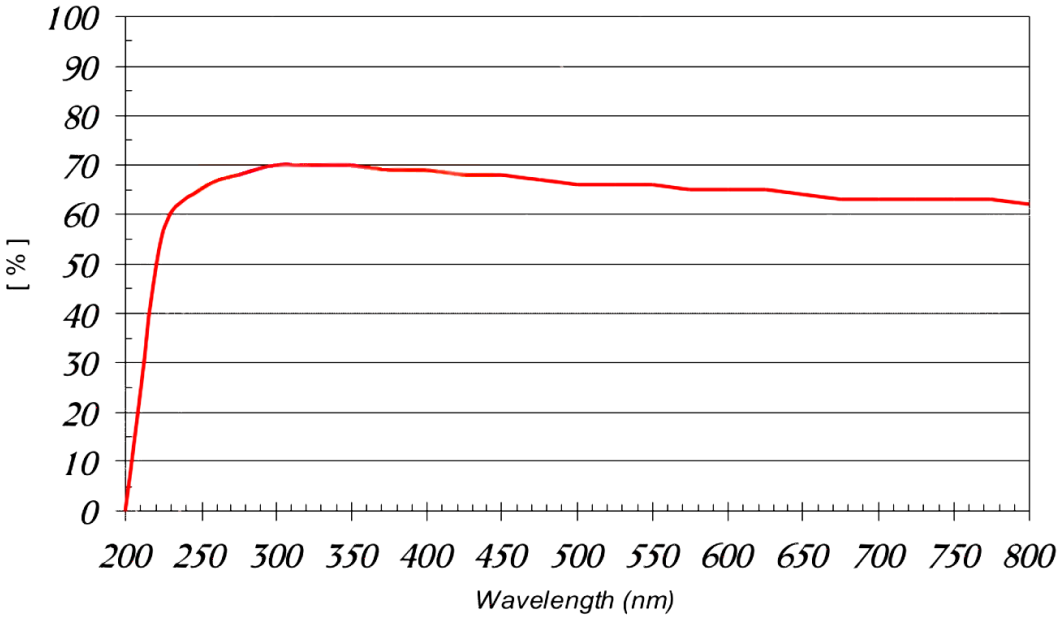

Figure A.1: Pentax H2520-UVM transmission curve, modified after Gon Cho (2014).

A.3 'Curtain Plots'

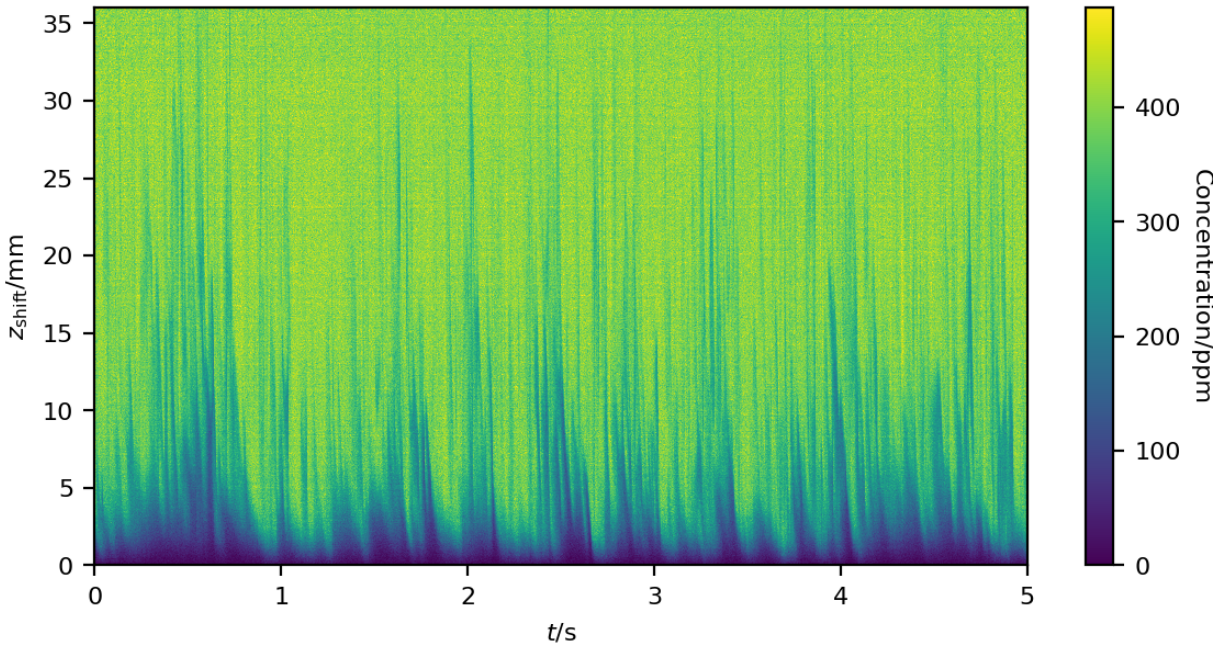

(a) 5 Hz, low fetch.

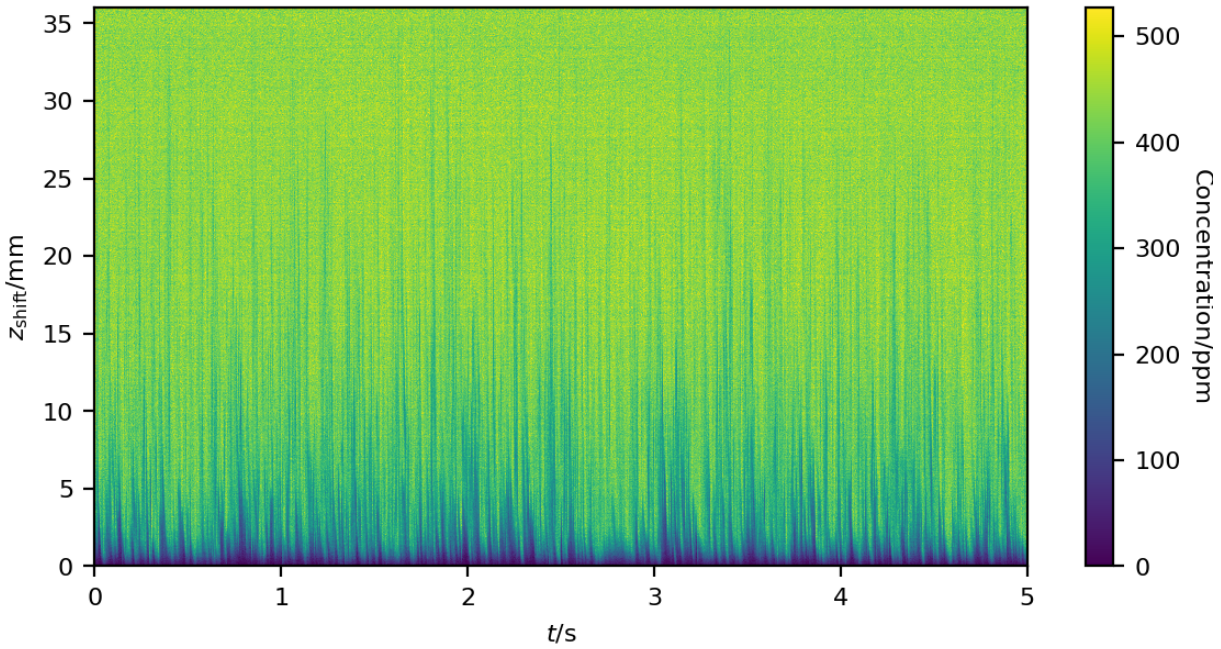

(b) 10 Hz, low fetch.

Figure A.2: 1000 subsequent concentration profiles from the two lowest wind conditions at low fetch.

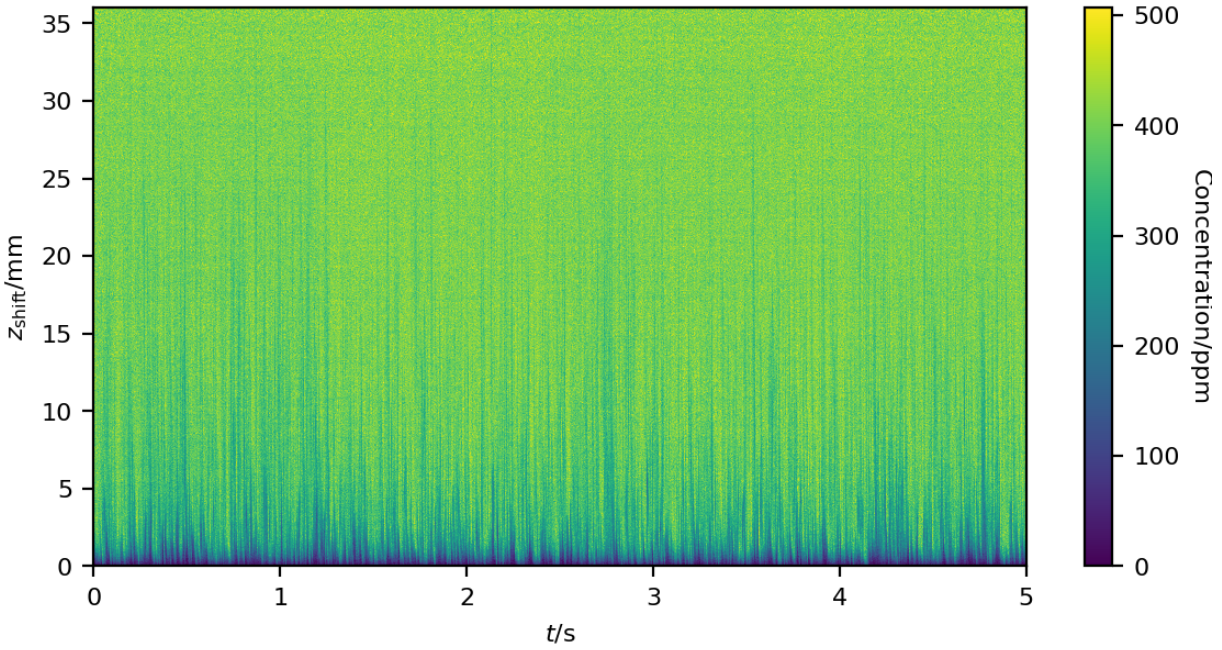

(a) 15 Hz, low fetch.

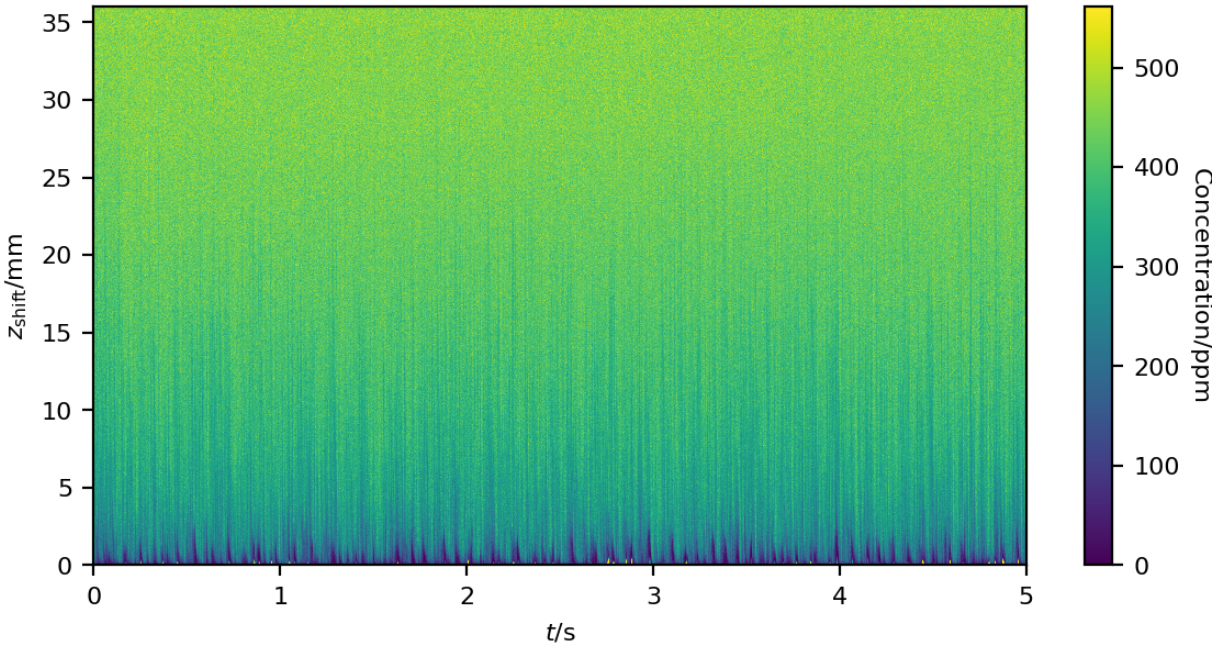

(b) 20 Hz, low fetch.

Figure A.3: 1000 subsequent concentration profiles from the two highest wind conditions at low fetch.

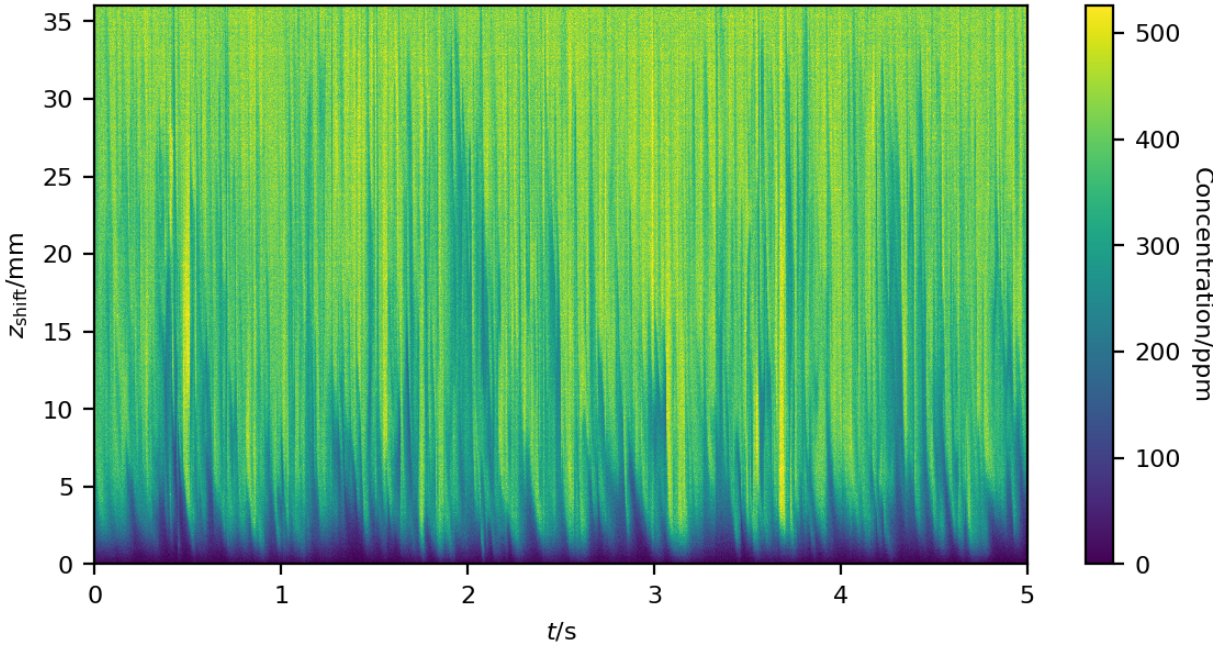

(a) 5 Hz, high fetch.

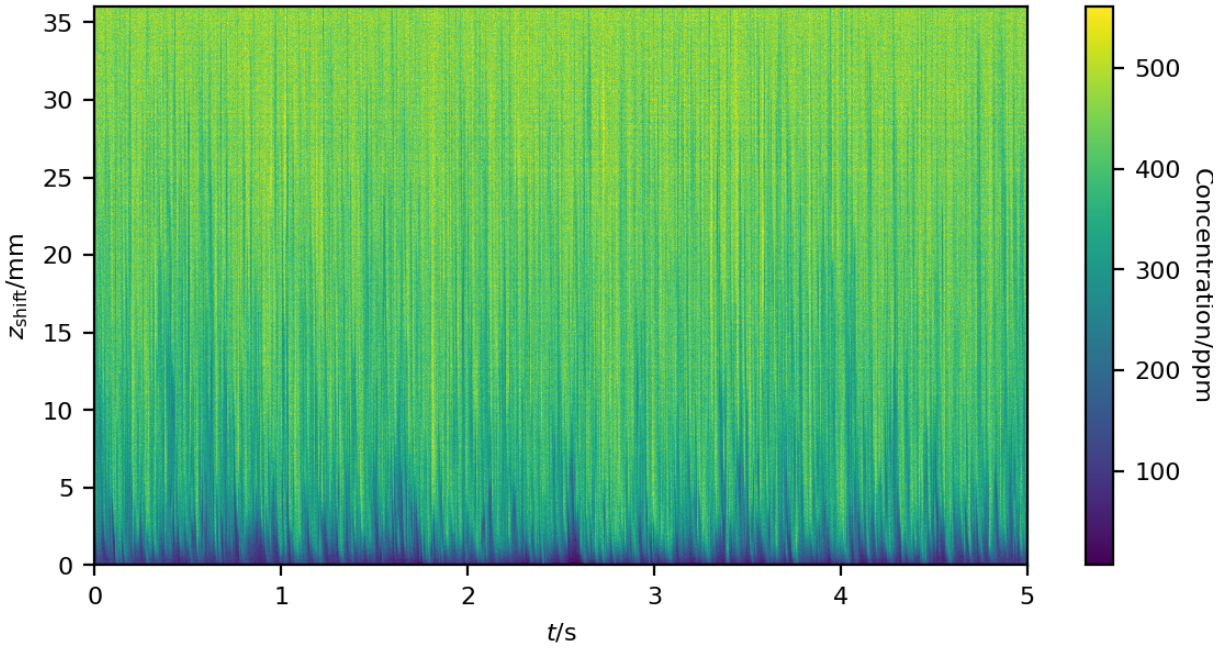

(b) 10 Hz, high fetch.

Figure A.4: 1000 subsequent concentration profiles from the two lowest wind conditions at high fetch.

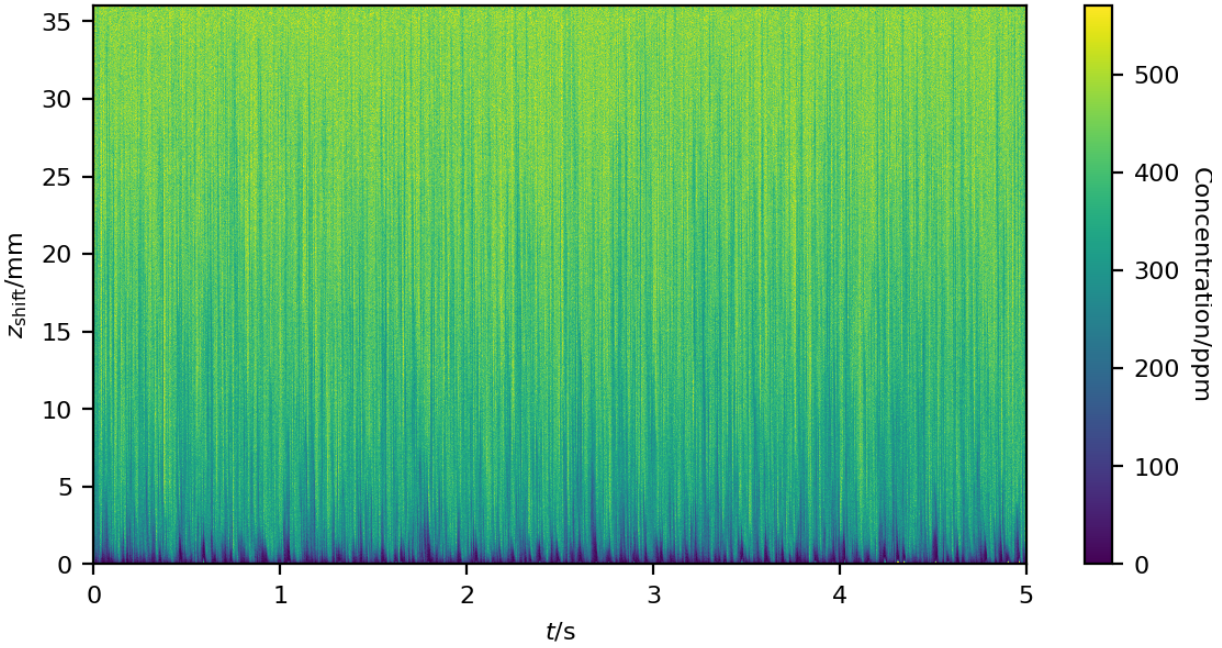

(a) 15 Hz, high fetch.

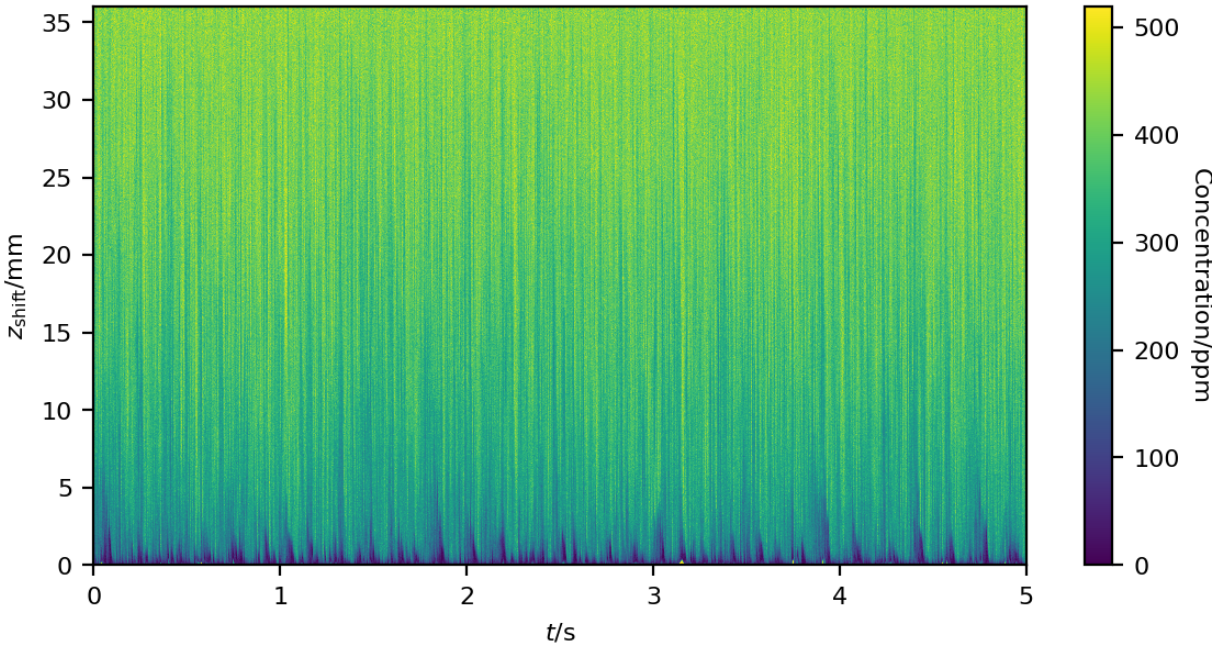

(b) 20 Hz, high fetch.

Figure A.5: 1000 subsequent concentration profiles from the two highest wind conditions at high fetch.

A.4 Concentration Histograms

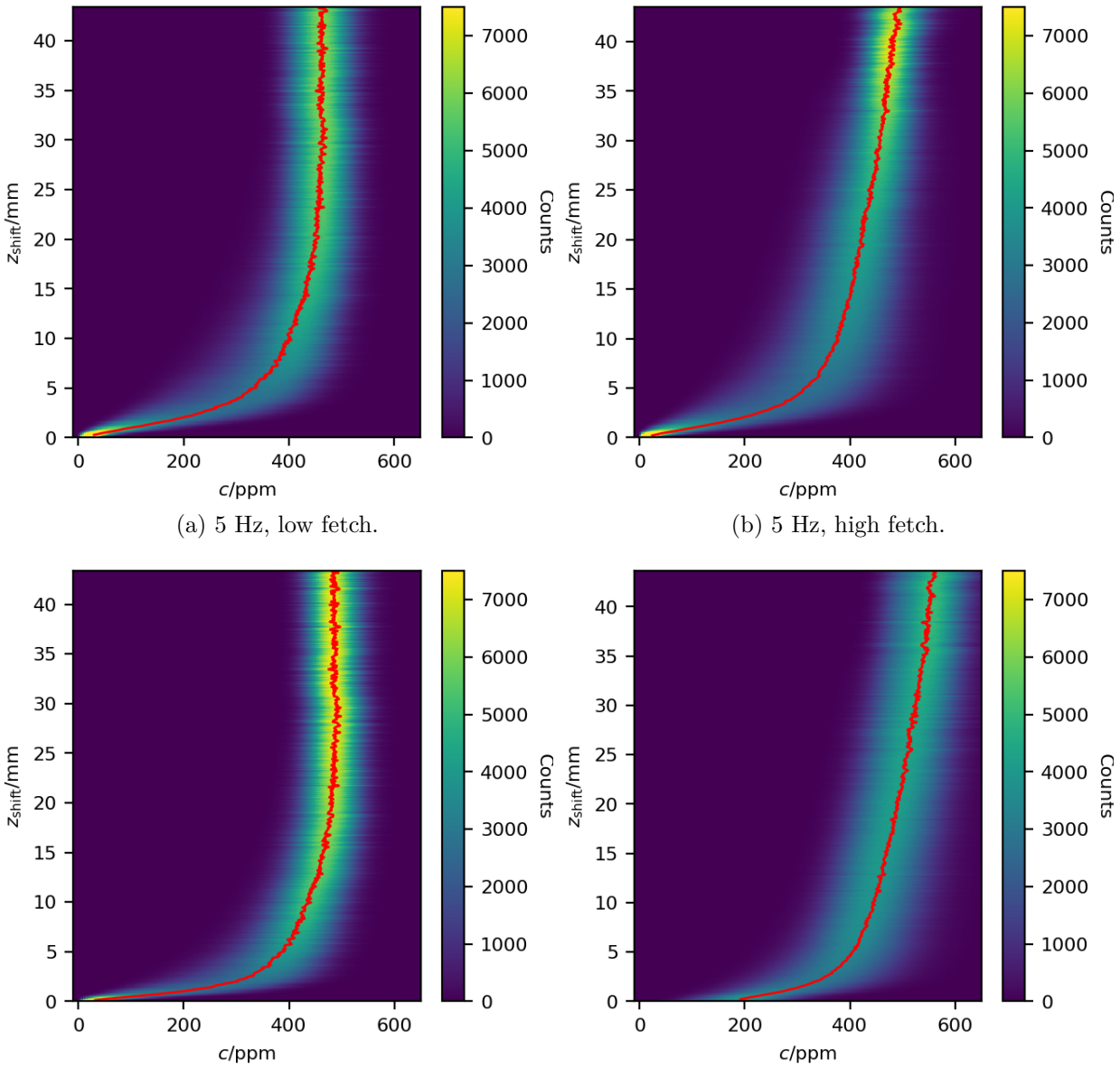

(a) 5 Hz, low fetch.

(b) 5 Hz, high fetch.

(c) 10 Hz, low fetch.

(d) 10 Hz, high fetch.

Figure A.6: Histograms of the concentration c for the height above the water surface z_{shift}, measured at the two lowest wind speeds at low fetch (a, c) and high fetch (b, d) in the fetch experiment. The mean profiles are shown with red lines.

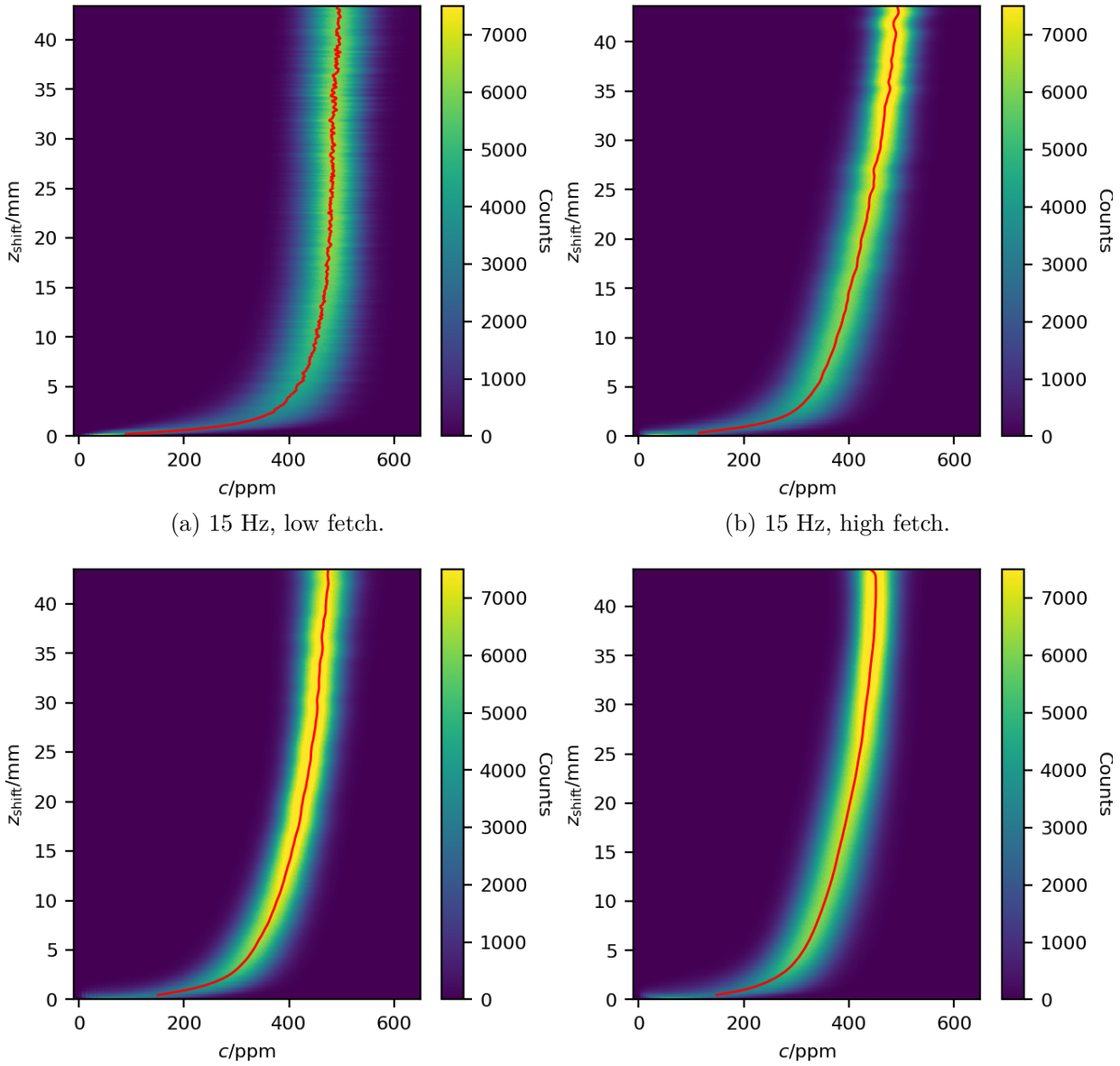

(a) 15 Hz, low fetch.

(b) 15 Hz, high fetch.

(c) 20 Hz, low fetch.

(d) 20 Hz, high fetch.

Figure A.7: Histograms of the concentration c for the height above the water surface z_{shift}, measured at the two highest wind speeds at low fetch (a, c) and high fetch (b, d) in the fetch experiment. The mean profiles are shown with red lines.

A.5 Probe Data

As mentioned in Sec. 5.2, the probes measuring water, air and lab temperatures, humidity and water pH were in operation during each measurement of the fetch experiment. There values at the beginning and at the end of each measurement are listed in Tab. A.1. Generally, the temperatures did not change significantly during the measurements, while the pH decreased slightly. The humidity increased a lot, already during the preparations for the experiments. This is illustrated in Fig. A.8 where the humidity in one measurement is shown exemplarily. The orange region marks the time interval when the probe was in the tank, the gray region corresponds to the measurement time. It is obvious that the humidity in the tank is significantly higher than outside the tank.

Table A.1: Probe data from the fetch experiment: water, air and lab temperatures T_a, T_w and T_l, water pH pH and humidity H; with the wind generator frequency W. The first value is taken from the beginning of a measurement, the second from the end.

Fetch	W Hz	T_w °C	T_a °C	T_l °C	pH	H %
Low	5	20.92 ± 0.01	23.72 ± 0.01	23.36 ± 0.01	11.5 ± 0.1	87.8 ± 0.1
		21.09 ± 0.01	23.789 ± 0.003	23.578 ± 0.004	11.3 ± 0.1	93.8 ± 0.1
	10	20.591 ± 0.007	23.455 ± 0.005	23.36 ± 0.01	11.40 ± 0.09	91.7 ± 0.1
		20.830 ± 0.009	23.578 ± 0.004	23.384 ± 0.005	11.16 ± 0.08	95.0 ± 0.1
	15	20.288 ± 0.004	23.125 ± 0.005	22.867 ± 0.007	11.38 ± 0.07	92.2 ± 0.1
		20.74 ± 0.01	23.326 ± 0.005	23.02 ± 0.01	10.84 ± 0.06	96.0 ± 0.1
	20	18.920 ± 0.006	22.510 ± 0.006	22.38 ± 0.01	11.30 ± 0.04	84.9 ± 0.1
		19.730 ± 0.008	22.680 ± 0.006	22.470 ± 0.007	10.45 ± 0.03	92.6 ± 0.1
High	5	18.08 ± 0.02	21.844 ± 0.008	22.24 ± 0.07	12.5 ± 0.3	77.0 ± 0.1
		18.46 ± 0.02	21.982 ± 0.004	22.40 ± 0.03	12.3 ± 0.3	84.7 ± 0.1
	10	17.45 ± 0.04	22.02 ± 0.01	22.48 ± 0.06	12.3 ± 0.2	72.9 ± 0.1
		18.09 ± 0.03	22.19 ± 0.01	22.73 ± 0.04	11.8 ± 0.3	81.9 ± 0.1
	15	19.431 ± 0.003	22.300 ± 0.007	22.47 ± 0.02	12.3 ± 0.2	85.6 ± 0.2
		19.661 ± 0.006	22.374 ± 0.005	22.45 ± 0.02	11.8 ± 0.2	90.6 ± 0.1
	20	19.096 ± 0.006	22.513 ± 0.004	22.721 ± 0.007	11.8 ± 0.1	83.0 ± 0.2
		19.496 ± 0.005	22.532 ± 0.005	22.81 ± 0.02	11.25 ± 0.09	90.5 ± 0.1

A.6 Data from Fits

In Tab. A.2, the data as obtained from fits to the wind and concentration profiles from the fetch experiment are listed: From the mean wind profiles, the friction velocities and roughness lengths were derived via fitting a logarithmic function to the logarithmic parts.

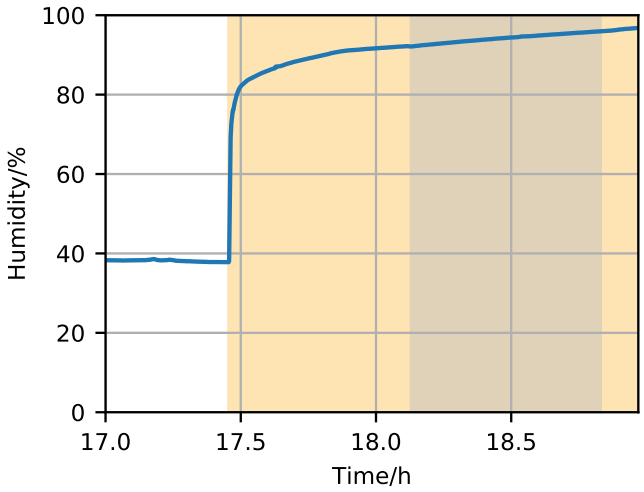

Figure A.8: Humidity during the second highest wind condition at low fetch, with the time interval when the probe was in the tank marked in orange and the measurement time interval marked in gray.

Single concentration profiles yielded averaged local transfer velocities by polynomial fits. The mean concentration profiles were fitted with a polynomial function as well as the Deacon model, resulting in local averaged transfer velocities.

Table A.2: Friction velocities u_* and roughness lengths z_0 from the mean wind profiles and transfer velocities k from the four applied methods - Absorption spectroscopy (Abs), single polynomial fits (PS), mean polynomial fits (PM) and mean Deacon model fits (DM) -; with the wind generator frequency W.

Fetch	W Hz	u_* cm/s	z_0 mm	k_{Abs} cm/s	k_{PS} cm/s	k_{PM} cm/s	k_{DM} cm/s
Low	5	7.9 ± 0.2	0.07 ± 0.01	0.40 ± 0.04	0.4 ± 0.2	0.38 ± 0.001	0.4880 ± 0.0008
	10	14.4 ± 0.4	0.026 ± 0.005	0.77 ± 0.08	0.8 ± 0.3	0.79 ± 0.01	1.011 ± 0.002
	15	19.8 ± 0.5	0.010 ± 0.002	1.2 ± 0.1	1.2 ± 0.5	1.15 ± 0.04	1.492 ± 0.004
	20	31.5 ± 0.4	0.032 ± 0.003	1.6 ± 0.2	2.1 ± 3.8	0.93 ± 0.06	0.863 ± 0.001
High	5	7.6 ± 0.3	0.07 ± 0.02	0.51 ± 0.05	0.4 ± 0.2	0.4042 ± 0.0005	0.5341 ± 0.0008
	10	13.5 ± 0.6	0.021 ± 0.006	0.58 ± 0.06	0.7 ± 0.4	0.638 ± 0.005	0.7172 ± 0.0008
	15	21 ± 1	0.021 ± 0.008	1.2 ± 0.1	0.8 ± 1.8	0.92 ± 0.01	1.0906 ± 0.0003
	20	32.6 ± 0.6	0.067 ± 0.006	1.8 ± 0.2	2.4 ± 3.3	0.96 ± 0.01	1.49 ± 0.05

A.7 Friction Velocities from Wind Fluctuations

As described in Sec. 7.5.2, the friction velocity can be derived from the correlation $\overline{u'w'}$ for $z^+_{\text{shift}} > 50$. Figures A.9 and A.10 show histograms of the horizontal wind fluctuations versus the vertical wind fluctuations for all measurements in the fetch experiment. They all show a certain tilt as expected, indicating a correlation between both fluctuations. The resulting values for u_* are given in Tab. A.3 in comparison with the values from the mean wind profiles, as well as the Pearson correlation coefficients of the horizontal and vertical wind fluctuations. The Pearson correlation coefficients show a clear correlation, however, this method to obtain u_* from $\overline{u'w'}$ underestimates the friction velocities systematically.

Table A.3: Friction velocities obtained from the mean wind profiles $u_m athrm*, fit$ and from the wind fluctuation correlation $u_{*,\text{corr}}$ as well as the Pearson correlation coefficients of the horizontal and vertical wind fluctuations P; with the wind generator frequency W.

Fetch	W Hz	P	$u_{*,\text{corr}}$ cm/s	$u_{*,\text{fit}}$ cm/s
Low	5	-0.41	4.4	7.9 ± 0.2
	10	-0.41	9.5	14.4 ± 0.4
	15	-0.4	13	19.8 ± 0.5
	20	-0.38	18	31.5 ± 0.4
High	5	-0.41	4.8	7.6 ± 0.3
	10	-0.4	9.8	13.5 ± 0.6
	15	-0.37	15	21 ± 1
	20	-0.33	23	32.6 ± 0.6

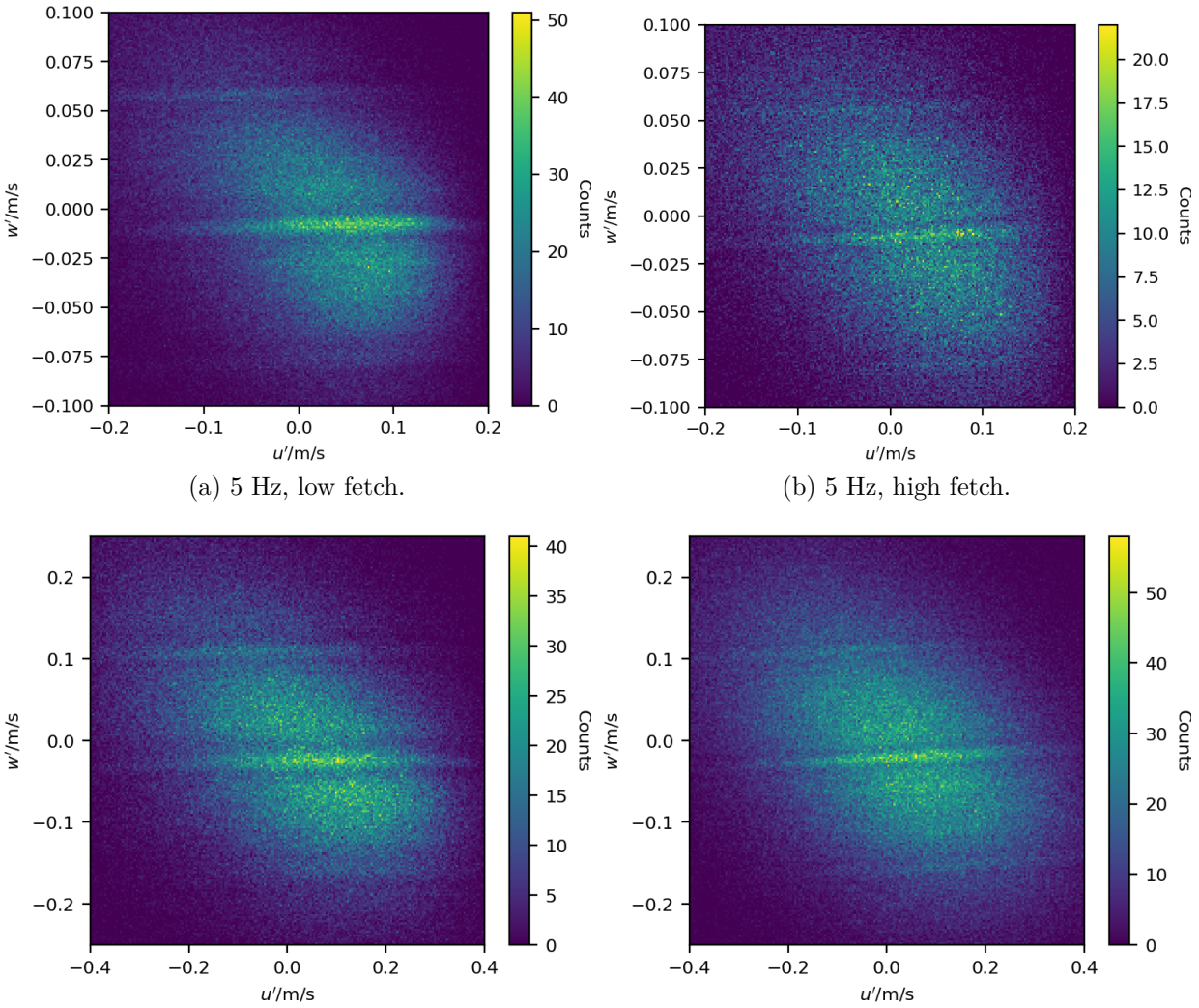

(a) 5 Hz, low fetch.

(b) 5 Hz, high fetch.

(c) 10 Hz, low fetch.

(d) 10 Hz, high fetch.

Figure A.9: Histograms of the horizontal wind fluctuations versus the vertical wind fluctuations, for $z^{+}_{\mathrm{shift}} > 50$, measured at the two lowest wind speeds at low fetch (a, c) and high fetch (b, d) in the fetch experiment.

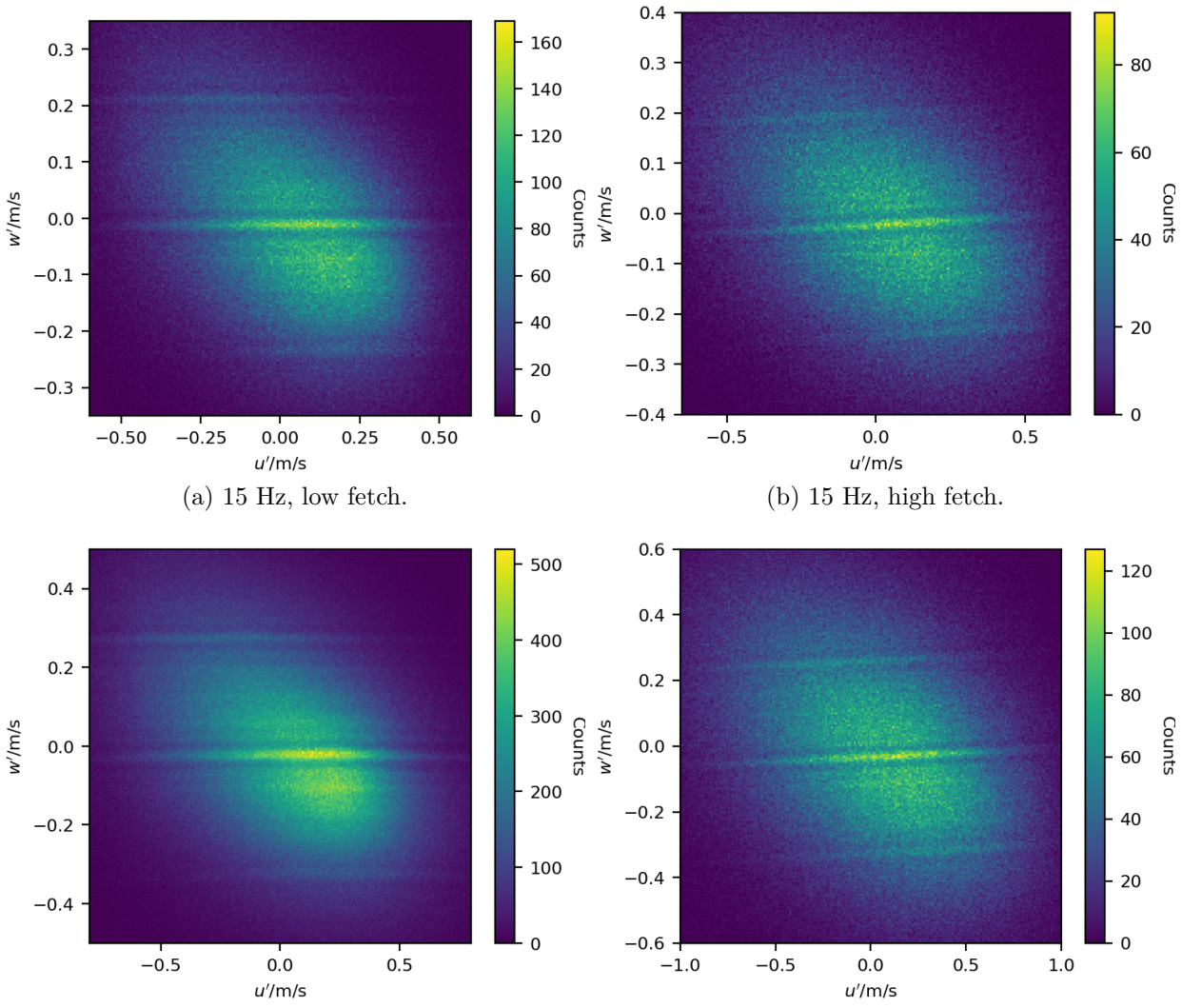

(a) 15 Hz, low fetch.

(b) 15 Hz, high fetch.

(c) 20 Hz, low fetch.

(d) 20 Hz, high fetch.

Figure A.10: Histograms of the horizontal wind fluctuations versus the vertical wind fluctuations, for $z^{+}_{\mathrm{shift}} > 50$, measured at the two highest wind speeds at low fetch (a, c) and high fetch (b, d) in the fetch experiment.

Glossary

List of Symbols

α	Dimensionless solubility. In this thesis, the effective solubility is meant when α is written. 14
A	Water surface area 30
α_{eff}	Effective solubility 24
α_m	Momentum solubility 10
a_n	Amplitudes of the modes of a wavy surface profile 29
α_{phys}	Physical solubility 23
abs	Absorbance 20
α_{Ch}	Charnock coefficient 106
c	Volume concentration of a gas in air or water, i.e. the ratio of the volumes of the tracer and the fluid. Unit: ppmv, parts per million in volume. In this document, ppm is written, meaning ppmv. 5
c_{a}	Air-side concentration 14
c_s	Concentration at the surface 13
c_{w}	Water-side concentration 14
$\bar{c}$	Mean concentration 7
c'	Concentration fluctuations 7
D	Diffusion coefficient 6
δ	Optical depth 20
ϵ	Molar attenuation coefficient 20
η_{opt}	Optical path length 22
η	Surface elevation 29
f	Transformation function for the vertical coordinate z 29
$\vec{g}$	External forces in the Naver-Stokes equation 6
g	Gravitational acceleration 106
H^{cp}	Henry constant 23
I	Light intensity 20
$\vec{j}$	Mass flux density field 5
$\boldsymbol{j}_m$	Momentum flux density tensor 6
j_m	x, z component of the momentum flux density tensor, $j_{m,xz} = \tau_{xz}$ 9

k	Transfer velocity, equal to the inverse transfer resistance 13
K	Turbulent diffusion coefficient 8
K_m	Viscous diffusion coefficient 8
k_n	Wave vectors of the modes of a wavy surface profile 29
κ	von Kármán constant 11
l	Optical path length 20
λ	Wavelength 20
m	Magnification factor 53
μ	Dynamic viscosity 6
n	Schmidt number exponent 16
N_A	Avogadro constant 21
ν	Kinematic viscosity, defined as $\nu = \mu/\rho$ 6
p	Pressure 6
Φ	Fluorescence quantum efficiency 22
Φ_n	Phases of the modes of a wavy surface profile 29
pK_a	Decadic logarithm of an acid dissociation constant K_a 43
R	Transfer resistance 13
R_a	Air-side transfer resistance 15
R_g	Universal gas constant 23
R_w	Water-side transfer resistance 15
ρ	Mass density 6
ρ_a	Air density 9
ρ_N	Number density 20
ρ_w	Water density 9
Sc	Schmidt number, defined as the quotient of the kinematic viscosity ν and the diffusion coefficient D 6
σ	Absorption cross section 20
σ_d	Decline parameter 29
t	Time 7
T	Temperature 22
τ	Shear stress 6
tr	Transmittance 20
u	Along-wind horizontal component of $\vec{u}$ 8
U_{10N}	Wind speed at 10 m height adjusted to neutral conditions 106
u_s	Surface velocity 10
u_*	Friction velocity 9
$\vec{u}$	Velocity field 6
$\bar{\vec{u}}$	Mean velocity field 7
$\vec{u}'$	Velocity field fluctuations 7

v	Cross-wind horizontal component of $\vec{u}$ 8
V	Volume 10
V_a	Air volume 30
$\dot{V}_\mathrm{in}$	Inward gas flux 30
$\dot{V}_\mathrm{out}$	Leaking rate 30
$\vec{v}$	Eigen vector of differential equation 31
V_w	Water volume 30
w	Vertical component of $\vec{u}$ 8
x	Along-wind horizontal coordinate 8
$\vec{x}$	Position vector 7
y	Cross-wind horizontal coordinate 8
z	Vertical coordinate 8
z_0	Roughness length 11
z_l	Viscous boundary layer thickness 11
z_*	Mass boundary layer thickness 15

Abbreviations

FOV	Field Of View 44
HF	High Fetch 41
LF	Low Fetch 41
LHC	Laser Height Camera 25
LIF	Laser Induced Fluorescence 25
PIV	Particle Image Velocimetry 25
PSV	Particle Streak Velocimetry 25
PTFE	Polytetrafluoroethylene 38
PTV	Particle Tracking Velocimetry 27
PVC	Polyvinyl Chloride 38
ROI	Region Of Interest 44

Bibliography

Adrian, R. J. and J. Westerweel (2011). *Particle Image Velocimetry*. Cambridge.

Ahmed, S. M. and V. Kumar (1992). "Quantitative photoabsorption and fluorescence spectroscopy of SO_2 at 188-231 and 278.7-320 nm". In: *J. Quant. Spectrosc. Radiat. Transf.* 47 (5), pp. 359–373. DOI: 10.1016/0022-4073(92)90038-6.

Aubinet, M., T. Vesala and D. Papale (2012). *Eddy Covariance: A Practical Guide to Measurement and Data Analysis*. Springer Atmospheric Sciences. Springer. ISBN: 978-94-007-2351-1. DOI: 10.1007/978-94-007-2351-1.

Bauer, M. et al. (2009). "Exterior surface damage of calcium fluoride outcoupling mirrors for DUV lasers". In: *Opt. Express* 17.10, pp. 8253–8263. DOI: 10.1364/OE.17.008253.

Beer, A. (1852). "Bestimmung der Absorption des rothen Lichts in farbigen Flüssigkeiten". In: *Annalen der Physik und Chemie* 86.5, pp. 78–88.

Belton, M. J. S. (1982). "An interpretation of the near-ultraviolet absorption spectrum of SO_2: Implications for Venus, Io, and laboratory measurements". In: *Icarus* 52.1, pp. 149–165. DOI: 10.1016/0019-1035(82)90175-0.

Bopp, M. (2018). "Air-flow and stress partitioning over wind waves in a linear wind-wave facility". PhD thesis. Institute of Environmental Physics, Heidelberg University. DOI: 10.11588/heidok.00024741.

Bouguer, P. (1729). *Essai d'optique, sur la gradation de la lumière*. Paris, France: Claude Jombert.

Brooks, S. D. et al. (2019). "Biogeochemical Coupling between Ocean and Atmosphere – A Tribute to the Lifetime Contribution of Robert A. Duce". In: *J. Atmos. Sci.* 76.11, pp. 3289–3298. DOI: 10.1175/JAS-D-18-0305.1.

Buckley, M. P. and F. Veron (2018). "The turbulent airflow over wind generated surface waves". In: *Eur. J. Mech. B-Fluid*. DOI: 10.1016/j.euromechflu.2018.04.003.

Burkholder, J. B. et al. (2015). "Chemical Kinetics and Photochemical Data for Use in Atmospheric Studies, Evaluation No. 18". In: *JPL Publication 15-10, Jet Propulsion Laboratory, Pasadena*. URL: http://jpldataeval.jpl.nasa.gov (visited on 2019-11-03).

Coantic, M. (1986). "A model of gas transfer across air–water interfaces with capillary waves". In: *J. Geophys. Res.* 91, pp. 3925–3943. DOI: 10.1029/JC091iC03p03925.

Danckwerts, P. V. (1951). "Significance of liquid-film coefficients in gas absorption". In: *Ind. Eng. Chem.* 43, pp. 1460–1467. DOI: 10.1021/ie50498a055.

Danielache, S. O. et al. (2008). "High-precision spectroscopy of ^{32}S, ^{33}S, and ^{34}S sulfur dioxide: Ultraviolet absorption cross sections and isotope effects". In: *J. Geophys. Res-Atmos.* 113.D17. DOI: 10.1029/2007JD009695.

Deacon, E. L. (1977). "Gas transfer to and across an air-water interface". In: *Tellus A* 29, pp. 363–374. DOI: 10.3402/tellusa.v29i4.11368.

Degreif, K. (2006). "Untersuchungen zum Gasaustausch - Entwicklung und Applikation eines zeitlich aufgelösten Massenbilanzverfahrens". PhD Thesis. Institute of Environmental Physics, Heidelberg University. DOI: 10.11588/heidok.00006120.

Edson, J. B. et al. (2013). "On the exchange of momentum over the open ocean". In: *J. Phys. Oceanogr.* 43, pp. 1589–1610. DOI: 10.1175/JPO-D-12-0173.1.

Friedl, F. (2013). "Investigating the Transfer of Oxygen at the Wavy Air-Water Interface under Wind-Induced Turbulence". PhD thesis. Institute of Environmental Physics, Heidelberg University. DOI: 10.11588/heidok.00014582.

Friman, S. I. and B. Jähne (2019). "Investigating SO_2 transfer across the air–water interface via LIF". In: *Exp. Fluids* 60. DOI: 10.1007/s00348-019-2713-6.

Gon Cho, M. (2014). *UV lens pentax*. Slide show. URL: https://www.slideshare.net/mingoncho7/uv-lens-pentax (visited on 2019-11-03).

Gruber, N. et al. (2019). "The oceanic sink for anthropogenic CO2 from 1994 to 2007". In: *Science* 363.6432, pp. 1193–1199. ISSN: 0036-8075. DOI: 10.1126/science.aau5153.

Haynes, W. M., ed. (2016). *CRC Handbook of Chemistry and Physics, 97th Edition*. CRC Press. ISBN: 9781498754293.

Henry, W. (1803). "Experiments on the Quantity of Gases Absorbed by Water, at Different Temperatures, and under Different Pressures". In: *Philos. Trans. Royal Soc.* 93, pp. 29–274. DOI: 10.1098/rstl.1803.0004.

Herlina and G. H. Jirka (2008). "Experiments on gas transfer at the air–water interface induced by oscillating grid turbulence". In: *J. Fluid Mech.* 594, pp. 183–208. DOI: 10.1017/S0022112007008968.

Herzog, A. (2010). "Imaging of Water-sided Gas-Concentration Fields at a Wind-Driven, Wavy Air-Water Interface". PhD thesis. Institute of Environmental Physics, Heidelberg University. DOI: 10.11588/heidok.00011220.

Higbie, R. (1935). "The rate of absorption of a pure gas into a still liquid during short periods of exposure". In: *Trans. Am. Inst. Chem. Eng.* 31, pp. 365–389.

Ho, D. T. et al. (2011). "Toward a universal relationship between wind speed and gas exchange: Gas transfer velocities measured with $^3He/SF_6$ during the Southern Ocean Gas Exchange Experiment". In: *J. Geophys. Res.* 116, C00F04. DOI: 10.1029/2010JC006854.

Honza, R. et al. (2017). "Flame imaging using planar laser induced fluorescence of sulfur dioxide". In: *Appl. Phys. B* 123.9, p. 246. DOI: 10.1007/s00340-017-6823-7.

Horn, J. (2013). "Hochaufgelöste optische Wellenhöhenmessung am Aeolotron mit Laser-induzierter Fluoreszenz". Bachelor's thesis. Institute of Environmental Physics, Heidelberg University.

Hsu, C. T., E. Y. Hsu and R. L. Street (1981). "On the structure of turbulent flow over a progressive water wave: theory and experiment in a transformed, wave-following coordinate system". In: *J. Fluid Mech.* 105, pp. 87–117. DOI: 10.1017/S0022112081003121.

Hui, M. and S. A. Rice (1972). "Decay of fluorescence from single vibronic states of SO_2". In: *Chem. Phys. Lett.* 17.4, pp. 474–478. DOI: 10.1016/0009-2614(72)85083-8.

IPCC (2013). *Climate Change 2013: The Physical Science Basis. Contribution of Working Group I to the Fifth Assessment Report of the Intergovernmental Panel on Climate Change*. Cambridge, United Kingdom and New York, NY, USA: Cambridge University Press, p. 1535. ISBN: ISBN 978-1-107-66182-0. DOI: 10.1017/CBO9781107415324.

Jähne, B. (1982). "Trockene Deposition von Gasen über Wasser (Gasaustausch)". In: *Austausch von Luftverunreinigungen an der Grenzfläche Atmosphäre/Erdoberfläche, Zwischenbericht für das Umweltbundesamt zum Teilprojekt 1: Deposition von Gasen, BleV-R-64.284-2*. Ed. by D. Flothmann. Frankfurt: Battelle Institut. DOI: 10.5281/zenodo.10278.

– (1985). "Transfer processes across the free water interface". Habilitation thesis. Institute of Environmental Physics, Heidelberg University. DOI: 10.11588/heidok.00016798.

– (2009). "Air-sea gas exchange". In: *Encyclopedia of Ocean Sciences*. Ed. by J. H. Steele, K. K. Turekian and S. A. Thorpe. 2nd ed. Elsevier, pp. 147–156. DOI: 10.1016/B978-012374473-9.00642-1.

– (2012). *Digitale Bildverarbeitung und Bildgewinnung*. 7th ed. Berlin: Springer. DOI: 10.1007/9783642049521.

– (2019). "Air-Sea Gas Exchange". In: *Encyclopedia of Ocean Sciences*. 3rd ed. in press. Academic Press. ISBN: 9780128130810. URL: https://www.elsevier.com/books/encyclopedia-of-ocean-sciences/cochran/978-0-12-813081-0.

Jähne, B. et al. (1989). "Investigating the transfer process across the free aqueous boundary layer by the controlled flux method". In: *Tellus B* 41B.2, pp. 177–195. DOI: 10.3402/tellusb.v41i2.15068.

Kadoya, K., N. Matsunaga and A. Nagashima (1985). "Viscosity and Thermal Conductivity of Dry Air in the Gaseous Phase". In: *J. Phys. Chem. Ref. Data* 14.4, pp. 947–970. DOI: 10.1063/1.555744.

Keeling, R. F. and C. D. Keeling (2017). "Atmospheric Monthly In Situ CO2 Data-Mauna Loa Observatory, Hawaii". In: *Scripps CO2 program data. UC San Diego Library Digital Collections*.

Kiefhaber, D. et al. (2014). "High-speed imaging of short wind waves by shape from refraction". In: *J. Europ. Opt. Soc. Rap. Public.* 9, p. 14015. DOI: 10.2971/jeos.2014.14015.

Kiskin, N. et al. (2002). "The efficiency of two-photon photolysis of a "caged" fluorophore, o-1-(2-nitrophenyl)ethylpyranine, in relation to photodamage of synaptic terminals". In: *Eur. Biophys. J.* 30, pp. 588–604. DOI: 10.1007/s00249-001-0187-x.

Klebanoff, P. S. (1955). *Characteristics of turbulence in boundary layer with zero pressure gradient*. Report 1247. Nat. Advis. Com. Aeronaut.

Klein, A. (2019). "The Fetch Dependency of Small-Scale Air-Sea Interaction Processes at Low to Moderate Wind Speeds". PhD Thesis. Institute of Environmental Physics, Heidelberg University. DOI: 10.11588/heidok.00026559.

Koziel, J. A., V. P. Aneja and B. Baek (2006). "Gas-to-Particle Conversion Process between Ammonia, Acid Gases, and Fine Particles in the Atmosphere". In: *Agricultural and Biosystems Engineering Publications* 67. URL: https://lib.dr.iastate.edu/abe_eng_pubs/67.

Krah, N. (2014). "Visualization of air and water-sided concentration profiles in laboratory gas exchange experiments". PhD thesis. Institute of Environmental Physics, Heidelberg University. DOI: 10.11588/heidok.00016895.

Krall, K. E. et al. (2019). "Air–sea gas exchange at wind speeds up to 85 m/s". In: *Ocean Sci.* 15, pp. 1783–1799. DOI: 10.5194/os-15-1783-2019.

Krall, K. E. (2013). "Laboratory Investigations of Air-Sea Gas Transfer under a Wide Range of Water Surface Conditions". PhD Thesis. Institute of Environmental Physics, Heidelberg University. DOI: 10.11588/heidok.00014392.

Kräuter, C. (2015). "Visualization of air-water gas exchange". PhD thesis. Institute of Environmental Physics, Heidelberg University. DOI: 10.11588/heidok.00018209.

Kühlein, F. (2019). "Vertikaler Impulstransport bei kleinen Windwirklängen in einem linearen Wind-Wellenkanal". Bachelor's thesis. Institut for Environmental Physics, Heidelberg University. DOI: 10.11588/heidok.00021977.

Kundu, P., I. Cohen and D. Dowling (2015). *Fluid Mechanics*. 6th. San Diego, CA: Academic Press, Elsevier.

Kunz, J. and B. Jähne (2018). "Investigating small scale air-sea exchange processes via thermography". In: *Front. Mech. Eng.* DOI: 10.3389/fmech.2018.00004.

Lambert, J. (1760). *Photometria sive de mensura et gradibus luminis, colorum et umbrae*. Augsburg, Germany: Eberhardt Klett.

Landau, L. D. and E. Lifshitz (1987). *Fluid Mechanics*. 2nd. Vol. 6. Course of Theoretical Physics. Pergamon Press.

Laufer, J. (1954). *The structure of turbulence in a fully developed pipe flow*. Report 1174. Nat. Advis. Com. Aeronaut.

Le Quéré, C. et al. (2018). "Global Carbon Budget 2017". In: *Earth System Science Data* 10.1, pp. 405–448. DOI: 10.5194/essd-10-405-2018.

Mackay, D. and A. T. K. Yeun (1983). "Mass transfer coefficient correlations for volatilization of organic solutes from water". In: *Environ. Sci. Technol.* 17.4, pp. 211–217. DOI: 10.1021/es00110a006.

Manatt, S. L. and A. L. Lane (1993). "A compilation of the absorption cross-sections of SO_2 from 106 to 403 nm". In: *J. Quant. Spectrosc. Ra* 50.3, pp. 267–276. ISSN: 0022-4073. DOI: 10.1016/0022-4073(93)90077-U.

Matsumi, Y., H. Shigemori and K. Takahashi (2005). "Laser-induced fluorescence instrument for measuring atmospheric SO_2". In: *Atmos. Environ.* 39.17, pp. 3177–3185. ISSN: 1352-2310. DOI: 10.1016/j.atmosenv.2005.02.023.

Mohn, J. and L. Emmenegger (2014). "Determination of Sulphur Dioxide by Pulsed UV-Fluorescence". In: *Environ. Technol.* 76, pp. 1–11.

Münnich, K. and D. Flothmann (1975). "Gas exchange in relation to other air/sea interaction phenomena". In: *SCOR Workshop on "Air/Sea Transport of Pollutants", Miami*. DOI: 10.5281/zenodo.13345.

Münsterer, T. (1996). "LIF Investigation of the Mechanisms Controlling Air–Water Mass Transfer at a Free Interface". PhD thesis. Institute of Environmental Physics, Heidelberg University. DOI: 10.5281/zenodo.14542.

Musker, A. J. (1979). "Explicit Expression for the Smooth Wall Velocity Distribution in a Turbulent Boundary Layer". In: *AIAA Journal* 17.6, pp. 655–657. DOI: 10.2514/3.61193.

Nagel, L., K. E. Krall and B. Jähne (2015). "Comparative heat and gas exchange measurements in the Heidelberg Aeolotron, a large annular wind-wave tank". In: *Ocean Sci.* 11, pp. 111–120. DOI: 10.5194/os-11-111-2015.

Nairn, J. and W. Forster (2015). "Photostability of pyranine and suitability as a spray drift tracer". In: *New Zealand Plant Protection* 68, pp. 32–37. DOI: 10.30843/nzpp.2015.68.5795.

Nielsen, R. (2004). "Gasaustausch - Entwicklung und Ergebnis eines schnellen Massenbilanzverfahrens zur Messung der Austauschparameter". PhD thesis. Institute of Environmental Physics, Heidelberg University. DOI: 10.11588/heidok.00005032.

Papst, M. (2019). "Development of a method for quantitative imaging of air-water gas exchange". Master's thesis. Institute of Environmental Physics, Heidelberg University. DOI: 10.11588/heidok.00027271.

Pearson, K. (1905). "The problem of the random walk". In: *Nature* 72.294. DOI: 10.1038/072294b0.

Perkins, R. (May 2019). Private communication.

Pettenkofer, M. (1858). *Über den Luftwechsel in Wohngebäuden: Besprechung allgemeiner auf die Ventilation bezüglicher Fragen*. München: Cotta.

Porter, J. G. et al. (2020). "Air/sea transfer of highly soluble gases over coastal waters". In: *Geophys. Res. Lett.* DOI: 10.1029/2019GL085286.

Raffel, M. et al. (2007). *Particle Image Velocimetry: A Practical Guide*. 2nd ed. Heidelberg, Berlin: Springer-Verlag. DOI: 10.1007/978-3-540-72308-0.

Reichardt, H. (1951). "Vollständige Darstellung der turbulenten Geschwindigkeitsverteilung in glatten Leitungen". In: *Zeitschrift für angewandte Mathematik und Mechanik* 31, pp. 208–219.

Rollins, A. W. et al. (2016). "A laser-induced fluorescence instrument for aircraft measurements of sulfur dioxide in the upper troposphere and lower stratosphere". In: *Atm. Meas. Tech.* 9.9, pp. 4601–4613. DOI: 10.5194/amt-9-4601-2016.

Schlichting, H. and K. Gersten (2006). *Grenzschicht-Theorie*. 10th ed. Heidelberg, Germany: Springer-Verlag. DOI: 10.1007/3-540-32985-4.

Schott (n.d.). *Schott Borofloat 33 - Produktinformation*. Tech. rep.

Schwarz, K. (2016). "Spatio-Temporal Measurements of Water-Wave Height and Slope using Laser-Induced Fluorescence and Splines". Bachelor's thesis. Institut for Environmental Physics, Heidelberg University. DOI: 10.11588/heidok.00021977.

Sick, V. (2002). "Exhaust-gas imaging via planar laser-induced fluorescence of sulfur dioxide". In: *Appl. Phys. B-Lasers O* 74, pp. 461–463. DOI: 10.1007/s003400200813.

Simeonsson, J. B., A. Matta and R. Boddeti (2012). "Direct Measurement of SO_2 in Air by Laser Induced Fluorescence Spectrometry Using a Nontunable Laser Source". In: *Anal. Lett.* 45.8, pp. 894–906. DOI: 10.1080/00032719.2012.655681.

Spalding, D. B. (1961). "A Single Formula for the "Law of the Wall"". In: *J. Appl. Mech.* 28, p. 455. DOI: 10.1115/1.3641728.

Thurber, M. C. et al. (1998). "Measurements and modeling of acetone laser-induced fluorescence with implications for temperature-imaging diagnostics". In: *Appl. Optics* 37.21, pp. 4963–4978. DOI: 10.1364/AO.37.004963.

Townsend, A. A. (1976). *The structure of turbulent shear flow*. 2nd ed. Cambridge University Press, London.

Troitskaya, Y. et al. (2011). "Statistical parameters of the air turbulent boundary layer over steep water waves measured by the PIV technique". In: *J. Phys. Oceanogr.* 41, pp. 1421–1454. DOI: 10.1175/2011JPO4392.1.

Varlas, G. et al. (2018). "Implementation of a two-way coupled atmosphere-ocean wave modeling system for assessing air-sea interaction over the Mediterranean Sea". In: *Atmos. Res.* 208. High Impact Atmospheric Processes in the Mediterranean, pp. 201–217. ISSN: 0169-8095. DOI: 10.1016/j.atmosres.2017.08.019.

Wanninkhof, R. (1992). "Relationship between wind speed and gas exchange over the ocean". In: *J. Geophys. Res.* 97 (C5), pp. 7373–7382. DOI: 10.1029/92JC00188.

Wanninkhof, R. et al. (2009). "Advances in quantifying air-sea gas exchange and environmental forcing". In: *Annu. Rev. Marine Sci.* 1, pp. 213–244. DOI: 10.1146/annurev.marine.010908.163742.

Warken, P. (2010). "Hochauflösende LIF-Methode zur Messung von Sauerstoffkonzentrationsprofilen in der wasserseitigen Grenzschicht". Diploma thesis. Institute of Environmental Physics, Heidelberg University. DOI: 10.5281/zenodo.2560318.

Watson, A. J., R. C. Upstill-Goddard and P. S. Liss (1991). "Air-sea exchange in rough and stormy seas measured by a dual tracer technique". In: *Nature* 349.6305, pp. 145–147. DOI: 10.1038/349145a0.

Whitman, W. G. (1923). "The two-film theory of gas absorption". In: *Chemical and Metallurgical Engineering* 29.4, pp. 146–148.

Winter, R. (2011). "Fluorescent Tracers for air-sided Concentration Profile Measurements at the Air-Water Interface". PhD thesis. Institute of Environmental Physics, Heidelberg University. DOI: 10.11588/heidok.00012105.

Wu, C. Y. R. et al. (2000). "Measurements of high-, room-, and low-temperature photoabsorption cross sections of SO_2 in the 2080- to 2950-Å region, with application to Io". In: *Icarus* 145.1, pp. 289–296. DOI: 10.1006/icar.1999.6322.

Yaws, C. L. (2014). *Transport Properties of Chemicals and Hydrocarbons*. Gulf Professional Publishing. DOI: 10.1016/C2013-0-12644-X.

Danksagung

An dieser Stelle möchte ich mich bei allen bedanken, die mich während meiner Doktorarbeit unterstützt und begleitet haben.

Zuallererst gilt mein Dank Herrn Prof. Dr. Bernd Jähne, der mir die Arbeit an diesem spannenden Projekt ermöglicht und mich bei der Durchführung betreut hat. Zahlreiche anregende Diskussionen, hilfreiche Vorschläge und Ideen seinerseits waren sehr förderlich für das Gelingen dieser Arbeit ebenso wie die relative Freiheit während der Arbeit und das stete Vertrauen, die meine Selbständigkeit gefördert haben. Auch für die Möglichkeit, an der Messkampagne in Miami (USA), der SOLAS Summer School in Cargèse (Frankreich) und der SOLAS Konferenz in Sapporo (Japan) teilzunehmen, bedanke ich mich.

Prof. Dr. André Butz danke ich für die Übernahme des Zweitgutachtens.

Im Folgenden möchte ich einigen 'Windis' meinen Dank aussprechen, die zu der stets angenehmen, fast schon familiären Atmosphäre im Windkanal-Labor beigetragen haben, unter anderem während der gemeinsamen Mittagspausen ('Frage des Tages') sowie bei gelegentlich stattfindenden Kaffeerunden.

Besonders möchte ich mich bei Dr. Kerstin Krall bedanken, unter anderem für das für jede Frage stets offene Ohr, für jeden experimentellen Kniff, den sie mir in den letzten dreieinhalb Jahren beigebracht hat, für viele bereichernde und anregende Unterhaltungen und ihre optimistische Grundeinstellung, dass nichts unmöglich ist und jedes Problem lediglich eine Herausforderung, die es zu lösen gilt, darstellt.

Dr. Günther Balschbach danke ich für zahlreiche Erklärungen und Ratschläge, hilfreiche Diskussionen und motivierende Anregungen. Und für den Kuchen.

Ich bedanke mich bei meinem ehemaligen Bürokollegen Dr. Maximilian Bopp für ausführliche Erläuterungen bei der Übergabe der PSV- und LHC-Messtechniken und für manche Problembehebung aus der Ferne.

Nicolas Roth danke ich sowohl für Hilfestellungen beim Experimentieren als auch seine stets gute Laune, die geradezu ansteckend ist.

Philipp Voigt möchte ich 'tusen takk' sagen, für seine tatkräftige Hilfe beim Justieren von Optiken und Programmierproblemlösungen sowie für seine motivierende Art und sein Interesse an fast allem.

Darüber hinaus danke ich den ehemaligen 'Windis' Leonie Flothow, Habib Gahbiche, Dr. Angelika Klein, Dr. Jakob Kunz, Fritz Kühlein, Maximilian Papst, Christin Proß, Leif-Sebastian Rembeck und Cornelis Schwenk.

Die Messkampagne im SUSTAIN lab an der RSMAS, University of Miami mit Dr. Kerstin Krall und Jan Bug war ein einmaliges Erlebnis. I want to thank Prof. Brian Haus, PhD, for giving us the opportunity for experiments in his lab. What a great experience to produce a hurricane in the lab, to watch it and not get (too) wet.

Für das sorgfältige Korrekturlesen (von Teilen) der Thesis bedanke ich mich bei Dr. Kerstin Krall, Prof. Dr. Bengt Friman, Dr. Udo Friman-Gayer, Dr. Günther Balschbach und Philipp Voigt.

Ich danke Karin Kruljac für die Hilfe bei administrativen Aufgaben.

Bei den Mitarbeitern der IUP Werkstatt bedanke ich mich für ihre Unterstützung, u.a. für das Bohren der Löcher in den Glasdeckel des Wind-Wellen-Kanals.

Xiton Photonics, im Speziellen Thorsten Bauer, danke ich für die freundliche Leihgabe des UV-Lasers und die Serviceleistungen am Laser.

Prof. Dr. Ulrich Platt und Prof. Dr. Norbert Frank möchte ich für die Beratung in Karrierefragen danken, ebenso wie Prof. Dr. Thomas Walther für das stete Interesse an meinem akademischen Werdegang.

Danke auch an die HGS MathComp: durch meine Mitgliedschaft dort habe ich viele interdisziplinäre Projekte kennen gelernt. Für die Bereitstellung der Überbrückungsfinanzierung danke ich der HGSFP.

Ganz besonders möchte ich auch meiner lieben Familie, meinen Eltern Gertraud und Bengt sowie meinem Bruder Torsten, für ihr Verständnis, ihre Geduld und uneingeschränkte Unterstützung auf meinem bisherigen Lebensweg bei allem, was ich mir vornehme, danken.

Last but not least danke ich meinem wunderbaren Mann Udo, der mich in allen meinen Entscheidungen unterstützt und immer für mich da ist.